Eclipsing Binaries and Period Changes in the SuperWASP Archive

Thesis

Eclipsing Binaries and Period Changes in the SuperWASP Archive

Marcus Lohr BSc (Open) MPhil MA PhD (Cantab)

Submitted for the degree of PhD on 22 September 2014

Astronomy Discipline (Department of Physical Sciences)

The Open University

Abstract

The aim of this research project has been to investigate eclipsing binaries using archival data from the SuperWASP (Wide Angle Search for Planets) survey, and specifically to search for evidence of orbital period variations. The short cadence and long time base of SuperWASP light curves make them highly suitable for variable star research of many kinds, and the size of the database (∼30 million objects) allows for the discovery and study of rare objects and stellar types.

Techniques optimized for analyzing SuperWASP data were developed over the course of the research, using custom IDL codes, and proved successful in measuring orbital periods and detecting period changes in real and synthetic test data. Employing these, original results were achieved in a range of areas. A sample of 143 eclipsing binary candidates were found with periods close to the short-period limit of the period distribution for main sequence binaries, which shed light on the likely cause of the limit. Significant period increases and decreases were detected in many of these, and several individual objects were followed up with spectroscopic and multicolour photometric observations, by ourselves and others, to allow confirmation of their binary nature and modelling to determine system and component parameters. Amongst these were a probable close triple system containing a low-mass contact binary, and a doubly-eclipsing quintuple system, only the sixth known of its kind. Eleven post-common-envelope eclipsing binaries were also studied for evidence of period changes, potentially associated with circumbinary planets; our findings add to the ongoing debate on the reality and stability of planetary systems in such environments. Finally, we used our findings on period changes in ∼14000 candidate SuperWASP eclipsing binaries of all types to estimate the higher-order multiplicity fraction of such systems.

(294 words)

Acknowledgements

Thanks are first due to my primary supervisor Andrew Norton, for suggesting this research project in the first place, and for his unfailing guidance and encouragement over the last three years. I have also benefited from a number of discussions with my secondary supervisor Ulrich Kolb, and with other members of the Department of Physical Science at the Open University. My coauthors on the five papers which form the basis of five chapters in Part III of this thesis have in many cases made valuable comments and suggestions on the draft versions, as have the anonymous referees of those papers. I am also grateful to colleagues who have furnished me with observational data or results useful for my work: Simon Hodgkin, Ed Gillen, David Boyd, Richard Busuttil and Chris Koen in particular. Finally, my partner has provided me with enduring support throughout this PhD.

This doctoral research was supported by the Science and Technology Funding Council and the Open University.

The WASP project is funded and operated by Queen's University Belfast, the Universities of Keele, St. Andrews and Leicester, the Open University, the Isaac Newton Group, the Instituto de Astrofisica de Canarias, the South African Astronomical Observatory and by STFC.

Some parts of this work were previously published in the following refereed journal papers (details given in the text):

Lohr M E, Norton A J, Kolb U C, Anderson D R, Faedi F and West R G (2012) 'Period change in three SuperWASP eclipsing binary candidates near the short-period limit', *Astronomy & Astrophysics*, 542, A124.

Lohr M E, Norton A J, Kolb U C, Maxted P F L, Todd I and West R G (2013) 'Period and period change measurements for 143 SuperWASP eclipsing binary candidates near the short-period limit and discovery of a doubly eclipsing quadruple system', *Astronomy & Astrophysics*, 549, A86.

Lohr M E, Norton A J, Kolb U C and Boyd D R S (2013) 'One, two or three stars? An investigation of an unusual eclipsing binary candidate undergoing dramatic period changes', *Astronomy & Astrophysics*, 558, A71.

Lohr M E, Hodgkin S T, Norton A J and Kolb U C (2014) 'Parameters of two low-mass contact eclipsing binaries near the short-period limit', *Astronomy & Astrophysics*, 563, A34.

Lohr M E, Norton A J, Anderson D R, Cameron A C, Faedi F, Haswell C A, Hellier C, Hodgkin S T, Horne K, Kolb U C, Maxted P F L, Pollacco D, Skillen I, Smalley B, West R G and Wheatley P J (2014) 'Period and amplitude variations in post-common-envelope eclipsing binaries observed with SuperWASP', *Astronomy & Astrophysics*, 566, A128.

Contents

List of Figures

List of Tables

Introduction

This thesis is the result of a research project for which the initial proposed goal was to "use SuperWASP data to investigate aspects of stellar variability". Since the SuperWASP (Wide Angle Search for Planets) survey was primarily designed to search for exoplanetary transit signatures in the light curves of stars, this use of its archival data to study photometric variations in the stars themselves would inevitably be a repurposing of the data: an instance of serendipitous astronomical research. At a time of economic challenges for the astronomical community, archival data mining and recycling of this kind can be seen as an inexpensive and efficient way to advance scientific understanding.

There is also much scope for making worthwhile discoveries from such a large archive. Since it was already clear that SuperWASP could detect variable stars of many kinds, this project had a more specific focus on "those variable stars for which evidence of a varying period may be detected"; stars which might be called variably-variable. Four main areas of potential enquiry were originally considered: the cause of the varying periods and amplitudes of some RR Lyrae stars (the Blazhko effect), ∼10000 of which are found in the archive; a statistical analysis of the hundreds of thousands of SuperWASP stars exhibiting rotational modulation associated with latitudinal migration of star spots; a search for third bodies in the archive's tens of thousands of eclipsing binaries via cyclical orbital period variations; and a speculative hunt for binaries approaching stellar merger, which would be expected to exhibit exponential orbital period decrease.

It soon became apparent that the abundant evidence in SuperWASP data for period changes in eclipsing binaries provided a more-than-ample foundation for a PhD project, and so this research has been mainly directed towards the latter two of these suggested topics (though evidence for varying periods in pulsating and rotating variables was also encountered in the course of the work). However, a number of unexpected discoveries were made while exploring SuperWASP's eclipsing binaries, and some of these were followed up with additional observations and analysis, allowing light to be shed on other areas of astrophysical interest not originally conceived as part of the project.

This thesis, then, is organized into three main parts. In Part I, the background to the project will be set out, addressing the significance of SuperWASP data in comparison with other similar surveys; the main types of stellar variability which might be encountered in such a survey; and the key astrophysical questions which research into variably-variable stars could hope to address. Part II describes the gradual development and refining of analytical methods suited to determining orbital periods and detecting period changes in SuperWASP eclipsing binary light curves; it concludes with a description of various tests carried out to check the validity of the custom-written codes. Part III is the longest: it presents, in broadly chronological order, the main results of the research project, in the form of seven case studies, five of which are closely based upon my first-author published papers.

Part I

Background

Chapter 1

SuperWASP in context

In this first chapter, the SuperWASP project will be described in the context of other comparable recent surveys. Of particular interest is the capacity of these surveys to detect and study variable stars.

1.1 Characterizing sky surveys

SuperWASP is one of a large and growing number of wide-field surveys dedicated to time domain astronomy i.e. repeatedly observing the same region of the sky to reveal object variability over time. Djorgovski *et al.* (2013) review the field of sky surveys in general, and provide a number of useful definitions and distinctions (e.g. they characterize wide-field surveys as those covering "at least of the order of $\sim$1% of the entire sky"), together with a listing of major surveys categorized according to the regions of "observable parameter space" they cover (see Fig. 1.1).

As a minimum, they note that "[e]ach survey covers some solid angle (Ω), over some wavelength range (λ), and with some dynamical range of fluxes (F)". The synoptic surveys to be discussed here, however, also must be distinguished according to cadence: the time between repeated observations of a given field, which determines the minimum period of variation detectable i.e. twice the

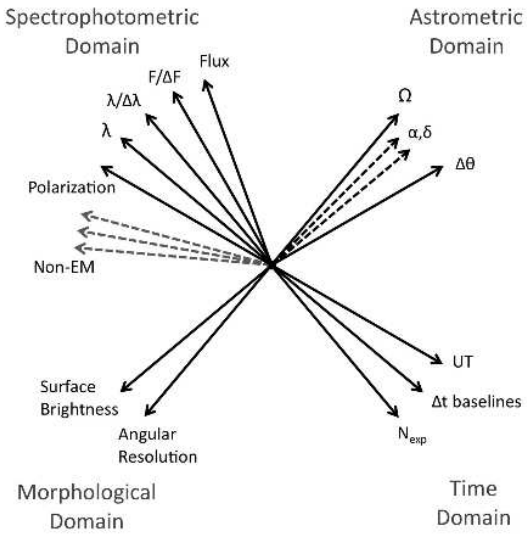

Figure 1.1: Schematic illustration of observable parameter space for sky surveys (from Djorgovski *et al.* (2013), Fig. 1)

cadence. The total duration of operation of a survey is likewise relevant in determining the maximum detectable period of variation.

Survey parameters are sometimes combined into a single "figure of merit" such as the etendue: "the product of the telescope area, A, and the solid angle subtended by the individual exposures, Ω"; however, Djorgovski *et al.* dismiss this as merely characterizing instrumental properties, and suggest a number of other figures of merit more appropriate to the scientific goals of particular survey types. None seem optimal for capturing the usefulness of different surveys in detecting and studying variable stars specifically (as opposed to transient events such as supernovae), so Table 1.1 includes a range of parameters for the major surveys considered here, and the following sections discuss their differences and capabilities more qualitatively.

1.2 SuperWASP

The UK's Wide Angle Search for Planets project (Pollacco *et al.*, 2006; Haswell, 2010) began in 2000 with the primary aim of finding exoplanetary candidates by

Survey name	Magnitude range	Sky area covered	Cadences	Duration of operation
SuperWASP	V ∼8–15	whole sky	6–40 mins	7–9 years
OGLE	down to V ∼22 and I ∼21	∼100 sq. deg. near Galactic Bulge + LMC and SMC	1–3 days	5–22 years
ASAS	down to V ∼14 and I ∼13	whole sky	1–3 days	8–14 years
Kepler	V ∼9–17	105 sq. deg. in Kepler field	1–30 mins	7 years (projected)
RATS	g' ∼12–23	110 fields totalling $>$ 31 sq. deg.	1–2 mins	3–8 days per field, over 5 years
CoRoT	R ∼5.5–16	selected fields within ∼20 sq. deg. area	1 s–15 mins	6 years
Gaia	V ∼2–20	whole sky	7–45 days	5 years (projected)
LSST	r ∼16–24	half of sky: 18000 sq. deg.	3–4 days	10 years (projected)

Table 1.1: Parameters of major surveys

the transit method. It has largely used low-cost commercially-available instruments e.g. 11 cm-diameter telephoto lenses coupled to CCDs, with an emphasis on high-cadence observations of bright stars over almost the whole sky. After the WASP0 single camera demonstrated notable successes (Mislis *et al.*, 2006), two SuperWASP facilities each with eight cameras were built and have been observing since 2003 (SuperWASP-N on La Palma, covering the northern hemisphere) and 2005 (SuperWASP-S at the South African Astronomical Observatory, for the southern hemisphere).

Although SuperWASP has been highly successful in detecting transiting exoplanets (92 published in refereed journals or announced at conference by late August 2014, out of 433[1]), its capabilities also make it highly suitable for detecting and studying variable stars of many kinds, including those with periods

[1] `exoplanet.eu/catalog-transit.php`

as short as about 20 minutes. By early May 2012 (after which general survey observations were no longer added to the database), its archive covered 1849 nights and 30874261 unique objects, and has produced results on short period eclipsing binaries (Norton *et al.*, 2011), periodic variables coincident with X-ray sources (Norton *et al.*, 2007), pulsating Am (Smalley *et al.*, 2011) and A (Holdsworth *et al.*, 2014) stars, cataclysmic variables (Thomas *et al.*, 2010) and a rare pre-helium white dwarf (Maxted *et al.*, 2012) amongst others[2]. It has even been used to obtain asteroid light curves (Parley *et al.*, 2005, 2008). Smith and WASP (2014) gives a recent summary of the project's achievements.

1.3 OGLE

The Optical Gravitational Lensing Experiment is a Polish project which has operated in four phases since 1992, with a primary goal of collecting gravitational microlensing events to give evidence for dark matter (Udalski *et al.*, 1997; Udalski, 2003; Udalski *et al.*, 2008). Located at Las Campanas Observatory in Chile, it has used 1 m and 1.3 m-diameter telescopes with CCD cameras containing first one chip (OGLE-I, OGLE-II), then a mosaic of eight (OGLE-III), and finally 32 chips (OGLE-IV), allowing relatively deep imaging of selected fields in the Magellanic Clouds and Galactic Bulge. In addition to identifying several thousand microlensing event candidates, it has discovered exoplanets (by the transit and microlensing methods), Kuiper Belt objects, and tens of thousands of variable stars[3]. In particular, the OGLE-III Catalog of Variable Stars[4] is discussed in 16 papers to date (Soszyński *et al.*, 2008a,b, 2009a,b,c; Poleski *et al.*, 2010a; Soszyński *et al.*, 2010a,c,b; Poleski *et al.*, 2010b; Soszyński *et al.*, 2011a; Graczyk *et al.*, 2011; Soszyński *et al.*, 2011c,b, 2013b,a), according to field and variable

[2] `www.superwasp.org/publications.htm`
[3] See publications section of `ogle.astrouw.edu.pl`
[4] `ogledb.astrouw.edu.pl/~ogle/CVS/`

type.

1.4 ASAS

The All Sky Automated Survey (Pojmański, 1997, 2002) is another Polish project, inspired by an appeal for wide-field variability surveys (Paczyński, 1997). Like SuperWASP, it has used relatively low-cost commercially-available hardware: 75 mm and 70 cm-diameter telephoto lenses with single-chip CCD cameras, with between one and four instruments operating simultaneously at various times in the project's history. After pilot phases, the current system has two ASAS-3N telescopes in Haleakala, Hawaii covering the northern hemisphere since 2006, and two ASAS-3 telescopes in Chile (next to OGLE's telescope) covering the southern hemisphere since 2000. Unlike SuperWASP and OGLE, its explicit science goal is to discover and catalogue bright variable stars over the whole sky, and to date it has classified ∼50000 variables, mainly in the southern sky[5] (Pojmański, 2002, 2003; Pojmański and Maciejewski, 2004, 2005; Pojmański *et al.*, 2005), and ∼1000 in the Kepler field (Pigulski *et al.*, 2009).

1.5 Kepler

NASA's Kepler mission uses a space-based 1.4 m-diameter telescope to monitor a single sky field containing over 150000 stars[6] (Borucki *et al.*, 2010). Originally proposed in 1992, launched in 2009, and continued as K2 in 2014 after a hiatus in 2013, its primary goal is to search for transiting terrestrial planets in the habitable zone. Its high-precision, short-cadence photometry makes it optimal for this role, but also for detecting stellar variability, especially at short periods and with low amplitudes e.g. Szabó *et al.* (2013) on the discovery of period doubling in RR

[5] `www.astrouw.edu.pl/asas/?page=acvs`
[6] `kepler.nasa.gov`

Lyrae stars, García (2013) on large-scale asteroseismology, Uytterhoeven *et al.* (2011) on pulsational variability in A–F type stars, and Coughlin *et al.* (2011) on low-mass eclipsing binaries.

1.6 RATS

The RApid Temporal Survey is a mainly-European project operating since 2003 (Ramsay and Hakala, 2005; Barclay *et al.*, 2011), which has used 2.2 m and 2.5 m telescopes with wide-field CCD cameras at La Palma and La Silla in Chile to study the faint variable sky at very high cadence. A particular goal was to search for new AM CVn systems, and several candidates have now been identified, amongst 1.2×10^5 variable objects of other kinds. Hundreds of contact binaries were identified and modelled approximately (Hakala *et al.*, 2012). The latest phase of RATS is a deep survey of the Kepler field to detect short-period variability which may be missed by Kepler's longer cadence observations (Ramsay *et al.*, 2014).

1.7 CoRoT

The COnvection, ROtation and planetary Transits space mission[7] (Auvergne *et al.*, 2009) is a French/ESA project first proposed in 1994, launched in 2006, and decommissioned in 2014 (though its scientific results are still being explored). It had two main goals: asteroseismology of 150 bright stars, and a search for exoplanetary transits around 200000 stars. The telescope's 30 cm-diameter mirror with 4 CCD cameras monitored multiple selected star fields within two regions in opposite directions on the sky, and the project has yielded results on variables including studies of pulsating B stars (Degroote *et al.*, 2011); the periods (mainly rotational) of a large sample of solar-type stars (Affer *et al.*,

[7] `smsc.cnes.fr/COROT/`

2012); and the discovery and analysis of an eclipsing binary containing a δ Scuti pulsator (da Silva *et al.*, 2014).

1.8 Other

Many other current and forthcoming surveys and projects are capable of yielding photometric data on variable stars, while not being direct comparators to SuperWASP for various reasons, and this brief review cannot pretend to cover all of them. The VISTA Variables in the Vía Láctea (VVV) survey[8] is an ongoing five-year ESO project to monitor variability in the Galactic bulge and adjacent disk, using a near-infrared filter (Minniti *et al.*, 2010), which is hoped to result in a catalogue of $\sim 10^6$ variables. The related VISTA Magellanic Cloud (VMC) survey has obtained ~ 2000 high-quality light curves for RR Lyrae and Cepheids (Ripepi *et al.*, 2012). NASA's Wide-field Infrared Survey Explorer (WISE) also surveyed in the infrared during its 2010 orbital mission, and over 8000 variable stars have been automatically classified in its source catalogue[9], mainly of Algol, RR Lyrae and W UMa types (Masci *et al.*, 2014).

The Catalina Real-Time Transient Survey (CRTS), associated with the Catalina Sky Survey (CSS)[10] which searches for near-Earth objects, uses three medium-sized telescopes in Arizona and Australia to survey selected fields with varying cadences; about 10% of its few thousand real-time transient alerts have been for high-amplitude periodic variables such as Mira and RR Lyrae stars (Mahabal *et al.*, 2011). The three phases of the Robotic Optical Transient Search Experiment (ROTSE), although intended primarily to observe gamma-ray bursts in the optical[11], have revealed large numbers of variable stars, and resulted in the production of the Northern Sky Variability Survey (NSVS), containing some 14

[8] `mwm.astro.puc.cl/mw/index.php/VVV_Survey:About`
[9] `wise2.ipac.caltech.edu/docs/release/allsky/`
[10] `www.lpl.arizona.edu/css/`
[11] `www.rotse.net`

million objects[12] (Akerlof *et al.*, 2000; Woźniak *et al.*, 2004), recently analyzed as containing $\sim 1.8 \times 10^6$ possible variable candidates[13] (Shin *et al.*, 2012).

Looking to the future, the Panoramic Survey Telescope & Rapid Response System (Pan-STARRS) consortium is embarking on a range of projects related to time domain astronomy[14] (Saglia *et al.*, 2012), ranging from detection of near-Earth objects to studying variability in M31, though since the wide field survey will only image each source 12 times, it is unlikely to reveal much about variable stars. The Stellar Observations Network Group (SONG) plans to use a global network of small telescopes to determine radial velocities and search for gravitationally-lensed exoplanets (Creevey *et al.*, 2011); the second goal should reveal many variable stars. The Russian Mobile Astronomy System of TElescope Robots (MASTER II) is under expansion (Kornilov *et al.*, 2012), and while it is optimized for transient detection, should be capable of detecting some variables. Another ongoing small project, the Kilodegree Extremely Little Telescope (KELT), searches for transits around bright stars, but has also found a number of variables such as eclipsing binaries (Pepper *et al.*, 2012). The Pi of the sky apparatus, currently being developed to search for gamma-ray burst optical counterparts, is expected to yield results on variable stars as well (Siudek *et al.*, 2011).

A couple of other ongoing projects, not conceived as sky surveys in any sense, are nonetheless highly relevant to the study of variable stars. The Digital Access to a Sky Century @ Harvard (DASCH) project is underway to scan, digitize and make available online the 450000 plates in the Harvard College Observatory's collection[15]: this will provide access to variables with periods up a century, undetectable by any other survey described so far (Grindlay *et al.*, 2012). As Griffin points out (2012), our knowledge of the period distribution of binaries is strongly

[12] Available from `skydot.lanl.gov`
[13] Database available at `stardb.yonsei.ac.kr`
[14] `ps1sc.org/Surveys.shtml`
[15] `dasch.rc.fas/harvard.edu/project.php`

affected by observational bias towards shorter, more readily-observed periods.

Another example of what might be called serendipitous astronomy is the use of NASA STEREO images (Solar TErrestrial RELations Observatory[16]) to study variable stars: although the mission is a space-based continuous observation of the Sun, its imagers also record data on background stars in the field of view. This has allowed processing to reveal stellar variability of many kinds, including eclipsing binaries, δ Scuti and Mira pulsators, and chemically-peculiar rotating variables (Wraight *et al.*, 2011, 2012b,a,c; Paunzen *et al.*, 2013).

Finally, the Next Generation Transit Survey (NGTS)[17] is seen as a successor to SuperWASP. Currently under construction at ESO-Paranal, this will use a robotic array of twelve 20 cm telescopes to search for transiting Neptune-size planets and super-Earths around bright stars, in an area some fifteen times greater than that surveyed by Kepler. The goal is to detect planets which can be readily confirmed by radial velocity measurements; however, it is likely that its archived data will provide ample material for the study of variable stars, similarly to SuperWASP.

1.9 The future

In the proceedings of a 2011 conference "New Horizons in Time-Domain Astronomy" (Griffin *et al.*, 2012), several papers consider forthcoming developments in observational technologies and data processing. Djorgovski *et al.* (2012) look towards the future of time domain astronomy using synoptic sky surveys in general; however, of particular relevance here are planned surveys which should yield photometric data suitable for discovering and studying periodic variable stars in enormous numbers.

[16] `stereo.gsfc.nasa.gov/`
[17] `www.ngtransits.org/`

Eyer *et al.* (2012b; see also Eyer *et al.* (2012a)) consider how the Gaia mission[18] will build on ESA's earlier Hipparcos survey mission. This space-based programme, using a 1.45×0.45 m mirror, was successfully launched in late 2013, and after a longer-than-expected commissioning phase is now (August 2014) ready to start its science mission. Over the next five years it should obtain astrometric and photometric measurements for ∼1 billion sources: about 1% of the Milky Way's stars. (Radial velocities should also be measurable for ∼150 million stars.) In particular, it will image sources repeatedly, and though its cadence is not optimized for periodic variable stars, it is expected to detect several million, and perhaps 50–150 million variable objects in total. Its full results should be available by 2020–21.

The Large Synoptic Survey Telescope (LSST)[19] will be a ground-based 8.4 m-diameter telescope in Chile (Eyer *et al.*, 2012a; Walkowicz, 2012), which will obtain about 1000 photometric measurements in six wavelength bands for each of 10^{10} stars, making it suitable for detection and detailed study of faint variables of many kinds. It has been estimated that it may detect 2.4×10^7 eclipsing binaries alone. It has just (August 2014) been officially authorized to start construction; first light is projected in five years.

[18] `sci.esa.int/gaia/`
[19] `www.lsst.org/lsst/`

Chapter 2

Stellar variability

This chapter will give an outline of the main classes of variable stars, where this variability is amenable to detection through optical light curves. Although the main focus of this research is on eclipsing binary stars, other variable types can mimic eclipses, or co-occur with eclipsing variability[1], so it is important to consider the broader context of stellar variability. Mention will be made of different variable stars' capacity to exhibit period changes over time, and of the value of different variable types to astrophysics more generally.

2.1 The classification of variable stars

The General Catalogue of Variable Stars[2] currently lists, in its fourth edition (GCVS4), 47811 designated variable stars mainly within the Milky Way, 10979 variables in external galaxies, and 984 extragalactic supernovae (Samus *et al.*, 2007-2013). The Catalogue classifies variables into eight groups containing more than 100 variability types[3], while noting that an object may fall into multiple types simultaneously e.g. an eruptive star within an eclipsing binary system. Sterken (1996b) notes the difficulty of producing a "physically sound and con-

[1] This will be of particular relevance in Ch. 10.

[2] `www.sai.msu.su/gcvs/gcvs/`

[3] `www.sai.msu.su/gcvs/gcvs/iii/vartype.txt`

Variability type	Stellar types	Period range	Amplitude of variation
EA	Detached or semi-detached systems; one or both components main sequence (O–M) or evolved (giant/dwarf)	0.2 d to several decades	0.01–several magnitudes
EB	Often semidetached; components mostly types B–A	mostly > 1 d	usually < 2 magnitudes
EW	Contact systems; MS mainly F–K	mostly 0.2–1 d	usually < 0.8 magnitudes
δ Scuti	A0–F5	0.01–0.2 d	0.003–0.9 mag.
RR Lyrae	Giant A–F	$\sim$0.2–1 d	0.2–2 mag.
Cepheids	F–K	mostly $\sim$1–50 d, some up to $\sim$200 d	$\sim$0.02–2 mag.
Mira	Post-MS giants with late-type emission spectra	80 to thousands of days	2.5–11 mag.
Ap	CP magnetic MS stars B8p–A7p	mostly $\sim$1–7 d, some up to $\sim$100 d	0.01–0.1 mag.
BY	Dwarfs dKe–dMe	fraction of day–120 d	$\sim$0.02–0.5 mag.
Dwarf novae	Close binaries; white dwarf primary and G–M secondary	80 m–14 h (orbital)	usually < 1 magnitude (orbital)

Table 2.1: Parameters of selected types of variable star relevant to the identification of eclipsing binaries

sistent taxonomy of classes and types of variable stars", due to factors such as ongoing improvements in observational technology, the increasing time-base of observations, and the tension between classifications based on observable features (e.g. light curves) and those based on derived physical characteristics (e.g. masses). In the end, he and Jaschek broadly follow the six main GCVS classes in their useful atlas of variable star light curves: eruptive, pulsating, rotating and cataclysmic variables; and eclipsing and X-Ray binaries (Sterken and Jaschek, 1996).

However, not all types of stellar variability are readily detectable in SuperWASP data (e.g. variability at non-optical wavelengths, very low amplitude

changes, variability of very faint stars, very long or extremely short period variation), or are of equal relevance to this research project (e.g. non-periodic irregular or transient phenomena, or indeed utterly regular periodic variation). Therefore, this chapter will focus mainly upon those types of variable star most amenable and interesting to research in the present context, with a summary of key parameters of the major types in Table 2.1.

2.2 Eclipsing binaries

Systems of two gravitationally-bound stars, orbiting a common centre of mass, will produce dips in system flux level twice each orbital period, when one star eclipses (partially or totally) the other, provided the system's orbital plane lies sufficiently close to our line of sight to the system (see Fig. 2.1). More specifically, we will see eclipses provided that

$$\sin(90^\circ - i) \leq \frac{R_1 + R_2}{a}$$

(Hilditch (2001), Equation 5.36), where i is the angle of inclination of the orbit to the tangent plane of the sky, $R_{1,2}$ are the radii of the two stars, and a is the semimajor axis of the orbit, i.e. we are more likely to see eclipses in close binary systems, and those containing relatively large stars.

Eclipsing binaries can be classified into three main observational types according to the shapes of their light curves (Figure 2.2). Type EA or Algol-type binaries, named for the prototype star Algol= β Persei, have well-defined eclipse first and fourth contacts, and relatively constant light out of eclipse i.e. flat maxima. The secondary eclipse may be too shallow to observe. Type EB or β Lyrae-type exhibit continuous variation in light level out of eclipse i.e. somewhat curved maxima, and generally a clear difference in the depths of primary and secondary eclipses (Hall, 1996a,b). Type EW or W Ursae Majoris (W UMa)-

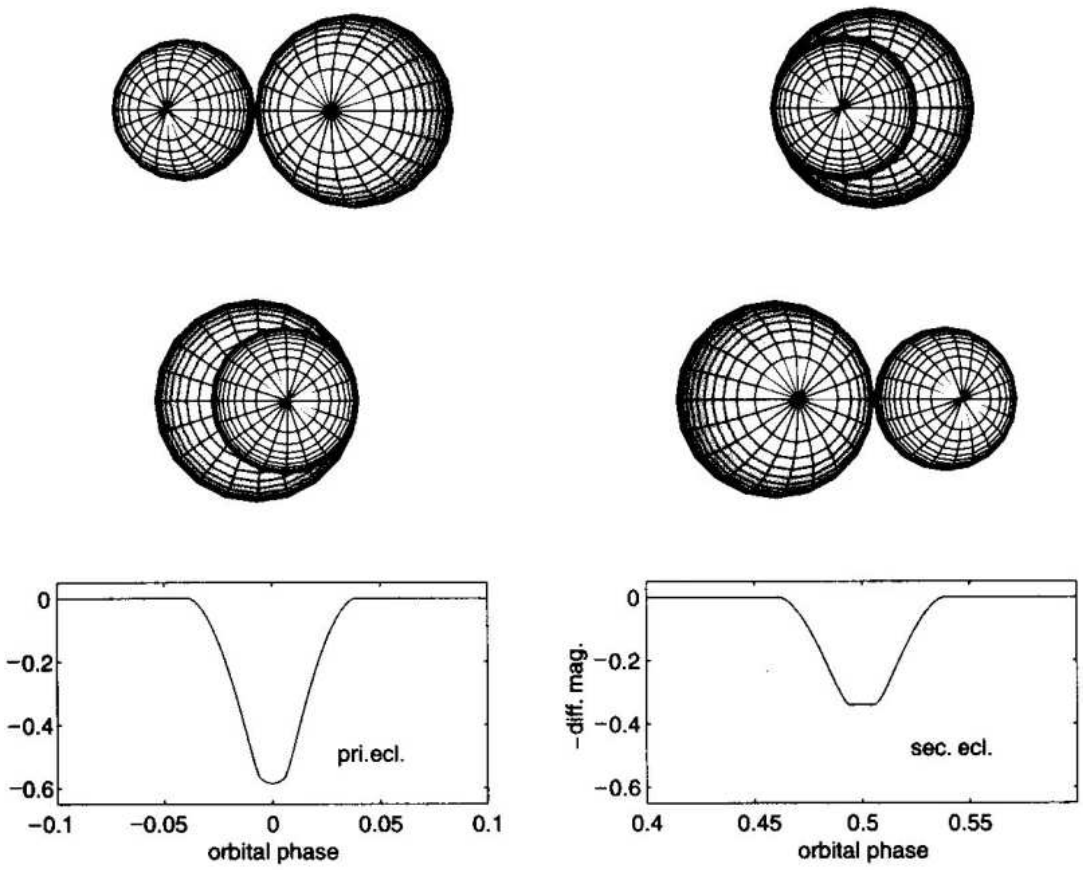

Figure 2.1: A schematic eclipsing binary system (from Hilditch (2001), Fig. 5.8), seen at $i = 90°$, containing spherical stars with $R_1 = 0.1a$, $R_2 = 0.138a$. On the bottom left, the deeper primary eclipse is created when the larger, hotter primary star is partially occluded by the smaller, cooler secondary star; on the bottom right, the shallower secondary eclipse occurs when the secondary is wholly occluded by the primary. Orbital phase $\phi = 0.0$ is set to the mid-point of the primary eclipse; in a circular orbit, the midpoint of the secondary eclipse will occur at $\phi = 0.5$. The upper four pictures show the four contacts of the primary eclipse: the first and fourth contacts (top left and middle right) correspond to the start and end of the whole eclipse, while the second and third contacts (top right and middle left) correspond to the start and end of the flattened bottom of the light curve eclipse. The secondary eclipse has a flat bottom because the secondary star is totally occluded, while the primary eclipse shows a more curved bottom due to the limb darkening of the partially occluded primary star. If this system were observed at a shallower angle e.g. $i = 85°$, both partial eclipses would appear V-shaped.

type show continuous variation in brightness, preventing identification of first and fourth contacts for eclipses, and generally little difference between primary

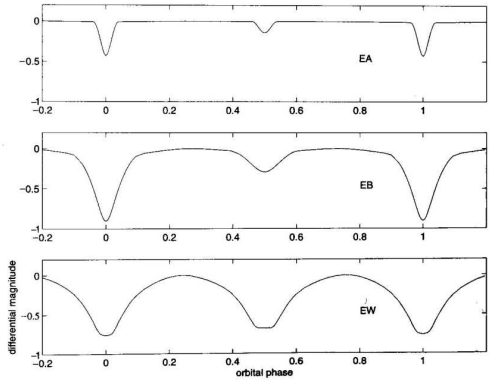

Figure 2.2: Schematic light curves of eclipsing binaries of types EA, EB and EW (from Hilditch, Fig. 1.2)

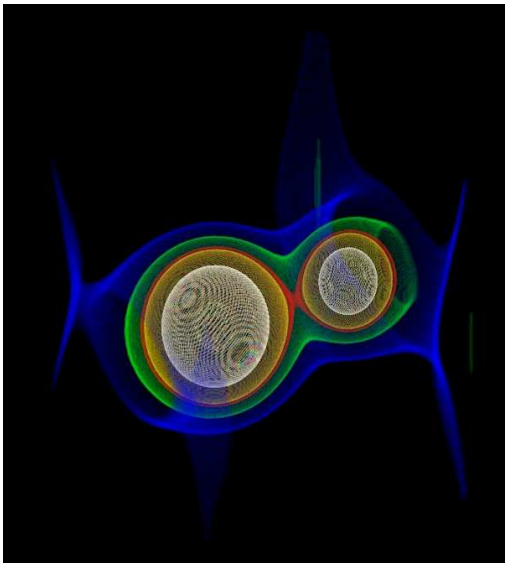

Figure 2.3: 3-dimensional visualization of equipotential surfaces around a binary with mass ratio $q = 0.38$, produced by the author using custom IDL code. The spherical white and ellipsoidal yellow volumes represent possible detached configurations; the red surface represents the Roche lobes, and the blue and green surfaces correspond to contact binaries.

and secondary eclipse depths (Duerbeck, 1996). They are also defined in the GCVS4 as having periods shorter than a day. In the GCVS, 9.7% of variables are classified as EA, 2.3% as EB and 2.7% as EW.

Binary systems can also be classified by assumed physical type (given spectroscopic observations in addition to photometric data), following the Roche model of Kopal (Kopal (1955, 1959), and summarized in Hilditch). We consider a rotating frame of reference with origin at the centre of mass of the more massive primary M_1, and with the secondary's centre of mass (M_2) at distance $a \equiv 1$ (assuming synchronous rotation and a circular orbit). A Roche potential Φ can then be determined at any point $P(x, y, z)$ around the two centres of mass, which is

the sum of their point-mass gravitational potentials and the rotational potential:

$$\Phi = -\frac{GM_1}{r_1} - \frac{GM_2}{r_2} - \frac{\omega^2}{2}\left[\left(x - \frac{M_2}{M_1 + M_2}\right)^2 + y^2\right]$$

where $r_1 = \sqrt{x^2 + y^2 + z^2}$ and $r_2 = \sqrt{(x-1)^2 + y^2 + z^2}$. Using

$$\omega^2 = \left(\frac{2\pi}{P}\right)^2 = \frac{G(M_1 + M_2)}{a^3} = G(M_1 + M_2)$$

and defining

$$\Phi_n = \frac{-2\Phi}{G(M_1 + M_2)} \qquad \text{and} \qquad q = \frac{M_1}{M_2} \qquad (0 < q \leq 1)$$

we obtain the normalized potential

$$\Phi_n(x, y, z) = \frac{2}{(1+q)r_1} + \frac{2q}{(1+q)r_2} + \left(x - \frac{q}{1+q}\right)^2 + y^2$$

(Hilditch, Equations 4.46-4.48). Fig. 2.3 illustrates the shapes taken by several equipotential surfaces in a binary system, which can be used for classification. The surfaces which just touch (at Lagrange point L_1) between the two point masses define the critical Roche lobes of a system: these are the maximum volumes that each individual star can occupy. Stars occupying volumes within their Roche lobes form a detached system; systems where one star fills its Roche lobe and the other is within it are called semidetached; systems where both stars overfill their Roche lobes are called contact or sometimes overcontact binaries.

In close binary systems, the equipotential surfaces filled by stars near or overflowing their Roche lobes are non-spherical, producing ellipsoidal variation in the light curve of the system: even if the stars are non-eclipsing, they will present different surface areas to us at different phases, and hence different light levels. This produces a large part of the out-of-eclipse variation seen in W UMa

and some EA/EB light curves. The shared gas envelope of contact systems is also believed to equalize their temperatures, producing near-equal depth primary and secondary eclipses even when the system's mass ratio is very low, and this would explain the light curve shapes of W UMa eclipsing binaries, which generally have spectroscopic mass ratios less than 1 (Duerbeck, 1996). Thus there are some links between the two classification systems, especially between W UMa and contact binaries, though the correspondences EA-detached and EB-semidetached are far less reliable: Hilditch comments that "There is no suggestion that an eclipsing binary with an EA light curve must have the same physical characteristics as Algol, and probably, in most cases, they will not. [...] An EB system does not need to have the same physical characteristics as β Lyrae" (2001).

Period changes have been observed in all types of eclipsing binary system, indeed Kim *et al.* (2003) claim that about 46% of the 1140 systems in Kreiner *et al.*'s collection of $O-C$ diagrams (2001) show at least some evidence of period change. Contact binaries seem to exhibit particularly frequent period changes; Kubiak *et al.* (2006) surveyed a large sample of OGLE W UMa-type systems and found period increases and decreases to be of similar frequency, with the majority of changes falling within ± 0.02 s yr^{-1}, and none exceeding about ± 0.4 s yr^{-1}. Causes for these changes are believed to include mass transfer between system components and/or mass and angular momentum loss from the system as a whole, associated with such physical processes as stellar winds, magnetic braking, unstable Roche lobe overflow, and gravitational wave radiation (Hilditch, 2001; Eggleton, 2006). A third body in the system (star or giant planet) can also alter the period.

Even when the period does not vary over time, eclipsing binaries have the capacity to tell astrophysicists much about fundamental stellar properties. Medium-resolution spectroscopic time series for an eclipsing system will often reveal spectral line splitting and shifting: each observed spectrum is the sum of the spectra of

the two component stars in the binary, and can show a red-shifted line associated with a component travelling away from the observer (along a radial line of sight), together with a blue-shifted line associated with a component travelling towards the observer. By measuring the shifts in wavelength relative to the laboratory wavelength of a known spectral line, the radial velocities of each component in each spectrum in the time series can be calculated, using the equation:

$$v_r = c\left(\frac{\lambda_{obs}}{\lambda_{em}} - 1\right).$$

where λ_{obs} is the observed wavelength of the line, λ_{em} is the emitted (laboratory) wavelength, and c is the speed of light.

By plotting the radial velocities against orbital phase, we can construct radial velocity curves whose amplitudes give us the mass ratio and orbital separation of the binary components. In combination with light curves which can tell us the angle of inclination and Roche potentials of the system, we can thus determine absolute masses and radii for the components of double-lined spectroscopic and eclipsing binaries: stellar parameters which are difficult if not impossible to measure precisely by any other method.

2.3 Pulsators

These are variable single stars whose outer layers pulsate, radially or sometimes nonradially (i.e. non-spherically), periodically or more or less irregularly. This produces intrinsic variation in the light curve (as opposed to extrinsic variation produced by our perception of the object, as with eclipsing binaries). Several of the most common types of pulsating variables lie on the instability strip of the Hertzsprung-Russell (H–R) diagram (Fig. 2.4), and are post-main sequence stars going through relatively short-term evolutionary stages in between more stable states (Ryan and Norton, 2010)

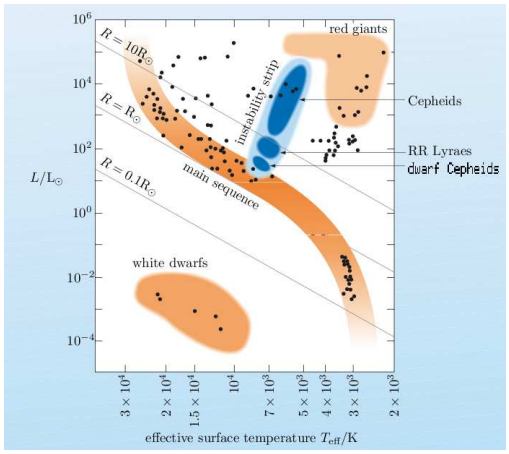

Figure 2.4: The near-vertical instability strip on the Hertzsprung-Russell diagram, showing locations of δ Scuti, RR Lyrae and Cepheid pulsating variables (from Ryan and Norton (2010), Fig. 4.8). The pulsations in such stars are caused by the varying opacity of an unstable layer within the envelope, which drives global oscillations (Green and Jones, 2004).

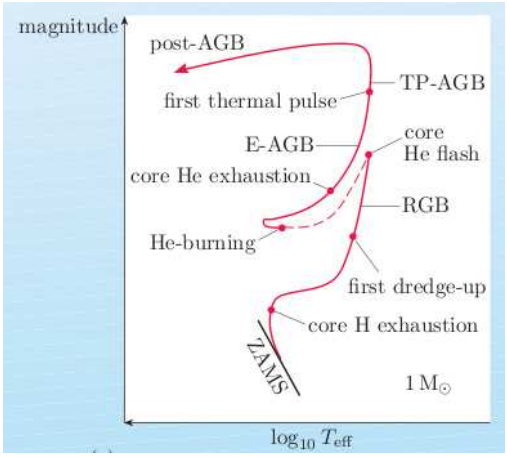

Figure 2.5: Evolutionary track for 1 $M_\odot$ star after leaving main sequence (from Ryan and Norton, Fig. 5.5). The red-giant branch (RGB), early-asymptotic giant branch (E-AGB) and thermally-pulsing asymptotic giant branch (TP-AGB) are indicated. More massive stars would have differently shaped trajectories on the H–R diagram.

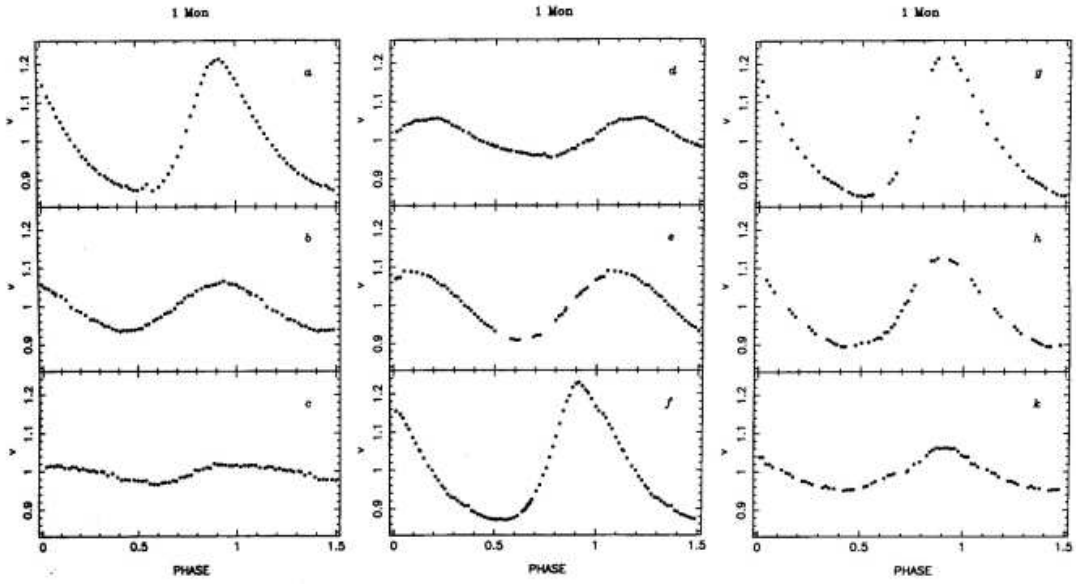

Figure 2.6: Light curves of δ Scuti star 1 Mon, $P = 0.13612$ d, over 9 sequential nights a–k (from Feast (1996b), Fig. 3.20). Pulsation in multiple simultaneous modes produces the changing shape of the light curve.

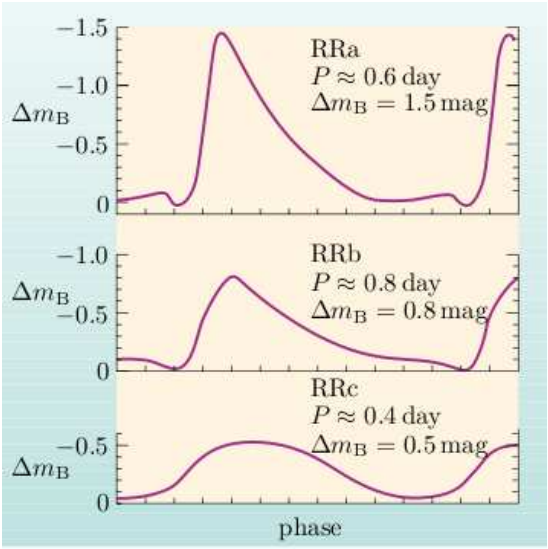

Figure 2.7: Schematic light curves, typical periods and amplitudes for three classes of RR Lyrae pulsators (from Ryan and Norton, Fig. 5.3). RRa and RRb exhibit asymmetric light curves and substantial amplitudes, while RRc have more sinusoidal light curves and lower amplitudes.

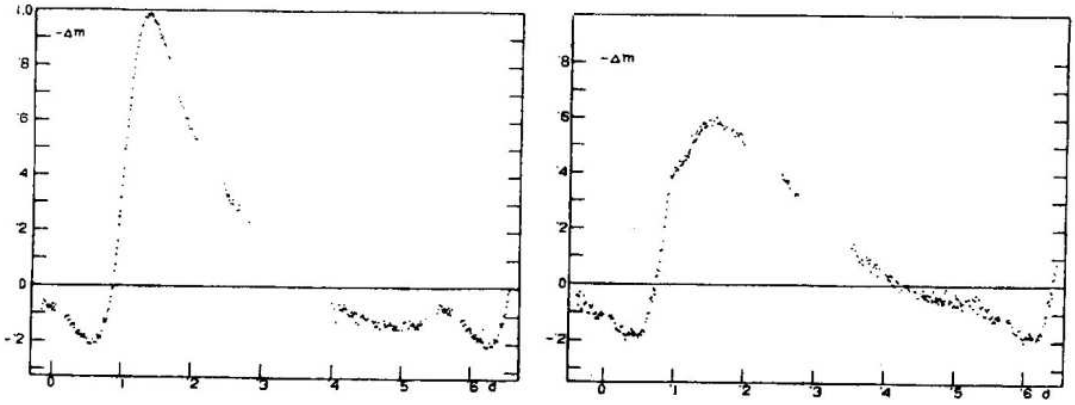

Figure 2.8: RR Lyr at two phases of its Blazhko cycle, each plotted over ~ 0.6 d (from Feast (1996c), Fig. 3.21).

δ Scuti or dwarf Cepheids are the shortest-period variables on the instability strip (Feast, 1996b). They are low-mass ($\sim$2 $M_\odot$) subgiants making their first transition off the main sequence, towards the red-giant branch (Fig. 2.5), and pulsations occur in the hydrogen envelope surrounding their hot helium-rich core. Although their light curves are usually near-symmetrical, these stars can pulsate in radial and nonradial modes simultaneously, producing light curves that may vary in shape from cycle to cycle (Fig. 2.6).

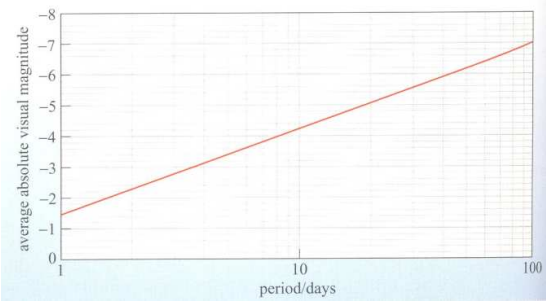

Figure 2.9: The period-luminosity relationship of classical Cepheids, with magnitudes plotted against log P (from Jones and Lambourne (2004), Fig. 2.25).

Low-mass stars which have already ascended the red-giant branch and begun core helium burning will occupy a position on the horizontal branch of the H–R diagram according to their metal content, prior to ascending the giant branch a second time (Ryan and Norton, Feast (1996c)). If they fall into the instability strip, they will be radially pulsating variables with longer periods than δ Scuti stars, known as RR Lyrae stars. These serve as standard candles to determine distances, having a single luminosity and distinctive light curve shapes (Fig. 2.7 shows schematic light curves for subtypes RRa, RRb and RRc).

Some RR Lyrae stars exhibit periodic changes in their pulsation period and/or amplitude. This is known as the Blazhko effect, after observations by Blažko of RW Dra, in which he noted "aus den weiteren Beobachtungen erwies es sich, daß die Momente der Maxima durch keine konstante Periode dargestellt werden können, und daß es notwendig ist, eine periodische Veränderung der Periode anzunehmen" (1907). Fig. 2.8 illustrates this phenomenon for RR Lyr itself.

Cepheids, also called δ Cephei variables, Type I or classical Cepheids, are relatively young, higher-mass giant and supergiant stars executing loops back and forth across the instability strip, as they switch between different forms of nuclear burning. They also constitute standard candles, since their magnitudes are directly related to their periods, as discovered by Leavitt when studying Cepheids in the Magellanic Clouds: "A remarkable relation between the brightness of these variables and the length of their periods will be noticed [...] A straight line can

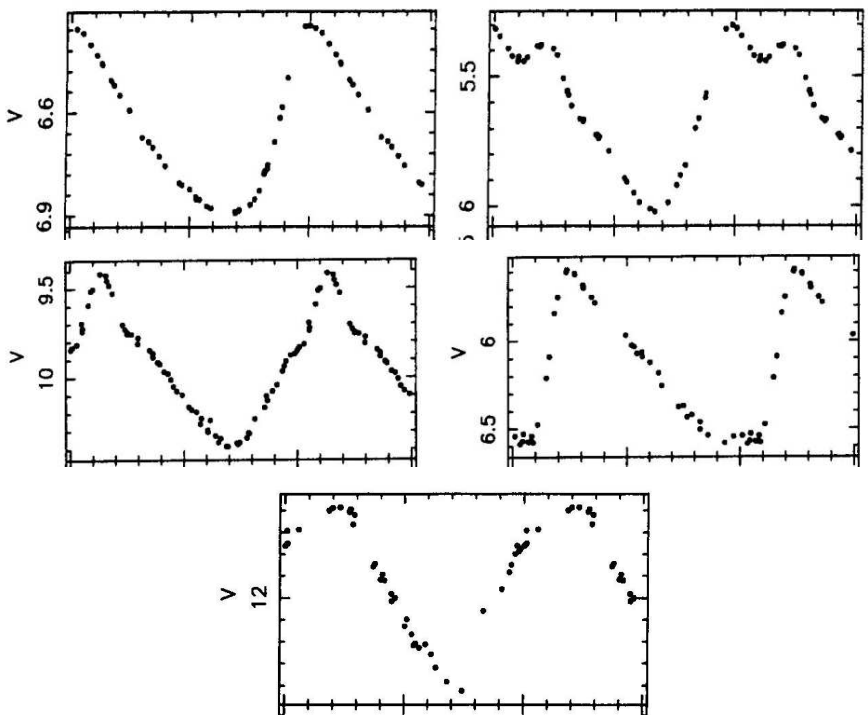

Figure 2.10: Phase-folded light curves of Cepheids with increasing periods, illustrating aspects of the Hertzsprung progression (Feast (1996a), from Figures 3.24–3.26). Top left: R TrA (P = 3.389287 d) shows steep narrow maxima; top right: S Sge (P = 8.382173 d) has broader, double-peaked maxima; middle left: SS CMa (P = 12.3580 d) shows bumps on both rising and falling branches; middle right: T Mon (P = 27.0197 d) has a very steep rising branch; bottom: HV 821 (P = 127.6 d) shows a more sinusoidal light curve.

readily be drawn among each of the two series of points corresponding to maxima and minima [...] The logarithm of the period increases by about 0.48 for each increase of one magnitude in brightness" (Leavitt and Pickering, 1912). A recent recalibrated version of the relationship is shown in Figure 2.9.

Another interesting and astrophysically-useful relationship seen in Cepheids is between their light curve shapes and their periods: the Hertzsprung progression, illustrated in Fig. 2.10 (Feast, 1996a).

In the GCVS, classical Cepheids and δ Scuti stars each represent 1.3% of designated variables, while the heavily-studied RR Lyrae constitute 16.5%. Other common types of pulsators are semi-regular (SR: 14.6%; Fig. 2.11) and irregular (LB: 7.4%) giants late in their evolution (Whitelock, 1996b), and Mira or Long

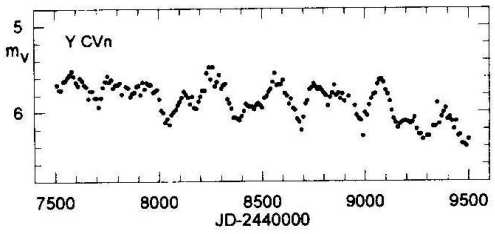

Figure 2.11: Light curve of semi-regular (SRb) giant star Y CVn, covering over 5 years (from Whitelock (1996b), Fig. 3.37).

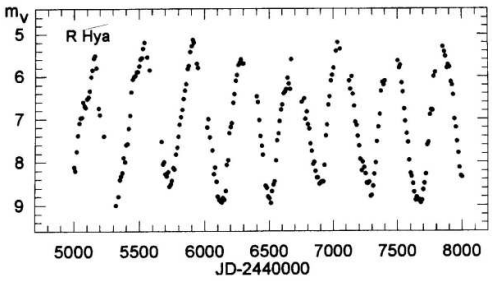

Figure 2.12: Light curve of Mira variable R Hya ($P = 388.9$ d) over about 8 years (from Whitelock (1996a), Figure 3.46). Some variation in amplitude from cycle to cycle is apparent.

Period Variables, constituting 18.2% - the commonest variable type in the Catalogue. The latter seem to represent objects at the tip of the asymptotic giant branch, prior to evolution into planetary nebulae, and may exhibit variations in amplitude and period from cycle to cycle (Whitelock, 1996a); see Figure 2.12.

Pulsating variables of many types are now yielding much valuable information about stellar structure in the field of asteroseismology: high-cadence, high-precision light curves such as those of Kepler (Ch. 1) can reveal oscillations over a wide range of frequencies, allowing determination of such parameters as stellar mean density, surface gravity and effective temperature.

2.4 Rotating variables

These constitute another type of external variables, like eclipsing binaries, and may be single or multiple systems. Rotational variation is often seen in combination with another source of light variability such as pulsation, flares or binary eclipses, and is associated with non-uniform brightness of the surface of the star concerned, or non-spherical shape (i.e. ellipsoidal variation, as discussed earlier in Section 2.2).

The commonest types of rotators in the GCVS are α^2 Canum Venaticorum

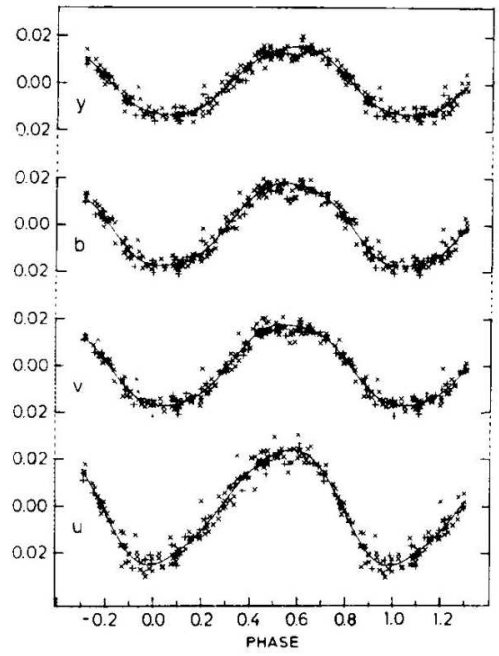

Figure 2.13: Light curves in four filters of Ap star HD 66255 (P = 6.8178 d, from Sterken (1996a), Fig. 4.1).

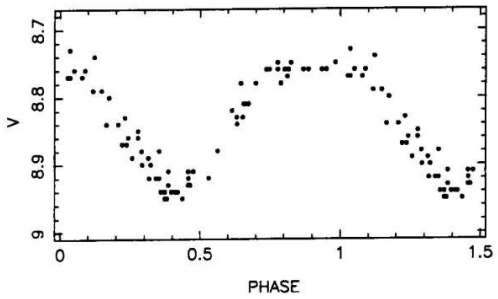

Figure 2.14: Folded light curve for BY Dra-type star CC Eri (P = 1.56145 d, from Hall (1996c), Fig. 4.10).

(Ap or roAp) main sequence stars and BY Draconis-type (BY) late dwarfs, each constituting about 1.4% of the Catalogue. The former are chemically-peculiar stars with unusually strong magnetic fields ($\sim$ 0.3–30 kG) not aligned with their axis of rotation; this appears to create spots with an abundance of metals such as iron or silicon, whose rotation on the star's surface causes the light variation, often approximately sinusoidal in shape (Sterken, 1996a); see Fig. 2.13. The latter exhibit cool spots associated with chromospheric activity (Hall, 1996c); see Figure 2.14.

Spotted stars can exhibit changes in their light curve periods due to spot latitudinal migration and differential rotation of the stellar surface.

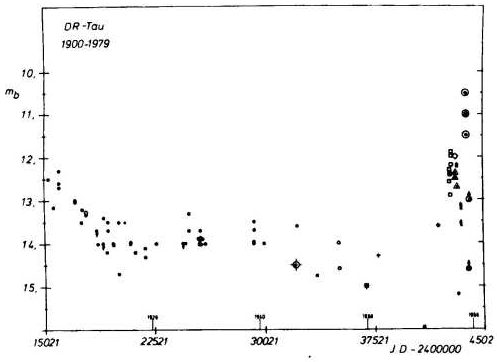

Figure 2.15: Light curve of T Tauri object DR Tau over about 80 years (from Krautter (1996b), Fig. 2.20). An outburst of amplitude ~ 5 magnitudes is observed towards the end of the period.

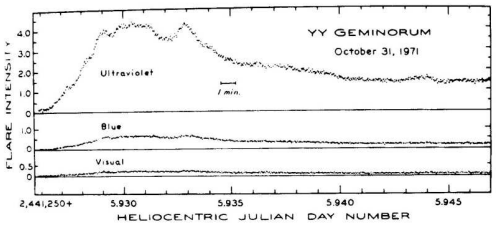

Figure 2.16: Light curve for YY Gem in 3 filters, showing one flare (from Krautter (1996a), Fig. 2.35). The flare intensity is clearly greater at higher frequencies; indeed, a significant part of the energy output for such flares is in X-rays.

2.5 Eruptive and explosive variables

Eruptive variables, another type of intrinsic variables, exhibit irregular violent outbursts and brightness variations associated with their chromospheres and coronae, often accompanied by mass outflows and interaction with the interstellar medium. A common type are the so-called Orion variables (3.9% of the GCVS), which are mainly protostellar objects such as T Tauri or FU Ori stars, moving towards the main sequence. Outflows and jets seem to be associated with the protoplanetary/accretion disks surrounding these young stars, producing light curves such as in Fig. 2.15 (Krautter, 1996b). Another common eruptive group are flare stars (3.8% of the GCVS) or UV Ceti-type variables; these seem to be late-main sequence, low-mass stars undergoing magnetic reconnection (similar to solar flares but at far higher energies). Fig. 2.16 illustrates such a flare across multiple wavelengths (Krautter, 1996a).

Explosive or cataclysmic variables include extremely violent transients (supernovae and novae of various kinds) whose outbursts are caused by thermonuclear processes. Many are close binary systems containing at least one post-main se-

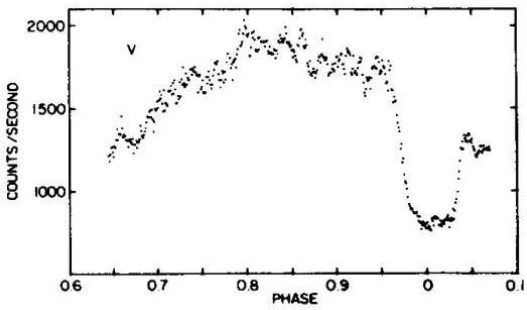

Figure 2.17: Light curve for SS Cygni-type dwarf nova U Gem ($P = 0.17690618$ d, from Vogt (1996), Fig. 5.24). The extended maximum corresponds to a hot spot on the accretion disk, where a stream of material strikes the disk; the minimum occurs when the disk is partially eclipsed by the secondary.

quence object. The commonest type in the GCVS (1.0%) are dwarf novae (or U Geminorum stars), which consist of a white dwarf primary accreting matter via a disk from a main sequence secondary filling its Roche lobe. If eclipsing, the orbital period (on the order of hours) may be revealed in the light curve (Fig. 2.17). Semi-regular outbursts of much greater magnitude also occur (Fig. 2.18), which "can be understood as the limit cycle evolution of an unstable accretion disc that alternates between a hot, high-viscosity state and a cool, low-viscosity state" (Kolb, 2010).

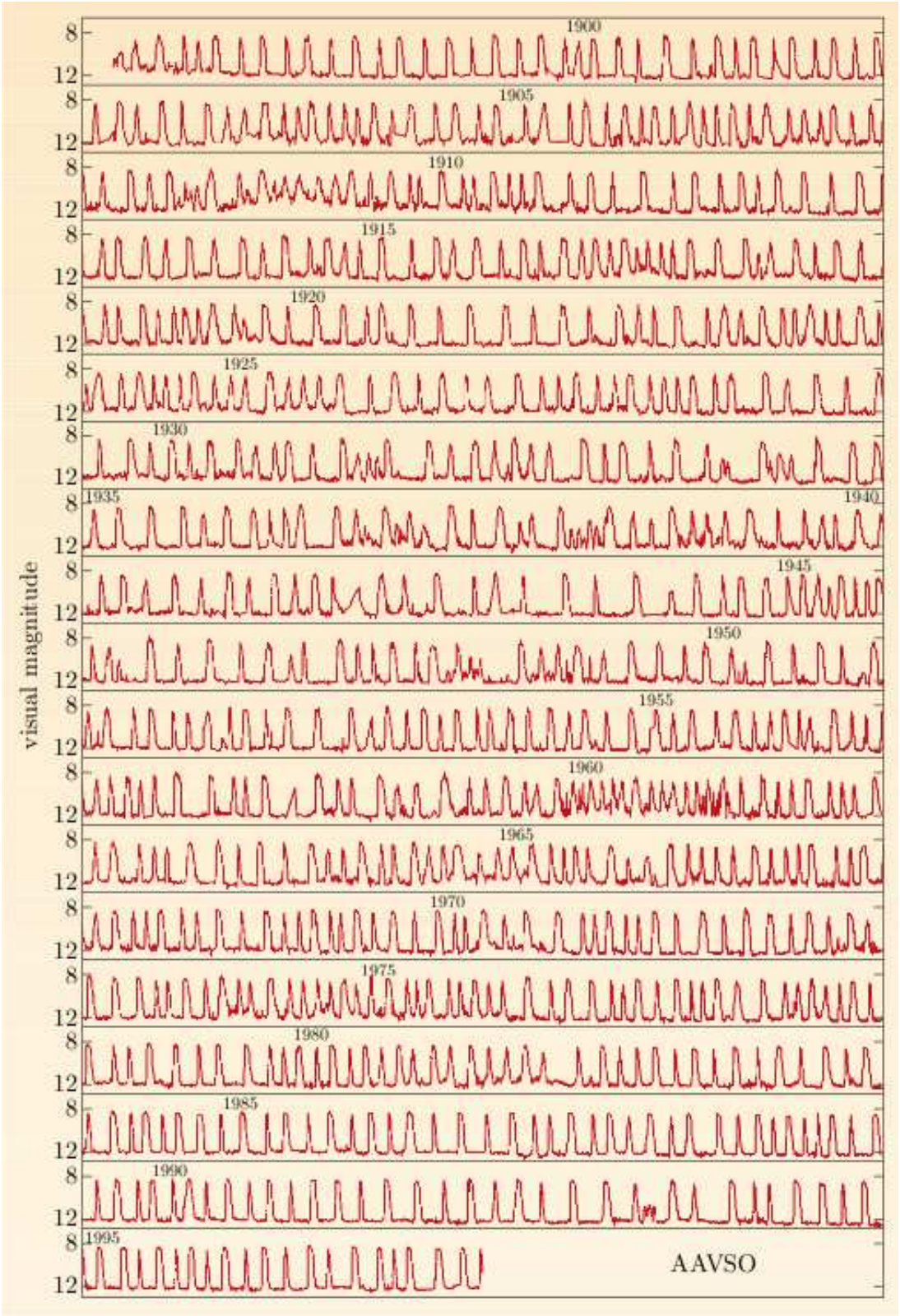

Figure 2.18: Light curve for dwarf nova SS Cygni showing semi-regular outbursts over nearly 100 y (from Kolb (2010), Fig. 4.5, constructed from observations made by the American Association of Variable Star Observers, courtesy John Cannizzo).

Chapter 3

Questions of interest

In this chapter, the background will be set out to a number of specific research questions which might be addressed using SuperWASP archive data on eclipsing binaries and their orbital period variations. These questions motivated several of the focused studies to be described in Part III, and were either suggested in the original proposal for this research project, or emerged during its course. The first three are related.

3.1 The short-period binary limit

When the period distributions of contact binary systems are plotted (Figures 3.1 and 3.2) a number of interesting features emerge. There is a peak at around 0.4 d, a long tail to the right, and a fairly sharp cut-off at around 0.2 d, below which no objects have been observed. (Here we are considering binary systems containing main sequence stars only; systems containing one or more compact objects such as a white dwarf, neutron star or black hole can have shorter periods.) The cause of this short-period limit is a matter of continuing debate.

Rucinski (1992) proposed a theory linking the short-period limit of W UMa systems to the limit of full convection for low-mass stars. He derived a formula

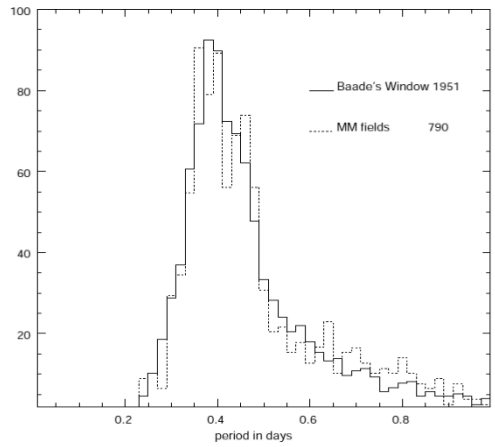

Figure 3.1: Period distributions of contact binaries observed by OGLE in two fields (from Szymański *et al.* (2001), Fig. 9).

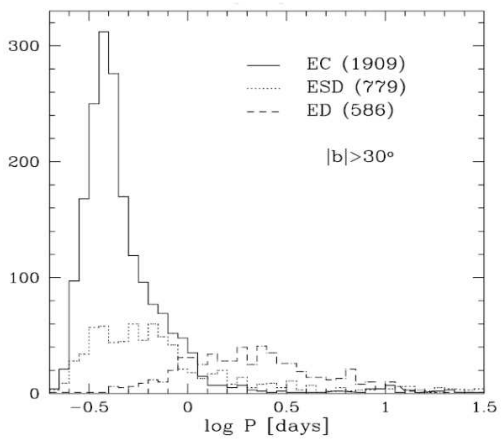

Figure 3.2: Period distributions of eclipsing binaries observed by ASAS (from Paczyński *et al.* (2006), Fig. 6). Contact systems are shown with a solid line; semidetached systems dotted; detached systems dashed.

for possible configurations of stellar parameters in a contact binary:

$$f(Q_1) \propto K(T_{\rm eff}) M_1^{-1/3} R_1^{-1}$$

where f is a very steeply rising function of Q_1, the ratio of core radius to total stellar radius, and K was calibrated using stellar models. Using these constraints, he argued that "there cannot exist dynamically stable contact binaries with effective temperatures lower [...] than the Hayashi limit" i.e. the low-temperature limit for fully-convective stars on the Hertzsprung-Russell diagram. Since there is an observed relationship between binary period and stellar colour, his suggestion was that the temperature limit would correspond to a period limit for contact binaries.

Unfortunately, when plotted on a period-colour graph (Fig. 3.3), the full convection limit lies some distance from observed contact systems, and he himself acknowledged that the theory could not provide a complete explanation of the period limit. However, we might note that many more contact binaries have been

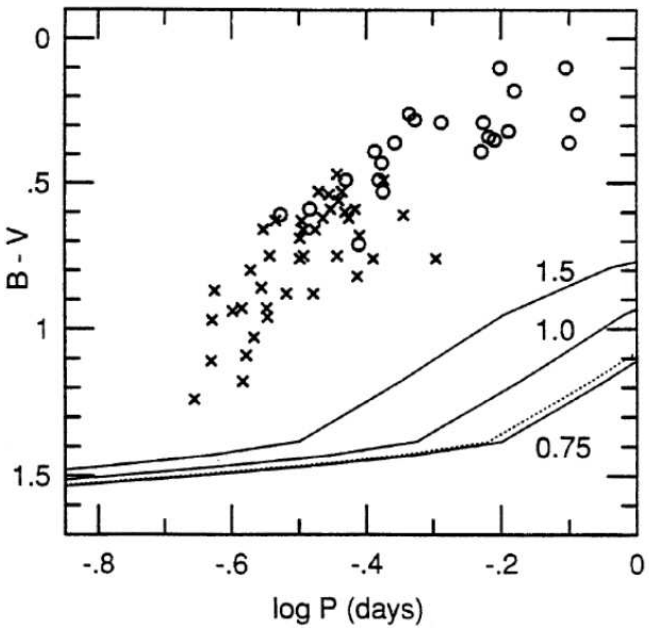

Figure 3.3: Period-colour relationship for observed W UMa systems, with lines indicating the limit of full convection for systems with various total masses (from Rucinski (1992), Fig. 5).

observed since 1992, and the inclusion of these extra data points on the graph, together with a potentially improved determination of K, might narrow the gap and make Rucinski's model more tenable.

Stepień (2006) proposed a totally different explanation. He obtained a formula for the angular momentum loss (AML) rate in a close detached binary due to magnetic braking:

$$\frac{\mathrm{d}H_{\mathrm{orb}}}{\mathrm{d}t} = -4.9 \times 10^{41} \omega \frac{R_1^2 M_1 + R_2^2 M_2}{P_{\mathrm{orb}}},$$

(where masses and radii are in solar units, P_{orb} is in days, t is in years and H_{orb} is in cgs units), which implies that lower-mass binaries will lose angular momentum more slowly than higher-mass systems, and so will take longer to reach a small-separation, short-period contact orbit. (The assumption must be that the AML ceases once a contact configuration is achieved.) By his calculations, "[b]inaries with initial component masses lower than 0.7 $M_\odot$ have not lost enough AM within

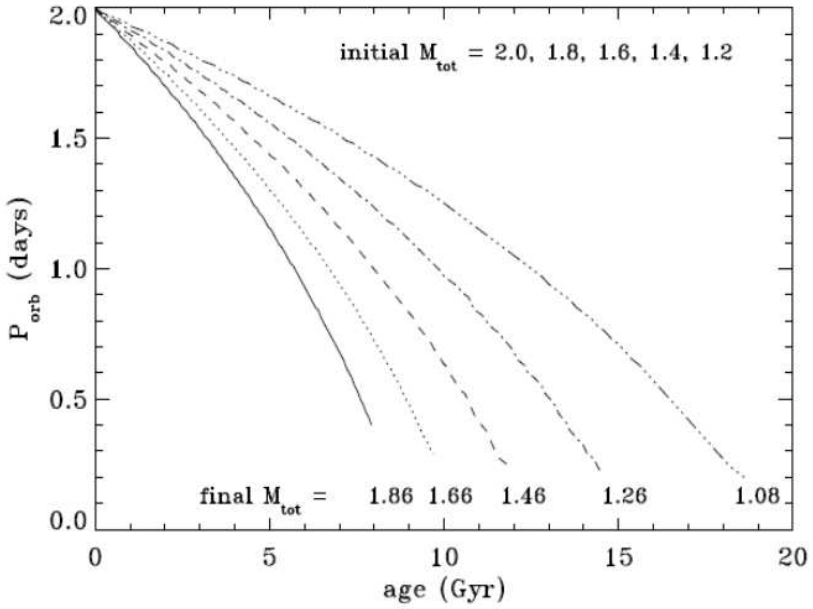

Figure 3.4: Orbital periods of detached binaries plotted against age, using Stepień's model for mass-related AML (from Stepień (2006), Fig. 2). The mass ratio q=1; the different lines indicate calculations for systems with different total masses, decreasing left to right.

the age of the Universe to form contact systems and they remain [...] detached", and this then provides a reason for the period limit: the Universe simply has not existed long enough for any binaries to evolve to an orbital period below 0.2 d (Fig. 3.4). We may note that this model implies a *changing* short-period limit: in the far future, astronomers could expect to observe contact systems with a period cut-off below 0.2 d, as more low-mass systems evolve into stable contact configurations at small separations.

A problem with this theory is that a number of recent observations conflict with it, as pointed out by Jiang *et al.* (2012), who collected published parameters for a number of short-period binaries. GSC 01387-00475 is a contact system with period 0.2178 d and primary mass 0.638 $M_\odot$: according to Stepień, such a low-mass binary should not have had time yet to evolve into contact, even if it was one of the first stars to form in the Universe (which is most unlikely). The shortest-period binary known is GSC 2314-0530 (Figure 6.3), a semidetached system

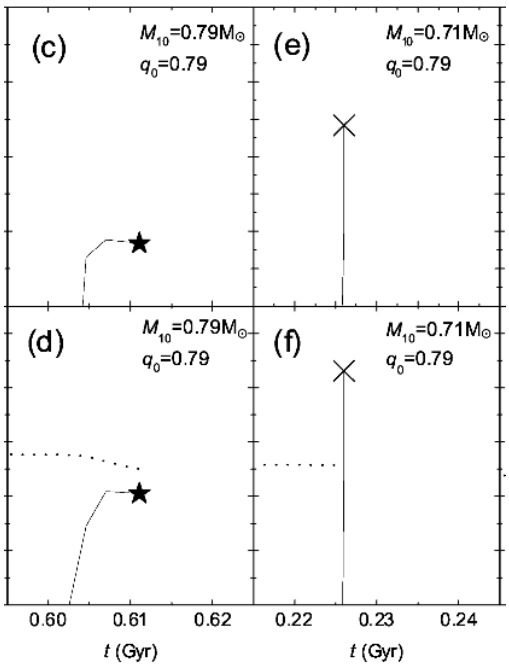

Figure 3.5: Two binary evolution calculations with different initial primary masses and initial mass ratio 0.79 (from Jiang *et al.* (2012), Fig. 1). On the left, a system with initial primary mass 0.79 $M_\odot$ undergoes mass (lower panel) and radius (upper panel) changes over several million years, reaching a stable contact configuration at the point marked by the star. On the right, a system with initial primary mass 0.71 $M_\odot$ undergoes mass and radius changes so rapid as to appear instantaneous on this scale, reaching an unstable state at the point marked by the cross, at which point it may be expected to merge into a single star.

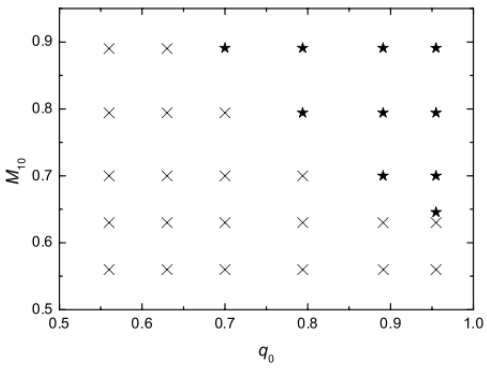

Figure 3.6: Binary evolution outcomes in an initial primary mass–mass ratio plane (from Jiang *et al.*, Fig. 2). Filled stars indicate stable systems; crosses indicate unstable systems. The notional diagonal line separating the two regions corresponds to the short-period limit.

with period 0.192 d and primary mass just 0.51 $M_\odot$; if Stepień's evolutionary calculations are remotely correct, a system of such low mass should have a much greater separation and longer period at the current time, rather than being on the brink of contact and actually below the short-period cut-off.

Therefore, Jiang *et al.* explored a third possible explanation, carrying out a

suite of calculations for binaries with various initial primary masses and mass ratios, using an evolutionary code of Eggleton. They found (Figs. 3.5 and 3.6) that systems with particular combinations of low primary mass and low mass ratio evolved into unstable states and did not reach contact at all; rather, they would be expected to undergo rapid mass transfer and merge on a dynamic timescale. We would expect in general to observe only those systems where stable mass transfer is possible within a long-term contact configuration: these will have primary mass/mass ratio combinations corresponding to periods greater than ∼0.20 d. This, then, provides an explanation for the short-period limit which is consistent with observation, at least for the moment.

Given the uncertainties inherent in all these models, and the lack of reliable parameters available for W UMa-type systems, it would be unwise to completely rule out any of the three explanations at this stage, or indeed other explanations not yet thought of. It might be that multiple factors combine to produce the observed period limit. In any case, further identifications and investigations of short-period contact binaries close to the limit (as in Norton *et al.* (2011)), especially those undergoing period changes, would be expected to make a useful contribution to resolving the issue.

3.2 Stellar mergers

A related issue concerns the possibility of mergers of close binary systems (which may be triggered by reaching the short-period limit). A pair of stars losing angular momentum and declining in orbital separation might be expected ultimately to spiral in towards each other and form "a single, rapidly-rotating object such [as] has been suggested for FK Com stars and blue stragglers" (Bradstreet and Guinan, 1994). Rasio (1995) considered conditions for the onset of tidal instabilities in a close binary system with low mass ratio, which could lead to orbital

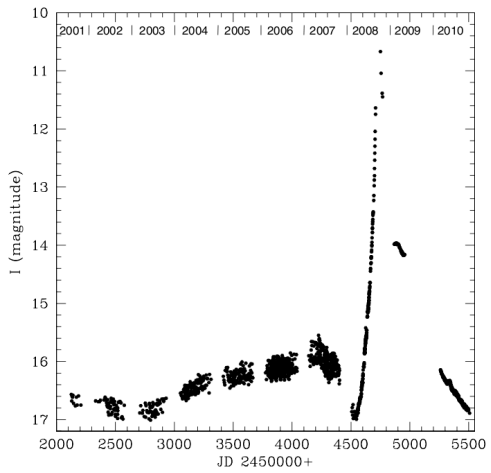

Figure 3.7: OGLE lightcurve of V1309 Sco (from Tylenda *et al.* (2011), Fig. 1). The nova outburst, corresponding to the merger event, is seen on the right, and reached a maximum magnitude of $I \simeq 6.8$.

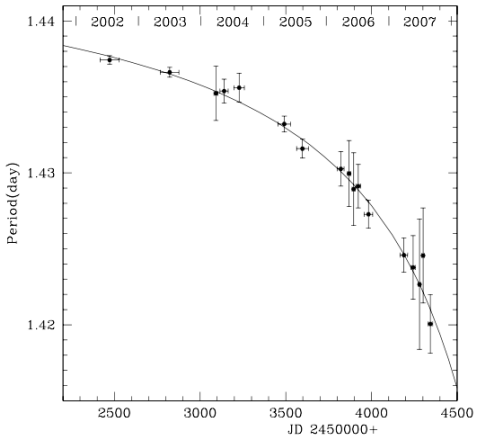

Figure 3.8: Period decrease of contact binary progenitor of V1309 Sco (from Tylenda *et al.*, Fig. 2). The data points indicate periods found for subsamples of OGLE photometry in particular seasons, containing $\sim$50 observations each, and the best-fit exponential function is overplotted.

decay and merger, and Jiang *et al.* explored similar instabilities associated with low mass ratio through simulation, as outlined above.

On only one occasion, however, does such a stellar merger appear to have been observed (Tylenda *et al.*, 2011), and only then in retrospect, through archival searches of OGLE, to try to identify the precursor of the 2008 nova V1309 Sco (Fig. 3.7). They determined it to have been a contact binary, with decaying orbital period P (in days) best fitted over the eight years of observation by the exponential function:

$$P = 1.4456 e^{\frac{15.29}{t-2455233.5}},$$

where t is the time of observation in Julian date (Fig. 3.8). Locating further candidates for imminent binary merger, perhaps members of the population of contact systems near the short-period limit which are undergoing rapid period decrease, would provide a valuable addition to this exciting area.

3.3 W UMa period changes

Within the general topic of close binaries, we might also note the mysterious changes of rate and direction of period change itself in W UMa-type contact systems, which we might call $\ddot{P}$ or "variably-variable variability". Hilditch comments that "[t]he more common kind of ephemeris curve does not display simple linear or quadratic behaviour, but is composed of subregions that can be well represented by straight lines, quadratics, or higher-order polynomials that are piecewise continuous", and argues that the Applegate mechanism (Applegate, 1992) could explain it, in terms of a stellar magnetic activity cycle producing variable tidal effects on the binary orbit. However, this mechanism does not yet seem universally accepted, and further exploration and exemplification of contact binary period variation should help to resolve the issue.

3.4 Third bodies and stellar multiplicity

Finally, the original research proposal also suggested a search for third bodies in eclipsing binary systems. As mentioned in Section 2.2, periodically-varying periods of such binaries could indicate the presence of a third star in a hierarchical triple system (as investigated using Kepler data in Gies *et al.* (2012)), or even a circumbinary exoplanet. Several transiting circumbinary planets have recently been reported from Kepler data: Kepler-16b (Doyle *et al.*, 2011), Kepler-34b and Kepler-35b (Welsh *et al.*, 2012), Kepler-47b,c and Kepler-48b (Orosz *et al.*, 2012b,a), and PH1b (Schwamb *et al.*, 2013). Since tens of thousands of eclipsing binaries have been provisionally identified in SuperWASP data, one might reasonably hope that a thorough search for period variability would yield further third bodies of both kinds. A large enough sample of additional massive bodies in binary systems could even be used to estimate the higher-order multiplicity fraction of SuperWASP stars.

Part II

Analytical Methods

Chapter 4

Orbital period determination

Before changes in eclipsing binary orbital periods could be searched for, it was necessary to have a means to determine reference (initial, or average) periods from SuperWASP light curves reliably and as precisely as possible. The approach used has been developed and refined by the author over the course of the research, and different versions of it were described in our resulting publications (Lohr *et al.*, 2012, 2013b, 2014b). This chapter is based in part on the method sections of these papers, and traces the development process chronologically, starting with some background on the archive data itself.

4.1 SuperWASP archive data

Data was located and downloaded from the SuperWASP archive using two command-line interface tools: *wcatquery* and *wlcextract*, which form part of the WASP Query Language (WQL) written by R. West. The *wcatquery* tool returns WASP catalogue names[1] and other optional catalogue data for objects, and can filter the search according to criteria such as sky location, magnitude range, time of observation, and even candidate periods as found by a code written by A. Norton (a form of this is described in Norton *et al.* (2007)). As a simple example, the

[1]Format 1SWASP Jhhmmss.ss±ddmmss.s, using USNO B-1.0 coordinates.

command

```
wcatquery --query='cone ''NY Vir'' 1m'
```

implements a 1 arcminute cone search around the coordinates returned by SIMBAD for the named object NY Vir, and returns the single result

```
1SWASP J133848.16-020149.3
```

which can then be extracted as a FITS file using *wlcextract*:

```
wlcextract --object=''1SWASP J133848.16-020149.3''
```

Lists of objects can also be extracted using an input file, which is practical for obtaining up to a few thousand data files.

SuperWASP FITS files contain a primary header, a null primary image and a binary table extension containing the photometric data, listed in 23 columns and a row per data point. The columns of interest here are

TMID: time in seconds of mid-point of exposure = (Heliocentric Julian Date − 2453005.5) ∗ 86400

TAMFLUX2: calibrated, Sys-Rem-corrected flux from middle of three camera aperture sizes

TAMFLUX2_ERR: standard deviation of each TAMFLUX2 data point

Other raw and calibrated flux values, from all three apertures, with standard deviations, are also available. The fluxes chosen here have been corrected by the Sys-Rem algorithm which identified trends common to large numbers of SuperWASP lightcurves and removed them (Tamuz *et al.*, 2005; Mazeh *et al.*, 2006), with the main systematic trends being associated with nightly airmass and temperature variations. The times of observations are occasionally imperfectly ordered in some files, due to observations of the same field being made by northern

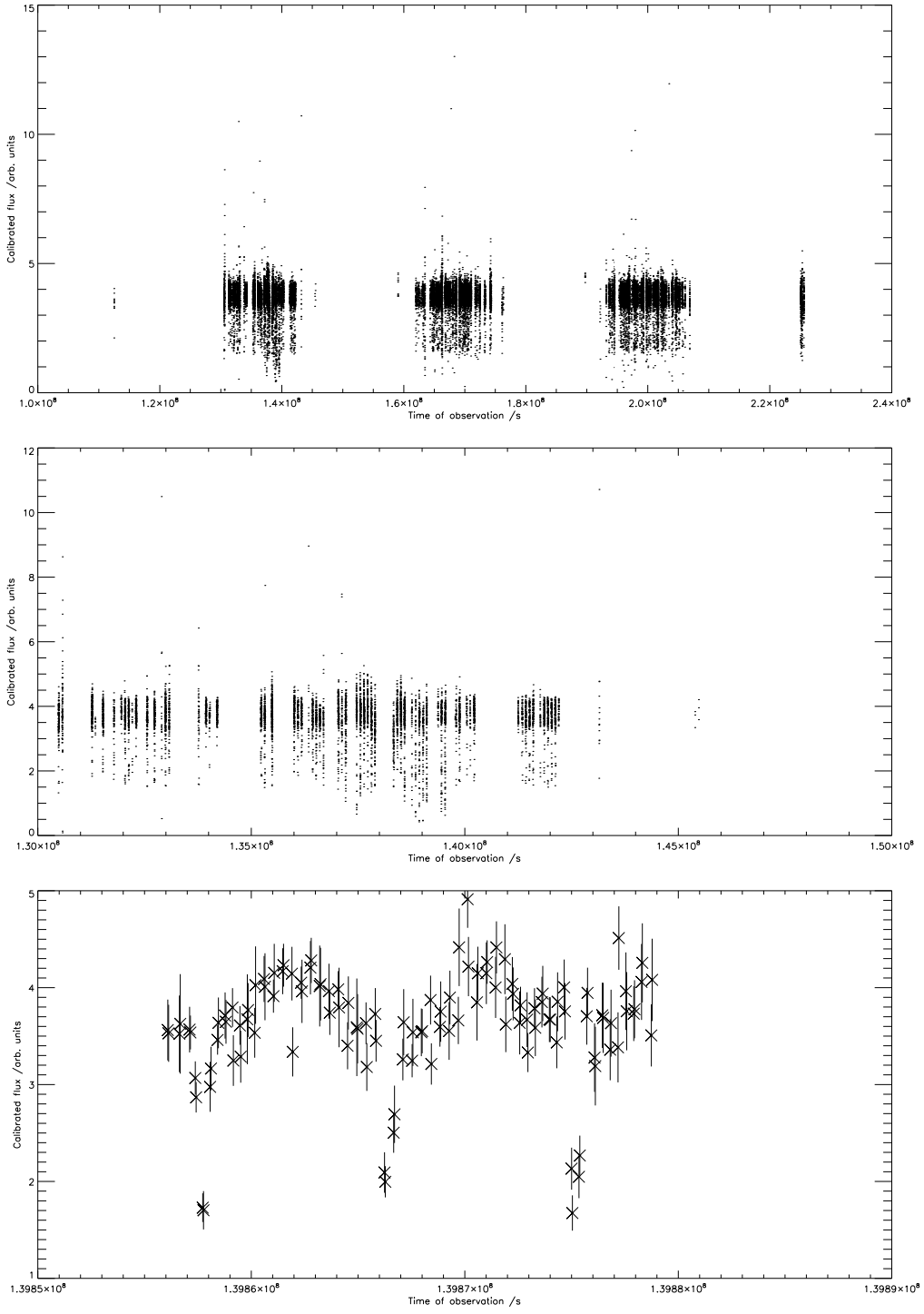

Figure 4.1: SuperWASP lightcurve for NY Vir plotted using IDL. The top image covers the whole observation timescale of several years; the middle one covers a single year's observations; at the bottom a single night's observations are plotted together with uncertainties. NY Vir was selected here as having a distinctive lightcurve despite being relatively faint; it is an eclipsing post-common-envelope binary (see Ch. 12).

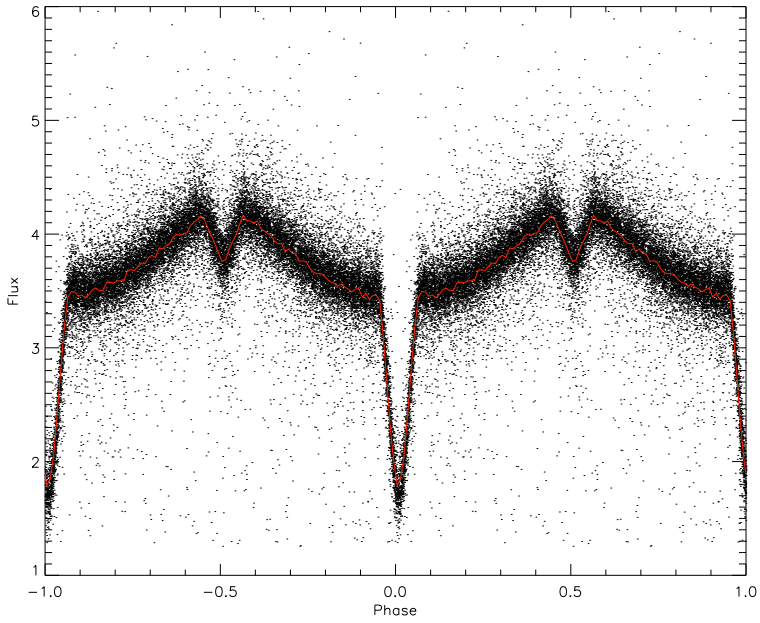

Figure 4.2: Folded lightcurve for NY Vir plotted using IDL, with overplotted binned mean curve in red.

and southern hemisphere cameras on the same night[2]; this potential problem was resolved by applying an initial sort to all downloaded object files. Fig. 4.1 plots SuperWASP data from these three columns to exemplify a typical lightcurve.

4.2 Manual determination with *handle*

An initial trial of the NASA Exoplanet Science Institute (NExScI) online period-detection service[3] was made, but the periods found did not reach the precision levels required. For example, obtaining NY Vir's period to 4 s.f.(as 2.424 h) does not produce a convincing phase-folded lightcurve i.e. a plot of fluxes against times modulo the assumed period, to "fold" the data on its period. After manual trial and error an improved period of 8727.776 s ($\sim$ 2.42438 h) was obtained, giving the folded lightcurve in Fig. 4.2, which clearly shows distinct primary and secondary eclipses at different depths; qualitatively this is obviously the "true" period of

[2]R. West, personal communication
[3]`exoplanetarchive.ipac.caltech.edu/cgi-bin/Periodogram/nph-simpleupload`

the object.

An IDL program called *handle* was written at this point to facilitate manipulation of previously-downloaded SuperWASP FITS files: it plotted the data allowing interactive rescaling, so that the author could estimate periods by eye from individual nights of data (as in Fig. 4.1); it could then fold the data according to various input periods, and output an image once a satisfactory folding was achieved. This approach still had a number of drawbacks: it was slow, requiring many trials to home in upon the best period; it was subjective, lacking any means to quantify the uncertainty in period once a preferred folding was achieved; finally, it could not always produce an unambiguous single best folding for a data set e.g. in objects which might be either rotating single stars or contact binaries with primary and secondary eclipses of near-identical depth.

Therefore an intermediate stage was introduced which employed the IDL module *periodogram.pro*[4] to search for periods within user-specified limits, by the Lomb-Scargle periodogram method (Lomb, 1976; Scargle, 1982; Horne and Baliunas, 1986). This is one of a class of period-searching algorithms using Fourier transforms with unevenly-sampled time-series data, which produce a frequency or period power spectrum indicating the varying significance of different periodicities across a range (see Fig. 4.3). Such techniques are widely used in the field to detect periodicities in variable stars, and generate reproducible results with quantifiable uncertainty (see e.g Schwarzenberg-Czerny (1996, 2003, 2012)). However, aliasing issues associated with the sampling frequency (i.e. the windowing function of the data) can create spurious periodicities in the data, and it is still easy to confuse the true period of an eclipsing binary with the half-period, since a strong peak may be expected in the power spectrum here also. Also, harmonics of a sidereal day tend to show up as misleading periodicities in SuperWASP data in spite of Sys-Rem detrending; finally, the techniques can

[4]Freely available as part of the Solarsoft Library at
`www.astro.washington.edu/docs/idl/htmlhelp/slibrary32.html`

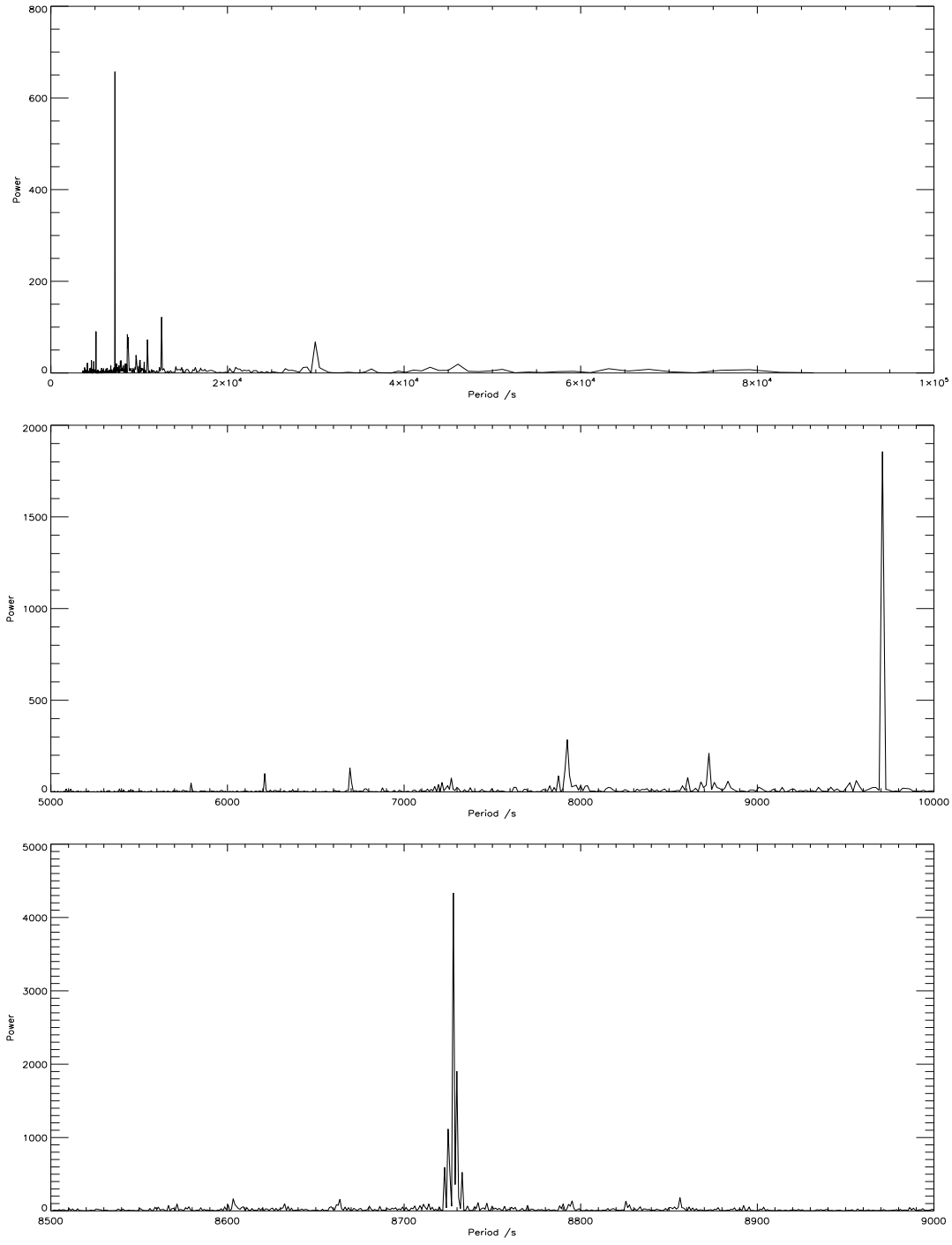

Figure 4.3: Lomb-Scargle periodograms for NY Vir covering decreasing period ranges. At the top, the range between 1 hour and 1 day reveals peaks at shorter periods; in the middle, the range 5000–10000 s indicates three large peaks near 1/9, 1/10 and 1/11 of a sidereal day, two of which are spurious periods. At the bottom, a more constrained search of the range 8500–9000 s produces a strong peak at 8727.9 s which is very close to the "true" period illustrated in Fig. 4.2.

be slow to run if a wide range of possible periods are to be evaluated at high resolution.

Norton *et al.* (2007, 2011) used a CLEANed power spectrum (using the approach of H. Lehto) to minimize the first problem, and combined the technique with other approaches to reduce misclassifications. Since we were primarily interested in short-period objects at this point, for which a whole period could readily be observed in a single night's data, the author used visual estimation to narrow the range over which the periodogram was determined (thus speeding up the calculation and avoiding spurious periodicities), and then repeated the periodogram calculation over gradually decreasing period ranges until the maximum power corresponded to a period at the desired precision. This method was repeatable, justifiable, quantifiable, and produced results which tallied with those found in the literature for known sources.

4.3 *autohandle*

Using *handle* to determine periods was clearly not practical for larger numbers of objects; even for the 53 candidate short-period W UMa-type stars identified in Norton *et al.* (2011), which formed an initial test-case for the research project (Ch. 7). Therefore a new automated version of the code (*autohandle*) was developed to reproduce the manual steps described above.

The data were initially filtered to remove unphysical values e.g. negative fluxes, and values more than 3 σ from the mean flux. Then, a first approximation to the half-period was found by fitting a sinusoidal function, using the Levenberg-Marquardt algorithm (Levenberg, 1944; Marquardt, 1963) to light curve data from three optimal nights of observation (optimized for length, number of data points, and low uncertainties). This reproduced the visual estimation stage using *handle*; the half-period was used to simplify the fitting of a sinusoid to a light

curve with (usually) two minima of nearly equal depth.

The inverse-variance-weighted average half-period, and its uncertainties, were then used to constrain the search range for a Lomb-Scargle periodogram to determine a more precise estimate for the half-period, which was doubled to give an estimate for the orbital period. Finally, the light curve data set was folded on trial periods within a narrow range, and the dispersion of flux values (specifically, their standard deviation) within 100 phase bins was minimized to find the optimum period to the nearest 0.01 s: a form of phase dispersion minimization (Lafler and Kinman, 1965; Stellingwerf, 1978), conceived independently.

A reference light curve minimum was then automatically selected as near to the middle of the data set as possible (since the period here would be expected to approximate the "average" period found for the whole data set in cases where the period was changing linearly). The time of zero-point minimum t_0 was more precisely found by again fitting a sinusoidal function to nearby points.

4.4 *ah2*

Although useful for an initial proof of concept, *autohandle* became unwieldy and hard to maintain as new functionality was added to it over several months. Also, it was optimized for a limited set of objects pre-selected as probable short-period W UMa-type eclipsing binaries, and so would not be expected to work so well with a much larger set of candidate periodic variables of different types (for the project described in Ch. 8). Finally, it could not readily detect sinusoidally-varying changes in period (as opposed to linear decreases or increases) due to the method used to find reference (average) periods, and there were substantial uncertainties associated with the O−C values it determined (see Ch. 5 and 6).

Therefore a new version was written: *ah2*, which streamlined and structured the code more clearly; it also incorporated a number of improvements in its meth-

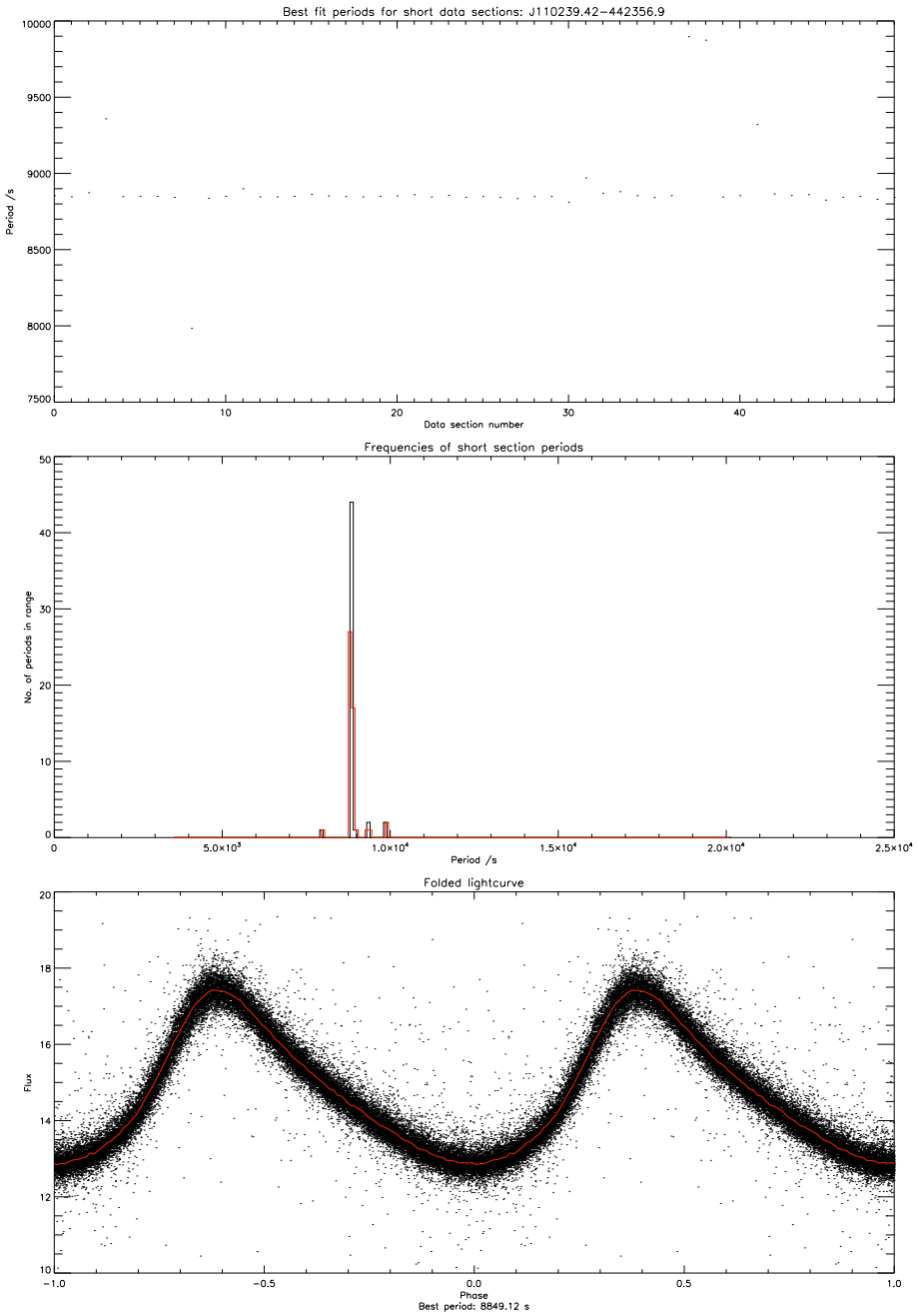

Figure 4.4: Sample graphical output for period-determination part of *ah2* code. At the top are the best periods found for 50 short data sections; they are clearly strongly clustered around a period of ∼8850 s, though a few very different periods are also found. In the middle, the clustering is quantified in terms of frequencies within period ranges; the frequencies are calculated twice using different period range bins, shown here in black and red, to avoid missing a cluster which falls over two bins. At the bottom, the optimal period has been refined by trial phase foldings to minimize dispersion, and the resulting folded lightcurve is plotted, with the binned average overplotted in red. This object appears to be a pulsating variable with period just under 2.5 h.

ods of determining periods and detecting period change. Rather than a three-step period-determination process, it skipped the Lomb-Scargle periodogram stage and went directly from sinusoidal fitting of short data sections to phase dispersion minimization. This improved its ability to detect sinusoidally-varying periods.

During the initial fitting stage, rather than selecting just three "good nights", up to 50 (depending on file size) data sections containing a fixed number of observations were fitted with sinusoids, to obtain a more reliable estimate of the period ready for refinement by trial foldings. Sinusoidal functions proved successful at identifying periods even for markedly non-sinusoidal lightcurves such as NY Vir (Fig. 4.2) or the probable pulsating variable shown in Fig. 4.4. If a frequency plot of the resulting periods yielded a single dominant approximate period, this was used as the period estimate for the second step; otherwise the object was classified as probably non-periodic or possessing a period outside the range of interest.

The approximate periods found for these objects were then refined to the nearest 0.001 s by phase dispersion minimization (as in *autohandle*). This step was repeated with the initial trial period being doubled, and objects were given a preliminary classification as possible eclipsing binaries if the minimum phase dispersion was lower with the doubled period than with the single period; the doubled period was then retained as the binary's orbital period. If the single period yielded a lower minimum phase dispersion, the object was tentatively classified as a periodic variable of a different type (probably a pulsating or rotating variable, or a non-eclipsing contact binary), and the single period was retained as the star's pulsational or rotational period. Objects could also be flagged as exhibiting very low amplitude variability or small numbers of data points, enabling easier identification of interesting objects in a large list of output results.

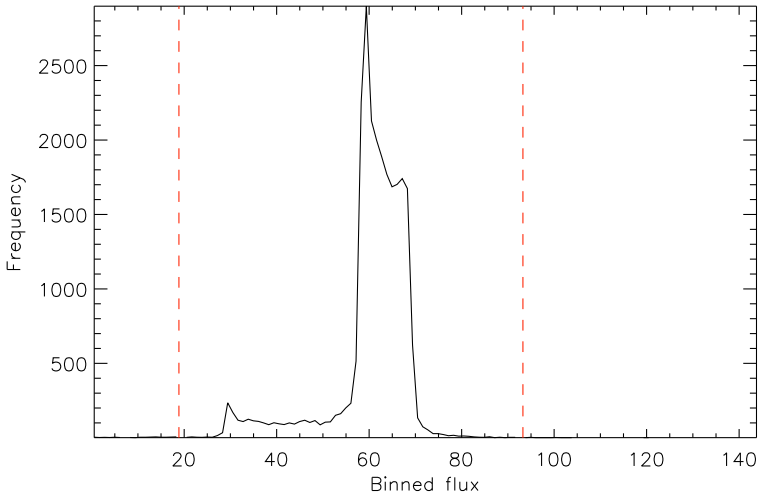

Figure 4.5: SuperWASP observations for HW Vir, showing the binned flux distribution. The limits of the distribution envelope (marked with dashed vertical lines) were used to exclude outliers.

4.5 *ah3*

The most recent version of the code, *ah3*, was developed to incorporate a number of improvements on *ah2*: better exclusion of outliers producing cleaner folded light curves; elimination of the initial period estimation stage involving sinusoidal fitting of short data sections, to allow handling of light curves of any shape whatsoever; more efficient phase dispersion minimization to speed up the running of the code; and better period change determination (described in Ch. 5).

Extreme outliers often complicated the analysis of SuperWASP light curves; here, a first pass stripped out physically-impossible data points, and then an envelope enclosing a plausibly-relevant range of fluxes was determined from the flux frequency distribution (Fig. 4.5). Incidentally, these "horizontally binned" light curves proved to have shapes characteristic of their variability type in most cases e.g. detached eclipsing binaries generally have two or three clear peaks, the highest being strongest, with a low plateau in between; contact eclipsing binaries have two broad peaks of similar height; pulsators tend to have the lower of two peaks being strongest; non-variables do not show peaks at all. In future work,

this insight could perhaps be used to hunt for variables rapidly amongst very large collections of light curves, without needing to search for periodicity at all.

Reference orbital periods were then found using pure phase dispersion minimization: folding each light curve on a range of trial periods (initially separated by 1 s), binning the folded curves by pseudo-phase, and summing the standard deviations of fluxes in each bin to give a total dispersion measure per trial period. The lowest dispersion should correspond to the best folding, where the data points have minimal scatter about the mean light curve shape. The period could then be refined further by repeating the search with smaller time steps between trial periods. It was observed that slightly different final periods were found if different numbers of phase bins were used to calculate dispersions; therefore, by repeating the whole period-determination procedure with a range of binnings, a mean reference period and an improved measure of its uncertainty were determined for each object.

A third stage of outlier-removal was then applied, iteratively cleaning out points lying 4.5 standard deviations from the binned mean flux values. This allowed a smoother light curve template shape to be determined for each object (needed for period change determination); the number of points used for each template also affected its out-of-eclipse smoothness and the sharpness of its eclipses, and this could be optimized by visual inspection if a small number of objects were being studied in depth (e.g. Ch. 12).

As yet the folded curves had arbitrary pseudo-phases associated with their minima, so each deeper (primary) minimum was aligned with phase zero in a two-step process. First, an approximate zero-phase was found from the bin with the lowest mean flux (this would give inaccurate results if each bin covered a significant fraction of the orbital period, or if the primary eclipses were flat-bottomed). Then, folded data points within 0.1 phases of the approximate zero point were used to define the true zero, by "mirror-folding" about a number of

trial zeroes, and applying phase dispersion minimization again.

This method has the advantage of using all the data near eclipse, rather than just the binned means, and so is able to benefit from SuperWASP's long time-base and extensive cycle-coverage. However, it does rely on the assumption of basically symmetric primary eclipses, like the method of Kwee and van Woerden (1956), which is still used widely with high-quality photometric light curves covering a small number of nights. Where eclipses are clearly asymmetric, a minimum-flux approach to finding the zero phase would probably be more meaningful; in the objects studied in Ch. 12, however, primary eclipses were indeed highly symmetric, and so a method allowing direct comparison between SuperWASP eclipse timings and those measured by others using Kwee and van Woerden's approach was preferred.

Chapter 5

Detecting and measuring orbital period variation

Here the four versions of my IDL code introduced in the last chapter will be described in their application to detecting and quantifying orbital period changes in eclipsing binaries for which a reference period has already been determined. Several parts of this chapter are again based on the method sections of Lohr *et al.* (2012, 2013b, 2014b).

5.1 Early attempts using *handle*

My first attempts to detect period changes in SuperWASP data were implemented in *handle*. Having found an "average" period for a whole data set, periodograms were calculated for different subsections of the timescale of observation: first disjoint, then overlapping, to form a moving time window within which the most significant period (i.e. the one with the maximum power on the period spectrum) could be automatically captured. When this gave a series of periods apparently randomly scattered about the mean period, a dynamic power spectrum was used to display the results, as in Clarkson *et al.* (2003) for X-

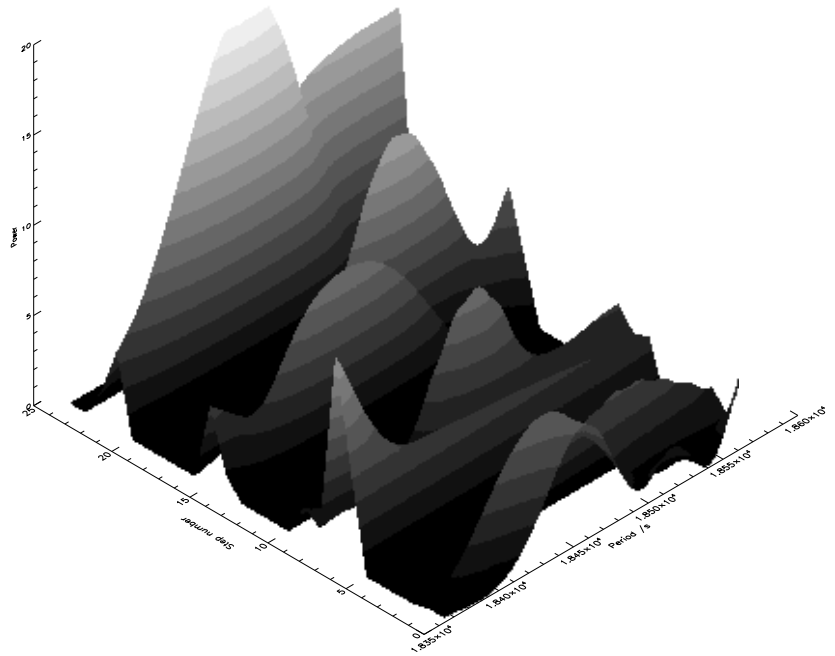

Figure 5.1: 3-D dynamic power spectrum for object 1SWASP J234401.81-212229.1 (discussed in Ch. 10). At each of 25 time steps through the data set, a periodogram is calculated over a time window twice the length of the time step, within a period range 18461.591±100 s, provided each window contains at least 200 data points. The power at each periodicity is represented by both height and intensity of shading. Although this object in fact exhibits rapid period decrease over the timescale of observation, no clear trend is apparent from the dynamic power spectrum.

ray binaries. Fig. 5.1 illustrates a typical result of the implementation of this approach in *handle*.

This approach did not seem to yield fruit for the data considered, even for objects later found to be exhibiting genuine and substantial period change.

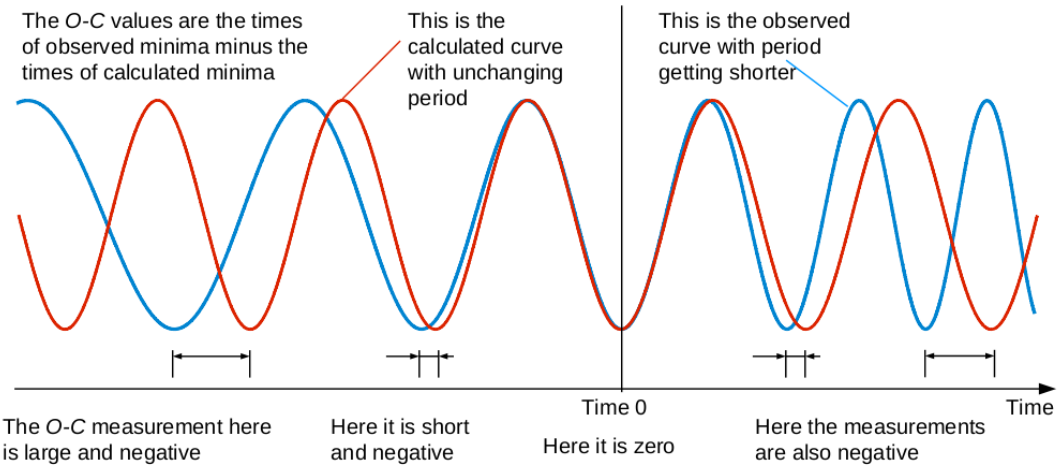

Figure 5.2: Graphical explanation of determination of O−C values from a light curve where the period is already known (taken from a poster developed to explain my research to the general public). This also illustrates intuitively why the O−C diagram forms a parabola opening downwards for an object whose period is reducing linearly with time; a parabola opening upwards would be formed for an object with linearly increasing period. An object with period varying sinusoidally would have an O−C diagram also varying sinusoidally.

5.2 *autohandle*

When developing *autohandle*, the aim was to implement a different method used in many studies of period changes in variable stars: the observed minus calculated (O−C) diagram. This uses the difference between observed times of eclipse minima in the object's (unfolded) light curve, and calculated times of minima relative to an arbitrary zero-point minimum, on the assumption that the period does not vary. Fig. 5.2 illustrates this process graphically and intuitively.

The implementation in *autohandle* was as follows. A reference light curve minimum was automatically selected as near to the middle of the data set as possible (since the period here would be expected to approximate the "average" period found for the whole data set in cases where the period was changing linearly). The time of zero-point minimum t_0 was more precisely found by fitting a sinusoidal function to nearby points; the optimum period length P_{calc} was then used to calculate expected times of minimum light ($C = t_0 + P_{\mathrm{calc}}E$, where E is

the period number, or epoch, relative to t_0) within the full time-range observed. Actual times of minimum O near these values were determined using quadratic fitting (which proved more robust than Gaussian or sinusoidal fits), with poor fits and inadequately-sampled minima being automatically rejected.

In this way a series of O−C values were obtained, and plotted against epoch. A second series was found for the other set of light curve minima (i.e. the secondary eclipses if the primary eclipses had formed the first series, or vice versa). Such O−C diagrams will be expected to follow a quadratic curve if the period is changing linearly, as illustrated in Fig. 5.2: essentially they are the integral of the function $P(E)$, which approximates the continuous function $P(t)$. The derived parameters of this curve then allow us to determine the rate of change of period with respect to epoch. Since $O(E) = C(E) + \Delta T(E)$, we can write the differences in the general form of a quadratic function: $\Delta T(E) = aE^2 + bE + c$. Then we have:

$$\begin{aligned} P(E) &= O(E) - O(E-1) \\ &= C(E) + \Delta T(E) - [C(E-1) + \Delta T(E-1)] \\ &= t_0 + P_{\rm calc}E + aE^2 + bE + c - [t_0 + P_{\rm calc}(E-1) + a(E-1)^2 + b(E-1) + c] \\ &= P_{\rm calc} + 2aE - a + b, \end{aligned}$$

and differentiate this with respect to E to obtain simply $\frac{{\rm d}P}{{\rm d}E} = 2a$ i.e. the rate of period change is twice the observed coefficient of the quadratic term. If there is no observed period change, there will be no quadratic term, and any discrepancy between the true value of the period and the calculated value will be given by $O - C = \Delta T(E) = bE + c$ i.e. the O−C diagram will follow a straight line with slope b, intersecting the y-axis at c.

Therefore an attempt was made to fit a quadratic function to each O−C series using the IDL function SVDFIT, from which a value for the rate of period

change (per cycle) could be determined. The inverse-variance weighted average period change (across both O−C series) was thus found for each star, and could be converted into an approximate rate of change $\frac{\mathrm{d}P}{\mathrm{d}t}$ in s y^{-1}. Uncertainties in period change were taken from the fitting function's output uncertainties for the quadratic term's coefficient; where these error bars included zero, the period change was regarded as non-significant.

5.3 *ah2*

During the development of *ah2*, several modifications to the algorithms for detecting and quantifying period change by means of O−C diagrams were trialled. One idea was to measure the times of observed minima with sinusoidal rather than quadratic fitting functions: this tended to produce better fits to minima and thus located the times of eclipses more accurately, reducing the uncertainties in the resulting O−C diagrams. Different functional fits to O−C curves were also tried, in various combinations: linear, quadratic and sinusoidal; and residual O−C diagrams were evaluated after subtraction of the best fitting function (see Fig. 5.3 for an example of this intermediate stage of code development).

However, the final version of *ah2*, used in Lohr *et al.* (2013b), found an even better way to determine accurate times of observed (primary) minima. Rather than trying to fit local regions of the light curve with quadratic, Gaussian, sinusoidal or other analytic functions, the binned mean light curve for each object, found during phase dispersion minimization, was used as a fitting "function". This shape, being derived from the combined observations of hundreds of cycles, might be expected to provide an excellent fit for each individual observed cycle, since it represents the true underlying shape of the object's light curve. (A similar approach was apparently used by Pribulla *et al.* (2008) for finding eclipse minima in a close quadruple system.)

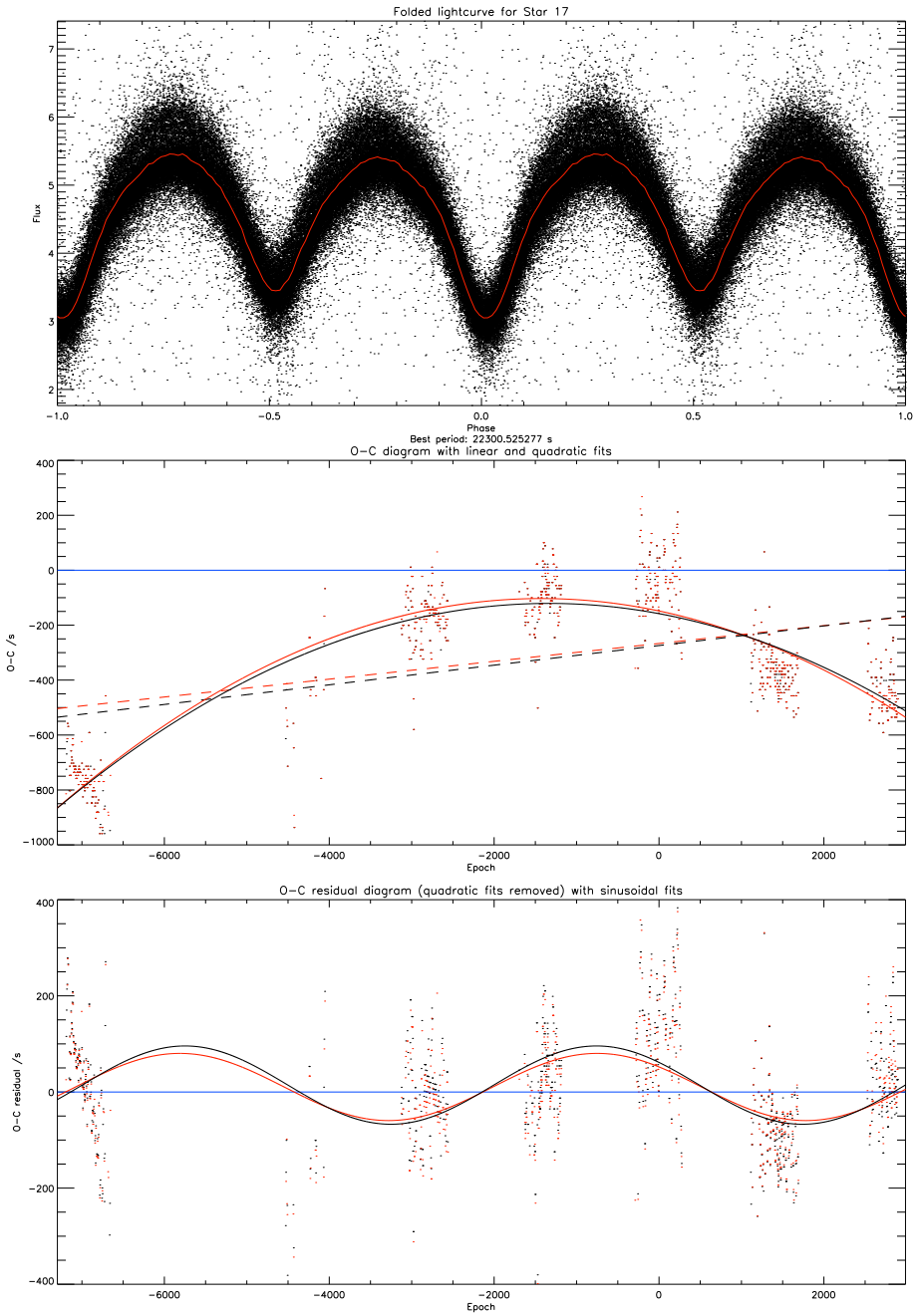

Figure 5.3: Sample graphical output for period-change-analysis part of a form of *ah2* code, applied to "Star 17" i.e. 1SWASP J174310.98+432709.6 (see also Figs. 7.1 and 7.2 in Ch. 7). At the top, the light curve is almost identical to that found with *autohandle*, being folded at a period of 22300.525 s, where *autohandle* had 22300.517±0.009 s. In the middle, the O−C values show less scatter than before, and are demonstrated to be better fitted by a quadratic (solid red and black curves) than a linear function (dashed lines). At the bottom, the quadratic fits have been subtracted from the O−C values, and the residual is plotted with a best-fit sinusoidal function. There is perhaps some support here for this object exhibiting periodic variability in orbital period, in addition to the linear decrease already found.

This approach has the advantages that it does not require the eclipses to be remotely symmetrical, or the same phase range to be used for each fit, as is preferred with the method of Kwee and van Woerden (1956). The method might be expected to break down, however, in objects whose light curve varies in shape over time, such as RR Lyrae pulsators exhibiting the Blazhko effect (see Ch. 2). The number of phase bins to be used for the fitting curve needs to be chosen carefully: if too many bins are used, the fitting curve will appear spiky, with features which are not part of the underlying light curve; if too few bins are used, the fitting curve will blur distinctive features of the underlying light curve which may be necessary for optimal fits e.g. a difference in depth or shape between primary and secondary eclipses.

For the study described in Ch. 8, the program automatically picked a bin number based on the number of data points in the object file and the brightness of the object, though this was optimized by hand in some cases. An optimal night for fitting the zero epoch (essential for determining reliable calculated times of eclipses for the O−C diagram) was also selected manually from a range near the middle night of each object file.

After construction of each O−C diagram, a small number of locally-outlying O−C values were stripped out automatically; manual checking of the corresponding nights of observation indicated that these were typically caused by irregular features of the data (instrumental or astrophysical) rather than failures of the fitting method. Linear and quadratic fits of the O−C values were then attempted; where a quadratic function gave a superior fit (i.e. its reduced χ^2 value was lower than that of the linear fit), and the rate of change was significantly different from zero ($\geq 1\sigma$), the object was counted as exhibiting secular period change.

5.4 *ah3*

In the latest version of my period change detection code, this internal template-based method for finding times of minima was refined further, allowing for local variations in the flux level or amplitude of the light curve. The issue of outliers in O−C diagrams was also addressed more thoroughly. This version of the code was optimized for a small set of very short-period objects with extremely well-defined primary eclipses (see Ch. 12), but was designed to be sufficiently general also to work for large numbers of eclipsing binaries of different types and with a range of periods (Ch. 13).

The expected times of primary eclipse were determined using the reference periods found in the first part of the code (Ch. 4), in combination with the location of phase zero in the phase-folded data, relative to the start-time of the observations. No "epoch zero" thus needed to be determined independently, though in cases of obvious period change, the cycles corresponding most closely to the reference period would typically be located near the middle of the data set, since the reference period itself was an average.

Using these calculated eclipse times, each night of observed data was compared with a fitting template covering appropriate phases, derived from the binned mean light curve template generated earlier, interpolated by a spline curve as necessary to match the exact times of observation. The template could be adjusted using three parameters: x-axis position (time), y-axis position (flux), and scaling in the y-direction (amplitude of curve). At each fitting step, the observed curve was compared with 125 synthetic curves generated from the template by varying the three parameters simultaneously according to a cubic grid of possible values, and the minimum χ^2 value was chosen as indicating the best fit.

The first step had the expected x-y location and scale of the template as the centre of the parameter "cube"; subsequent steps recentred the cube on the

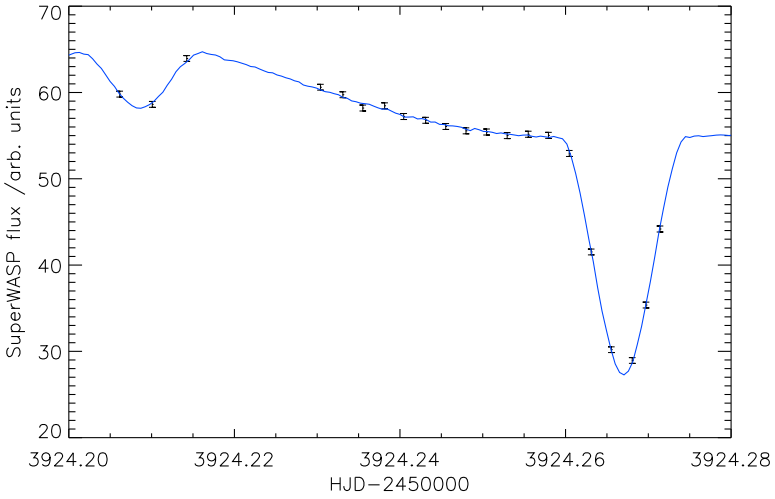

Figure 5.4: First night of SuperWASP observations of HW Vir, with best fit overplotted (final uncertainty in timing < 2 s).

parameter combination with the lowest χ^2 value at the previous step. If a fitting attempt repeatedly moved the centre to the edge of the previous cube, it was deemed not to be converging, and was abandoned. If the cube's centre did not move between steps, the separation between grid points was reduced, and the fitting step was repeated. This continued until the difference between adjacent steps' minimum χ^2 values fell below a critical threshold (0.001).

In this way, an optimum fit between the light curve template found for the whole data set folded at its mean (reference) period, and each night of observed data, could be determined. This best fit provided an x-axis offset from the expected value, which corresponded to an O−C value for the night as a whole, but which could also be combined with the nearest time of calculated minimum to produce a heliocentric Julian date (HJD-UTC) for that eclipse, allowing direct comparison with other published times of minima for the same source.

Our approach here, fitting an adjustable template light curve to the whole of a night's data (which could cover several orbital cycles in the case of some short-period binaries e.g. Ch. 12), aimed to take full advantage of SuperWASP's strengths: long-term, numerous, fairly high-cadence observations; without being

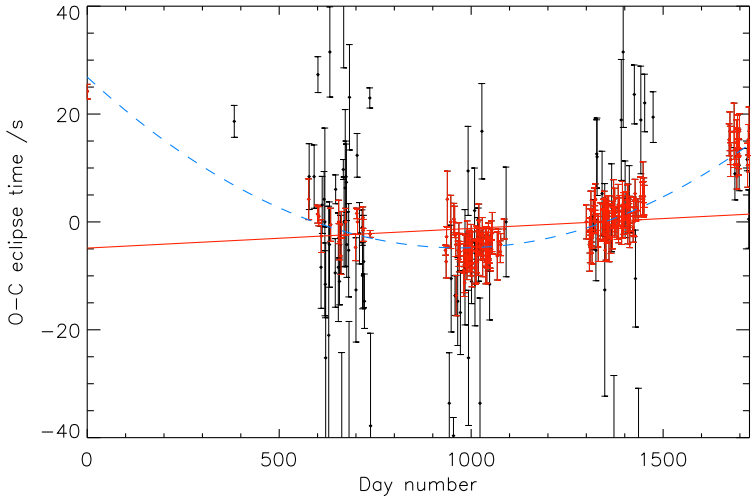

Figure 5.5: O−C diagram for HW Vir (SuperWASP data), with automatically excluded outliers in black and selected good minimum timings in red (colour online only). A small number of more extreme outliers lie outside the bounds of the plot. Best linear (red solid line) and quadratic (blue dashed line) fits to the selected data points are overplotted; the preferred quadratic fit indicates highly significant (p=0.002) period increase of 0.00287±0.00009 s yr^{-1}.

hampered by its relatively low signal-to-noise photometry in comparison with larger telescopes. On some occasions, a useful time of primary eclipse could be obtained even when the eclipse itself was not captured by the night's observations, if a reflection effect and/or shape of secondary minimum provided sufficient information for an excellent fit (see Fig. 5.4 for an example single-night fit).

Changes in light curve amplitude could also be measured, using the y-scaling parameter adjustment for the best fit. The remaining fixed-scale y-shifting parameter would track any changes in flux level for the whole night's curve, relative to the full light curve's out-of-eclipse mean flux; such changes might be expected to result from varying air mass or Moon proximity on different nights, or from instrumental noise. Approximate starting uncertainties for each of the three parameter values were obtained from the curvature of the χ^2 volume in the final cubic grid.

After all nights had been processed, convergent results could be plotted on

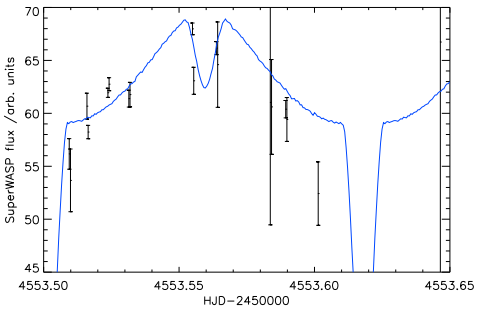

Figure 5.6: Night 629 of SuperWASP observations of HW Vir, with best fit overplotted (O−C value −21 s where the local trend is close to 0; final uncertainty in timing 24 s).

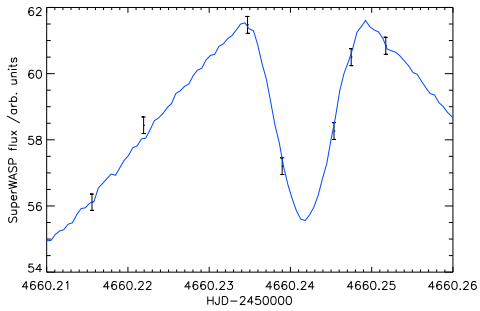

Figure 5.7: Night 736 of SuperWASP observations of HW Vir, with best fit overplotted (O−C value +23 s where the local trend is close to 0; final uncertainty in timing 2 s).

three diagrams corresponding to the different fitting parameters. Outliers in the O−C diagram in particular (e.g. Fig. 5.5) tended to complicate the determination of period change. Night-by-night visual checks of the fitted data did not typically suggest any underlying physical cause for short-term variations such as spots or additional eclipses. We may note that similar visual checks of apparent contact eclipsing binary 1SWASP J093010.78+533859.5, occasioned by its erratic O−C diagram, revealed a second eclipsing binary (Ch. 11); the outlying values here generally presented a far more chaotic appearance, and were most probably produced by a range of atmospheric and instrumental complicating factors, like the outliers in SuperWASP light curves in general.

To some extent, these O−C outliers could be excluded by the size of their uncertainties: some nights of data contained only a handful of apparently erratic observations, and the resulting poor fits had large uncertainties for their parameter values (e.g. Fig. 5.6). However, some nights resulted in well-constrained good fits despite being obvious outliers relative to the local O−C trend (e.g. Fig. 5.7), so this criterion was not sufficient. Excluding nights with small numbers of observations would also have removed many perfectly good values from the O−C diagram (where those observations were spaced closely around the primary mini-

mum, for example). Removing points on the basis that they lay several standard deviations from the mean O−C value would also have been unhelpful, since it would have removed valid points if the underlying shape of the data set was parabolic (e.g. in Fig. 5.5, excluding the outliers from Figs. 5.6 and 5.7 in this way would also have removed the very valuable point shown in Fig. 5.4: the only representative from that year of SuperWASP observations).

It was of course not known in advance whether a linear or quadratic fit would be appropriate for each O−C diagram, and the presence of outliers could easily change which function gave a better fit to the data set. Therefore, an automated iterative procedure was carried out (without any prior preference for either function) attempting linear and quadratic fits alternately to each O−C diagram, and removing points lying >3 standard deviations from the better fit or with uncertainties >3 standard deviations larger than the mean uncertainty size. Sinusoidal fits were not attempted, since this would introduce too many degrees of freedom, and since the time-base covered was usually short enough that sinusoidal variation would show up as approximately quadratic in any case[1].

The plot of amplitude variation was also used to exclude extreme outliers in that dimension; however the absolute flux variation plot was not used, since sudden and substantial variations in that dimension appeared entirely physically plausible. If the reduced χ^2 value of the better fit ever fell below 1, the uncertainties of the remaining points were rescaled accordingly. The process halted when no further points needed to be removed.

It should be noted that, while this form of my period change detection code worked very well for eclipsing binaries with periods below a few days, it struggled to fit eclipses in objects with P >5 d or so, since the fitting algorithm operated on a single night at a time. An obvious modification to make to the code, which would fix this limitation, would be to expand the time range to be fitted

[1]Though see Ch. 13 for a number of examples where this was not quite true.

according to the period of the object itself e.g. for an object with $1 < P < 2$ d it would select adjacent pairs of nights for fitting eclipse minima; for an object with $8 < P < 9$ d it would select sets of nine adjacent nights etc.

Chapter 6

Testing the method

At several stages during the development of the code described in the last two chapters, synthetic SuperWASP light curves were generated to test the validity of the approach using data with known values of period and period change. Parts of this chapter are based on the method sections of Lohr *et al.* (2012) and Lohr *et al.* (2014b). A final section describes a test of binary modelling software with SuperWASP data; this software was used repeatedly during follow-up of individual objects of interest (Ch. 7, 9, 10 and 11).

6.1 *autohandle*

This version of the author's code was first tested for its capacity to measure reference periods accurately using two synthetic data sets:

(1) a sinusoidal function with the sampling, amplitude, period and average flux value of the SuperWASP observations of NY Vir ($3.8 + 0.5 \sin(\frac{2\pi t}{8727.77})$), and with fixed small uncertainties of 0.05 flux units;

(2) as (1), but with data points perturbed by normally-distributed pseudo-random variations with standard deviation about half the amplitude of the light curve, and with uncertainties equal to the modulus of the pertur-

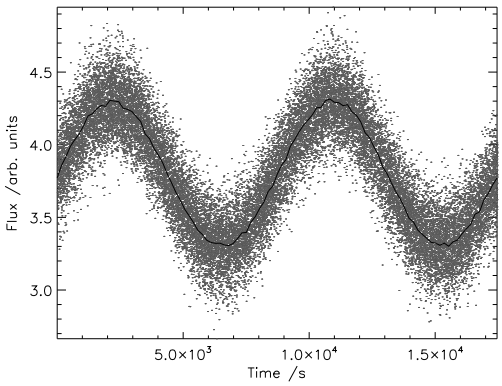

Figure 6.1: Light curve for test data set (2), folded at "orbital period" of 17455.529 s, with mean values for binned data overplotted. The input "orbital period" was 17455.540 s i.e. double the period of NY Vir, since the program assumes it is dealing with eclipsing binaries which exhibit *two* minima per orbit. The random scatter of this folded data set closely resembles a typically-noisy SuperWASP light curve.

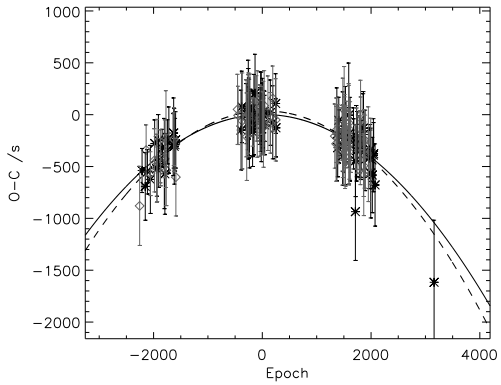

Figure 6.2: O−C diagram for test data set 4, with best-fit quadratic curves overplotted. Black stars and solid line indicate primary eclipse series; grey open diamonds and dashed line indicate secondary eclipse series.

bations plus 0.05 (to simulate a rather noisy data set with uncertainties in part proportional to each data point's displacement from the expected value, but with a minimum value).

The program was able to recover the input period of (1) correct to 7 s.f. and of (2) correct to 6 s.f.; Figure 6.1 shows the folded light curve obtained.

The method was then tested for its sensitivity to genuine period change using several synthetic data sets:

(1) and (2) as described earlier;

(3) as (1), but with the period losing 1 s over 4 years
$(3.8 + 0.5\sin(\frac{2\pi t}{8727.77-(3.961\times10^{-9}t)}))$;

(4) as (3), but perturbed by noise and with uncertainties as in (2).

For neither (1) nor (2) was any significant period change detected, as would be hoped. For (3) and (4) the "average" period corresponding to approximately the middle of the data set was recovered as expected, and the O−C diagram shows a clear quadratic shape indicating the period decrease, found to be significant at 28 σ and 7 σ respectively (see Figure 6.2). The amount of period change was also recovered correct to 0.1 s y^{-1}, where the error was largely due to the approximation of a continuous function of time by a discontinuous function of epoch in the customary differential equation, as pointed out by Kopal and Kurth (1957).

Additional tests indicated that the method failed to detect sinusoidally-varying period change unless the period of meta-variation was very long (more than a decade). This was apparently because the initial stage of period determination failed when there was no single well-defined peak in the periodogram corresponding to an "average" period: if the period itself became longer and shorter sinusoidally, it would actually be changing most rapidly when it passed through the mean period, and most slowly when it neared extrema on each side of the mean, making period detection challenging by this method. Later versions of the code addressed this limitation by eliminating the periodogram stage of period determination altogether (Ch. 4).

6.2 *ah3*

By the time this version of the code was being used, its approach to period change determination had changed sufficiently that further tests were desirable to ensure its continued validity. These tests were carried out using the set of eclipsing binaries discussed in Ch. 12 as a starting point.

Following the O−C diagram function-fitting procedure described in the last chapter, period change was either supported, if a quadratic function gave a better

fit to the remaining data points in the O−C diagram, or unsupported, if a linear function gave a better fit. (A linear fit with slope significantly different from zero would also arise if the period used were too long or too short, though irregular or sparse coverage of the time base could also produce a non-zero gradient even with an accurate period.) However, some cases of apparent period change were only marginally supported, in that the best linear fit produced a (modified) χ^2 value only slightly higher than the best quadratic fit. Since the points' uncertainties had been adjusted during the process of outlier removal, it was not clear how large a difference in χ^2 values would be required to indicate e.g. a 95% confidence level in a measurement of period change. In particular, there seemed no reason to believe that the same level would be valid in all cases.

Therefore, tests using synthetic light curves were carried out to determine the reliability of the program. Each object's mean (template) light curve was used as the basis for generating a large number of "background" synthetic curves, and the time sampling and point uncertainties of the original light curve were applied to each synthetic curve. Each flux value was then perturbed randomly according to a normal distribution with standard deviation equal to the corresponding original data point's uncertainty.

Correlations between observations made on the same night in SuperWASP light curves were accounted for by determining the mean residual flux of each night's observations relative to the template, and adding one of these values, chosen at random, to each night's fluxes in the synthetic curve. Histograms of the final synthetic curves' residual fluxes, relative to their mean curves, followed approximately Gaussian distributions (like the original objects), but with slightly greater widths i.e. the synthetic curves had slightly larger uncertainties than the real light curves. No period change was included in the synthetic curves.

The synthetic curves were then processed by *ah3* in exactly the same way as the real light curves, to see what proportion of them produced false positives,

and how large the difference between best linear and quadratic fit χ^2 values was. This allowed us to distinguish between statistically significant and non-significant period changes.

A similar approach was used to check the sensitivity of the code to genuine period change. Synthetic curves were generated as before, with the characteristics of the test objects; here, however, steady period change was included, with a known sign and magnitude. *ah3* was then run on the synthetic curves, to determine lower limits of detectability for each system i.e. how rapid a period change would need to be in order to be reliably detected and accurately measured using SuperWASP archive data.

The outcomes of these tests will be described in detail in Ch. 12, where it is clear that *ah3* has the capacity to detect statistically-significant period change in SuperWASP light curves at rates as small as 0.0003 s yr^{-1}. However, the characteristics of individual light curves (brightness, noise, amplitude, time base, intrinsic shape) have a substantial impact on the detectability of significant period variation.

6.3 PHOEBE binary modelling software

The code of Wilson and Devinney (1971) is able to model binaries of all kinds, including contact systems (which many other codes cannot). PHOEBE (PHysics Of Eclipsing BinariEs) is a graphical front-end developed around a recent version of Wilson and Devinney's code (Prša and Zwitter, 2005). To check that this software would yield acceptable parameters from SuperWASP data, I used it to model a short-period eclipsing binary (GSC 2314-0530 = 1SWASP J022050.85-+332047.6 = BX Tri) for which parameters had already been published (Dimitrov and Kjurkchieva, 2010). This has the shortest-known orbital period of any binary system with main-sequence components: 16643.64 s or 0.1926347 d as found by

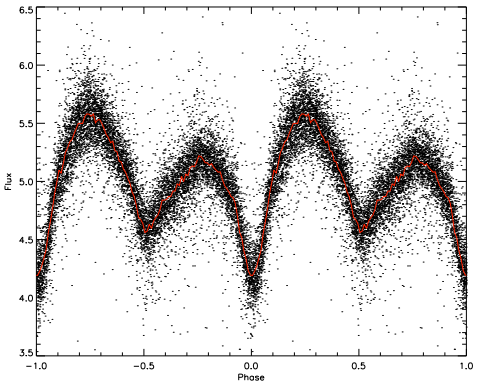

Figure 6.3: Light curve for J022050 folded at period of 16643.64 s, with binned mean curve used in PHOEBE modelling.

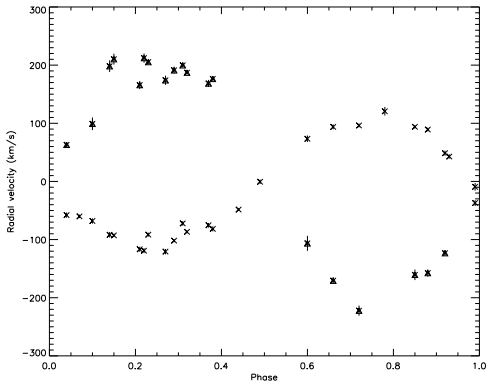

Figure 6.4: Radial velocity curves for J022050 used in PHOEBE. Crosses indicate primary radial velocities; triangles indicate secondary velocities.

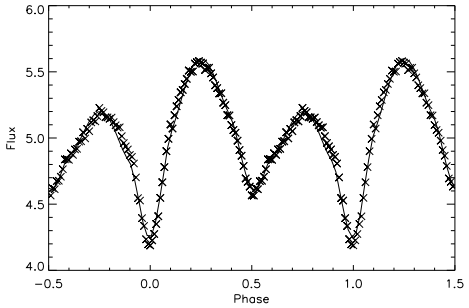

Figure 6.5: Light curve data with overplotted best fit line found with PHOEBE for J022050.

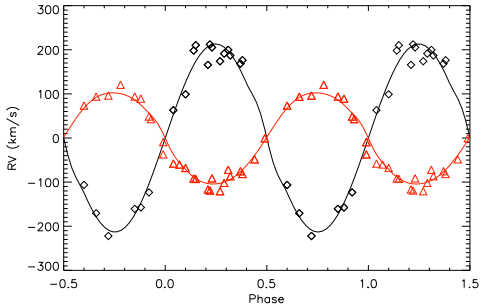

Figure 6.6: Radial velocity fits found with PHOEBE for J022050. Primary radial velocities are red; secondary black.

autohandle in Ch. 7.

The folded light curve obtained from SuperWASP data was used, and average flux values in 100 phase bins were extracted (Fig. 6.3) to keep the fitting procedure manageable (complete SuperWASP data sets had caused the software to crash or run very slowly). Radial velocity measurements based on spectroscopic observations were taken from Dimitrov and Kjurkchieva (2010) (Fig. 6.4).

Using PHOEBE, the best-fit input parameters were found, to minimize the difference between synthesized and observed light curves and radial velocity curves (Figs. 6.5 and 6.6). A single large spot was included in the model to

Parameter source	M_1 ($/M_\odot$)	M_2 ($/M_\odot$)	q (M_2/M_1)	R_1 ($/R_\odot$)	R_2 ($/R_\odot$)	a ($/R_\odot$)	i ($^\circ$)
Dimitrov & Kjurkchieva	0.51	0.26	0.52	0.55	0.29	1.28	72.5
Own modelling with PHOEBE	0.55	0.28	0.50	0.58	0.27	1.32	70.0

Table 6.1: Parameters for J022050.

account for the difference in maxima heights: the O'Connell effect (O'Connell, 1951), but I was reluctant to include more in the absence of direct evidence. Prša cautions "With proper tuning, spots may account for *any* flux variation that is exhibited in light curves, be it of magnetic origin or not"[1].

The resulting output parameters (Table 6.1) were all within 3–8% of the values found by Dimitrov and Kjurkchieva, who used high-precision four-colour photometric light curves obtained over 14 nights, and modelled *two* spots as well as a third light in order to obtain their fits. This suggests that PHOEBE can be used with SuperWASP binned-average light curves to obtain reasonable parameters.

[1]PHOEBE Scientific Reference manual:
`phoebe-project.org/1.0/docs/phoebe_science.pdf`

Part III

Results

Chapter 7

Proof of concept

As an initial demonstration that period changes, if present, could be detected and measured in SuperWASP light curves using the tools developed, a small sample of probable short-period eclipsing binaries was investigated. The following account is closely based on Lohr *et al.* (2012).

7.1 Introduction and method

Norton *et al.* (2011) presented evidence for 53 candidate W UMa-type eclipsing binaries observed using SuperWASP, with periods close to the short-period limit, of which 48 were new discoveries. Some of these, when folded at their determined period, failed to give well-defined light curves, which could be the result of period variability. Therefore our aim here was to determine whether any of these candidate binaries showed evidence of period changes during their observation by SuperWASP. Period decreases might indicate a detached or semi-detached binary undergoing unstable mass transfer likely to end in merger, or even a contact binary approaching merger.

The light curve data for the 53 candidate objects was extracted from the SuperWASP archive and the custom IDL code *autohandle* was run on each file,

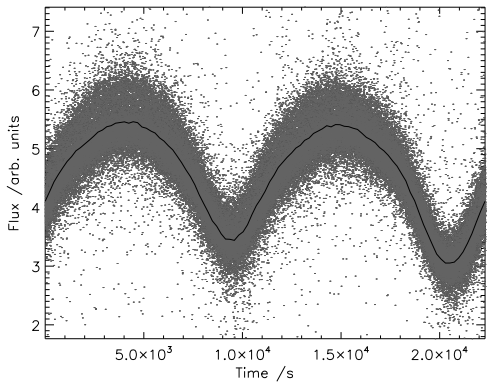

Figure 7.1: Light curve for object J174310, folded at period of 22300.517 s, with mean values for binned data overplotted.

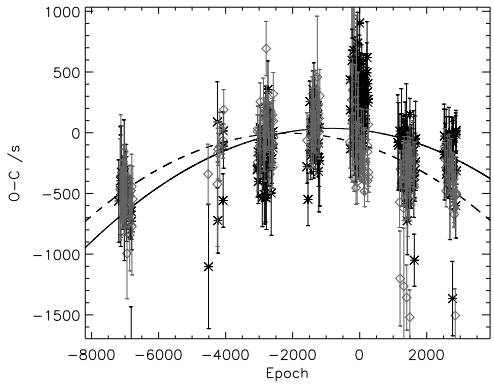

Figure 7.2: O−C diagram for object J174310, with best fit quadratic curves overplotted. Black stars and solid line indicate primary eclipse series; grey open diamonds and dashed line indicate secondary eclipse series. Period decrease significant at 21 σ is indicated (i.e. the period change found differs from zero by at least 21 times the size of the uncertainty).

as described in Ch. 4 and 5. This provided a measure of their orbital periods, to confirm the findings of Norton *et al.*, and attempted to detect and quantify any steady change in the period over the time they were observed by SuperWASP.

7.2 Results

The optimum orbital periods found for the 53 stars are given in Table 7.1. In the majority of cases, identical periods (to 4 or 5 s.f.) to those found in Norton *et al.* were obtained. Object J055418's period was given incorrectly in table 1 of Norton *et al.*, but correctly in the appendix. For nine objects, a period approximately 1/8 longer was obtained by this method; manual checks indicated that the longer periods found here were more plausible (e.g. the folded light curve was more clearly defined; the primary and secondary minima exhibited more difference in depths). In the earlier paper, only candidate periods below

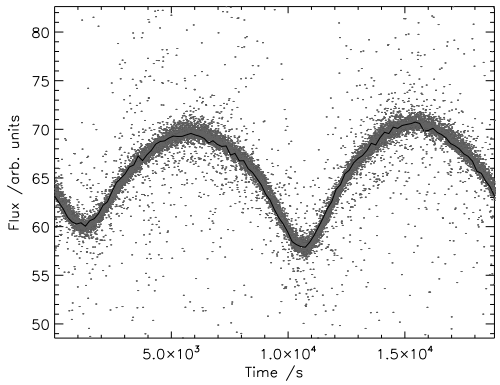

Figure 7.3: Light curve for object J133105, folded at period of 18836.380 s.

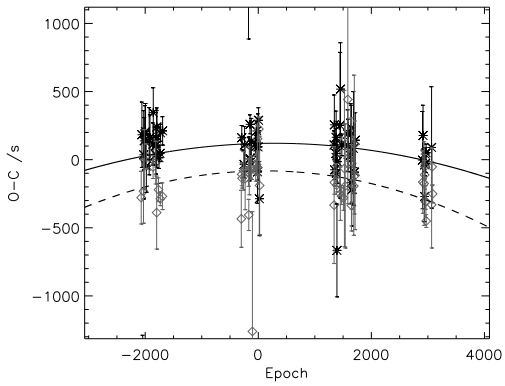

Figure 7.4: O−C diagram for object J133105, with best fit quadratic curves overplotted. Period decrease significant at 5 σ is indicated.

20000 s ($\sim$ 0.2315 d) had been investigated, allowing these longer periods to be missed. Therefore the 53 stars probably do not all possess periods below 20000 s, but since all are below about 22600 s ($\sim$ 0.2616 d), they still constitute a useful sample of notably short-period eclipsing binary candidates.

Table 7.1 also gives the period change results. Object J173828 only had enough minima data for a single O−C series, so was excluded. Object J093012 appeared to show significant period increase, but its folded light curve and O−C diagram suggested an anomaly in the data, and a check of the sky within 1″ of the object revealed a nearby bright star which appears to have contaminated the light curve; this object was also therefore excluded at this stage[1]. Of the remaining 51 objects, 17 showed period change inconsistent with zero, at 1 σ confidence, with six cases of apparent period increase and eleven of decrease. However, given the number of objects studied, we might expect approximately this number of marginally-significant results purely by chance, and so we do not claim that all these 17 results indicate genuine period changes (although this is a possibility).

More notable is that three objects show a period change significant at more

[1]See Ch. 11 for our subsequent fuller investigation of this object.

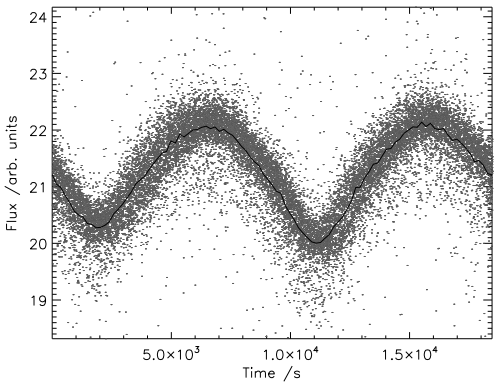

Figure 7.5: Light curve for object J234401, folded at period of 18461.591 s.

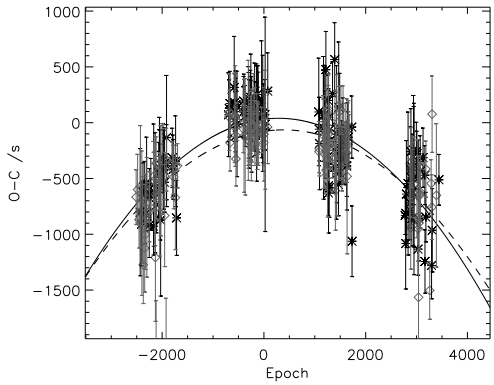

Figure 7.6: O−C diagram for object J234401, with best fit quadratic curves overplotted. Period decrease significant at 16 σ is indicated.

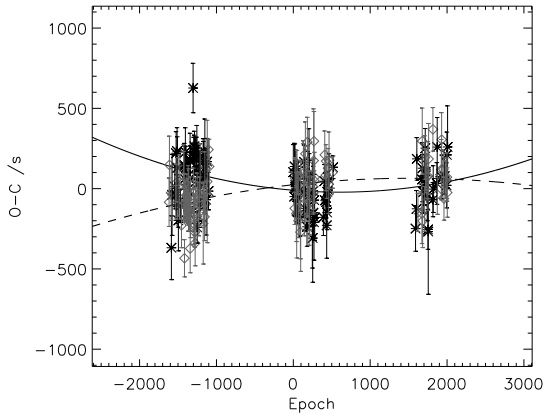

Figure 7.7: O−C diagram for object J050904, with best fit quadratic curves overplotted. No significant period change is indicated.

than 3 σ, where we would expect no significant results by chance alone in a set of 51 objects. These three stars underwent significant decreases in period during the time they were observed by SuperWASP: objects J174310 (-0.055 ± 0.003 s yr^{-1}, significant at 21 σ), J133105 (-0.075 ± 0.013 s yr^{-1}, significant at 5 σ) and J234401 (-0.31 ± 0.02 s yr^{-1}, significant at 16 σ). Figs. 7.1–7.6 show the folded light curves and O−C diagrams for these three objects, while Fig. 7.7 illustrates a non-significant result (object J050904) for comparison. Given the method of period determination, the choice of a precise zero point for the ephemerides of these three objects is somewhat arbitrary. However, using the zero points

assigned by the program, and the optimum periods for the whole observation set, we have approximate eclipse times:

J174310 HJD $2454997.688926 + 0.258108E - 4.5 \times 10^{-10}E^2$

J133105 HJD $2454976.358606 + 0.218014E - 5.2 \times 10^{-10}E^2$

J234401 HJD $2454417.284057 + 0.213676E - 2.1 \times 10^{-9}E^2$.

7.3 Discussion

We may note that period changes have been observed in many eclipsing binaries (Kim *et al.* 2003 claim that about 46% of the 1140 binaries in Kreiner *et al.*'s (2001) collection of O−C diagrams show at least some evidence of period change). Moreover, in short-period W UMa-type systems, period increases and decreases have been found to be of similar frequency, with the majority having $|\dot{P}| \leq 0.02$ s yr^{-1} and none exceeding about ± 0.4 s yr^{-1} (Kubiak *et al.* 2006), which would make our three main examples of period change notably rapid, but not exceptionally so. Therefore, we do not suggest that our evidence for period change is in itself especially surprising, nor would we argue for period decreases being generally dominant in this stellar population, on the basis of such a small sample. Rather, the particular interest of (relatively rapid) period decrease in the three objects J174310, J133105 and J234401 is that they are already near or below the short-period limit for W UMa objects of 0.22 d, and have timescales $P/\dot{P}$ between 4×10^5 and 6×10^4 years. The underlying processes which may be operating in these objects therefore merit further consideration.

To investigate possible causes of the period decreases apparently observed for these three objects, the eclipsing binary modelling software PHOEBE (see Ch. 6) was used to estimate component masses, radii and other system parameters. In the absence of radial velocity measurements, values for semimajor axis a could

not be determined, so best-fit parameter combinations were found for a range of physically-plausible values of a.

Several external constraints were applied: from general light curve morphology, such as continuous light variation, the systems were taken to be W UMa-type contact binaries (overcontact in PHOEBE's terms) i.e. with filling factors in (0,1]. The values for M_1 were required to be approximately consistent with system temperatures as indicated by spectral types, themselves estimated from $V-J$ and $V-K$ colours using 2MASS data (J174310 was taken to be approximately type K2, with temperature $\sim$ 4600 K; J133105 type G9, $T_{\rm eff} \sim$ 5000 K; J234401 type K9, $T_{\rm eff} \sim$ 3700 K). Mass ratios q were taken to be in the range 0.08–0.8, as typical for W UMa systems (Hilditch, 2001), subject to the hydrogen-burning requirement for M_2 to be at least $0.08 M_\odot$. Maximum and minimum values of a could then be derived from the possible radii of the (contact) component stars.

The resulting best-fit masses and radii (found to 2 s.f. by minimizing χ^2 values) are given in Table 7.2. Object J133105 could not be as well-fitted as the other two objects, by any combination of a, q, inclination i and Kopal potential Ω, because its maxima differ significantly in height, probably due to spots on the stellar surfaces. However, spots were not modelled here, in the absence of direct evidence.

Period decrease might be caused by magnetic braking, removing angular momentum from the system. The plausibility of this was assessed using Guinan and Bradstreet's equation (1988)[2]:

$$\dot{P} \approx -1.1 \times 10^{-8} q^{-1} (1+q)^2 (M_1+M_2)^{-\frac{5}{3}} k^2 (M_1 R_1^4 + M_2 R_2^4) P^{-\frac{7}{3}} \qquad (7.1)$$

Although this applies properly only to detached systems, Bradstreet and Guinan

[2]Lohr *et al.* (2012) quoted the equation given in Bradstreet and Guinan (1994), which contained a misprint; however, the calculations were carried out using the correct version of the equation.

suggest that magnetic field strengths would be weaker in contact binaries. So we may at least use their formula to estimate an upper limit for the effect of magnetic braking on a contact system. Therefore, taking the gyration constant k^2 as 0.1 (typical for main sequence stars, Bradstreet and Guinan 1994), the value of the RHS was evaluated for the various system parameter combinations and compared with $\mathrm{d}P/\mathrm{d}t$ for the three stars. The results, given in Table 7.2, are between about 20% and 1% of the observed quantities.

Other estimates of the effect of magnetic braking were made from equations for $\dot{J}$ from Rappaport *et al.* (1983) and Hurley *et al.* (2002), as calibrated by Davis *et al.* (2008) by using the angular momentum loss rate at the upper edge of the cataclysmic variable period gap (the binary systems were approximated as single, fully-convective stars in order to use these equations). This produced significantly smaller estimates of expected period change: between 3 and 4 orders of magnitude too small. This suggests that magnetic braking is not the main cause of period decrease in any of the three systems, though the difference of 1 to 2 orders of magnitude in the estimates produced by the different equations also implies significant limitations in our ability to quantify magnetic braking.

Another possibility is angular momentum loss due to gravitational wave radiation (GWR). Combining expressions from Kolb (2010) and Hilditch (2001):

$$\frac{\dot{P}}{P} = 3\frac{\dot{J}}{J} = -1.27 \times 10^{-8}\mathrm{yr}^{-1} \frac{M_1 M_2}{(M_1 + M_2)^{\frac{1}{3}} M_\odot^{\frac{5}{3}}} \left(\frac{P_{\mathrm{orb}}}{\mathrm{h}}\right)^{-\frac{8}{3}} \tag{7.2}$$

the expected $\dot{P}/P$ was calculated for each parameter combination (Table 7.2). However, these quantities are about 6 orders of magnitude smaller than the observed $\dot{P}/P$ values. GWR can be responsible for only a tiny fraction of the period decreases observed here.

This leaves mass transfer from M_1 to M_2 and/or mass (and hence angular momentum) loss from the system, from other mechanisms, as plausible causes.

Using equations as given by Hilditch:

$$\frac{\dot{P}}{P} = \frac{3\dot{M}_1(M_1 - M_2)}{M_1 M_2} \tag{7.3}$$

$$\frac{\dot{P}}{P} = 3\dot{M}_1 \left[\frac{(M_1 + M_2)}{M_1 M_2} \frac{d^2}{a^2} - \frac{M_2}{M_1(M_1 + M_2)} \right] \tag{7.4}$$

(where d is the distance from the binary centre of mass to Lagrange point L_2) for conservative and non-conservative mass loss respectively, we can calculate the necessary values of $\dot{M}_1$ to explain the observed $\dot{P}/P$ values (Table 7.2). These are of the order of 10^{-6}-$10^{-7} M_\odot$ yr^{-1}, which we may note is similar to the mass loss rate calculated by Hilditch for contact binary SV Cen, to explain its precipitous observed rate of period decrease. He argues that mass may be ejected during a rapid phase of Roche-lobe overflow (or more generally, in a contact system) through L_2, contributing to period decrease. Possible mechanisms for unstable mass transfer/loss leading to rapid period decrease in contact or near-contact binaries are also discussed in Rasio (1995), Tylenda *et al.* (2011) and Jiang *et al.* (2012). This explanation is left as the most plausible for the observed period decreases in the objects J174310, J133105 and J234401, with further small contributions from magnetic braking and GWR[3].

What future, then, might we envisage for these three systems? Since their primary masses and mass ratios cannot currently be determined with any precision, it is possible that they are subject to Jiang *et al.*'s low mass limit (2012), leading to unstable mass transfer, or to Rasio's tidal instabilities (1995), and will undergo merger on a relatively short timescale. Rasio proposes the orbital decay time $t_{\rm D} \sim 10^3$–10^4 years for an unstable W UMa system. Another indication of the possible timescale for merger is given by Tylenda *et al.*'s study (2011) of the decaying period of the contact binary progenitor of the V1309 Sco outburst. Us-

[3]Another explanation for the period change in J234401 is considered in Ch. 10, and for period changes detected in SuperWASP eclipsing binaries more generally in Ch. 13.

ing their exponential model for period decay, one can determine that their object would have been decreasing in period at a rate of 0.3 s yr^{-1} about 130 years before the observed outburst (and presumed merger). Since object J234401 appears to be currently undergoing period decrease at approximately this rate, and is already below the short-period limit, it is perhaps not inconceivable that it might merge on a timescale of centuries or even decades from now (assuming, of course, that its period decrease is maintained). Whatever their ultimate fate, these may be rare examples of objects caught in a brief transitional stage between stable states.

7.4 Conclusions

Our study of the periods of 53 W UMa candidate eclipsing binary stars, observed with SuperWASP, confirmed that they are all very close to the short-period limit, and thus constitute a useful sample of sources for investigating the causes of this limit. In three of the objects, period decrease significant at 5 σ or more was found during their time of observation; the remaining objects' period changes were consistent with zero change at 3 σ. Modelling estimates for possible system parameters indicated that neither magnetic braking nor GWR are likely to be the primary cause of these period decreases. The rates of change observed in these three objects can best be explained by unstable mass transfer from primary to secondary components, and/or mass and angular momentum loss from the systems, which could lead to merger on a relatively short timescale if the periods continue to decrease.

These are potentially unusual transitional objects, capable of shedding light on the evolution of close binaries and the causes of the short-period limit of main sequence binaries. As such they would repay further study and additional observations.

Table 7.1: Period results for 53 SuperWASP eclipsing binaries. Period changes included only where significance is at least 1σ.

SuperWASP ID (Jhhmmss.ss±ddmmss.s)	Orig. No.[0]	Short Name	P (s)	δP (s)	$\dot{P}$ (s yr^{-1})	$\delta\dot{P}$ (s yr^{-1})	$\frac{\dot{P}}{P}$ (yr^{-1})	Sig. (σ)
J000437.82+033301.2	3	J000437	22593.528[4]	0.009	+0.095	0.087	$+4.2 \times 10^{-6}$	1
J003033.05+574347.6	27	J003033	19580.280	0.004				
J004050.63+071613.9	15	J004050	19809.204	0.004				
J022050.85+332047.6[5]	53	J022050	16643.642	0.009				
J022727.03+115641.7	47	J022727	18226.361	0.009				
J030749.87−365201.7	26	J030749	19584.395	0.009				
J034439.97+030425.5	11	J034439	19861.395	0.009				
J040615.79−425002.3	34	J040615	19209.980	0.009	−0.029	0.026	-1.5×10^{-6}	1
J041120.40−230232.3	43	J041120	18690.406	0.009				
J041655.13−492709.8	5	J041655	19959.767	0.009				
J044132.96+440613.7	19	J044132	19712.787	0.006				
J050904.45−074144.4	13	J050904	19835.305	0.009				
J051501.18−021948.7	6	J051501	19950.121	0.009				
J052036.84+030402.1	1	J052036	19993.301	0.009	−0.037	0.025	-1.8×10^{-6}	1
J055418.43+442549.8	39	J055418	18878.004	0.003				
J064501.21+342154.9	37	J064501	21480.415[1]	0.009				
J074658.62+224448.5	38	J074658	19081.403	0.005				
J080150.03+471433.8	42	J080150	18793.167	0.007				
J092328.76+435044.8	50	J092328	20292.982[1]	0.004	+1.90	0.95	$+9.37 \times 10^{-5}$	2
J092756.25−391119.2	30	J092756	19469.696	0.009	−0.10	0.05	-5.1×10^{-6}	1

[0] In Norton *et al.* (2011).
[4] Period found here is longer than in Norton *et al.* (2011).
[5] GSC 2314−0530 = BX Tri.

Table 7.1: (continued)

SuperWASP ID (Jhhmmss.ss±ddmmss.s)	Orig. No.[0]	Short Name	P (s)	δP (s)	$\dot{P}$ (s yr^{-1})	$\delta\dot{P}$ (s yr^{-1})	$\frac{\dot{P}}{P}$ (yr^{-1})	Sig. (σ)
J093012.84+533859.6	22	J093012	19674.550	0.001	(+1.40)	(0.13)	$(+7.11 \times 10^{-5})$	(10)[6]
J111931.48−395048.2[7]	14	J111931	19827.651	0.007	+0.033	0.014	$+1.7 \times 10^{-6}$	2
J114929.22−423049.0	23	J114929	19639.554	0.009				
J115557.80+072010.8	25	J115557	19614.222	0.009				
J115605.88−091300.5	48	J115605	18222.626	0.005				
J120110.98−220210.8	24	J120110	19627.832	0.009	−0.21	0.09	-1.1×10^{-5}	2
J121906.35−240056.9	29	J121906	19558.186	0.009				
J130920.49−340919.9	33	J130920	19253.528	0.009				
J133105.91+121538.0	41	J133105	18836.380	0.004	−0.075	0.013	-4.0×10^{-6}	5
J142312.63−222425.1	51	J142312	18112.792	0.009				
J150822.80−054236.9	10	J150822	22469.214[1]	0.007	−0.026	0.016	-1.2×10^{-6}	1
J151652.90+004835.8	49	J151652	18207.370	0.009				
J155822.10−025604.8	9	J155822	22470.705[1]	0.009	−0.19	0.13	-8.3×10^{-6}	1
J160156.04+202821.6	28	J160156	19572.134	0.009	+0.12	0.05	$+6.0 \times 10^{-6}$	2
J161334.28−284706.7	12	J161334	19852.817	0.004	−0.063	0.055	-3.2×10^{-6}	1
J170240.07+151123.5[8]	4	J170240	22589.758[1]	0.004				
J173003.21+344509.4	32	J173003	19328.922	0.009				
J173828.46+111150.2	35	J173828	21546.731[1]	0.009	[9]			
J174310.98+432709.6[10]	17	J174310	22300.517[1]	0.009	−0.0546	0.0025	-2.45×10^{-6}	21

[6]Data contaminated by nearby star's light curve.
[7]ASAS J111932−3950.8.
[8]ROTSEI J170240.11+151122.7.
[9]Insufficient data to calculate both O−C series.
[10]V1067 Her.

Table 7.1: (continued)

SuperWASP ID (Jhhmmss.ss±ddmmss.s)	Orig. No.[0]	Short Name	P (s)	δP (s)	$\dot{P}$ (s yr^{-1})	$\delta\dot{P}$ (s yr^{-1})	$\frac{\dot{P}}{P}$ (yr^{-1})	Sig. (σ)
J180947.64+490255.0[11]	20	J180947	19688.490	0.009	+0.028	0.010	$+1.4 \times 10^{-6}$	2
J183738.17+402427.2	36	J183738	19121.227	0.009				
J195900.31−252723.1	46	J195900	20575.395[1]	0.009				
J210318.76+021002.2	16	J210318	19750.199	0.009				
J210423.76+073140.4	52	J210423	18065.091	0.009				
J212454.61+203030.8	21	J212454	19684.790	0.009	−0.41	0.29	-2.1×10^{-5}	1
J212808.86+151622.0	31	J212808	19426.310	0.009				
J214510.25−494401.1	18	J214510	19712.951	0.009				
J220734.47+265528.6	2	J220734	19978.751	0.009				
J221058.82+251123.4	45	J221058	18402.957	0.009				
J224747.20−351849.3	40	J224747	18853.775	0.009	+0.77	0.64	$+4.1 \times 10^{-5}$	1
J232607.07−294130.7	8	J232607	19882.132	0.004				
J234401.81−212229.1	44	J234401	18461.591	0.007	−0.313	0.019	-1.70×10^{-5}	16
J235333.60+455245.8	7	J235333	19936.123	0.009				

[11] V1104 Her.

Table 7.2: Model parameters and theoretical period/mass changes for three objects.

Star Short Name	a ($R_\odot$)	q (M_2/M_1)	M_1 ($M_\odot$)	M_2 ($M_\odot$)	R_1 ($R_\odot$)	R_2 ($R_\odot$)	Magnetic Braking $\frac{\dot{P}}{P}$ (yr^{-1})	GWR $\frac{\dot{P}}{P}$ (yr^{-1})	Non-conservative $\dot{M}_1$ ($M_\odot$ yr^{-1})	Conservative mass transfer $\dot{M}_1$ ($M_\odot$ yr^{-1})
J174310	1.5	0.32	0.52	0.17	0.74	0.45	-1.7×10^{-7}	-2.9×10^{-11}	-5.1×10^{-7}	-2.0×10^{-7}
	1.6	0.24	0.67	0.16	0.88	0.49	-3.5×10^{-7}	-3.4×10^{-11}	-5.9×10^{-7}	-1.7×10^{-7}
	1.7	0.23	0.81	0.18	0.94	0.52	-4.4×10^{-7}	-4.4×10^{-11}	-7.0×10^{-7}	-1.9×10^{-7}
	1.8	0.31	0.90	0.28	0.91	0.55	-2.7×10^{-7}	-7.0×10^{-11}	-8.8×10^{-7}	-3.3×10^{-7}
J133105	1.4	0.12	0.69	0.09	0.79	0.31	-7.5×10^{-7}	-3.0×10^{-11}	-8.0×10^{-7}	-1.3×10^{-7}
	1.5	0.20	0.80	0.16	0.79	0.38	-4.3×10^{-7}	-5.9×10^{-11}	-1.1×10^{-6}	-2.6×10^{-7}
	1.6	0.41	0.82	0.34	0.74	0.49	-1.7×10^{-7}	-1.2×10^{-10}	-1.5×10^{-6}	-7.6×10^{-7}
	1.7	0.65	0.84	0.55	0.71	0.58	-1.2×10^{-7}	-1.9×10^{-10}	-1.9×10^{-6}	-2.1×10^{-6}
J234401	1.3	0.14	0.57	0.08	0.72	0.30	-5.3×10^{-7}	-2.6×10^{-11}	-2.9×10^{-6}	-5.4×10^{-7}
	1.4	0.45	0.56	0.25	0.63	0.44	-1.3×10^{-7}	-7.3×10^{-11}	-4.5×10^{-6}	-2.6×10^{-6}

Chapter 8

EBs near the short-period limit

Following the demonstration of period change detectability in SuperWASP eclipsing binaries, the code used was improved, and it was felt desirable to search the archive again with its help, to seek to increase the sample of objects in this period range. It seemed plausible that any binaries approaching imminent stellar merger would be found near the short-period limit of the distribution; moreover, a larger sample would allow us to make more convincing claims about the limit itself. In fact, a number of inherently intriguing objects were discovered in the course of this search, which will be discussed further in later chapters. This chapter is closely based on Lohr *et al.* (2013b).

8.1 Introduction

Here we have used the SuperWASP archive of ∼30 million objects to search for and analyse main sequence eclipsing binaries with very short orbital periods (<20 000 s or ∼0.2315 d). This should yield an interesting sample around the observed short-period limit for such binary systems of ∼0.2 d, potentially illuminating the causes of this cut-off point in the period distribution. (We should note, however, that systems in this period range must be expected to be relatively low

in mass and hence intrinsically faint, such that SuperWASP will not detect them with the same efficiency as longer-period eclipsing binaries.) In earlier work, Norton *et al.* (2011) presented 53 candidate eclipsing systems in this period range, using SuperWASP archived data; here, with a more thorough search, we have sought to detect further such objects which might have been missed. Also, Lohr *et al.* (2012) presented the results of a search for period changes in these 53 objects, finding three which exhibited statistically significant period decrease; here again, we have used an improved period change detection method to search for period changes in the eclipsing systems found with periods below 20 000 s. This work, then, is primarily intended to update Norton *et al.* (2011) and Lohr *et al.* (2012).

8.2 Method

An initial list of 36 758 SuperWASP identifiers was obtained from the catalogue, with associated possible periods in the range 8000–10 000 s. This range would correspond to potential binary orbital periods below 20 000 s, since there are two eclipses per cycle. (The catalogue periods are the result of a uniform period search applied to the majority of data as part of the initial processing pipeline; the code used is described in Norton *et al.* (2007) and is run separately for data from different seasons and cameras. As a consequence, several different periods can be listed in the catalogue for a single object.) A frequency plot of the periods revealed substantial excesses of objects in the ranges 8610–8625 s and 9565–9586 s i.e. in the neighbourhood of 1/10 and 1/9 of a sidereal day respectively. Since the vast majority of these harmonic periodicities are expected to be spurious, objects in these ranges were excluded from further consideration. It can be estimated that only about three genuine eclipsing binaries with periods below 20 000 s are likely to have been missed as a consequence. Repeated identifiers

(occurring when a single identifier had multiple possible periodicities listed in the catalogue, in the ranges of interest) were also removed at this stage.

This left 5743 distinct identifiers, of which around 5190 probably represented distinct astrophysical sources: since SuperWASP uses the USNO-B1 input catalogue to label objects, it is possible for a single bright source in a field of view containing many faint sources to be catalogued under multiple identifiers. Such "duplicates" can usually be easily recognised by their near-identical periods and coordinates; however, they were not excluded at this stage so that the brightest or clearest lightcurve for each source could be preferentially selected for more detailed analysis later. Lightcurves with fluxes corrected by the Sys-Rem algorithm were obtained from the archive for these objects.

The updated IDL code *ah2* described in Ch. 4 was then used to try to find the optimum period of each object, and to attempt an automatic classification of it as a candidate eclipsing binary, a different kind of periodic variable, or non-periodic / with a period outside the range of interest (4434 objects were classed as periodic variables of some kind at this stage).

Since this method would not always separate pulsators and eclipsing binaries reliably (e.g. in cases where eclipsing systems show primary and secondary eclipses of equal depth), a final visual check was made of the folded lightcurves of the more distinctive objects with detected periods below 20 000 s. This included all those where the amplitude of the mean lightcurve exceeded the amplitude of data scatter about the mean lightcurve, facilitating a clear identification of variable type. It also included some where the amplitude of variation was between 50% and 100% of the scatter, but where the objects might be expected to have distinctive lightcurves on other grounds e.g. very bright objects, objects with high numbers of observations, or objects whose detected periods had very low uncertainty.

Approximately 1000 identifiers were checked, and 201 were selected as proba-

ble eclipsing binaries of W UMa type, corresponding to 143 distinct astrophysical objects. Fainter duplicates were rejected at this stage. The selected objects had nearly all been automatically classified as eclipsing binaries, and many showed a clear difference in depths of primary and secondary eclipses; some had different heights of maxima, presumably due to the O'Connell effect; others were chosen for their relatively broad, symmetric maxima and narrow eclipses. Purely sinusoidal lightcurves were excluded; although some of them were probably generated by genuine eclipsing binaries, our photometric data was insufficient to distinguish them from other periodic variable types with reasonable probability. Radial velocities would need to be determined for these ambiguous objects to establish their variability type.

8.3 Results

During the checking process described above, periodic variables of several different types were observed. A large number of pulsators (probably δ Scuti and RR Lyrae variables in this short-period range; see Ch. 2) were evident, characterized by narrow maxima and broad minima, and/or asymmetric lightcurve shapes. As well as eclipsing binaries in the period range of interest, many eclipsing binaries were seen with periods between 32 000 and 40 000 s, whose quarter-periods had evidently been picked up by the period detection code used in the SuperWASP catalogue. Also, the subdwarf B (sdB) eclipsing binaries NY Vir, HS 2231+2441 and NSVS 14256825, which have orbital periods in the range 8000–10 000 s, were detected and phase-folded appropriately in spite of their strongly non-sinusoidal lightcurves[1]. These detections suggest that the period determination method used here, despite using sinusoidal fitting during the initial stage, is effective with periodic variables exhibiting a wide variety of lightcurve

[1]These objects, along with other SuperWASP post-common-envelope eclipsing binaries in different period ranges, are the subject of Ch. 12.

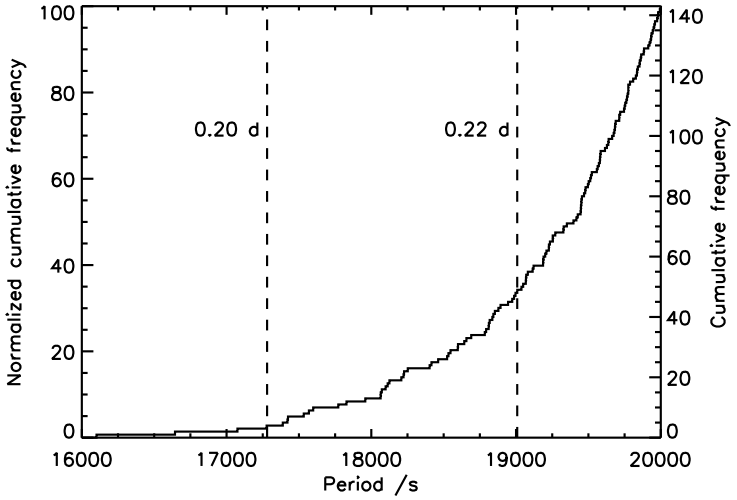

Figure 8.1: Cumulative period distribution of 143 candidate eclipsing binaries. Typical values for the short-period limit are shown.

shapes.

8.3.1 Periods

Period and magnitude statistics for the 143 candidate (main sequence) eclipsing binaries found with periods under 20 000 s are presented in Table 8.1. They include 44 of the 53 short-period candidate eclipsing binaries presented in Norton *et al.* (2011). (The other nine, as discussed in Ch. 7, have periods slightly longer than 20 000 s.) Three of the 99 additional objects presented here are known periodic variables: CC Com, listed as a W UMa-type eclipsing binary in the GCVS, with the same period as found here; LL Eri, listed as a rotating ellipsoidal binary in the GCVS, again with the period found here; and ROTSE1 J164349.58+325637.8, listed in Akerlof *et al.* (2000) as a δ Scuti variable with period half that found here. Since the SuperWASP lightcurve for the latter object is particularly well-observed, and its folded lightcurve exhibits clear (though small) differences in the depths of primary and secondary minima, we suggest that the object is more likely to be an eclipsing binary. Therefore, 97 of the objects presented here are new candidate eclipsing binaries near the short-

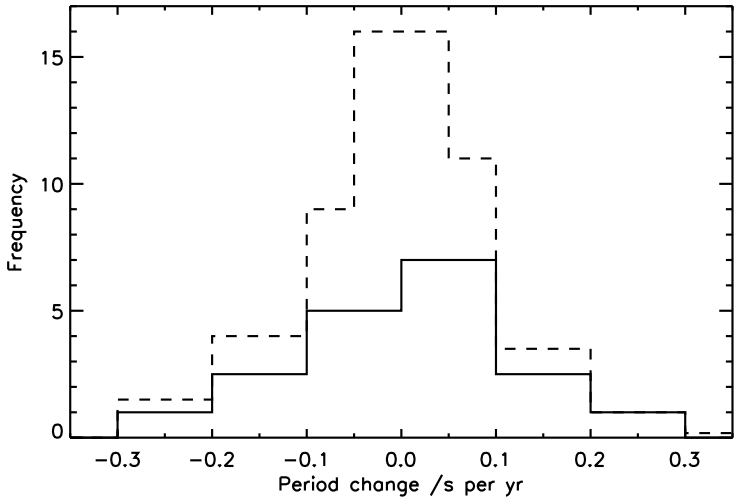

Figure 8.2: Period change distribution of 74 candidate eclipsing binaries showing significant change. Period changes found with at least 3σ confidence are indicated with solid lines (38 objects); dashed lines indicate changes found at a 1σ level or more.

period limit. Fig. 8.1 gives their cumulative period distribution, and Appendix A shows their individual folded lightcurves.

8.3.2 Period changes

12 objects were excluded from the period change search, since only a single year of data was available for them. Of the remaining 131, 74 showed evidence of significant secular change i.e. the uncertainty ranges on their $\dot{P}$ values did not include zero. (Note that highly significant period change may be small in magnitude: J121206 shows a change of just 0.0265 s yr^{-1}, but its remarkably bright and well-defined lightcurve makes this value significant at 23σ.) The remainder have not necessarily been demonstrated to have unchanging periods: although the O−C diagrams of some were indeed better fitted by a linear function than a quadratic one, others exhibited apparent secular change at a non-significant level, and may be regarded as having indeterminate status. Period changes and significance levels are listed for these 74 objects in Table 8.1, and the distribu-

tion of significant changes is plotted in Fig. 8.2. Appendix A shows the O−C diagrams of all objects.

Since a few of the changes significant at 1 or 2σ might be expected to be spurious, resulting by chance alone in a data set of this size, the distribution of changes significant at $\geq 3\sigma$ is also shown in Fig. 8.2 (38 objects); we would not expect to find even one instance of period change this significant out of 131 objects by chance. Two of the objects found to exhibit highly significant period change in Ch. 7 are in this set (J133105 and J234401); the third (1SWASP J174310.98+432709.6) has a period slightly greater than 20 000 s and so was not included in the present study. The reproduction of our earlier findings supports the validity of the modified period change detection approach, and the increased number of highly-significant period changes detected implies an improvement in sensitivity.

8.4 Discussion

8.4.1 Periods

It may be seen that the period distribution found here (Fig. 8.1) straddles two frequently-quoted values for the period cut-off (0.20 and 0.22 d), and follows a smooth tail-off towards shorter periods. It tallies well with similar distributions found from other wide-field time-domain surveys, covering wider period ranges, such as those in Szymański *et al.* (2001), Fig. 9, and Paczyński *et al.* (2006), Fig. 6, which show contact binary periods tailing off towards lower periods from a maximum around 0.38 d, with none observed below 0.20 d (see Ch. 3).

Only one object (J201816) is included here with a period shorter than that of BX Tri (=GSC 02314-0530, here J022050), generally regarded as the main-sequence eclipsing binary with the shortest-known period (see Ch. 6). However, since this object is very poorly-observed by SuperWASP, with only a couple of

thousand data points mostly from a single year, we are reluctant to make too strong a claim for it. Although it apparently exhibits substantial differences in the heights of its maxima, as well as small differences in primary and secondary minima depths, it is possible that these are artefacts of the limited observations, and that the object is really a pulsating variable.

Thus our search supports the existence of a short-period limit at around 0.20 d, and perhaps favours particular types of explanation for it. As introduced in Ch. 3, Stepień (2006) argued that the current age of the Universe indirectly explained the limit, on the grounds that lower-mass detached binaries lose angular momentum more slowly than high-mass systems, and so take longer to evolve into (stable) contact configurations; 0.20 d would then simply be the current minimum period that a system would have had time to reach. Such a model might imply a much sharper, more cliff-like cut-off point for the binary period distribution than seen here (and indeed, a cut-off period which would become shorter as the Universe aged). Also, Jiang *et al.* (2012) have indicated a number of known short-period binaries with measured masses lower than Stepień's formula should allow, and Nefs *et al.* (2012) have claimed the discovery of four M-dwarf eclipsing binaries with periods below 0.18 d (one as short as 0.11 d), which would certainly conflict with Stepień's model.

However, other models suggest that objects are leaving the short-period end of the distribution through rapid merger, in addition to entering it from above through evolution from detached into contact configurations. Jiang *et al.* (2012) argued that binary systems with particular combinations of low primary mass and low mass ratio would evolve into unstable states and merge rapidly; 0.20 d would then be the shortest period corresponding to a possible stable configuration. Stepień and Gazeas (2012) also proposed a new series of binary models including evolution towards coalescence within the contact stage; the lowest period obtained for any of these models, at the time of coalescence, is 0.201 d. Such

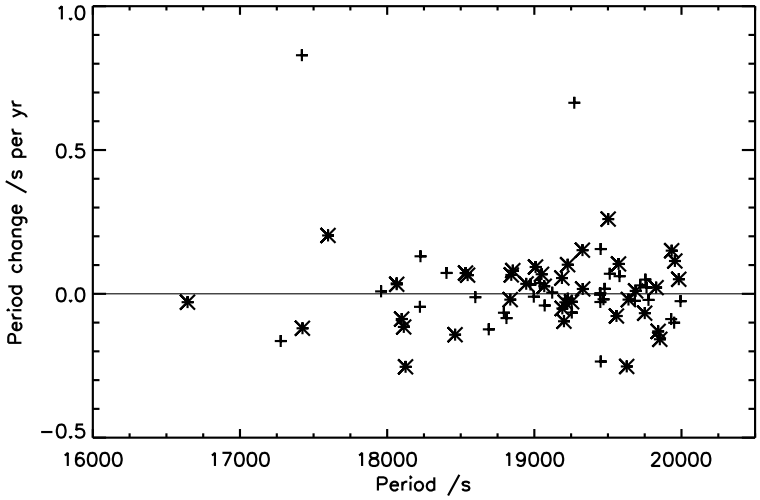

Figure 8.3: Plot of significant period changes against periods, for 74 objects significant at $\geq 1\sigma$ (small crosses) and 38 objects significant at $\geq 3\sigma$ (larger diagonal crosses).

explanations might fit better with the observed distribution of binary periods, with some objects reaching unstable states and heading rapidly towards merger at periods somewhat above 0.20 d, and others able to remain stable even at the cut-off point.

8.4.2 Period changes

The distribution of significant period changes observed here (Fig. 8.2) also tallies broadly with one found by Kubiak *et al.* (2006), Fig. 5, for 134 OGLE contact binaries with periods below 1 d. It is symmetrical around zero (a Kolmogorov-Smirnov test supports symmetry at $P = 0.91$ for the 74 objects with period change significant at $\geq 1\sigma$ and at $P = 0.69$ for the 38 objects significant at $\geq 3\sigma$), and approximately normal, with a half-width at half-maximum around 0.1 s yr^{-1}, where Kubiak *et al.* found a rather lower value around 0.03 s yr^{-1}. The extremely short-period objects considered here, then, appear equally likely to show increases and decreases in period[2]. Figure 8.3 plots significant period changes against

[2]Ch. 13 suggests an explanation for this unexpected finding.

periods. No particular relation between either direction or magnitude of period change and period length seems apparent.

It might be argued that the period change distribution found here has an effective hole at zero, and a deficiency near zero, since we do not include objects where no significant change was detected. As indicated in Subsect. 8.3.2, these objects are not of a single type, and cannot be confidently claimed to have unchanging periods. To include all or some of them in our distribution would distort it and make it hard to compare with other results obtained using different methods. Kubiak *et al.*'s distribution of objects (with $\mathcal{P}$-statistic > 63.3, described as "statistically confirmed" period changes) also has a gap near zero, for similar reasons to ours: it is more difficult to detect and quantify small period changes since their uncertainties must also be small.

Another potential confounding factor would be the presence of wandering spots on the surface of a star. These could in theory change the lightcurve shape in such a way as to move the detected times of minima and so create a spurious curvature in the O-C diagram, leading us to conclude erroneously that the object's orbital period is changing. In practice, visual checks of individual nights suggest the lightcurves do not vary substantially in shape for the objects showing the most significant period change, though it is possible that spot movement is contributing to data scatter in some of the fainter and less well-observed lightcurves.

Some of the O−C diagrams suggest a periodic, sinusoidal variation in period, in addition to or instead of a secular trend (e.g. J142312, J172717, J210423). Such cyclical variations are often interpreted as indicating the presence of a third body in the binary system (e.g. Lee *et al.* (2011)), through the light-time effect. However, the Applegate mechanism (Applegate, 1992), involving the magnetic activity cycle of a star in a close binary system, may sometimes provide a more plausible explanation (Hilditch, 2001; Christopoulou *et al.*, 2012); this mechanism

explains orbital period changes as gravitational quadrupole responses to a cyclic redistribution of angular momentum within the layers of an active, convective star, associated with varying levels of differential rotation at different times in the star's magnetic cycle. In such a case, longer-term luminosity variations would be expected to show the same period as the orbital period modulation, since they arise from a common cause, and any other variability associated with magnetic activity e.g. coronal X-ray luminosity, should also show this period[3].

8.4.3 J234401 and J093010

One candidate eclipsing binary which showed particularly marked sinusoidal period changes was J234401, which initially had appeared to show rapid period decrease (Ch. 7) on the basis of a shorter SuperWASP coverage. This object will be discussed fully in Ch. 10. Another object which stood out was J093010: its apparently significant period change detected in Ch. 7 had been initially dismissed as the result of contamination by the light of a nearby star, but was discovered to have a much more interesting cause in Lohr *et al.* (2013b); this and the subsequent follow-up observations of the system will be covered together in Ch. 11.

8.4.4 J102328

Another object of note was J102328 (Figs. 8.4 and 8.5), which shows period decrease nearly as rapid as that apparently seen in J234401 on the basis of its first four years of data: -0.254 ± 0.037 s yr^{-1}, significant at 6σ. If this decrease continued it would imply a merger timescale ($P/\dot{P}$) of at most 71 500 years; however, only three years of SuperWASP observations are available for this object, so caution is warranted: future years of data might support a sinusoidal period variation instead. We may also note that this magnitude of period decrease falls

[3]This issue will be addressed more fully in Ch. 13.

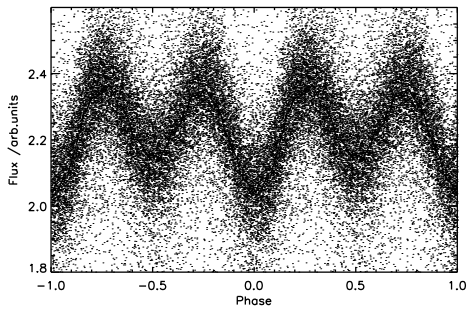

Figure 8.4: Lightcurve of object J102328 folded at period 18 125.146 s.

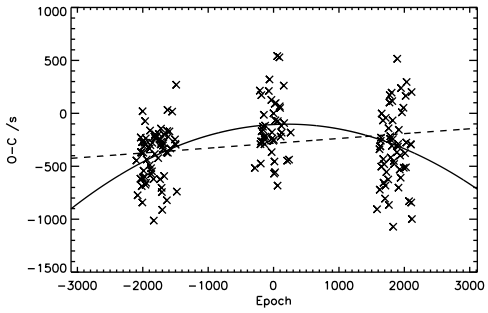

Figure 8.5: O−C diagram for object J102328 (uncertainties not plotted for clarity). Dashed line shows best linear fit (reduced $\chi^2 = 1.74$, 171 degrees of freedom); solid line shows best quadratic fit ($\chi^2 = 1.46$, 170 d.f.), corresponding to a secular period change of -0.254 ± 0.037 s yr^{-1}.

within the symmetrical distribution found for the 38 highly significant objects taken as a group.

8.4.5 Other systems of note

Several lightcurves in the appendix resemble β Lyrae-type variables (EB), showing notable differences in primary and secondary eclipse depths: J011732, J022050, J070953, J093443, J102328, J215826 and J222302 are perhaps the clearest examples. Surprisingly for such short-period objects, these may represent detached or semi-detached systems not in thermal contact. Indeed, J022050 (=BX Tri), which shows substantial differences in depths of minima, as well as a large O'Connell effect, has been studied in detail by Dimitrov and Kjurkchieva (2010), who modelled it as not quite in contact, but with one star nearly filling its Roche lobe. Other objects showing pronounced O'Connell effects (maxima of different heights) are J033242, J084408, J115326, J201816 (if a genuine eclipsing binary), and J221117, of which the last is particularly striking and unusual in shape. Finally, we observe significant variations in average flux in several objects, including

J121206 (which shows distinct well-defined curves at different levels), J134430, J150957, J151146, J152022, J172717 and J173003 (which show broader banding or continuous variation in average flux level). In some cases this variation seems intrinsic to the system, being observable within a single night's observations with a single camera; in other cases it probably has instrumental causes e.g. the object was observed over a long time-base by cameras in both the northern and southern hemispheres.

8.5 Conclusions

Our new search of the SuperWASP archive yielded 143 plausible candidate eclipsing binaries with orbital periods <20 000 s, of which 97 are new discoveries. This updates the findings of Norton *et al.* (2011), and provides a useful new sample of extremely short period eclipsing systems near the cut-off point. Their period distribution fits neatly at one end of previous period distributions found for eclipsing binaries seen by other comparable surveys. The shape of the distribution may also inform understanding of the reasons for the short-period limit for main sequence binaries.

An improved period change detection method was employed with the new sample, which measured observed times of minima by fitting each night of observations with the object's own binned mean lightcurve, obtained from its full data set during period determination. This approach confirmed some earlier results in Lohr *et al.* (2012), and found significant evidence for period change in 74 of the candidate binaries, of which 38 are significant at 3σ or more. The distribution of significant period changes found agrees substantially with a previous comparable distribution, showing equal numbers of systems increasing and decreasing in period. Of the highly significant period changes, none exceed 0.3 s yr^{-1} in magnitude, and the half-width at half-maximum of the distribution is $\sim$ 0.1 s yr^{-1},

slightly larger than that found in a previous study of binaries with longer periods.

Three of the systems found were of particular interest. J234401 and J093010 will be addressed more fully in later chapters. J102328 currently shows the most rapid period decrease of the whole sample: -0.254 ± 0.037 s yr^{-1}, significant at 6σ, which would indicate a merger timescale $\leq$70 000 years if the decrease continues.

8.6 Addenda

Since the publication of Norton *et al.* (2011); Lohr *et al.* (2012, 2013b), a number of the new SuperWASP short-period eclipsing binary candidates we identified and investigated have been followed up by other observers, who have claimed to confirm their binary nature via higher-precision multicolour light curves (though in no case, as far as we are aware, have they obtained the spectroscopic evidence necessary for an unquestionable confirmation or reliable parameter determination). Both Essam *et al.* (2013) and Liu *et al.* (2014) obtained BVRI photometry for J064501 in February 2013, described by each of them as the "first photometric study" of the system (they were apparently unaware of each other's work), and obtained very similar models for it as a contact binary exhibiting a total primary eclipse. Essam *et al.* (2014) also published a light curve-only solution for J160156, which will be discussed further in the Addendum to the next chapter. Another Egyptian group obtained BVRI light curves for J133105 (Elkhateeb *et al.*, 2014b) and J210318 (Elkhateeb *et al.*, 2014a), in each case modelling them as contact binaries. Terrell and Gross (2014) obtained BVI light curves for J080150 (=GSC 3408-0735) and modelled it quite convincingly as a contact binary exhibiting a total secondary eclipse. Most recently, Zhang *et al.* (2014) have published BV light curves for J055416 using SONG (see Ch. 1) and modelled it as a contact binary also. All of these models, except that of Terrell

and Gross, included one or more spots on the components' surfaces, and often a third light contribution as well; the added degrees of freedom in the models, unconstrained by spectroscopic evidence, should perhaps lead us to treat the parameters thereby derived with caution.

Terrell (2014) used the American Association of Variable Star Observers (AAVSO) Photometric All-Sky Survey data (Henden *et al.*, 2012) to try to check the plausibility of the 143 candidates presented here as being genuine W UMa systems rather than pulsating single stars. Using Johnson B-V colours for the 112 candidates having at least two nights of observations in the APASS database, he compared them with a period-colour relation for W UMa systems formulated by Rucinski (1998 version). He classified 25 as "ruled out as W UMa systems" on the grounds of being too blue, and 16 as "almost certainly W UMa systems", which lay on the red side of the theoretical curve; the remainder were seen as inconclusive. While the extremely blue colour of the very short-period J201816 supports our suspicion voiced above that it is likely to be a pulsating variable, many of the other "ruled out" systems lie much closer to the curve, which Rucinski inevitably calibrated mainly using W UMa systems with longer periods than these; the curve may thus not be so reliable a guide for contact binaries at the cut-off point. We may note, for instance, that Terrell ends up rejecting J133105, even though its bright, clear light curve exhibits clearly different primary and secondary eclipse depths (see Fig. 7.3, Appendix A and Elkhateeb *et al.* (2014b), which found a 0.25 B magnitude difference in depths), hard to explain using a pulsating model; moreover, the spectroscopically-confirmed contact binary J160156 (discussed in the next chapter) only appears in Terrell's "possible" list.

Finally, Drake *et al.* (2014) recently published a similar study to ours (though they were not initially aware of our work), identifying 367 binary candidates with periods below 0.22 d using Catalina Survey data (see Ch. 1), out of some 198 million distinct sources with V magnitudes between 12 and 20. They were able to

confirm some of these spectroscopically: some had periods as short as ∼12000 s, and all were too faint to have been detected by SuperWASP. A number of the shortest-period objects apparently contained white dwarf components, and thus they are not relevant to the period distribution for main sequence binaries.

Table 8.1: Period and period change determinations for 143 eclipsing binary candidates. Only period changes significant at 1 σ are shown.

SuperWASP ID (1SWASP Jhhmmss.ss±ddmmss.s)	Previous ID as variable star	Mean SW V mag	Prim. depth	Sec. depth	P (±0.0005 s)	$\dot{P}$ /s yr^{-1}	$\delta\dot{P}$ /s yr^{-1}	Signif. (σ)
J000205.32+381321.5		15.16	15.33	15.27	18064.547	0.036	0.026	1
J003033.05+574347.6	27[4]	15.13	15.63	15.57	19579.837			
J004050.63+071613.9	15	12.30	12.37	12.37	19809.222			
J004545.23−244516.2		15.37	15.52	15.52	19037.467	0.037	0.020	1
J010340.37−172138.8		14.80	14.99	14.96	19719.757	0.029	0.012	2
J010642.20−330857.9		13.95	14.14	14.09	19187.558	0.0549	0.0073	7
J011732.10+525204.9		13.98	14.09	14.02	19350.996			
J015100.23−100524.2		14.73	15.15	15.15	18532.806	0.072	0.021	3
J022050.85+332047.6	53; BX Tri	13.25	13.44	13.35	16643.640	−0.0290	0.0074	3
J022727.03+115641.7	47	15.08	15.23	15.22	18226.385	0.131	0.076	1
J023459.08−393704.6		15.69	16.27	16.24	19186.467			
J024148.62+372848.3		15.33	15.54	15.52	18986.466			
J025054.80+012357.5		12.03	12.05	12.05	19929.602	−0.088	0.033	2
J025959.18−395812.3		14.50	14.67	14.63	19254.539	−0.065	0.022	2
J030749.87−365201.7	26	15.14	15.57	15.54	19584.393			
J031700.67+190839.6		12.63	12.68	12.67	19496.300			
J033242.81−085525.9	LL Eri[5]	13.31	13.36	13.34	17420.557	0.83	0.32	2
J034439.97+030425.5	11	14.33	14.46	14.42	19861.387			
J040615.79−425002.3	34	14.31	14.68	14.63	19209.987	−0.0294	0.0047	6
J041120.40−230232.3	43	14.09	14.38	14.30	18690.347	−0.124	0.098	1
J041655.13−492709.8	5	15.14	15.40	15.31	19959.816			

[4]Numbers refer to Table 1 in Norton *et al.* (2011); duplicate objects are in parentheses.
[5]Identified as ellipsoidal variable in GCVS.

Table 8.1: (continued)

SuperWASP ID (1SWASP Jhhmmss.ss±ddmmss.s)	Previous ID as variable star	Mean SW V mag	Prim. depth	Sec. depth	P (±0.0005 s)	$\dot{P}$ /s yr^{-1}	$\delta\dot{P}$ /s yr^{-1}	Signif. (σ)
J042200.64−450312.5		13.63	13.69	13.69	18843.443	0.0657	0.0078	8
J044132.96+440613.7	19	14.38	14.59	14.57	19712.589			
J050128.17−041206.9		12.69	12.72	12.72	19512.511	0.070	0.035	2
J050520.94−374338.6		16.34	16.86	16.69	19933.344	0.150	0.032	4
J050723.00−502512.9		14.83	15.02	15.00	18251.638			
J050904.45−074144.4	13	13.51	13.95	13.90	19835.305			
J051459.80−021923.6	(6)	13.76	13.85	13.83	19950.123	−0.101	0.034	2
J052036.84+030402.1	1	12.46	12.62	12.62	19993.297	−0.025	0.011	2
J052825.85+093943.7		14.06	14.15	14.13	19068.472			
J052926.88+461147.5		14.66	14.91	14.86	19581.884			
J055215.51−551950.8		15.50	15.65	15.61	19637.229			
J055416.98+442534.0	(39)	12.73	12.95	12.93	18877.974			
J060334.52−283427.1		14.78	14.86	14.86	17828.542			
J061011.73−345809.0		11.6	11.61	11.61	19884.225			
J061236.44−281553.0		15.65	15.77	15.75	19955.086	0.114	0.036	3
J061850.43+220511.9		13.87	14.05	14.01	18523.570			
J062634.80−385650.1		15.69	15.87	15.80	19326.892	0.152	0.019	8
J070953.45+364417.3		12.06	12.10	12.08	19271.205	0.66	0.30	2
J072504.73+410212.3		9.75	9.76	9.76	19479.807			
J074658.62+224448.5	38	14.27	14.72	14.59	19081.403			
J075102.16+342405.3		14.69	14.91	14.88	18072.478			
J075149.14+362250.9		11.28	11.30	11.30	19974.770			
J080150.03+471433.8	42	13.62	14.05	14.04	18793.174	−0.066	0.043	1
J084408.68−040640.1		16.02	17.06	16.55	18812.053			

Table 8.1: (continued)

SuperWASP ID (1SWASP Jhhmmss.ss±ddmmss.s)	Previous ID as variable star	Mean SW V mag	Prim. depth	Sec. depth	P (±0.0005 s)	$\dot{P}$ /s yr^{-1}	$\delta\dot{P}$ /s yr^{-1}	Signif. (σ)
J084925.17−151516.5		15.27	15.37	15.37	17276.788	−0.164	0.058	2
J090758.16−153811.8		13.53	13.56	13.55	19775.555			
J092339.29−412648.9		9.71	9.72	9.72	17533.446			
J092754.99−391053.4	(30)	12.01	12.15	12.12	19469.694	−0.019	0.014	1
J093010.78+533859.5	(22)	9.56	9.67	9.66	19674.598			
J093443.60+420831.9		13.78	13.96	13.82	19201.572	−0.095	0.023	4
J095706.80−201408.7		15.55	15.82	15.77	19663.870			
J101618.12−085531.0		14.14	14.26	14.24	18546.804	0.065	0.020	3
J102328.57−153951.7		14.13	14.23	14.17	18125.146	−0.254	0.037	6
J104125.56−145842.3		15.47	15.67	15.65	19501.887	0.260	0.036	7
J104942.44+141021.5		14.93	15.09	15.06	19854.610			
J105455.18−352052.5		12.18	12.23	12.22	19981.603	0.0507	0.0083	6
J111501.66−361254.2		15.45	15.67	15.61	19008.433	0.0933	0.0090	10
J111931.48−395048.2	14; ASAS J111932 −3950.8	10.8	10.87	10.87	19827.728	0.0216	0.0022	9
J114929.22−423049.0	23	14.44	14.99	14.83	19639.528	−0.0201	0.0032	6
J115326.51+060756.0		14.69	14.83	14.80	19754.467	0.049	0.024	2
J115557.62+072009.1	(25)	15.36	15.67	15.65	19614.248			
J115605.88−091300.5	48	12.49	12.52	12.52	18222.626	−0.045	0.018	2
J120110.98−220210.8	24	14.27	14.36	14.33	19627.826	−0.253	0.012	20
J120230.52−211314.4		16.31	16.64	16.64	19998.711			
J121206.02+223158.7	CC Com	11.61	12.20	12.08	19067.304	0.0265	0.0011	23
J121359.79−414742.7		13.48	13.51	13.51	18944.739	0.0348	0.0077	4

Table 8.1: (continued)

SuperWASP ID (1SWASP Jhhmmss.ss±ddmmss.s)	Previous ID as variable star	Mean SW V mag	Prim. depth	Sec. depth	P (±0.0005 s)	$\dot{P}$ /s yr^{-1}	$\delta\dot{P}$ /s yr^{-1}	Signif. (σ)
J121906.35−240056.9	29	15.31	15.73	15.55	19558.142	−0.0771	0.0074	10
J123148.12−020602.3		14.97	15.23	15.19	19578.952	0.061	0.027	2
J130111.22+420214.0		15.34	15.69	15.55	19477.594	0.0174	0.0078	2
J130711.90+084159.9		15.23	15.37	15.36	19679.485			
J130920.49−340919.9	33	14.06	14.18	14.17	19253.458	−0.0276	0.0091	3
J132308.74+424613.3		14.06	14.22	14.18	19451.259	−0.24	0.13	1
J133105.91+121538.0	41	10.46	10.59	10.55	18836.380	−0.0202	0.0038	5
J133417.80+394314.4		14.86	15.03	15.03	19775.388			
J134430.51−270302.8		10.34	10.37	10.36	19841.554	−0.130	0.025	5
J135403.76−462948.7		14.46	14.64	14.62	19762.315	0.022	0.015	1
J140533.33+114639.1		16.20	16.51	16.42	19450.626	0.156	0.062	2
J142312.63−222425.1	51	13.21	13.24	13.24	18112.855	−0.1152	0.0099	11
J144331.57−421626.8		14.60	14.80	14.75	18598.876	−0.0116	0.0072	1
J150957.56−115308.4		14.80	15.09	15.07	19787.358			
J151144.56+165426.4		15.03	15.43	15.43	18996.306	−0.0100	0.0075	1
J151146.20−354721.9		12.14	12.20	12.19	19227.102	−0.0167	0.0096	1
J151652.90+004835.8	49	14.01	14.08	14.07	18207.339			
J152022.78−340512.8		15.16	15.42	15.40	18893.115			
J153951.12+105420.7		15.36	15.97	15.82	19070.320	−0.041	0.028	1
J160156.04+202821.6	28	14.31	14.80	14.72	19572.136	0.104	0.011	9
J160202.07+121213.5		13.27	13.34	13.32	18973.486	0.032	0.023	1
J161335.80−284722.2	(12)	12.55	12.94	12.83	19852.821	−0.158	0.018	8
J161858.05+261303.5		13.21	13.24	13.23	19766.679			
J162117.36+441254.2		15.13	15.36	15.26	17958.417	0.0084	0.0060	1

Table 8.1: (continued)

SuperWASP ID (1SWASP Jhhmmss.ss±ddmmss.s)	Previous ID as variable star	Mean SW V mag	Prim. depth	Sec. depth	P (±0.0005 s)	$\dot{P}$ /s yr^{-1}	$\delta\dot{P}$ /s yr^{-1}	Signif. (σ)
J162841.41−334419.8		13.96	14.02	13.99	17598.403	0.203	0.063	3
J164349.61+325637.8	ROTSE1 J164349.58 +325637.8[6]	12.12	12.23	12.21	19447.858	0.0024	0.0008	2
J165734.53+274827.7		14.51	14.63	14.62	19396.507			
J172717.97+431624.0		13.43	13.5	13.49	19446.039	−0.0035	0.0022	1
J173003.21+344509.4	32	13.94	14.13	14.09	19328.926	0.0169	0.0015	11
J180947.64+490255.0	20; V1104 Her	14.13	14.85	14.63	19688.482	0.0101	0.0008	12
J183738.17+402427.2	36	14.56	14.81	14.78	19121.225	0.0039	0.0023	1
J192218.68−303313.1		12.31	12.36	12.35	18098.762	−0.0876	0.0089	9
J193127.17+465809.1		12.12	12.14	12.14	17075.186			
J193537.06−401409.1		15.92	16.24	16.14	19517.575			
J194726.58−243941.0		12.42	12.45	12.45	17568.849			
J195730.89+000705.1		12.64	12.69	12.67	19563.661			
J200059.78+054408.9		14.31	14.44	14.43	17771.663			
J200503.05−343726.5		15.71	16.34	16.17	19775.546	−0.021	0.011	1
J200756.54−163408.0		11.68	11.73	11.72	19226.539	0.1012	0.0066	15
J201208.72+083509.8		12.55	12.58	12.57	18642.212			
J201808.68−231443.0		14.41	14.55	14.51	19683.179	−0.025	0.012	2
J201816.85+112452.8		10.34	10.35	10.35	16101.400			
J203831.39−593324.1		15.23	15.34	15.34	18810.617	−0.084	0.029	2
J204843.90−350912.7		13.29	13.34	13.32	19770.864			

[6]Identified as δ Scuti variable by ROTSE.

Table 8.1: (continued)

SuperWASP ID (1SWASP Jhhmmss.ss±ddmmss.s)	Previous ID as variable star	Mean SW V mag	Prim. depth	Sec. depth	P (±0.0005 s)	$\dot{P}$ /s yr^{-1}	$\delta\dot{P}$ /s yr^{-1}	Signif. (σ)
J204932.94−654025.8		14.22	14.31	14.27	19864.254			
J210318.76+021002.2	16	13.02	13.04	13.04	19750.171	−0.0672	0.0098	6
J210423.94+073104.8	(52)	13.67	13.72	13.72	18065.088	0.0332	0.0039	8
J211359.46+122712.4		14.87	15.08	15.02	19190.122	−0.0508	0.0035	14
J211625.31+251755.4		12.95	13.01	12.99	18782.483			
J212009.70−185220.8		14.19	14.29	14.27	18817.674			
J212454.61+203030.8	21	14.55	14.75	14.72	19684.798			
J212808.86+151622.0	31	14.66	15.01	14.89	19426.320			
J212813.35−520029.1		15.63	15.77	15.75	19913.352			
J213252.93−441822.6		16.69	17.22	17.13	19114.669			
J214046.44+130716.6		12.50	12.53	12.53	19523.322			
J214510.25−494401.1	18	14.69	14.79	14.78	19712.977			
J215826.52+253437.4		13.14	13.19	13.14	19233.919			
J220235.74+311909.7		14.02	14.20	14.19	19049.179	0.068	0.017	3
J220524.25+204151.1		15.34	15.55	15.50	19922.164			
J220734.47+265528.6	2	14.34	14.52	14.50	19978.747			
J221045.95+211842.3		15.48	15.71	15.71	19745.719			
J221058.82+251123.4	45	15.23	15.37	15.34	18402.959	0.073	0.035	2
J221117.26−150216.6		13.73	13.92	13.87	18597.484			
J222302.02+195031.8		15.75	16.05	15.89	19455.256			
J222514.69+361643.0		12.63	12.65	12.65	19416.976			
J224747.20−351849.3	40	13.97	14.10	14.05	18853.816	0.081	0.010	8
J230042.26−365859.7		15.47	15.67	15.63	19448.414	−0.029	0.020	1
J231505.30−010617.0		13.47	13.57	13.56	19836.479			

Table 8.1: (continued)

SuperWASP ID (1SWASP Jhhmmss.ss±ddmmss.s)	Previous ID as variable star	Mean SW V mag	Prim. depth	Sec. depth	P (±0.0005 s)	$\dot{P}$ /s yr^{-1}	$\delta\dot{P}$ /s yr^{-1}	Signif. (σ)
J231839.72+352848.2		14.91	15.02	14.98	17388.474			
J231943.31+134121.4		14.34	14.44	14.42	19944.234			
J232610.13−294146.6	(8)	13.58	13.92	13.84	19882.087			
J233120.96−145814.2		13.85	13.99	13.97	18657.047			
J234401.81−212229.1	44	11.68	11.75	11.73	18461.639	−0.1422	0.0041	35
J235216.40+465044.9		10.41	10.42	10.42	18416.616			
J235333.60+455245.8	7	14.88	15.10	15.06	19935.681			
J235935.22+362001.5		11.76	11.77	11.77	17424.406	−0.120	0.023	5

Chapter 9

Confirming candidate EBs

The short-period SuperWASP variables explored for evidence of period change in Ch. 7 and 8 were described only as eclipsing binary *candidates*, since non-binary stars might conceivably mimic eclipsing-type light curves in some cases. Here, spectra provided unexpectedly by S. Hodgkin allowed us to confirm two of these candidates as double-lined spectroscopic eclipsing binaries in contact configuration, and to explore their properties more thoroughly through modelling. This chapter is closely based on Lohr *et al.* (2014a).

9.1 Introduction

1SWASP J150822.80−054236.9 (J150822) and 1SWASP J160156.04+202821.6 (J160156) were initially identified in Norton *et al.* (2011); the period of J150822 was revised upwards to 22469.2 s in Lohr *et al.* (2012) and therefore it did not appear in Lohr *et al.* (2013b). We report system and component parameters obtained for these confirmed eclipsing binaries by simultaneous modelling of their SuperWASP light curves and radial velocities. These are of interest for the study of low-mass dwarfs and W UMa systems in general, and of very short period binaries specifically.

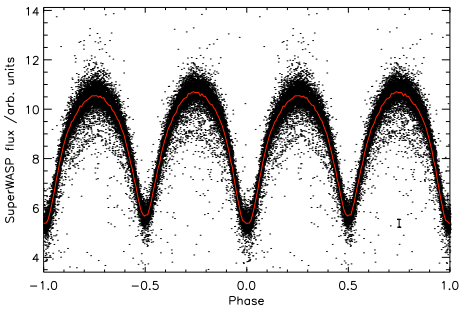

Figure 9.1: SuperWASP light curve for J150822, folded at a period of 22469.219 s, with the binned mean curve overplotted. A typical uncertainty range for a single observation is shown. These fluxes correspond to a visual magnitude range of ∼12.4–13.2.

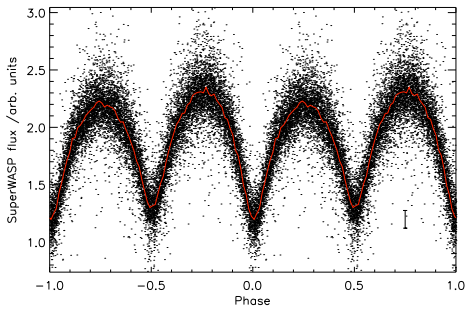

Figure 9.2: SuperWASP light curve for J160156, folded at a period of 19572.136 s, with the binned mean curve overplotted. A typical uncertainty range for a single observation is shown. These fluxes correspond to a visual magnitude range of ∼14.1–14.8.

9.2 Observations

9.2.1 Photometry

The SuperWASP archive contains 30131 photometric points for J150822, taken between 5 March 2008 and 29 March 2011. For J160156 there are 14651 observations, made between 2 May 2004 and 21 February 2011. Sys-Rem-corrected fluxes from the 3.5 pixel-radius photometric aperture (the middle of three available apertures) were used to construct the light curves used here, which correspond approximately to the Johnson V band. Periods and period-change measurements were obtained using a custom-written IDL program, (*ah2*, as described in Ch. 4 and Ch. 5), and the binned averaged phase-folded data produced high-precision phased light curves (Figs. 9.1 to 9.4). A small secular period decrease (-0.055 s y^{-1}) was measured for J150822, and a slightly larger secular period increase (0.094 s y^{-1}) for J160156; both values are fairly unexceptional for variables of this type (see Ch. 8 results). The scatter here is comparable to that seen in other SuperWASP light curves for objects of similar magnitude, and it is unlikely that either period variation over time or flux variability caused by surface spots

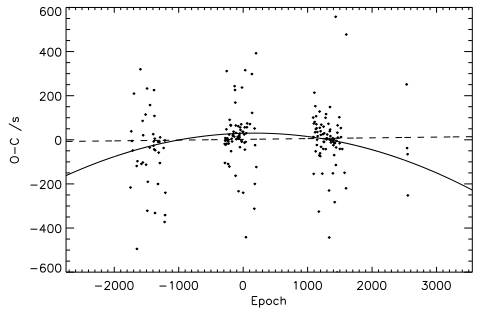

Figure 9.3: Observed minus calculated (O−C) diagram for J150822, with best linear (dashed line; reduced $\chi^2 = 5.25$, 283 d.f.) and quadratic (solid curve; $\chi^2 = 4.87$, 282 d.f.) fits overplotted. For clarity of presentation, uncertainties are not shown. Period decrease of -0.055 ± 0.006 s y^{-1} is indicated ($\sigma = 8$).

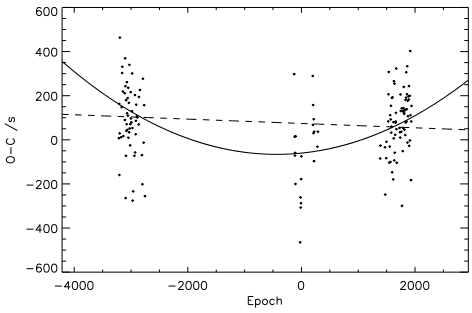

Figure 9.4: O−C diagram for J160156, with best linear (dashed line; $\chi^2 = 1.87$, 244 d.f.) and quadratic (solid curve; $\chi^2 = 1.64$, 243 d.f.) fits overplotted. For clarity of presentation, uncertainties are not shown. Period increase of $+0.094 \pm 0.015$ s y^{-1} is indicated ($\sigma = 6$).

significantly contribute to it. The uncertainties on the means in the light curves used in subsequent modelling were given by the standard deviation of points in each bin, divided by the square root of the number of observations per bin, i.e. $\sigma/\sqrt{n}$.

9.2.2 Spectroscopy

Thirty-six long-slit spectra were obtained by S. Hodgkin for J150822 and 28 for J160156 with the Intermediate Dispersion Spectrograph (IDS) on the 2.5 m Isaac Newton Telescope (INT) at La Palma in the Canary Islands. The observations for the two stars were interspersed with each other and cover three consecutive nights (11-13 March 2012) to optimise phase coverage. Exposures were 300 or 600 s to allow for the short orbital periods involved, and a wavelength range of ∼7915–9040 Å was chosen, which covers the Ca II triplet. The RED+2 CCD and R1200R gratings were used, providing a resolution of 0.51 Å per pixel. S/N values of ∼40–50 were obtained around quadrature for J150822, and ∼30–40 for J160156. The spectra were flat-fielded, bias-corrected and optimally extracted using standard

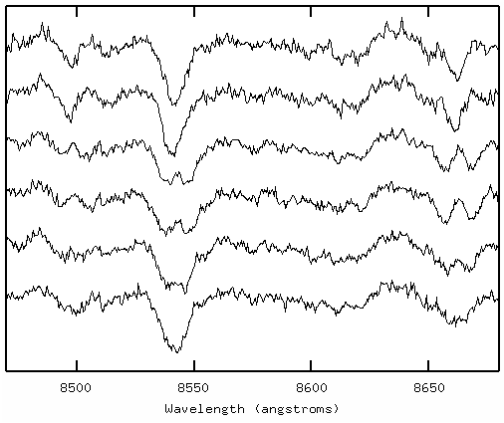

Figure 9.5: Selected spectra in the region of Ca II triplet (laboratory wavelengths: 8498.03, 8542.09 and 8662.14 Å) for J150822, taken from the final night of observations. Line splitting is readily apparent for all three calcium lines.

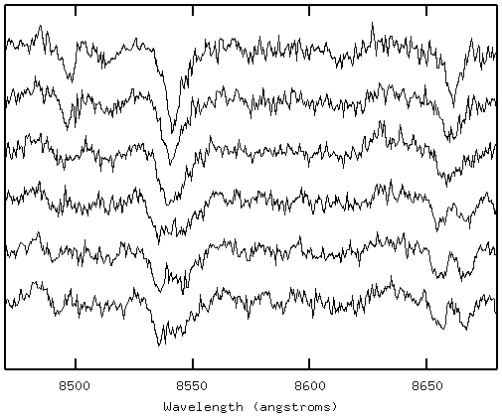

Figure 9.6: Selected spectra in region of Ca II triplet for J160156, taken from final night of observations. Line splitting is most obvious for the two calcium lines at longer wavelengths.

IRAF routines, and were calibrated using CuArNe arc lamp exposures.

Line splitting was clearly observable by eye (Figs. 9.5 and 9.6) and was used to estimate the phase. A suitable synthetic comparison spectrum was then selected by cross-correlation with a phase 0 program spectrum; the best-matching template for both objects had a temperature of 4500 K. Radial velocities (RVs) were measured by cross-correlation with the template using the IRAF task FXCOR. Uncertainties were minimized by excluding the broadest Ca II line from consideration. Improved phase determinations were obtained by fitting sinusoidal functions to the RV curves to locate cross-over points corresponding to phases 0 and 0.5.

These phasings were then compared with the predictions of the SuperWASP linear and quadratic ephemerides (implying constant periods and secular period change, respectively), and with internal simultaneous low-resolution light curves extracted from the spectra themselves (by evaluating a continuum fit at 8500 Å), and were found to be substantially self-consistent (Figs. 9.7 and 9.8). The divergence between different phase measures is greater for J160156; this is

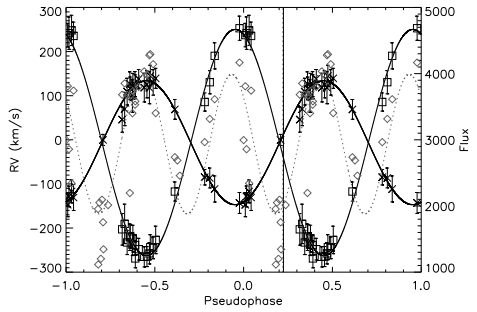

Figure 9.7: Radial velocities for J150822 (crosses indicate primary component, squares secondary) with preliminary fits (solid curves) used to obtain correct phasing of observations. Also shown are a light curve obtained from the spectra themselves (grey diamonds, fitted with dotted grey curve) and the predictions for time of minimum light from SuperWASP ephemerides (the solid vertical line indicates a linear ephemeris, i.e. no period change, the dotted vertical line a quadratic one, i.e. secular period change; the two are almost coincident).

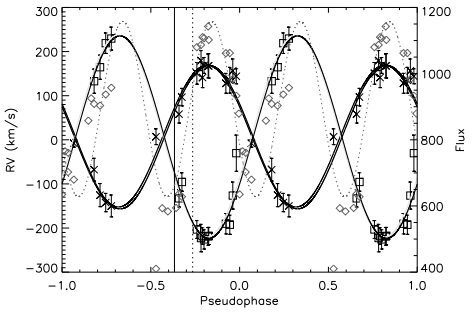

Figure 9.8: Radial velocities for J160156 with preliminary fits used to obtain correct phasing of observations. The primary and secondary curve fits were determined consecutively, with the second fit deriving some parameters from the first, and then refitted in the other order; this has resulted in the visibly double fit curve for the primary component. Also shown are a light curve obtained from the spectra themselves and the predictions for time of minimum light from SuperWASP ephemerides.

a consequence of its shorter period, more rapid predicted period-change, smaller data sets (both photometric and spectroscopic), and the longer time gap between the last archived photometry and spectroscopy. We note that in each system the deeper minimum of the light curve corresponds to the eclipse of the secondary, less massive binary component; the SuperWASP light curves were consequently refolded to locate phase 0 at the time of true primary eclipse. The resulting spectroscopic observations and derived quantities are given in Tables 9.2 and 9.3. The velocity uncertainties are those obtained with FXCOR; uncertainties in phase (using the sinusoidal fitting described above) are negligible in comparison, and were not included in subsequent modelling.

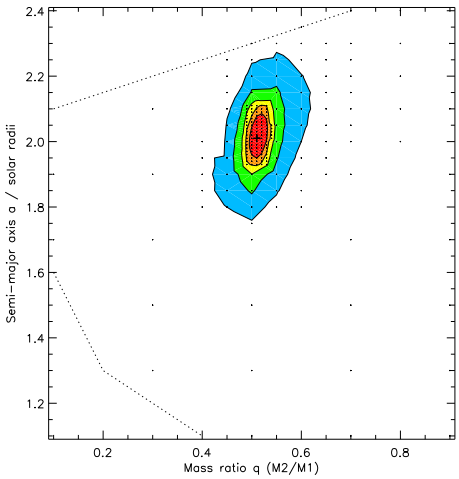

Figure 9.9: a–q parameter cross-section for J150822. Boxes indicate points sampled (other parameters are optimized) and the global minimum is marked with a cross. Contour lines show the 1, 2, 3, 4, and 5 σ uncertainty levels derived from the $\Delta\chi^2$ values of the sampled points. Points outside the plot boundaries or the dotted lines were not sampled since they corresponded to physically implausible masses for the stellar components (<0.08 or >1.5 $M_\odot$).

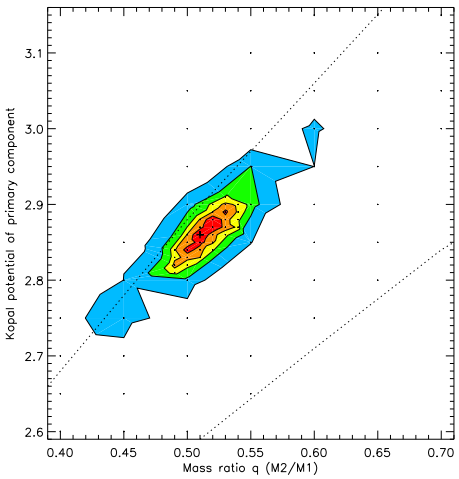

Figure 9.10: Ω_1–q parameter cross-section for J150822. Points below the lower dotted line were not sampled since they correspond to physically implausible filling factors ($F > 1$); very high potentials, corresponding to highly unlikely detached configurations, were not sampled either. The upper dotted line indicates the location of the binary's Roche lobe; the primary component is (with high probability) just below this line, and hence probably just overfills the Roche lobe.

9.3 Results

The eclipsing binary modelling software PHOEBE (see Ch. 6), was used to model simultaneously the binned SuperWASP light curves and INT radial velocity curves of the two systems. (The full SuperWASP light curves were also modelled as a final check on the validity of the optima found using binned curves; it would have been prohibitively time-consuming to carry out the full modelling procedure using curves consisting of tens of thousands of data points.) A semi-detached or contact configuration (one or both components overfilling their Roche lobes) was assumed on the basis of the continuous light variation in the light curves, so the unconstrained mode was used to allow for both possibilities. An approximate

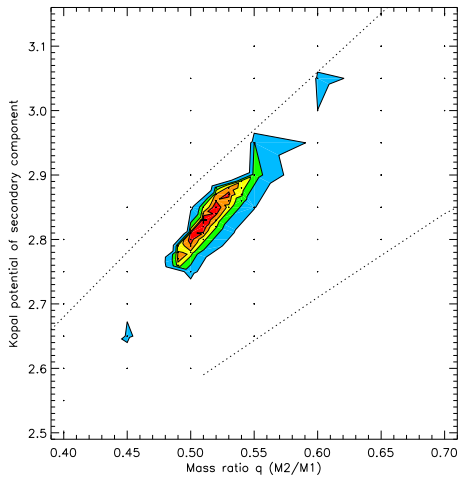

Figure 9.11: Ω_2–q parameter cross-section for J150822 (see caption to Fig. 9.10 for an explanation of the dotted lines). The secondary component is, with very high probability, overfilling the Roche lobe.

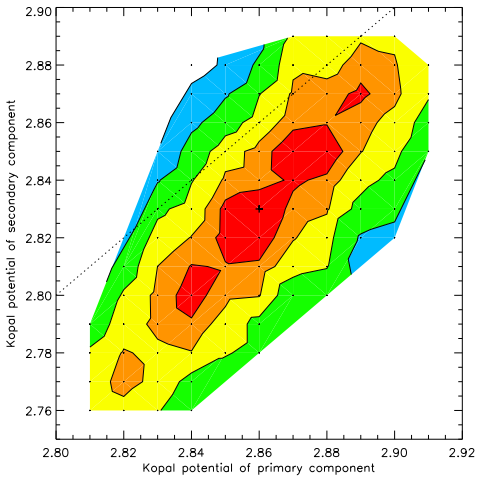

Figure 9.12: Ω_1–Ω_2 parameter cross-section for J150822. The dotted line here indicates equal potentials for the two components, which would necessarily be the case in a contact system; their probability distribution almost follows this line, showing a strong correlation between Ω_1 and Ω_2.

shared temperature (which would correspond to the envelope surrounding the components of a W UMa-type system) of 4500 ± 250 K was used for both binaries because a template with this effective temperature had provided the best match for phase 0 and phase 0.5 spectra during radial velocity determination; this was not varied during modelling because of the relatively low S/N of the spectroscopic data and the limited contribution of temperature to the goodness of model fit.

The shortness of the orbital periods involved constrained us to sub-solar or approximately solar parameters for masses and radii: large stars simply would not fit into the orbits implied, and so trial values of semi-major axes were limited accordingly. No third light was included since in each light curve the deeper eclipse has roughly half the flux of the higher maximum. The details of the light curve shape also constrained the possible angles of inclination: J150822 has slightly flattened eclipse bottoms, implying i close to 90°, while J160156 has

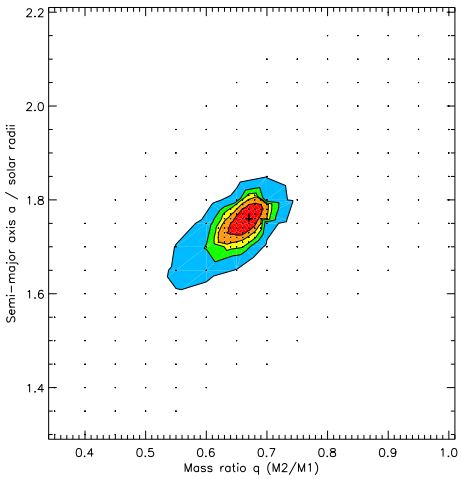

Figure 9.13: a–q parameter cross-section for J160156. A fairly strong correlation between semi-major axis and mass ratio is apparent.

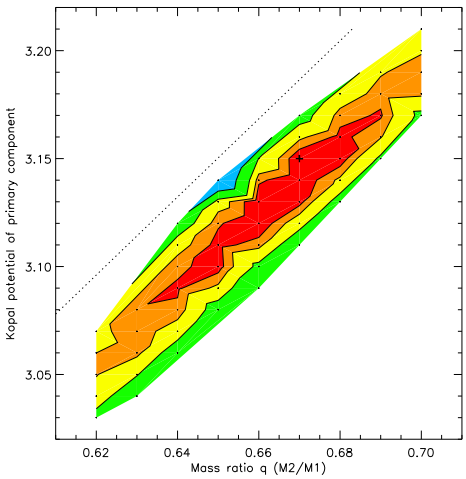

Figure 9.14: Ω_1–q parameter cross-section for J160156. The dotted line indicates the location of the binary's Roche lobe; the primary component is with high probability below this line, and hence very likely overfills the Roche lobe.

more pointed eclipse bottoms, ruling out such a high angle. The shapes of the shoulders of the maxima in each case implied Kopal potentials lower than the critical potential at Lagrange point L_1 , i.e. yielding binary filling factors in (0,1], using Prša's definition

$$F = \frac{\Omega - \Omega_{\rm crit}^{L_1}}{\Omega_{\rm crit}^{L_2} - \Omega_{\rm crit}^{L_1}}.$$

The radial-velocity curve amplitudes alone determined the semi-major axes of the orbits a and hence the absolute sizes of the components, while their mass ratios q were constrained by both light and radial-velocity curves via the relative eclipse depths and relative amplitudes of primary and secondary components. The light curves provided most of the information needed to determine the optimum angles of inclination i and Kopal potentials $\Omega_{1,2}$.

Using these guidelines and following a similar approach to that of Chew (2010), an initial best-fit solution was found manually for each system, which

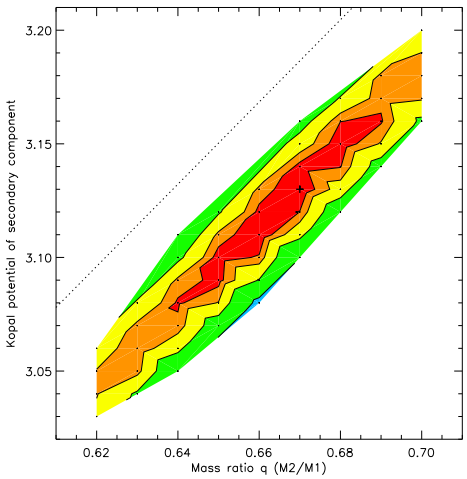

Figure 9.15: Ω_2–q parameter cross-section for J160156. The secondary component is also very likely overfilling the Roche lobe.

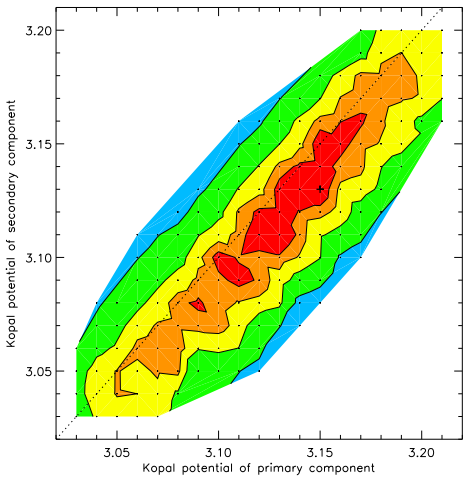

Figure 9.16: Ω_1–Ω_2 parameter cross-section for J160156. The region of highest probability closely follows the dotted line, suggesting near-identical potentials for the two components.

minimized the combined χ^2 values for the light curve and the two radial velocity curves. To ensure that these solutions corresponded to global rather than local minima, to explore the correlations between fitting parameters, and to determine realistic uncertainties for the best-fit parameter values, a series of heuristic scans of the five-dimensional parameter space (a, q, i, and $\Omega_{1,2}$) were carried out using the PHOEBE scripter. Initially, the entire physically plausible parameter space was scanned with widely spaced grids to ensure that no regions of low χ^2 values had been missed. The scans were then repeated with decreasing grid spacings, focusing on regions where the difference $\Delta\chi^2 = \chi^2 - \chi^2_{min}$ corresponded to an uncertainty lower than 3 σ (Press *et al.*, 2007), until the position of the minimum was determined with accuracy.

The global optima found for the two systems via the scans were very close to those found manually; the combined minimum χ^2 value for J150822 was 2.36 and for J160156 was 4.72. Since these values were much higher than 1, indicating poor model fits (for reasons explored below), the $\Delta\chi^2$ value at which to set the 1 σ uncertainty boundary was set with the assistance of a separate series of manually

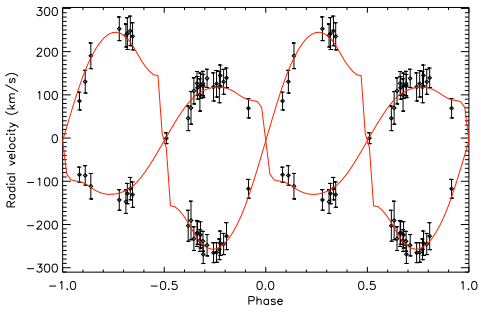

Figure 9.17: Radial velocity curves for J150822 with the best-fit model overplotted.

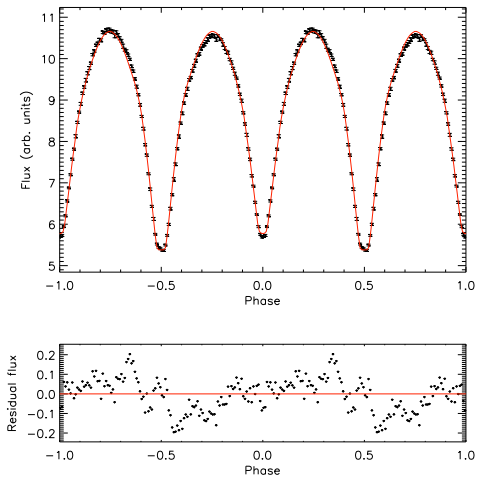

Figure 9.18: SuperWASP binned light curve for J150822 with the best-fit unspotted model overplotted, and residuals below.

determined best-fit solutions for simulated data sets, with data points randomly perturbed according to their original individual uncertainties. The standard deviations of the parameters, estimated by this method, were comparable in size with the formal uncertainties given by the Wilson-Devinney covariance matrix.

Figs. 9.9–9.16 illustrate some of the ten two-dimensional parameter cross-sections obtained from the scans. The $\Omega_{1,2}$–q planes are particularly revealing: both systems have best-fit solutions in which both components overfill their Roche lobes, and where the two potentials are strongly correlated with each other (Figs. 9.12 and 9.16), suggesting that the components of each system share a common potential within the shared envelope of a contact binary.

Figs. 9.17 to 9.24 show the best-fit PHOEBE models for the two systems. A weak Rossiter-McLaughlin effect (Rossiter, 1924; McLaughlin, 1924) is seen in the model for J150822 in the asymmetry of the radial velocity curves (Fig. 9.17); this is a consequence of the high inclination angle. The different heights of maxima visible in both light curves, but most notably in J160156, are most likely attributable to star spots, that is, the O'Connell effect. However, since

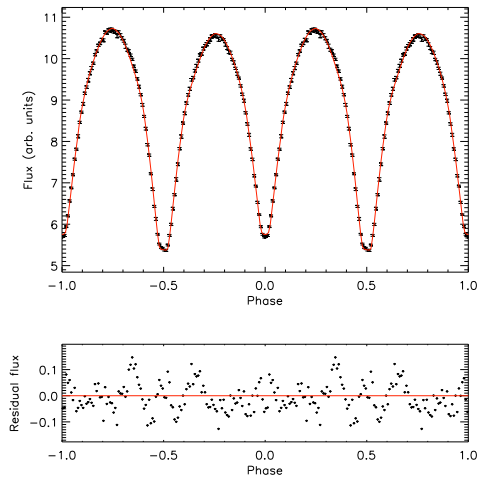

Figure 9.19: Best-fit model for J150822 with example spot included, and residuals below .

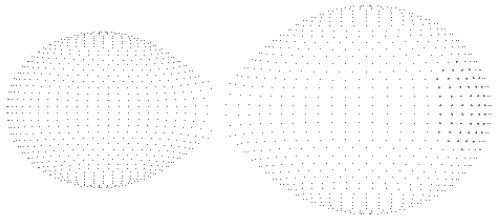

Figure 9.20: Image of J150822 PHOEBE best-fit model at phase 0.75, indicating location and size of example cool spot on primary.

we lack any direct evidence for the number, size, or location of spots e.g. via Doppler tomography (Marsh and Horne, 1988; Marsh, 2005), and being mindful of the additional modelling latitude provided by including spots, we sought to determine the best-fit model for the light curves without including any spots, and our final stellar parameters result from this model.

Figs. 9.19 and 9.23 indicate the improvement of fit resulting from adding a single cool spot to the primary component in each system without altering any other input parameters. Figs. 9.20 and 9.24 show the appearance of the modelled spotted systems, which reproduce both the different heights of maxima and the different depths of minima better than the unspotted models can. Addition of more spots might easily produce a perfect match of models to light curves, but at the expense of the plausibility of the modelling.

The residuals for the light curve fits reflect these assumed spots in their large-scale sinusoidal deviations (Figs. 9.18 and 9.22). However, there are additional clear sinusoidal variations at a smaller scale in the residuals for J150822 (Fig. 9.19): an oscillation with an amplitude of around ± 0.1 flux units and a frequency of six cycles per orbit. Possibly these correspond to pulsation of the

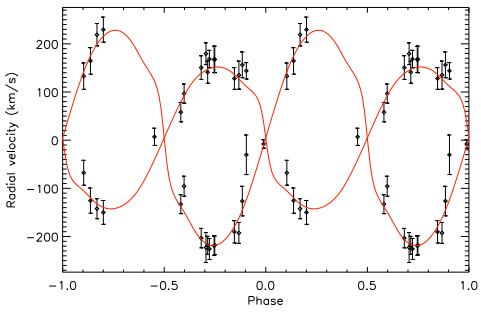

Figure 9.21: Radial velocity curves for J160156 with the best-fit model overplotted.

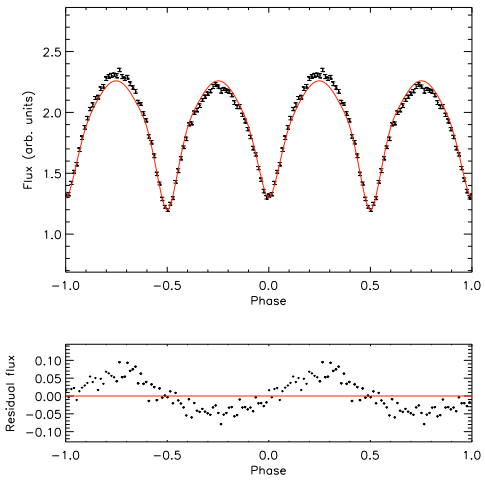

Figure 9.22: SuperWASP binned light curve for J160156 with the best-fit unspotted model overplotted, and residuals below.

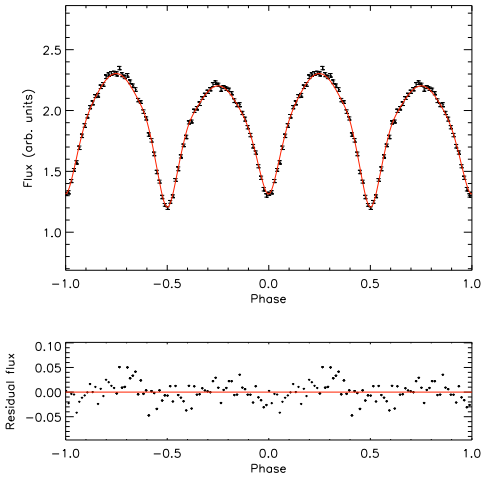

Figure 9.23: Best-fit model for J160156 with example spot included, and residuals below .

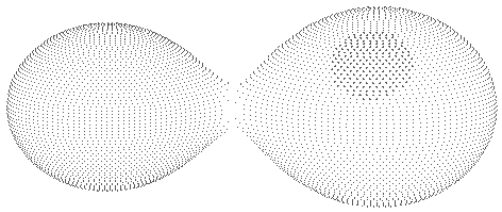

Figure 9.24: Image of J160156 PHOEBE best-fit model at phase 0.75, indicating location and size of example cool spot on primary.

primary (since they are obscured during primary eclipse), and are locked to the binary orbital period (since they are clearly visible in the folded light curve). However, it may be that these are simply fitting artifacts.

The final best-fit parameters for both systems are given in Table 9.3. We would emphasise that these parameters are not dependent on the inclusion of spots in the models. The uncertainties on a, q, i and $\Omega_{1,2}$ were obtained from

		J150822	J160156
Semi-major axis ($R_\odot$)	a	$2.01^{+0.07}_{-0.06}$	1.76 ± 0.03
Mass ratio	M_2/M_1	$0.51^{+0.02}_{-0.01}$	$0.67^{+0.02}_{-0.03}$
COM velocity (km s^{-1})	V_0	$-6.2^{+2.8}_{-2.5}$	$4.7^{+1.8}_{-1.2}$
Angle of incl. ($^\circ$)	i	90^{+0}_{-3}	79.5 ± 0.25
Kopal potentials	Ω_1	$2.86^{+0.03}_{-0.02}$	$3.15^{+0.02}_{-0.06}$
	Ω_2	2.83 ± 0.04	$3.13^{+0.03}_{-0.05}$
Filling factor	$\mathcal{F}$	$0.12^{+0.06}_{-0.04}$	$0.10^{+0.06}_{-0.00}$
Masses ($M_\odot$)	M_1	$1.07^{+0.12}_{-0.09}$	0.86 ± 0.04
	M_2	$0.55^{+0.06}_{-0.05}$	0.57 ± 0.04
Radii ($R_\odot$)	R_1	$0.90^{+0.04}_{-0.03}$	0.75 ± 0.01
	R_2	0.68 ± 0.03	0.63 ± 0.02

Table 9.1: Modelled system and stellar component parameters for J150822 and J160156

the 1 σ contours in the relevant parameter cross-sections. The uncertainties on the output parameters (masses and radii) are the maximum/minimum values obtainable using parameter combinations falling within these 1 σ contours.

9.4 Discussion

These results confirm J150822 and J160156, initially identified as candidate EBs on the basis of light curve shapes alone, as double-lined spectroscopic and eclipsing binaries. From modelling, both systems appear to be composed of late G–early M class dwarfs. J150822 is slightly more massive, with an approximately solar-mass primary and late K secondary; its masses have been determined with a precision of ∼10% and its radii within ∼4%. The components of J160156 are of more similar mass: a late-G or early-K primary and a late-K or early-M secondary; its masses have been found with a precision of ∼5% and its radii within ∼2%. Both appear to be W-type systems, in the sense of Binnendijk (1970), in that the less massive component is eclipsed during the deeper minimum.

The contact configuration and likely mass exchange associated with the apparent period changes make it difficult to compare directly the mass-radius relationships of these systems with those collected and discussed for example in

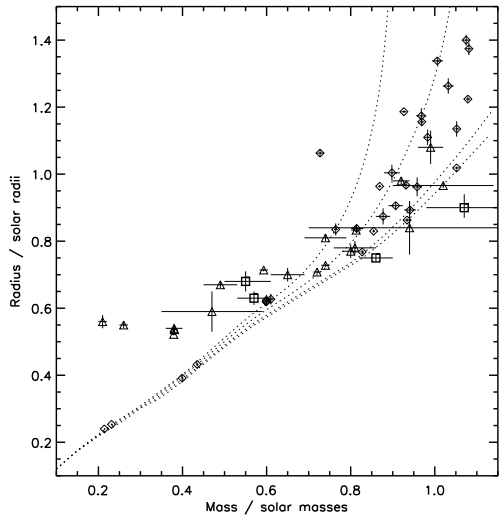

Figure 9.25: Masses vs. radii of J150822 and J160156 components (squares) compared with 32 components of low-mass detached binaries (diamonds) from Torres *et al.* (2010) and 20 components of short-period contact binaries (triangles) from Stepień and Gazeas (2012). Also plotted are theoretical isochrones derived from Dartmouth models (Dotter *et al.*, 2008) for solar metallicity, with ages of 0.25, 1, 5, and 10 Gyr, respectively (dotted lines, ascending).

Torres *et al.* (2010) (Fig. 2) and Torres (2013) (Fig. 4) for detached binaries containing low-mass components. Fig. 9.25 therefore compares our results with those of Torres *et al.* and of a selection of short-period contact systems collected by Stepień and Gazeas (2012). We note that like several other contact systems, the binaries studied here are somewhat discrepant with the Dartmouth model isochrones for solar metallicity (Dotter *et al.*, 2008)[1]models. Specifically, the primaries have smaller radii than their masses might suggest, while the secondaries have larger radii than expected. Possibly the primaries' less dense outer layers have been partially stripped and transferred to the secondaries, leaving denser "cores". Higher resolution spectroscopy and/or Doppler tomography would be required for confirmation.

[1]http://stellar.dartmouth.edu/∼

9.5 Conclusions

J150822 and J160156 are established to be spectroscopic double-lined and eclipsing binary systems in contact configuration, composed of low-mass dwarfs. J150822 was modelled as consisting of components of 1.07 and 0.55 $M_{\odot}$ (mass ratio 0.51), and J160156 as having components of 0.86 and 0.57 $M_{\odot}$ (mass ratio 0.67). The primary of J150822 appears to be pulsating with a period of 1/6 of the orbital period. Both systems are plausibly undergoing mass transfer; this may be related to the primaries' radii being smaller and the secondaries' radii being larger than would be typical for single stars with these masses.

The parameters obtained here contribute to our understanding of low-mass stars and contact binary systems, since relatively few binaries are known with such short orbital periods. It would be desirable to follow up more of the candidate short-period eclipsing binaries listed in Lohr *et al.* (2012) and Lohr *et al.* (2013b) with multi-colour photometry and spectroscopy, with a view to confirming their binary nature. Many of them are expected to be good prospects for full solution, and capable of significantly extending our knowledge of this aspect of the field.

9.6 Addendum

Since the publication of Lohr *et al.* (2014a), Essam *et al.* (2014) published BVRI light curves for J160156, and attempted to model the system and determine parameters for it on the basis of photometry alone, being apparently unaware of our published radial velocities. While some of their results appear close to ours (T_{hot} =4730 K, T_{cool} =4610 K, q ∼0.7, i=79.0±0.2°, $\Omega_1 = \Omega_2$ =3.1908, $\mathcal{F}$ =13.1), they were crucially misled about the mass ratio of the system: they assumed that the deeper eclipses were produced by the more massive primary, and that this component was therefore hotter. In fact, as the combination of radial velocity

curves with light curve evidence clearly shows (Fig. 9.8), the deeper light curve minima are associated with the less massive secondary's eclipses, meaning that this component must be hotter: most of their derived parameters for the two components are therefore the wrong way round. Essam *et al.* also included two cool spots in their model, one on each component, with completely different locations and sizes from the example spot used here (see their Fig. 2 bottom right panel); the fact that this also enabled them to achieve an excellent fit to their light curves simply demonstrates how ill-constrained and unreliable spot modelling is when based on photometry alone.

Table 9.2: Summary of spectroscopic observations and derived quantities for J150822

HJD −2450000	Phase	Prim. RV (km s^{-1})	δ Prim. RV (km s^{-1})	Sec. RV (km s^{-1})	δ Sec. at 8500 Å (km s^{-1})	Contin. flux (arb. units)
5997.5934	0.302	[1]				2995
5997.5977	0.319	-128	24	242	37	2858
5997.6015	0.333	-117	26	248	34	2342
5997.6406	0.484					1115
5997.6444	0.498					1202
5997.6482	0.513					1346
5997.6756	0.618	46	29	-203	36	3682
5997.6792	0.632	70	38	-191	45	3852
5997.6829	0.646	109	30	-233	27	3678
5997.7080	0.743	118	33	-265	23	4034
5997.7119	0.758	126	31	-265	23	3978
5997.7155	0.772	118	36	-257	24	4278
5998.6826	0.490					2050
5998.6863	0.504					2095
5998.7272	0.661	127	28	-221	30	2196
5998.7309	0.676	100	37	-237	25	3401
5998.7348	0.691	126	28	-239	23	3530
5998.7571	0.776	145	24	-243	28	4294
5998.7613	0.793	130	29	-245	24	4143
5998.7650	0.807	139	23	-227	31	3403
5999.5733	0.915	69	22	-117	22	2737
5999.5770	0.929					2689
5999.5806	0.943					2459
5999.6170	0.083	-85	18	86	21	2965
5999.6244	0.111	-86	23	131	26	3316
5999.6316	0.139	-111	30	190	30	3613
5999.6680	0.279	-143	24	253	27	4167
5999.6765	0.312	-147	27	237	27	3810
5999.6850	0.344	-131	29	235	31	3744
5999.7209	0.482					1954
5999.7282	0.510	0	13			1754
5999.7356	0.539					2014
5999.7681	0.664	116	26	-219	27	3669
5999.7719	0.678	121	29	-224	30	3737
5999.7755	0.692	121	27	-269	21	3582
5999.7804	0.711	138	21	-248	25	3802

[1] Radial velocities unusable.

Table 9.3: Summary of spectroscopic observations and derived quantities for J160156

HJD −2450000	Phase	Prim. RV (km s^{-1})	δ Prim. RV (km s^{-1})	Sec. RV (km s^{-1})	δ Sec. at 8500 Å (km s^{-1})	Contin. flux (arb. units)
5997.6567	0.923					635
5997.6605	0.940					765
5997.6643	0.957					702
5997.6902	0.071					858
5997.6939	0.087					925
5997.6976	0.104	-68	26	133	27	909
5998.7083	0.565					594
5998.7120	0.582	58	20	-133	20	637
5998.7157	0.598	97	20	-96	21	628
5998.7401	0.706	180	23	-223	31	1087
5998.7439	0.722	169	18	-226	22	1107
5998.7499	0.749	168	28	-218	19	1102
5998.7718	0.846	128	22	-190	23	1062
5998.7768	0.868	135	29	-193	22	1062
5998.7806	0.884	156	27	-126	31	983
5998.7851	0.904	144	17	-30	41	933
5999.5888	0.452	7	18			410
5999.5968	0.487					593
5999.6039	0.519					584
5999.6409	0.682	151	25	-203	20	1080
5999.6481	0.714	141	23	-218	19	1110
5999.6553	0.746	167	27	-219	20	1143
5999.6945	0.919					879
5999.7033	0.958					761
5999.7105	0.989	-8	9			680
5999.7439	0.137	-125	26	165	27	903
5999.7512	0.169	-142	21	219	23	937
5999.7583	0.200	-150	25	229	26	957

Chapter 10

A mystery solved?

In this chapter, the intriguing object J234401 mentioned in Ch. 7 and 8 is explored with follow-up spectroscopy and modelling to attempt to explain the apparently self-contradictory observations. This chapter is closely based on Lohr *et al.* (2013a).

10.1 Introduction

The object 1SWASP J234401.81−212229.1 (J234401) was identified as a candidate W UMa-type (contact) eclipsing binary in Norton *et al.* (2011), primarily on the basis of light curve shape. Using observations from the SuperWASP archive, a best period of 0.21367 d was found[1], giving it immediate interest as being very close to the observed lower limit in the period distribution of main sequence binaries of ∼0.2 d. Lohr *et al.* (2012) then found evidence of substantial period changes in J234401, which suggested rapid period decrease on the basis of the first four years of SuperWASP data, implying a stellar merger within 40 000 years at most (Ch. 7). However in Lohr *et al.* (2013b), which found the object's period

[1]The corresponding object ASAS J234402−2122.5 found from ASAS observations is listed in the AAVSO International Variable Star Index as a W UMa-type eclipsing binary with a period of 0.2136764 d; in the ASAS Catalog of Variable Stars as a semi-detached eclipsing binary, period 0.213678 d; and in the Machine-learned ASAS Classification Catalog as a δ Scuti pulsating variable with period 0.10684 d.

as 18 461.639±0.0005 s (0.21367638 d), more recently-available SuperWASP observations supported a subsequent increase in period: J234401 currently appears to be undergoing dramatic and approximately sinusoidal variations in period length (Ch. 8).

Two other objects from our collection of 143 SuperWASP candidate eclipsing binaries with periods below 20 000 s have since been followed up spectroscopically, and in spite of relatively low S/N spectra, were confirmed as low-mass double-lined spectroscopic and eclipsing binaries (Ch. 9). Therefore, with high-resolution spectra, the prospects seemed good for confirming J234401 as a binary system, determining its parameters and identifying the cause of its period variation. Observations were made with the Southern African Large Telescope (SALT) in mid-2012, from which we hoped to extract radial velocities for the system components. Moreover, additional photometric observations of J234401 were made during late 2012, with a view to measuring more recent eclipse timings.

Here we report the surprising results of the follow-up observations: that J234401 does not appear to be a straightforward eclipsing binary system. It remains a mysterious object, though certain explanations are supported by the data while others are ruled out. We consider three possible models, and identify one as most plausible on current evidence. Whatever the true nature of this object, it is hoped that this exploration will be of value for studies of low-mass stars and variables in general.

10.2 Observations

10.2.1 Photometry

The SuperWASP archive contains 21727 photometric points for J234401, obtained between 15 May 2006 and 2 August 2011. The fluxes, approximately corresponding to the Johnson V band, were corrected by Sys-Rem, and were ex-

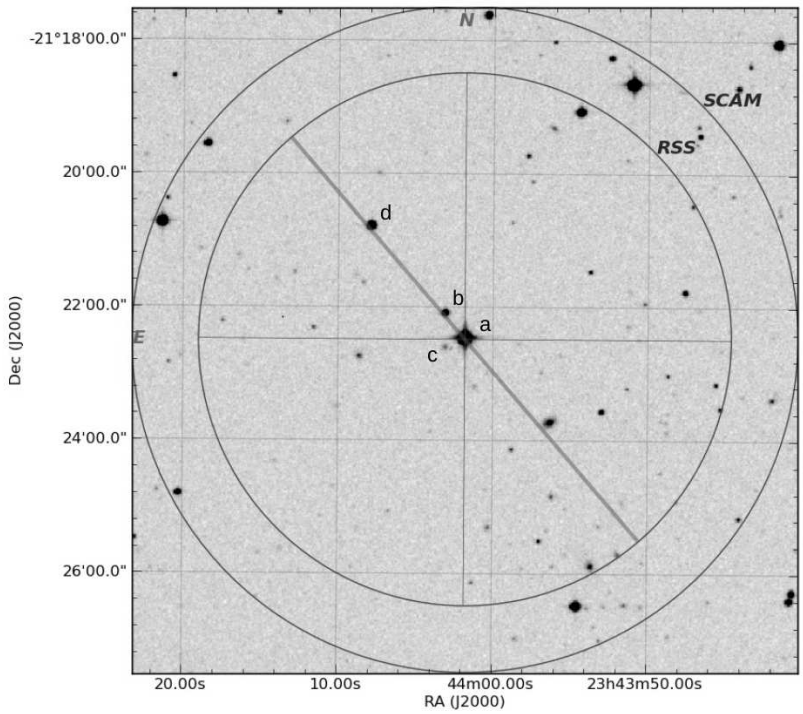

Figure 10.1: Local star field of J234401 (a). The outer circle shows the field of view of the SALTICAM imager; the inner is that of the Robert Stobie Spectrograph (RSS). The diagonal line shows the angle of the spectrograph slit, chosen to include potential comparison stars b and d. Sources b and c would have fallen within the SuperWASP photometric aperture for J234401.

tracted using the 3.5 pixel-radius photometric aperture, corresponding to 47.95″. Fig. 10.1 shows the local star field, including two nearby sources evaluated for their possible contribution to the observed SuperWASP light curve. Periods and period changes were measured using a custom IDL program (*ah2*, described in Ch. 4 and 5), resulting in a high-precision phase-folded light curve.

Additional photometric observations were made of J234401 and nearby sources by D. Boyd in the southern UK, for 0.5 h on 18 December and 1.1 h on 29 December 2012. A 0.35 m telescope with Starlight Xpress SXV-H9 CCD was used (pixel size 12.9 μm = 1.2″). On 18 December, the average FWHM was 3.6″, air mass 3.4, and exposure duration 30 s; on 29 December the corresponding values were 5.6″, 5.7 and 60 s; both nights were affected by moonlight and low-altitude haze. One additional eclipse timing (HJD 2456291.33132) was determined, and the variabil-

ity and magnitudes of several sources in the vicinity of J234401 were measured, using comparison stars GSC 06410-00829, GSC 06410-01027 and GSC 06410-00871 (magnitudes obtained from AAVSO APASS survey).

10.2.2 Spectroscopy

53 long-slit spectra were taken for J234401 according to an automated schedule, by duty astronomers at SALT (Buckley *et al.*, 2006), using the PG1800 grating on the RSS (Burgh *et al.*, 2003) on 1 June (16×60 s), 2 July (16×60 s), 1 August (4×60 s) and 3 August (16×60 s; 1×12 s). By chance there was substantial overlap in the phases covered by the second and fourth nights of observation; a total phase coverage of ∼22% was achieved. The slit, with a width of 0.9″, was intended to be aligned at 35.75° to capture two nearby stars for potential comparison with J234401 (see Fig. 10.1), but this was achieved to varying extents during the second, third and fourth nights, and not at all during the first night. A wavelength range of ∼5800–7100 Å was covered, to include the Na I D doublet, Hα and a large number of narrow metal lines characteristic of cool stars.

Primary reduction was carried out by the SALT pipeline, using the PySALT software package[2] (Crawford *et al.*, 2010). This included fidelity checking, gain and cross-talk correction, overscan bias subtraction and amplifier mosaicking. Master bias subtraction is not suggested for SALT data; also, flat-fielding, cosmic-ray rejection and fringe subtraction were not implemented in the pipeline at the time, pending calibration. After initial attempts to use unflattened spectra, a master flat was constructed as a median of 10 flats supplied with the August spectra, and applied to all program images. Spectra were then optimally extracted using standard IRAF routines (which effectively cleaned out cosmic rays), and calibrated using neon arc lamp exposures. A resolution of ∼0.41 Å per pixel was obtained.

[2]http://pysalt.salt.ac.za/

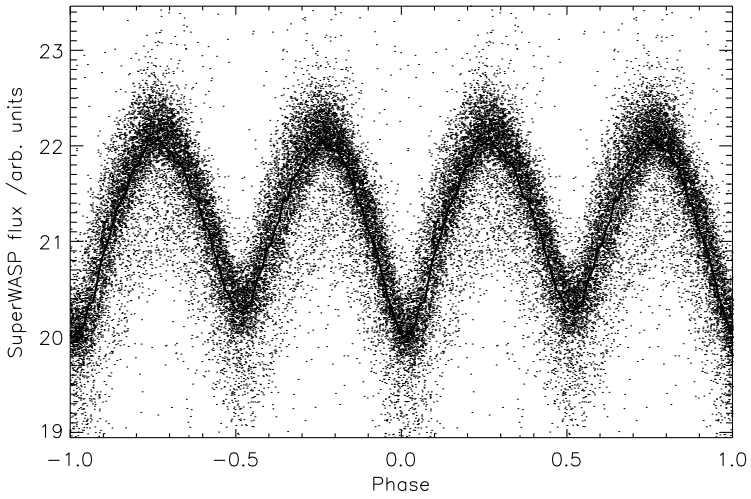

Figure 10.2: SuperWASP light curve for J234401, folded at period of 18 461.639 s, with binned mean curve overplotted.

In the apparent absence of visible line splitting or shifting in the spectra, no data-internal determination of phase was possible. Therefore phases were assigned to the spectra using a SuperWASP ephemeris in combination with D. Boyd's more recent eclipse timing. The source's spectral type was confirmed by cross-correlation using the IRAF task FXCOR, with comparison templates drawn from the Indo-U.S. Library of Coudé Feed Stellar Spectra (Valdes *et al.*, 2004), which uses a comparable resolution (0.44 Å) and wavelength range (3460–9464 Å). Cross-correlation with a program spectrum of phase 0 was used to measure radial velocities, since the assumed two component spectra would be coincident during the primary eclipse.

10.3 Results

Fig. 10.2 shows J234401's light curve, folded at its optimal period of 18 461.639 s. There is a small but consistent difference in the depths of primary and secondary minima, and continuous light variation, explaining its preliminary identification as an eclipsing binary in thermal contact. However, we may note the small

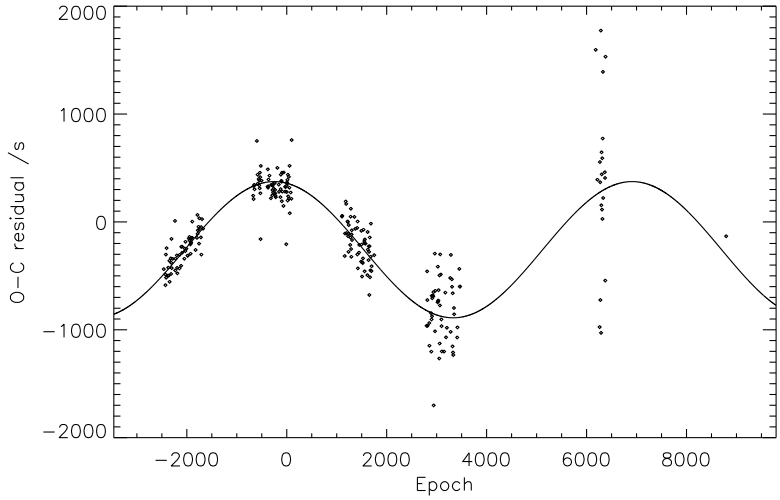

Figure 10.3: O−C diagram for J234401, following subtraction of best linear fit. Best sinusoidal fit is overplotted (meta-period 4.19 y; reduced $\chi^2 = 2.82$, 263 d.f.). Uncertainties on individual points are not shown for clarity, but are typically of the order of ±100 s. The final point, around epoch 9000, corresponds to the independent observation of D. Boyd, and has an uncertainty of ±60 s.

amplitude of variation relative to the maximum or "out-of-eclipse" flux level of ∼22 units (∼11.6 V mag): only about 1/11 of the light is lost during the assumed primary eclipse. This would imply a low angle of inclination of the system, a low mass ratio, and/or a third light entering the aperture.

Fig. 7.6 and Appendix A illustrate earlier data sets and fits for J234401's period changes. The first four years suggested a rapid period decrease (reflected in an O−C parabola opening downwards), but the most recent year of SuperWASP data conflicted with this model ($\chi^2 = 17.83$); assuming a half-cycle error in the primary minimum fits of the final year's data improved the quadratic fit ($\chi^2 = 10.86$) but left Year 4 clearly discrepant. Here, Fig. 10.3 gives the best sinusoidal fit to the SuperWASP data and the additional observation of a primary minimum from 2012; this provides an optimal model ($\chi^2 = 2.82$), and suggests a meta-period for J234401 of 4.19±0.04 years, with an amplitude of 631±11 s.

Fig. 10.4 shows an example full extracted and calibrated spectrum for J234401. The best-matching comparison spectra were around K5V (temperatures between

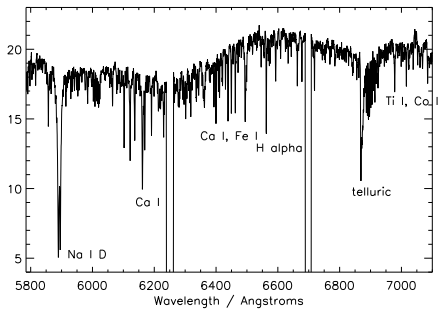

Figure 10.4: SALT spectrum at phase 0.588. The gaps around 6250 and 6700 Å correspond to the boundaries of the three CCDs.

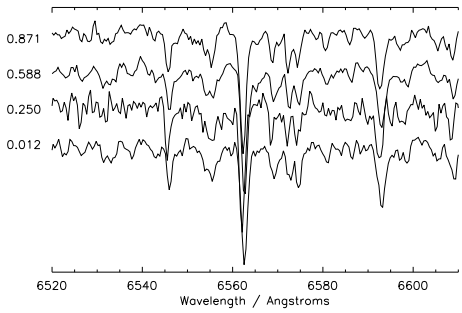

Figure 10.5: Sections of SALT spectra around Hα line at 6562.8 Å, selected from the four nights of observation, and covering as wide a phase range as possible (phases shown on left).

4000 and 4500 K), achieving cross-correlation peak heights in excess of 0.95. However, to our surprise, little to no splitting or even shifting of the many well-defined absorption lines observed was apparent to the eye, as would be expected in a close, short-period eclipsing binary (Fig. 10.5). Only for spectra near phase 0.25 is there any suggestion of a leftward shift, and unfortunately, these spectra are by far the faintest of all four sets of observations, reducing their reliability. Moreover, an approximate light curve extracted from the spectra themselves (by fitting a spline to each continuum and evaluating it at a given wavelength) did not reflect the SuperWASP light curve at all, being apparently dominated by systematic effects.

Table 10.1 gives the heliocentric times, estimated phases and radial velocities for J234401's spectroscopic observations. Only one clear cross-correlation peak was seen for each spectrum, rather than the two that we would expect for an eclipsing binary. (Repetition of the measurements using a template K5V spectrum produced very similar results, apart from a systematic offset due to relative centre-of-mass system velocities.) Fig. 10.6 plots the resulting radial velocity curve against phase. We may note that the amplitude of variation is very small: only ± 5 km s^{-1}, where we might expect values of tens or hundreds of

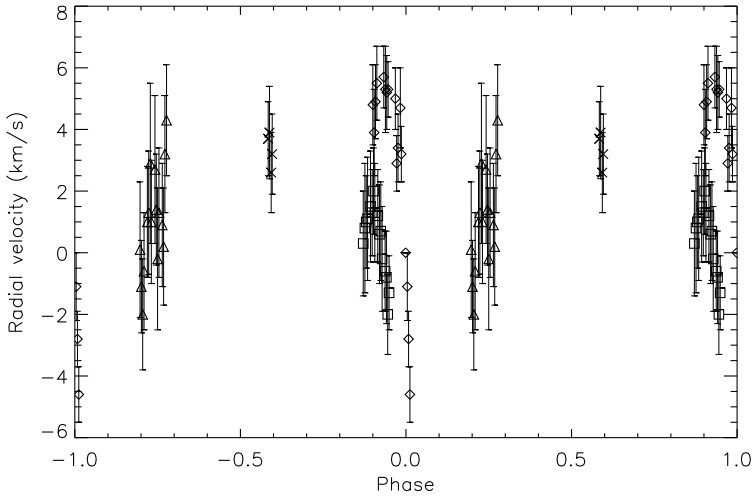

Figure 10.6: Radial velocity curve for J234401. First night's observations are plotted with triangles; second night: squares; third night: crosses; fourth night: diamonds.

km s^{-1}. Also, such trends as are suggested over the orbital cycle do not seem to correspond to expected velocity changes for either component of a spectroscopic binary: some sort of maximum appears around phase 0.9 during the region of overlapping phase coverage, but this is when we expect the primary's radial velocity to be decreasing, and the secondary's to be increasing; phase 0.25 should correspond to the primary's minimum radial velocity and the secondary's maximum, but actually shows a rising trend in our plot.

10.4 Discussion

Our spectroscopic results were not as expected given the photometric data for J234401. Its SuperWASP light curve (and indeed, the ASAS light curve of the corresponding source) strongly suggests a very short period eclipsing binary in contact configuration, like those of J150822 and J160156, confirmed as spectroscopic double-lined and eclipsing binaries, on the basis of fairly low-resolution INT spectra, and modelled as contact systems (Ch. 9). However, the SALT spectra for J234401 showed little to no evidence for line splitting or shifting,

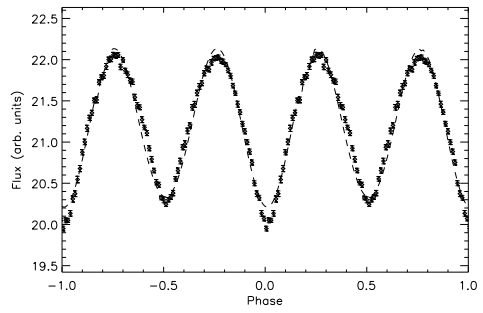

Figure 10.7: Best light curve fit for PHOEBE model 1 of eclipsing binary assuming primary has mass consistent with K5V star, and secondary is massive enough to burn hydrogen ($i = 44°$, $q = 0.11$, $M_1 = 0.73M_\odot$, $M_2 = 0.08M_\odot$). Binned input SuperWASP light curve shown with diamonds and uncertainty bars; fit with dotted line.

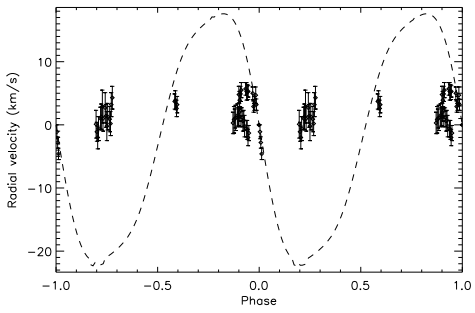

Figure 10.8: Best primary radial velocity curve fit for PHOEBE model 1 (parameters as for Fig. 10.7). SALT radial velocity curve shown with diamonds and uncertainty bars; fit with dotted line.

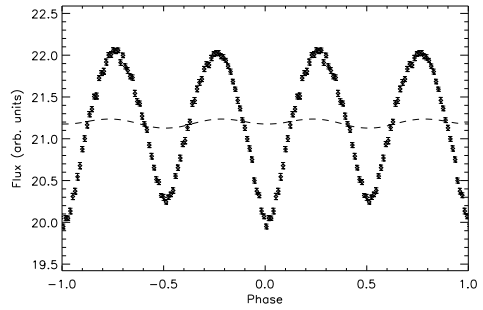

Figure 10.9: Best light curve fit for PHOEBE model 2 of eclipsing binary assuming primary has mass consistent with K5V star, and secondary is massive enough to burn hydrogen ($i = 10°$, $q = 0.11$, $M_1 = 0.73M_\odot$, $M_2 = 0.08M_\odot$).

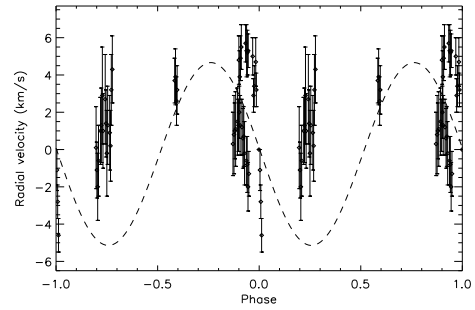

Figure 10.10: Best primary radial velocity curve fit for PHOEBE model 2 (parameters as for Fig. 10.9).

being instead strongly consistent with a single, stable mid-K star.

To confirm our impression of the inconsistency of the photometric and spectroscopic results, modelling was carried out using the eclipsing binary modelling software PHOEBE (Ch. 6). Figs. 10.7 to 10.10 illustrate the best light and radial velocity curve fits for two models: one optimizing light curve fit and the

second optimizing radial velocity curve fit. Input parameters of semi-major axis and mass ratio were constrained by the requirements that the more massive star in the assumed binary be consistent with a K5V spectrum, and its companion be massive enough to burn hydrogen, so that the system contains two main sequence stars. It may be seen that, with the minimum mass ratio $q = 0.11$, the observed light curve can be tolerably reproduced with a moderate angle of inclination $i = 44°$ (Fig. 10.7), but the corresponding primary radial velocities are then about three times larger than observed (Fig. 10.8). However, if i is reduced far enough to bring the modelled radial velocity curve into the observed range (Fig. 10.10), the corresponding light curve model has far too small an amplitude (Fig. 10.9). Higher mass ratios fail to reproduce either light or radial velocity curve, at any angle of inclination. Therefore we conclude that the observed photometry and spectroscopy, taken together, are incompatible with any low-mass eclipsing binary composed of main sequence stars.

One initial explanation considered was that J234401 was not in fact the source of the light variability observed by SuperWASP (and ASAS). Objects b and c, shown in Fig. 10.1, are close enough to J234401 to have fallen within the same SuperWASP photometric aperture. Could one of these be the expected eclipsing binary? Object b was captured within the SALT slit during three nights of observations, so its spectrum was also extracted and reduced. Although much fainter and noisier than J234401's spectrum, the strongest absorption lines (Hα and Na I D) were consistently visible, but showed no signs of shifting or splitting.

Also, the SuperWASP archive contains a light curve for object b (1SWASP J234403.11-212205.8) which we obtained and analysed; in the 3.5 pixel aperture it showed similar variability to J234401, but in the smaller 2.5 pixel aperture, which should have excluded most of its neighbour's flux, its variability was less periodic, while J234401's light curve exhibited the same periodic behaviour even in the small aperture.

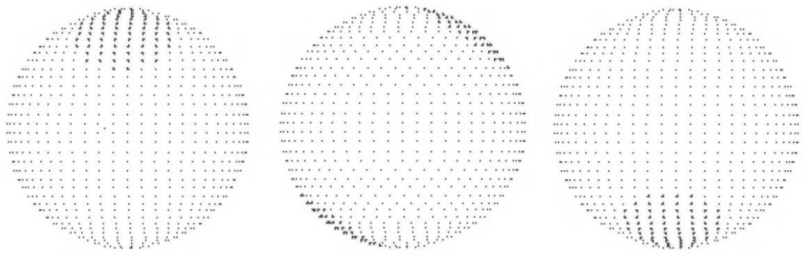

Figure 10.11: PHOEBE images of spotted star model at phases 0.0, 0.25 and 0.5, from left to right.

Finally, D. Boyd confirmed from his 18 December 2012 observations of the field of view that object b had an (unfiltered) magnitude of 15.46±0.21, corresponding to a SuperWASP flux variation of only about ±0.3 units: far smaller than J234401's amplitude of ±1 unit. He also noted that object c did not surpass his sky background level of 16.5–17.0 mag; it therefore would have been too faint to be detectable by SuperWASP, with its range of ∼8–15 V mag. We must conclude, then, that J234401 really is the source of the periodic photometric variation observed.

What, then, might explain an object with the light curve of a short-period binary but the spectrum of a single star? Moreover, what is the source of its dramatic period changes, with their 4.19 y meta-cycle? We have explored three physical models which provide potential explanations for these observations.

10.4.1 One-star model

Our first model regards J234401 as what its spectrum indicates: a single mid-K dwarf, rotating with a period of 18 461.6 s. The low amplitude of light curve variability would be consistent with rotational variation caused by cool surface spots. However, the alternating deeper and shallower minima at phases 0.0 and 0.5 (Fig. 10.2), observed over many years of ASAS and SuperWASP data, would require two large stable spots of different areas and/or temperatures, located on diametrically-opposite sides of the star (Fig. 10.11). This could be achieved if the

spots were somehow pinned to the star's magnetic poles (Harrison *et al.* (2012) claimed similar cool stable polar spots on many K-class rotational variables observed with Kepler), and if the star were an oblique rotator (Stibbs, 1950), having its magnetic axis at an angle to its axis of rotation. The small radial velocity excursions from zero would then be caused by a form of the Rossiter-McLaughlin effect associated with the spots, as observed by Huber *et al.* (2009). Precession due to the different alignments of magnetic and rotational axes might explain the 4.19 y meta-cycle of period changes (Monaghan, 1968).

Using PHOEBE again to test this idea, we modelled a single rotational variable in similar fashion to Harrison *et al.*, setting the input orbital period to the assumed rotational period and turning off the light from the detached companion. Since we were interested in reproducing the radial velocities as well as the light curve, we set the mass ratio as low as possible so that the modelled curves were both flat before the introduction of spots. The (primary) star was given a mass and effective temperature consistent with a K5V spectrum, and i was set to 90° for simplicity. Two spots were then added to the primary in accordance with the model, and adjusted manually until reasonable light and radial velocity curve fits were obtained. The final spot location parameters were colatitudes 35° and 145° and longitudes 0° and 180° respectively, to simulate stable location on the poles of a magnetic axis at 35° to the rotational axis. One was given a slightly larger radius (26° vs. 25°) to reproduce the different depths of light curve minima, but both were set to the same temperature (20% of average).

Figs. 10.12 and 10.13 show the resulting fits. The light curve is fairly well reproduced, both in amplitude and different minima depths. The fitted radial velocity curve is somewhat smaller in amplitude than that observed, but does match some of the velocity trends in the observed curve, notably the maximum around phase 0.9 and the rising trend around phase 0.25. Better fits might be obtained by modelling non-spherical spots, but these initial results may at least

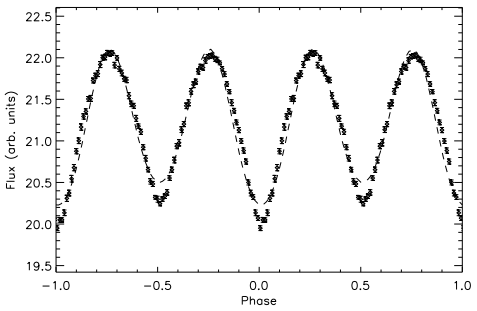

Figure 10.12: Best light curve fit for PHOEBE spotted star model.

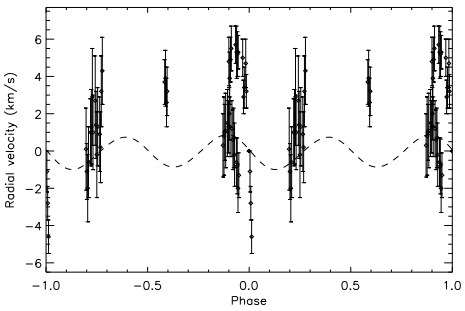

Figure 10.13: Best radial velocity curve fit for PHOEBE spotted star model.

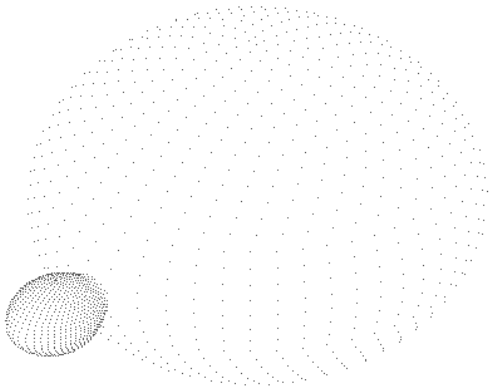

Figure 10.14: PHOEBE image of K dwarf+brown dwarf binary model at phase 0.9.

serve as proof of concept. A greater problem for the one-star model is the lack of evidence (to our knowledge) for other low-mass oblique rotators.

10.4.2 Two-star model

Our second model for J234401 takes the light curve at face value, seeing it as an eclipsing binary in contact configuration, with a mid-K dwarf as primary, and a secondary component making a very limited contribution to the spectrum. In order to reproduce the observed amplitude of radial velocity variation (associated with the primary, in this model), the secondary's mass must be in the brown dwarf range (Fig. 10.14). The observed shape of the radial velocity curve would then be due to the Rossiter-McLaughlin effect as the secondary obscures each

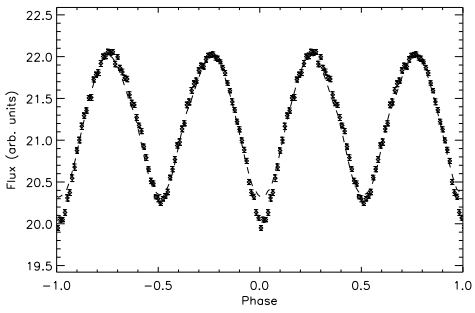

Figure 10.15: Best light curve fit for PHOEBE K dwarf+brown dwarf binary model.

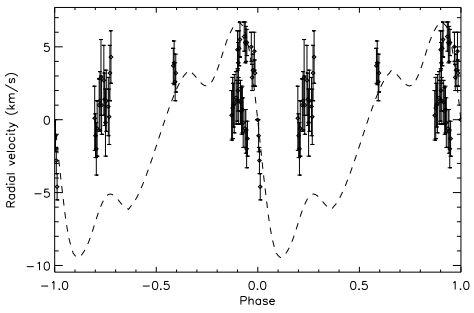

Figure 10.16: Best primary radial velocity curve fit for PHOEBE K dwarf+brown dwarf binary model.

side of the primary in turn, and the 4.19 y meta-cycle of period changes could be explained by the Applegate mechanism.

A PHOEBE model with $i = 59°$, $q = 0.025$, $M_1 = 0.79M_\odot$ and $M_2 = 0.02M_\odot$ produced an excellent fit to the observed light curve amplitude and shape, though the different depths of minima could not be easily reproduced (Fig. 10.15). The radial velocity fit (Fig. 10.16) was of slightly greater amplitude than the observed curve, but its Rossiter-McLaughlin effect-induced variations matched the velocity trends reasonably well, as with the spotted star model. We note, however, that PHOEBE is not intended to model planetary-mass companions, and may not model well objects in the brown dwarf range either, so these model outputs should be regarded with caution.

10.4.3 Three-star model

Our final model for J234401 is of a triple system, consisting of a very low-mass contact eclipsing binary orbiting a more massive mid-K star which dominates the spectrum and obscures the contribution from the binary. The light curve is then the sum of a constant flux contribution from the K star (providing up to 9/11 of the maximum system flux), and a periodically-variable contribution from the binary. The radial velocity curve is almost constant, since it largely represents

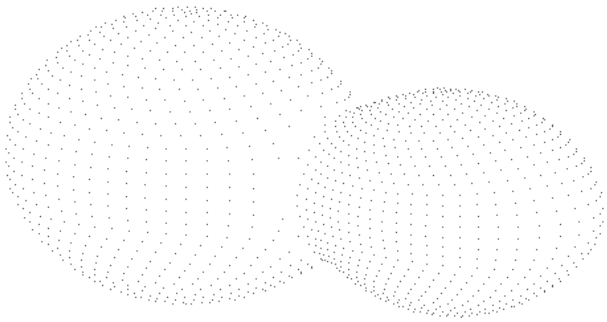

Figure 10.17: PHOEBE image of M+M dwarf binary model at phase 0.15.

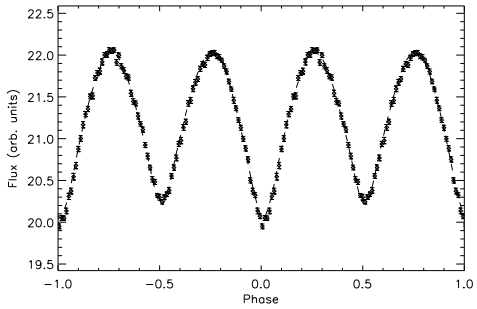

Figure 10.18: Best light curve fit for PHOEBE M+M dwarf binary model.

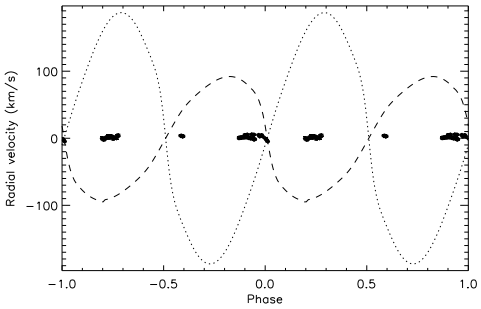

Figure 10.19: radial velocity curves corresponding to best light curve fit for PHOEBE M+M dwarf binary model (primary curve shown with dashed line; secondary with dotted line.)

the unvarying (on this timescale) position of the K dwarf. The 4.19 y cycle of period variation would be a light-time effect (LITE) resulting from the orbit of the contact binary around the most massive component of the triple.

A third light can be readily included in PHOEBE's models; Figs. 10.17 to 10.19 show the results of modelling the eclipsing binary in such a triple system, using parameters $i = 77°$, $q = 0.5$, $M_1 = 0.34M_\odot$ and $M_2 = 0.17M_\odot$ (i.e. M dwarfs), and a maximal third light of 18.0 SuperWASP flux units (11.86 V mag). Fig. 10.17 indicates the very deep contact required; assuming this, however, an excellent fit to the light curve is achieved, without even needing spots to be included for fine-tuning (Fig. 10.18). Fig. 10.19 shows the primary and secondary

radial velocity curves implied for such an eclipsing binary, for reference only, since our observed SALT velocities are expected to be dominated by the constant K star, which is not included in the PHOEBE model as a mass, only as a light source.

Using these masses, totalling $\sim 0.5 M_{\odot}$, for the binary, and a plausible $0.65 M_{\odot}$ for the K5 system primary, a binary-to-primary flux ratio of about 1:5 is implied, consistent with the modelled ratio of around 1:6 given by the SuperWASP light curve with maximum third light. We can also insert these values into the approximate formula for expected LITE changes for a binary in an edge-on circular orbit with a third body, given by Pribulla *et al.* (2012) in their Eq. 5:

$$\Delta T \approx \frac{2 M_3 G^{1/3}}{c} \left[\frac{P_3}{2\pi (M_1 + M_2)} \right]^{2/3}, \tag{10.1}$$

where $M_{1,2}$ are the masses of the binary components, M_3 is the mass of the K5 system primary, P_3 is the 4.19 y period of $O - C$ oscillations, and ΔT is the peak-to-peak amplitude of the $O - C$ variations. The result is 2640 s, about twice the observed amplitude (Fig. 10.3), which is entirely plausible if we do not expect the angle of inclination to be 90°. (Indeed, using Pribulla *et al.*'s Eq. 10 with these masses and our observed semi-amplitude of LITE of 631 s, $i = 56°$ is suggested.)

On the assumption that this model was approximately correct, a suitably-scaled constant K5 template spectrum was subtracted from each of our spectra to see whether some trace of an M+M eclipsing binary spectrum might be detectable in the residuals. Fig. 10.20 shows the resulting radial velocity curves, after cross-correlation with a phase 0 residual spectrum. A second cross-correlation peak was now marginally detectable in the spectra near quadrature, yielding radial velocities in a similar range, and following a similar upward trend, to those predicted for the primary curve in Fig. 10.19 near phase 0.25. The other radial

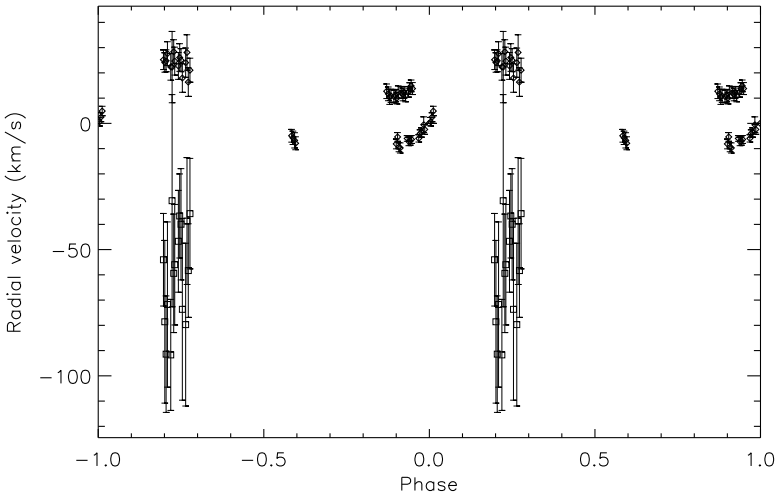

Figure 10.20: Residual radial velocity curves for J234401, following subtraction of scaled K5V template spectrum, and cross-correlation with phase 0 residual spectrum. The stronger cross-correlation peak velocities are shown with diamonds; the fainter cross-correlation peak visible near quadrature is plotted with squares.

velocities reached greater amplitudes than before (Fig. 10.6) and might conceivably represent a blending of lines from multiple stellar components. Given that our best model for the low-mass eclipsing binary in this putative triple system involves very deep contact, it is likely that their lines would be significantly broadened and blended even if no third spectrum were present to complicate the picture, making extraction of radial velocities challenging in any case.

2MASS and WISE colours for the source were also checked for evidence of an infrared excess which might support the presence of M dwarfs in the system. The results were inconclusive, however: 2MASS J−H and H−K colours were in ranges expected for a K5 star, while the WISE colours were inconsistent, possibly being contaminated by nearby sources.

Although we lack conclusive evidence for it, a triple system seems the most likely of our three models for J234401. We have not assessed the dynamical stability of such a triple, but note the recent detection of a young hierarchical triple composed of a late-K primary and a pair of mid-M dwarfs in wide orbits

(Deacon *et al.*, 2013) which shows some similarity to the system posited here. Using the observed and theoretical absolute magnitudes for the stars in this model, a distance of 80–90 pc is indicated. The calculated separation between system primary and contact binary is 2.7 AU, which would then correspond to an angular separation of $\sim$0.03″, making the components resolvable in principle. The expected radial velocity amplitude for the system primary, over a 4.19 y orbital period with the binary, would be around 8 km s^{-1} (assuming a circular orbit and the same angle of inclination as for the contact binary), which might also be detectable in the long term.

10.5 Conclusions

Object J234401, which we originally thought might be an eclipsing binary close to stellar merger, has proved to be unusual and intriguing in a different way. Of the three models investigated here, a triple system containing a low-mass eclipsing binary appears the most plausible explanation for the apparently conflicting photometric and spectroscopic data, and provides an appealing reason for the dramatic cyclic variations in period length observed as well. If confirmed, it should provide a useful contribution to studies of multiple systems, alongside the quadruple doubly-eclipsing system already detected in our collection of short-period SuperWASP eclipsing binary candidates (Lohr *et al.*, 2013b).

Alternatively, if one of our other explanations proves more likely, J234401 could add to our knowledge of brown dwarfs, or constitute a rare type of rotational variable. Still other explanations are no doubt conceivable e.g. involving higher multiplicity of the system; in any case, this appears to be an interesting object worthy of further observation. We would hope in the future to obtain multi-colour photometry and near-infrared spectroscopy of J234401, with improved phase coverage, in the expectation that the greater contrast available at

longer wavelengths would increase the opportunity of detecting cool, low-mass objects within the system.

10.6 Addendum

Since the publication of Lohr *et al.* (2013a), C. Koen obtained UBVRI photometry for J234401 with the SAAO 1 m telescope at Sutherland, South Africa (Koen, 2014). In combination with SuperWASP observations and results supplied by the present author, he concluded that our three-star model was supported; notably, "the amplitude of the [light curve] variability *increases* with increasing wavelengths, and the system is bluest during eclipses". The first effect would be expected if the variability is produced by components whose spectra peak in the near-infrared, while the second can be readily understood as due to the (hotter, bluer) K star contributing more light to the total while one of the (cooler, redder) M stars is obscured during eclipse. His detailed time series modelling of the combined SAAO V-band and SuperWASP observations also supported our claim of a detectable light-time effect on the period. He concluded by noting that this is apparently only the second confirmed contact system consisting of two M dwarfs, and that the K star may have played a role in shortening the period of the M binary through non-alignment of their orbits.

Table 10.1: Summary of spectroscopic observations and radial velocities for J234401

HJD −2450000	Phase	RV (km s^{-1})	δ RV (km s^{-1})	HJD −2450000	Phase	RV (km s^{-1})	δ RV (km s^{-1})
6079.6205	0.197	0.1	2.2	6110.5461	0.928	-0.2	1.7
6079.6214	0.201	-1.1	1.5	6110.5480	0.937	-0.6	1.3
6079.6222	0.205	-2.0	1.8	6110.5489	0.941	-0.8	1.5
6079.6231	0.209	-0.6	1.9	6110.5498	0.945	-2.0	1.3
6079.6252	0.219	1.0	1.8	6110.5506	0.949	-1.3	1.2
6079.6261	0.223	1.3	2.0				
6079.6270	0.228	2.9	2.6	6141.4557	0.584	3.7	1.2
6079.6278	0.231	1.0	2.0	6141.4566	0.588	3.9	1.5
6079.6300	0.242	2.7	2.4	6141.4575	0.593	2.6	1.3
6079.6309	0.246	1.4	1.8	6141.4583	0.596	3.2	1.3
6079.6317	0.250	-0.2	2.3				
6079.6326	0.254	1.3	2.1	6143.4463	0.900	4.8	1.3
6079.6348	0.264	0.9	2.0	6143.4471	0.904	3.9	1.4
6079.6357	0.268	0.2	1.9	6143.4480	0.908	4.9	1.2
6079.6366	0.272	3.2	1.9	6143.4489	0.912	5.5	1.2
6079.6375	0.277	4.3	1.8	6143.4534	0.933	5.7	1.0
				6143.4543	0.938	5.3	1.4
6110.5340	0.871	0.3	1.7	6143.4552	0.942	5.2	1.2
6110.5349	0.876	0.8	2.1	6143.4560	0.946	5.3	0.9
6110.5358	0.880	1.0	1.5	6143.4607	0.968	5.0	1.0
6110.5367	0.884	1.1	2.0	6143.4616	0.972	2.9	0.9
6110.5387	0.893	1.5	1.8	6143.4625	0.976	3.4	1.1
6110.5396	0.898	1.3	1.4	6143.4640	0.983	4.7	1.3
6110.5405	0.902	2.0	1.4	6143.4647	0.986	3.2	0.9
6110.5413	0.906	1.3	1.6	6143.4675	0.999	0.0	0.0
6110.5434	0.915	1.2	1.5	6143.4684	0.004	-1.1	1.1
6110.5443	0.920	0.6	1.6	6143.4693	0.008	-2.8	0.9
6110.5452	0.924	0.7	1.6	6143.4702	0.012	-4.6	0.9

Chapter 11

A rare doubly-eclipsing quintuple star system

11.1 Introduction

Another unusual system emerged from the search for orbital period variations in short-period eclipsing binary candidates, described in Ch. 7 and 8. This was 1SWASP J093010.78+533859.5 (hereafter J093010), which appears to be a doubly-eclipsing multiple system, one of only a handful of known systems of its type. Here, we describe our initial discovery of it as a candidate doubly-eclipsing system, and subsequent confirmation and more detailed exploration of its components by ourselves and other researchers.

11.2 Discovery

A near neighbour of J093010 (1SWASP J093012.84+533859.6, hereafter J093012) was identified as a candidate short-period eclipsing binary in Norton *et al.* (2011), and its period confirmed in Lohr *et al.* (2012). However, in our subsequent more thorough search for eclipsing candidates, J093010 was identified as exhibiting the

same period and light curve shape, but a higher mean flux and greater amplitude of flux variability; hence, it was regarded in Lohr *et al.* (2013b) as the most probable source of the eclipsing variation. (At the location of J093012 is an 18th magnitude source listed in the USNO-B1 catalogue, separated from J093010 by approximately 18″, which would not have been detectable by SuperWASP in its own right.)

The eclipsing source's apparently significant period change, associated with an erratic O−C diagram, had been rejected initially as the result of contamination by a nearby star, but in Lohr *et al.* (2013b) a fuller explanation was pursued. Prior to analysis, the data for J093010 was combined with that from J093012 to maximize the available observations. J093010's lightcurve, folded at 19 674.574 s (Fig. 11.1, top) then showed a typical contact binary shape, but with numerous non-random data points below the main curve. A visual examination of the object's full lightcurve suggested the cause was additional deep eclipses on certain individual nights, implying an additional eclipsing body in the field of view. A frequency power spectrum also supported an additional periodic signal near 1.3 d (Fig. 11.3). Stripping out the median binned lightcurve (corresponding to the contact binary) from the data yielded the lightcurve of an EA-type eclipsing binary with period 112 799.109 s (Fig. 11.1, middle). Stripping the median binned lightcurve of the latter object out of the combined data also yielded a clean lightcurve for the contact eclipsing binary (Fig. 11.1, bottom). Figure 11.2 illustrates how the observations during three representative nights of J093010 are well-reproduced as the sum of these two eclipsing binary lightcurves.

The question arose then, were these two systems physically related, or was their juxtaposition on the sky coincidental? Two sources were observed at this location by Hipparcos as TYC 3807-759-1 and TYC 3807-759-2, with equivalent Johnson V magnitudes 9.851 and 10.990 respectively (corresponding to SuperWASP fluxes around 110 and 42), a separation of 1.88″, and a proper motion of

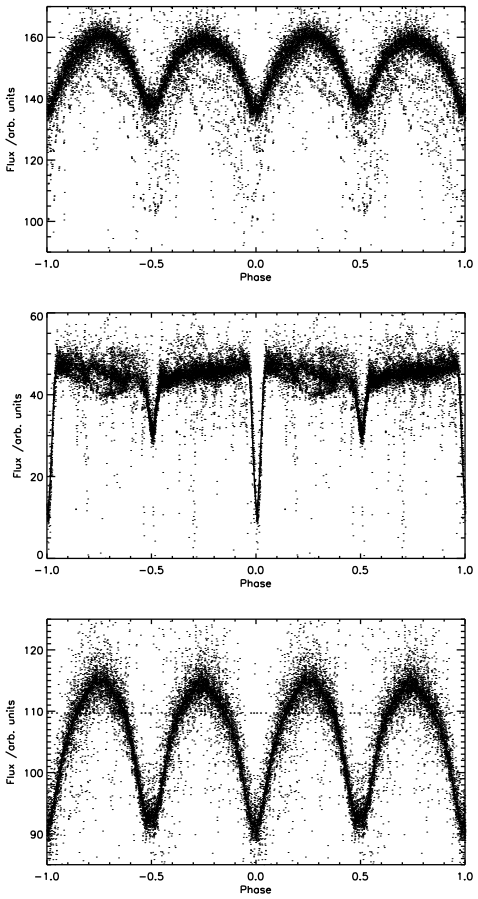

Figure 11.1: Top: lightcurve of object J093010 (combined with duplicate) folded at dominant contact binary period 19 674.574 s, with median binned lightcurve overplotted. Middle: lightcurve of Algol-type eclipsing binary folded at period 112 799.109 s, after subtraction of median binned lightcurve (absolute flux level is arbitrary). Bottom: lightcurve of W UMa-type eclipsing binary after subtraction of Algol median binned lightcurve (absolute flux level is arbitrary).

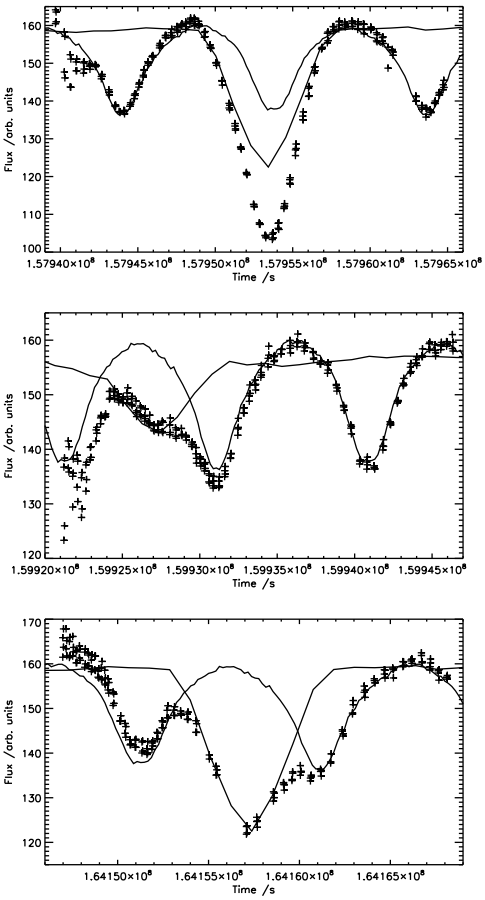

Figure 11.2: Individual nights of observations of object J093010, with median binned lightcurves of Algol and contact binaries overplotted (flux levels adjusted to allow direct comparison). Top: the Algol's primary eclipse coincides with the contact system's secondary eclipse. Middle: the Algol's secondary eclipse nearly coincides with a maximum of the contact system. Bottom: the Algol's primary eclipse falls between the contact system's minima.

pmRA: -8.0 mas yr^{-1}, pmDE: -9.4 mas yr^{-1}, measured at their joint photocentre. The tiny angular separation and similar magnitudes seemed to favour an interpretation of the two eclipsing binary systems as being gravitationally bound in a quadruple doubly-eclipsing system. The distance to TYC 3807-759-1 had

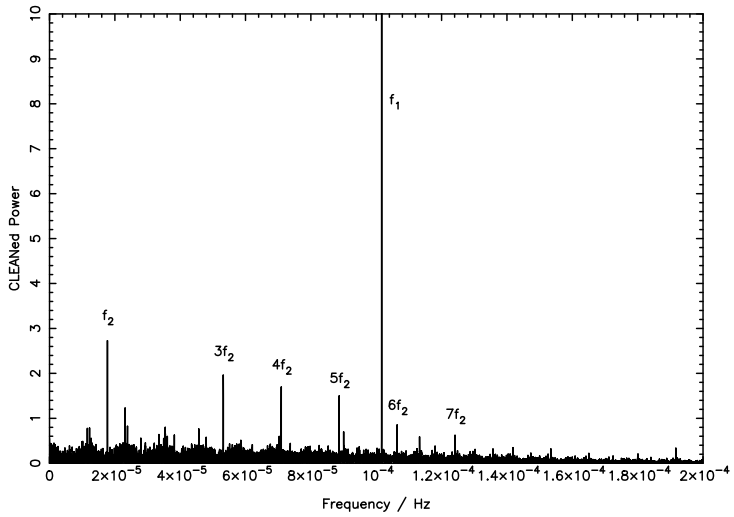

Figure 11.3: Power spectrum for J093010, showing strongest signal at f_1 (associated with the period of the contact binary) and a weaker signal at f_2 and its harmonics (associated with the period of the EA-type binary). This power spectrum was provided by A. Norton.

been calculated as 35.17 pc, implying a separation of 66.1 AU between the two binaries. If this separation corresponded to apastron, and the total mass for both systems was ~ 2 solar masses (assuming that all four stars are low-mass K class, as would be expected for the very short period contact binary), a meta-orbital period of ~ 400 years would be indicated.

Only five other doubly-eclipsing quadruple systems have been proposed to date: BV Dra+BW Dra, a contact+contact system (Batten and Hardie, 1965); V994 Her, an Algol+Algol system (Lee *et al.*, 2008); OGLE-LMC-ECL-16545, Algol+contact (Graczyk *et al.*, 2011); KIC 4247791, Algol+Algol (Lehmann *et al.*, 2012); and Cze V343, another Algol+contact system (Cagaš and Pejcha, 2012). The contact binary in this newly-proposed quadruple has a shorter period than any system in the other five quadruples, making it particularly amenable to further observations.

11.3 Follow-up observations

Following preliminary announcement of this proposed doubly-eclipsing system on arXiv (Lohr *et al.*, 2013b), a Korean group obtained BV photometry over several months in 2012–2013 for each eclipsing binary separately, and time-series spectra for the whole system (Koo *et al.*, 2014). Unfortunately, their chosen spectroscopic exposure time of 20 minutes was too long to permit measurement of any radial velocity variation in the short-period contact binary: each spectrum would have covered ∼6% of its orbital period, resulting in significant motion blur on top of the expected blending of spectral lines in a W UMa-type binary. However, Koo *et al.* did observe clear line splitting and shifting with the period of the proposed detached binary, confirming its reality. They also unexpectedly detected an additional set of static spectral lines associated with the detached binary, which they interpreted as a third star, making the whole system a highly unusual doubly-eclipsing quintuple. For clarity of reference, the elements of the system will be referred to hereafter according to the following assumed system structure:

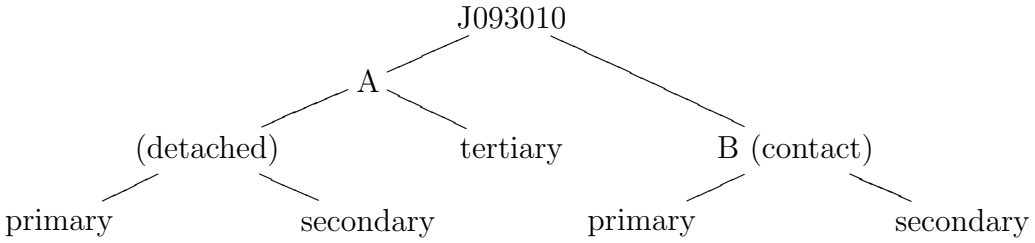

Independently, we obtained time-series spectroscopy over three nights in 2012–2013 for J093010A and J093010B separately, and near-simultaneous RGB photometry for the whole system to help establish the phases of the observations. Our new data thus complements that published by Koo *et al.*, allowing us to model both binaries quite fully; the revisited SuperWASP observations also provide further long baseline information.

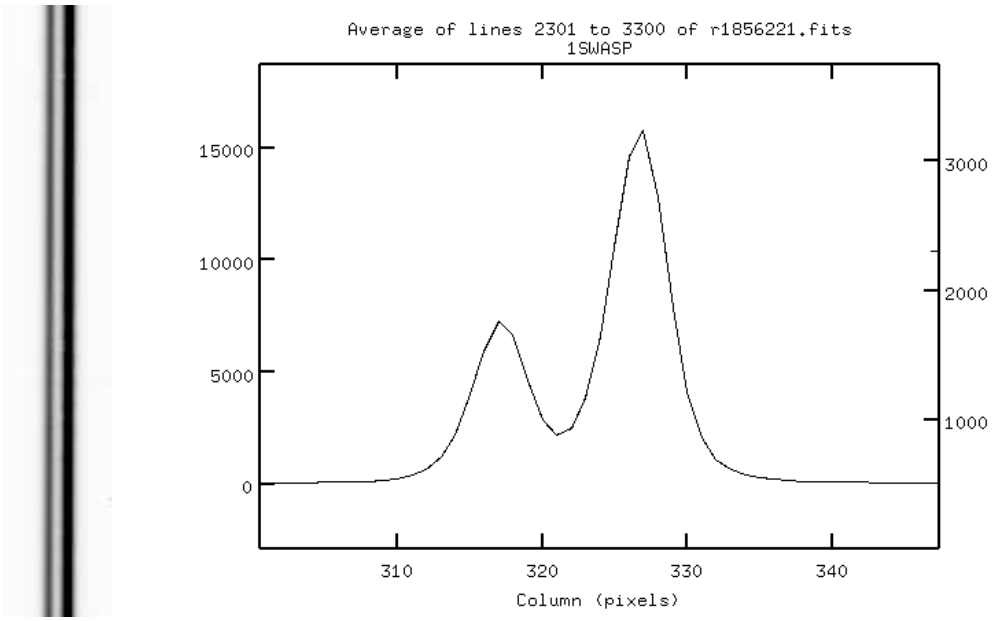

Figure 11.4: Left: Section of spectra for J093010A and J093010B from a single 360 s exposure, showing spatial separation. Right: Plot of spectral profile from same exposure, cut perpendicular to the dispersion axis, showing two clear peaks in the line dispersion function. The stronger peak on the right-hand side corresponds to J093010A.

11.3.1 Spectroscopy

49 long-slit spectra were obtained by E. Gillen for J093010 on 22 and 31 December 2012, and on 2 January 2013, using the red arm of the ISIS spectrograph on the 4.2 m William Herschel Telescope at La Palma. The R1200R grating provided an intermediate resolution of 0.24 Å per pixel. A usable wavelength range of ∼8350–9000 Å was obtained, which should capture the Ca II triplet, important in low-mass stars. Exposure lengths ranged from 5 to 360 s (see Table 11.3): short enough in all cases to avoid motion blur for the contact binary. The images were flat-fielded and bias-corrected by E. Gillen as part of a larger observing programme. On all but one image, two partially-overlapping dispersion lines were clearly visible (e.g. Fig. 11.4), corresponding to J093010A and J093010B, and the present author was able to extract separate spectra for each, using standard IRAF tools and optimal extraction. Wavelength calibration was carried out using arc spectra taken with CuArNe lamps. S/N ratios reached 340 for the brighter

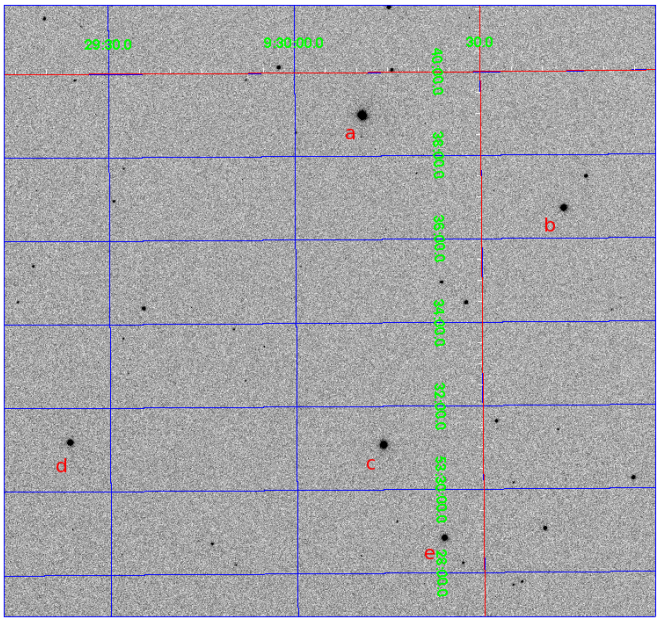

Figure 11.5: PIRATE field of view near J093010 (source a), showing locations of comparison stars TYC 3807-1509-1 (b), TYC 3807-54-1 (c), TYC 3807-1503-1 (d) and TYC 3807-621-1 (e).

J093010A and 220 for the fainter J093010B in the longest exposures, when both systems were near quadrature, and fell to 45 and 25 respectively in the initial 5 s exposure. Radial velocities were extracted using the IRAF task FXCOR, using a synthetic spectrum as the comparison template (a Kurucz model atmosphere template with T_{eff}=4500 K and log g=4.5 provided the best match to both sets of spectra).

11.3.2 Photometry

167 images of J093010 (55 each in Baader G and B filters, 57 in R) were taken with the Open University's robotic 0.425 m PIRATE telescope (Holmes *et al.*, 2011) in Mallorca on the night of 30–31 December 2012, monitored by R. Busuttil. Corrections for bias level, dark current and flat-fielding were made to the frames using standard IRAF tools, and four comparison stars were identified on the frames: TYC 3807-1509-1, TYC 3807-54-1, TYC 3807-1503-1 and TYC 3807-621-1 (Fig. 11.5). These had catalogue colours indicative of classes between late

F and G, and V magnitudes between 9 and 10, similar to J093010. They were checked for short and long-term variability with their SuperWASP light curves, and did not exhibit significant variations. Aperture photometry was carried out on all the stars using the IRAF APPHOT package, and the light curves of the comparison stars were combined in IDL. Differential light curves were then obtained for J093010 relative to this combined comparison curve.

The SuperWASP archive data for J093010 was also reconsidered: it contains 5964 photometric points in V, observed between October 2007 and April 2009. (The fainter duplicate object J093012 has 5950 points covering the same time span; its data was used here as a check on the results found for J093010.) Initial values for the orbital periods of the two eclipsing binaries were found with *ah3* (Ch. 4): 19674.594±0.005 s and 112799.10±0.15 s; then a variant of *ah3* (*twoperah3*) was written to separate the two eclipsing signals. The light curve was first folded on the shorter period corresponding to the contact binary, and phase-binned to give a smooth mean curve (90 bins were used); an optimally-weighted average was then found for the data points in each bin (which corresponded closely to the visible contact binary signal). A spline curve was interpolated to these binned average points, and subtracted from the full light curve. The residue was then folded on the longer period corresponding to the detached binary, and a binned average curve obtained as before. This was again subtracted from the full light curve, to leave a clean contact binary light curve which was output as a new .fits file. This clean mean contact curve was subtracted a second time from the full data set, to leave a clean detached binary light curve for output. *ah3* was run again on the separated files, and its resulting period values were used to initialize *twoperah3* for a second iteration. This continued until convergence was reached for both periods.

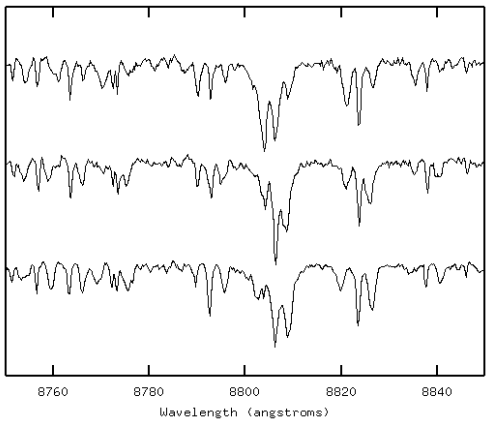

Figure 11.6: Extract of WHT spectra for J093010A at approximate phases 0.16, 0.64 and 0.75 (top to bottom). Relatively isolated absorption lines at around 8793, 8806 and 8823 Å exhibit three-way splitting, with the outer pair also shifting between phases.

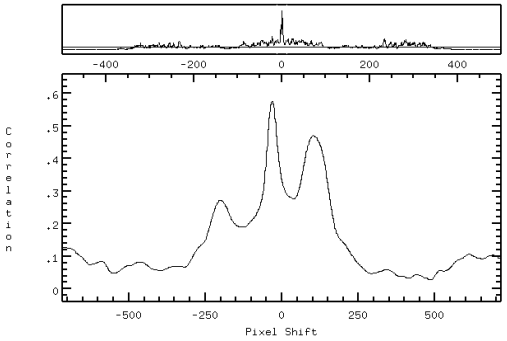

Figure 11.7: Cross-correlation plot for J093010A at phase 0.75, exhibiting three strong peaks corresponding to three stellar components (primary on the right, secondary on the left, tertiary in the middle). The broadest absorption lines were excluded from the cross-correlation to minimize the radial velocity uncertainties.

11.4 Results

The orbital periods based on SuperWASP data rapidly converged on 19674.47±0.03 s for the contact binary and 112798.90±0.16 s for the detached binary i.e. 0.2277138(3) d and 1.3055428(19) d respectively. (The periods for J093012 did not converge, but oscillated within the narrow ranges 19674.43–19674.52 and 112798.9–112800.0, which include and support the results for J093010.) These periods fall within the uncertainties of those found by Koo *et al.* from their photometry: 0.2277135(16) d and 1.30550(4) d, though their figure for the detached binary's period is based on a single measured primary eclipse time and three secondary eclipses. No period change was detected within the SuperWASP data for either binary; extrapolating forward from the most precisely-measured times of minimum for the SuperWASP data, using our periods, gives an O−C value of just −30 s for Koo *et al.*'s primary minimum for the detached system, and ∼+200 s for their primary minima for the contact system. The small size of these discrepancies further supports both

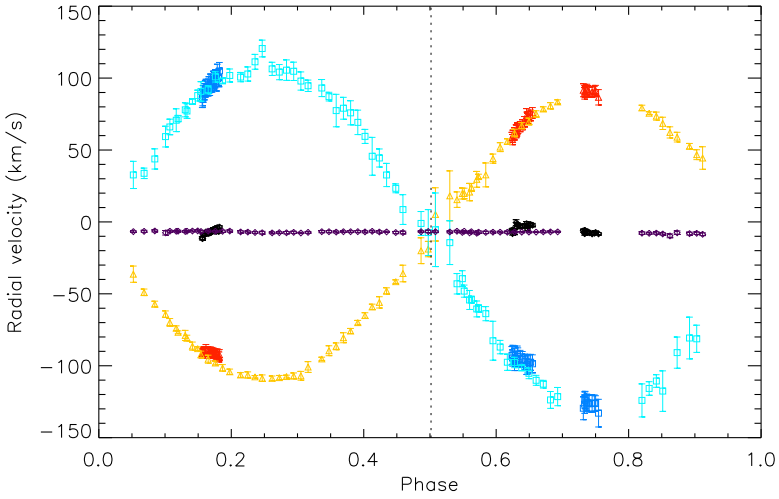

Figure 11.8: Radial velocity curves, with uncertainties, for J093010A. The primary is in yellow (data from Koo *et al.* (2014)) and red (our WHT data); the secondary in blue (pale from Koo *et al.*; dark from WHT); and the tertiary in purple (Koo *et al.*) and black (WHT). Phase-folding uses Koo *et al.*'s primary minimum time of HJD 2456346.78443 and our optimum period of 112798.9 s; the dashed vertical line indicates the mean location of Koo *et al.*'s secondary minima.

the absence of significant period change (especially in the detached system) and the reliability of our periods, calculated over long base lines using whole light curves, rather than minimum timings alone. We therefore prefer our periods for the remainder of the analysis, but use Koo *et al.*'s more precise and recent primary minimum timings to calculate phases.

Koo *et al.* measured radial velocities for J093010A by fitting three Gaussians simultaneously to five isolated absorption lines in their spectra, in the range 6400–6800 Å. Our longer wavelength range contained such a profusion of blended lines that this approach would have been impossible; indeed, it was hard to detect three-way line splitting from visual examination of the spectra over most of the range (Fig. 11.6 illustrates a small region where the triplets are relatively isolated). However, cross-correlation revealed three extremely clear correlation peaks for every spectrum (e.g. Fig. 11.7), allowing radial velocities to be measured easily for the system (Table 11.3). Fig. 11.8 shows our results,

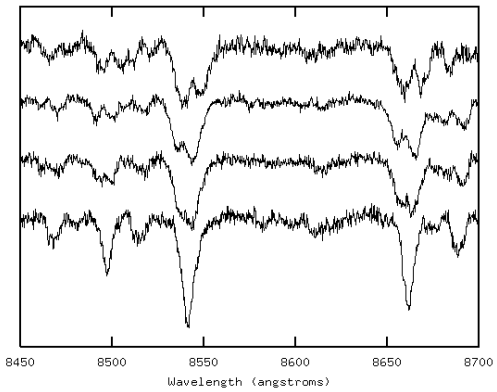

Figure 11.9: Extract of WHT spectra for J093010B at approximate phases 0.24, 0.66, 0.88 and 0.99 (top to bottom). The Ca II triplet of absorption lines at around 8498, 8542 and 8662 Å exhibit clear splitting and shifting between phases.

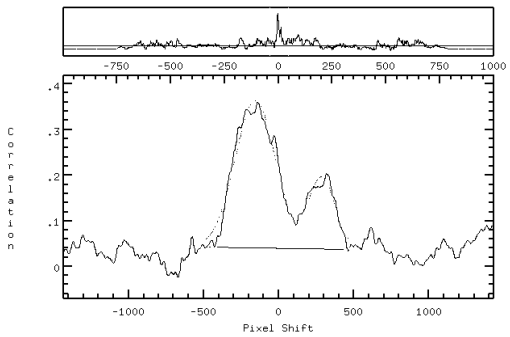

Figure 11.10: Cross-correlation plot for J093010B at phase 0.24, exhibiting two strong peaks corresponding to the binary components (primary on the left, secondary on the right). The two broadest calcium lines at 8542 and 8662 Å were excluded from the cross-correlation to minimize the uncertainty in the radial velocity measurements.

together with those of Koo *et al.*: where our observations overlap with theirs (around phases 0.15 and 0.65) there is close agreement in both the amplitudes and absolute values of the curves; we have also fortuitously been able to observe the system around its secondary maximum (phase 0.75) where Koo *et al.* had a gap.

Also notable is our confirmation of the third strong and near-static component of the detached system spectra: Koo *et al.*'s fifth star. Since we have obtained separate spectra for J093010A and J093010B, we can be certain that this additional source occurs at the same location as the detached eclipsing binary, rather than being near the contact system or mid-way between the two. There is also very good reason to regard it as part of a gravitationally-bound triple with the detached binary: its radial velocity (-6.6 ± 1.8 km s^{-1}) is visibly very close to the cross-over system velocity of the binary.

We were also able to measure radial velocities from most of the spectra for

the candidate contact system in J093010B (Table 11.3). Here, splitting and shifting of the strongest lines (primarily the Ca II triplet) was apparent from visual inspection of the spectra alone (e.g. Fig. 11.9), confirming this system as a double-lined spectroscopic binary. The results from cross-correlation (e.g. Fig. 11.10) are shown in Fig. 11.11: we have managed to capture the system around its primary maximum (phase 0.25) and on each side of its secondary maximum (near phases 0.6 and 0.9), giving usable phase coverage (though further observations around phases 0.4 and 0.75 would still be desirable). Around phase zero, the cross-correlation peaks merge too closely to allow meaningful deblending, so we have fitted some of these as single peaks to obtain a further measure of the system velocity. Their average is -12.3 ± 1.7 km s^{-1}; again, visibly close to the cross-over point of the two radial velocity curves, and to the system velocity of J093010A, strongly supporting the hypothesis that binary and triple are gravitationally bound within a quintuple system with a common motion relative to the Sun.

We can also compare the light curves obtained by Koo *et al.* with the separated SuperWASP light curves. In each case, the SuperWASP amplitudes are smaller, and the magnitudes lower, because there is an effective "third light" included containing the (maximum) contributions from the other three stars. For the contact binary (Figs. 11.12 and 11.13) the SuperWASP curve is evidently the same general shape as the BV curves: the secondary eclipses are visibly flat-bottomed with the primary minimum fractionally deeper than the secondary; the secondary maximum is also slightly lower than the primary one, though this effect is perhaps stronger in Koo *et al.*'s curves, which would support the presence of a long-term static spot on one of the components.

For the detached binary light curves in J093010A (Figs. 11.14 and 11.15), the relative depths of the two eclipses are comparable in the SuperWASP data and Koo *et al.*'s data, and together with the sharp ingresses and egresses of

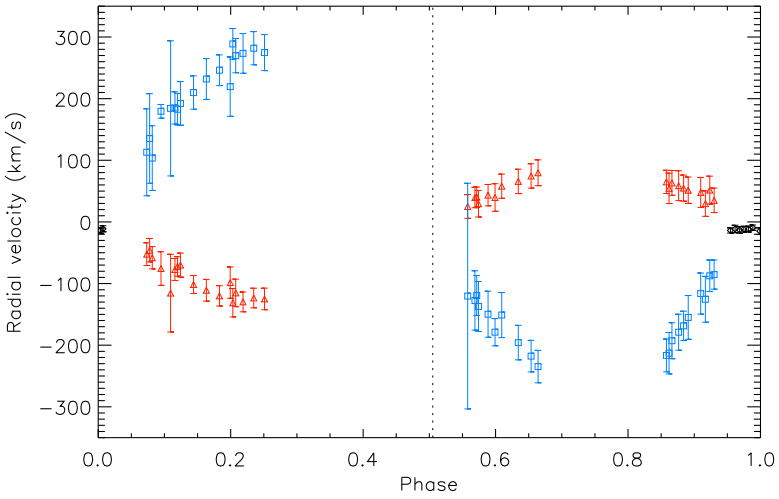

Figure 11.11: Radial velocity curves, with uncertainties, for J093010B, based on our WHT observations. The primary is in red and the secondary in blue; the points in black indicate the combined RV for both components measured near primary eclipse. Phase-folding uses the mean location of Koo *et al.*'s primary minimum times and our optimum period of 19674.47 s; the dashed vertical line indicates the mean location of Koo *et al.*'s secondary minima.

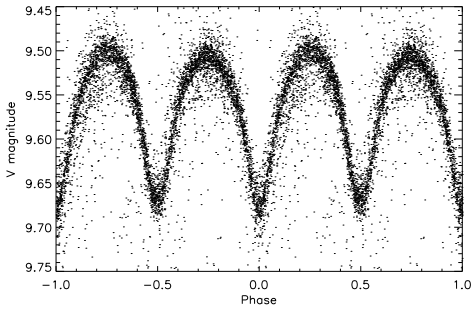

Figure 11.12: SuperWASP folded light curve for J093010B, converted to V magnitudes. The maximum magnitude is that of the quintuple system as a whole.

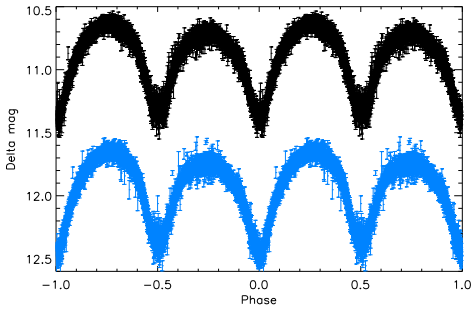

Figure 11.13: Koo *et al.* light curves for J093010B, in V (top) and B (bottom), converted from differential instrumental magnitudes to standard magnitudes using normalization indices provided in Koo *et al.* (their Table 6).

the eclipses they support a well-detached EA-type system. The primary eclipse is flat-bottomed while the secondary eclipse is not; this indicates that the secondary's radius is greater than that of the primary. However, the out-of-eclipse region would be expected to be essentially flat in such a light curve, but is not.

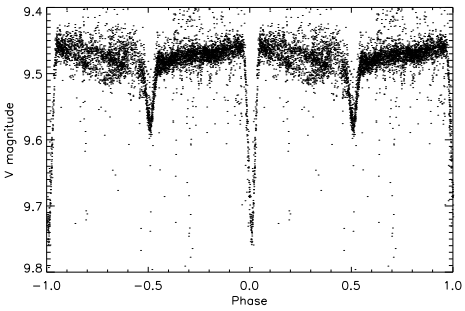

Figure 11.14: SuperWASP folded light curve for the detached binary in J093010A, converted to V magnitudes. The maximum magnitude is that of the quintuple system as a whole.

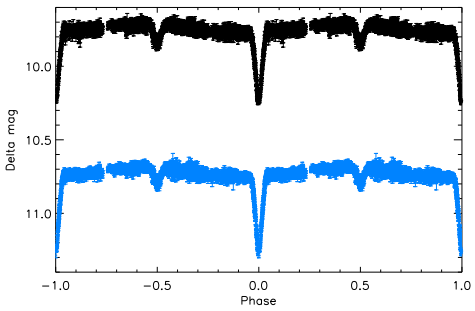

Figure 11.15: Koo *et al.* light curves for the detached binary in J093010A, in V (top) and B (bottom), converted from differential instrumental magnitudes to standard magnitudes using normalization indices provided in Koo *et al.* (their Table 6).

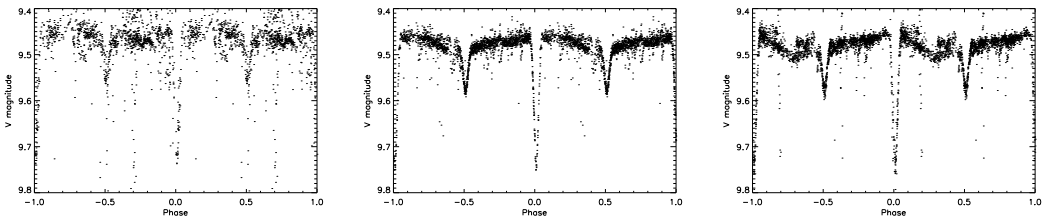

Figure 11.16: SuperWASP folded light curves for the detached binary, separated by time of observation. Left: times around HJD 2454510, with out-of-eclipse minimum around phase 0.8. Middle: times around HJD 2454820, with out-of-eclipse minimum around phase 0.4. Right: times around HJD 2454870, with out-of-eclipse minimum around phase 0.3.

In the SuperWASP curve, the region between phases 0.1 and 0.4 is far more scattered and noisy than the region between phases 0.6 and 0.9; moreover, the maximum is near the primary minimum, while it occurs just before the secondary minimum in Koo *et al.*'s curves; they suggest that this latter feature results from a moving spot on one of the components.

To explore this idea further, we split up the SuperWASP detached binary curve by time, into three sections of contiguous data covering several months. As can be seen in Fig. 11.16, the profile of the out-of-eclipse region changes over time, with its minimum apparently moving negatively in phase at a rate of

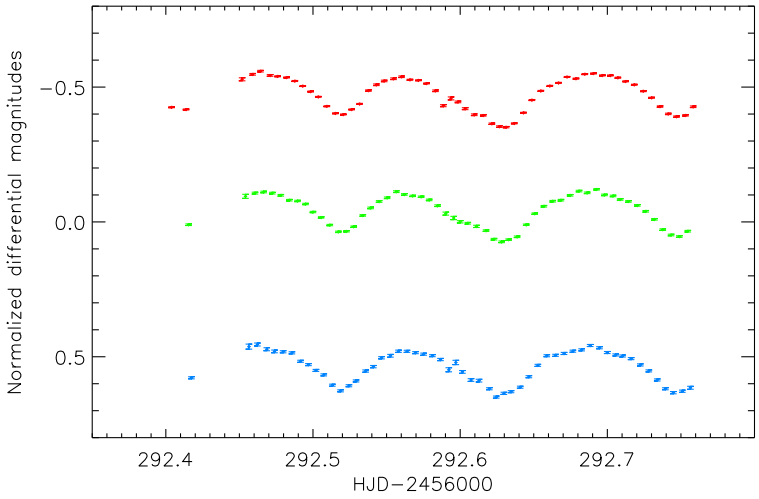

Figure 11.17: Normalized differential PIRATE light curves for J093010 in Baader R (red, top), G (green, middle) and B (blue, bottom) filters.

(very) roughly one cycle every two years. The superposition of the three fairly smooth curves produces the apparent scatter in the curve of Fig. 11.14. The most plausible explanation for this moving profile would indeed seem to be a spot on the surface of one of the detached system components, if they are not yet tidally locked but still rotating slowly on their own axes, relative to the binary rotational axis.

Finally, Fig. 11.17 shows the PIRATE RGB photometry obtained for the whole system during one night. As predicted by the SuperWASP ephemeris, contact binary primary minima occur around HJD 2456292.519 and 2456292.748, while the two eclipsing systems' secondary minima overlap in between (this is most clearly seen in the G curve, where the detached system secondary minimum occurs around HJD 2456292.60 and the contact one around HJD 2456292.63). The second night of our WHT spectra begins just as this photometry ends, and covers phases ∼0.07–0.25 of the contact system, which is entirely consistent with the light curve. Additional nights of photometry would be useful to establish the average shapes of the three-colour light curves; however, we may note that the three curves have very similar shapes. The primary eclipses are perhaps

fractionally deeper in B than R, with G intermediate i.e. the system is redder and cooler in eclipse, whenever a component hotter than the system average is hidden from view. This would suggest that the contact binary (whose components should have near equal temperatures since they share a gas envelope) is hotter than the average of J093010's five components. Similarly, Koo *et al.*'s standardized BV magnitudes for J093010A indicate that the primary eclipses are deeper in B, while the secondary eclipses are deeper in V i.e. the primary is hotter than the average for J093010A's three components, while the secondary is cooler; this suggests that the tertiary is closer in temperature to the primary than the secondary.

We can make further estimates of the relative flux contributions of the five stars from the photometry and spectroscopy. Starting with the SuperWASP light curves in SuperWASP flux units, if we assume that J093010A and J093010B's angles of inclination are close to 90° (since both systems contain flat-bottomed eclipses supporting near-totality), the depth of each component's eclipse gives a minimum value for its flux contribution (J093010A primary: 38, secondary: 15; J093010B primary: 25, secondary: 23). Adding these four fluxes and subtracting them from the total flux (160) when no component is eclipsed gives us a maximum flux estimate for the fifth component (59). These values would suggest that the tertiary makes up at most 53% of the flux in J093010A (in V), and the primary and secondary at least 34% and 13% respectively. Koo *et al.*'s V band data similarly supports contributions of around 53%, 37% and 10% respectively, using the same approach; in B the proportions are 53%, 40% and 8%. Furthermore, the SuperWASP fluxes allow us to estimate J093010B:J093010A flux contributions at the former's maximum and primary minimum as 43% and 21%. These figures can be compared with the spectroscopic fluxes, found from fits to the extracted spectra's continua, evaluated at 8500 Å and scaled to account for the different exposure lengths: near both systems' maxima (phase 0.75 of J093010A and 0.63 of J093010B) the ratio is 44%, and near contact primary minimum (around phase

0.18 of J093010A and 0.0 of J093010B) it is 24%, showing considerable similarity across optical and near-infrared observations. These consistent estimates can be used in further modelling of the five stars.

11.5 Modelling and Discussion

To determine parameters for the components of J093010, the two eclipsing binaries were modelled separately using PHOEBE (Ch. 6).

11.5.1 J093010A

The starting assumptions for J093010A, based on its light curve, were that it is a detached binary in a circular orbit viewed nearly edge-on, with $M_1 > M_2$, $T_1 > T_2$, $R_1 < R_2$, a third light contributing around half the total flux, and a spot on one component. The period was set to 1.3055428 d (from the SuperWASP data) and the starting HJD to 2456346.78443 (from Koo *et al.*'s single primary minimum timing); data was not binned or converted to phases prior to modelling. With the angle of inclination i set to 90°, the radial velocity curves were first fitted for $a \sin i$ (a proxy to the semimajor axis), mass ratio $q = M_2/M_1$, and system velocity γ_0 simultaneously, and the optimum values found were not adjusted subsequently, since light curves are largely insensitive to these parameters.

Figs. 11.18 and 11.19 show the best fits obtained for our data alone, and for the combination of our data and that of Koo *et al.*. (The fitting was also carried out for Koo *et al.*'s radial velocity curves alone, to confirm the results given in their Table 7, which was achieved within their quoted uncertainties despite some differences in modelling approach.) Very similar results were found for the individual data sets: $a \sin i$ of 5.55 $R_\odot$ and 5.60 $R_\odot$ for us and them respectively; q of 0.825 and 0.830; and γ_0 of -6.9 km s^{-1} and -10.1 km s^{-1}, supporting the plausibility of this modelling solution. The fit to the combined data sets reduced

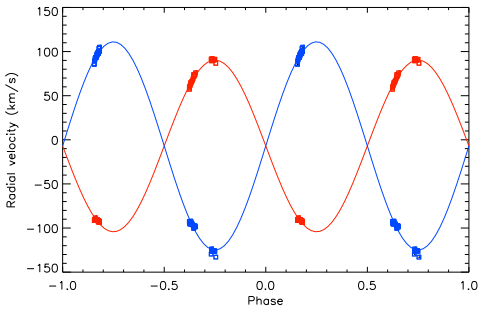

Figure 11.18: Best radial velocity curve PHOEBE fits for J093010A based on our WHT data alone. The primary curve is in red and the secondary in blue.

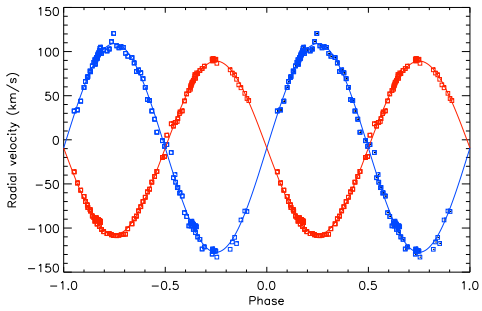

Figure 11.19: Best radial velocity curve PHOEBE fits for J093010A based on combined data from us and Koo *et al.*.

the formal uncertainties on the three parameters in comparison with each data set considered alone, and was used for the remainder of the modelling.

To model the light curves, a valid third light contribution needed to be included, more precise than the $< 53\%$ estimated above. While Koo *et al.* seem to have fitted their curves treating third light as a free parameter, we feared there might be strong correlations between this and other fitted parameters, and so sought to constrain the value of the third light independently. Since the eclipses of J093010A are total-annular, we could determine the phases of first, second, third and fourth contact ($\phi_{1,2,3,4}$) quite precisely for the primary eclipse, using Koo *et al.*'s BV photometry, and then estimate the radii using these formulae, modified from Hilditch (2001):

$$(\phi_2 - \phi_1) = (\phi_4 - \phi_3) = \frac{2R_1}{2\pi a}$$
$$(\phi_3 - \phi_1) = (\phi_4 - \phi_2) = \frac{2R_2}{2\pi a}.$$

This gave $R_1 = 0.650 \pm 0.018 \mathrm{R}_\odot$ and $R_2 = 0.808 \pm 0.018 \mathrm{R}_\odot$ (where Koo *et al.* found $R_1 = 0.757 \pm 0.008 \mathrm{R}_\odot$ and $R_2 = 0.743 \pm 0.010 \mathrm{R}_\odot$). Then, we made use of an eclipse modelling guideline from Wilson (1994): "the ratio of the depth of the

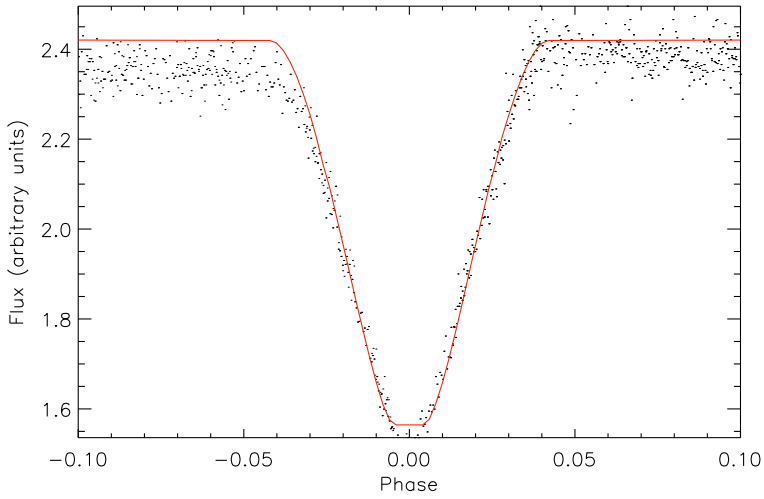

Figure 11.20: PHOEBE best fit (red) to primary eclipse of J093010A in V, showing good match to eclipse width, shape and depth (measured from right-hand side).

annular eclipse to the light remaining in the total eclipse is approximately the square of the ratio of smaller to larger star radii". We measured the depth of the annular (secondary) eclipse in V and B (in PHOEBE flux units) from the light curves, and combined this with the ratio $\frac{R_1^2}{R_2^2}$ to estimate the flux which would remain in the total (primary) eclipse, if there were no third light contribution: this would be the true contribution of the secondary star. By subtracting the primary and secondary fluxes from the maximum flux in the light curves, the tertiary's contribution could be estimated more precisely as 1.22 units in V (49%) and 0.51 in B (50%): substantially larger than the fitted values found by Koo *et al.* of 31% in V and 32% in B.

The Kopal potentials $\Omega_{1,2}$ for the two eclipsing stars were then set to values which would reproduce the radii determined above (9.445 and 6.859 respectively), indicating strongly negative filling factors, as expected for a well-detached system. These values gave excellent matches to the widths of the eclipses. The absolute temperatures of both components could not be found by fitting alone, only their ratio, so we set T_1 to 4500 K (the best-matching template temperature

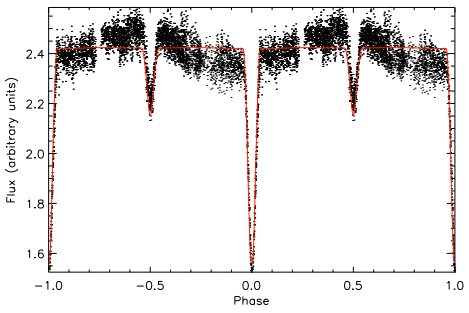

Figure 11.21: Best light curve PHOEBE fit for J093010A in V (unspotted model).

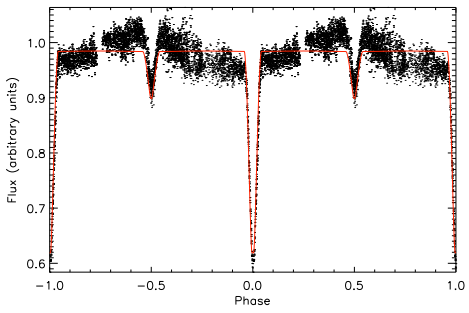

Figure 11.22: Best light curve PHOEBE fit for J093010A in B (unspotted model).

for our spectra, which would be expected to be dominated by the primary and tertiary stars' contributions), and allowed only T_2 to vary, along with i, until the eclipse depths were optimally fitted (e.g. Fig. 11.20).

The full optimal light curve fits are shown in Figs. 11.21 and 11.22. It is apparent that, while the eclipses are very well-fitted by this model, the out-of-eclipse portions are poorly fitted ($\chi^2 = 16.5$ in V, 2.53 in B). This is almost certainly due to the presence of the assumed moving spot discussed above. To test this explanation, a single large cool spot was placed on the primary and its four parameters varied manually until a fair match to the light curve was achieved (colatitude 90°, longitude 28°, radius 91° and temperature 0.982 × mean primary temperature). The resulting light curve fits are shown in Figs. 11.23 and 11.24, and an image of the model system in Fig. 11.25. These models reproduce the light variations much better ($\chi^2 = 8.83$ in V, 1.20 in B).

It should be emphasized that we do not regard this as the only possible spot configuration which would reproduce the observed light curve variations; a cool spot on the opposite side of the secondary also works passably well, and hot spots on either component would also achieve similar results. Koo *et al.* used cool spots with quite different parameters from ours on both components in their preferred model, to achieve a very close fit to the light curve; however, by

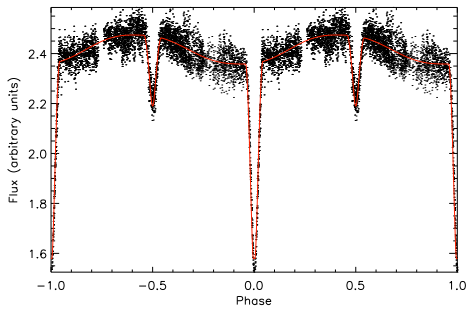

Figure 11.23: Best light curve PHOEBE fit for J093010A in V (spotted model).

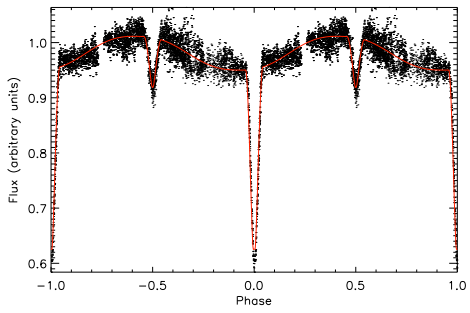

Figure 11.24: Best light curve PHOEBE fit for J093010A in B (spotted model).

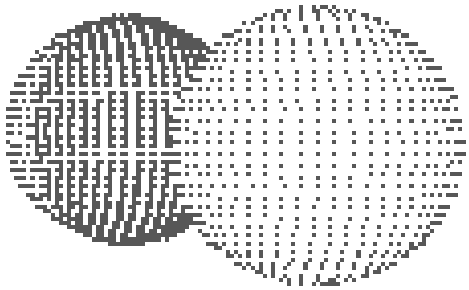

Figure 11.25: Image of best-fit PHOEBE spotted model for J093010A at phase 0.03. The large cool spot is visible over most of the face of the primary as it enters eclipse.

appropriate placement of multiple spots, any light curve features whatsoever can be reproduced, and we did not wish to include more components in our model than were justifiable. That said, it is very likely that there are multiple spots on this system, or non-circular spots, whose modelling would produce an even better fit to the light curve, but a method such as Doppler tomography would be required to determine their nature more rigorously.

Table 11.5.1 gives the final parameters determined for J093010A. The uncertainties on a, q, γ_0, i and T_2 are formal errors generated by PHOEBE and are probably underestimates; the uncertainties on T_1, $R_{1,2}$ and $\Omega_{1,2}$ were obtained from independent measurements as described above; and the uncertainties on

		Primary	Secondary
Semi-major axis ($R_\odot$)	a	5.594 ± 0.011	
Mass ratio	q	0.833 ± 0.003	
System velocity (km s^{-1})	γ_0	-9.25 ± 0.18	
Angle of incl. (°)	i	89 ± 1	
Kopal potentials	$\Omega_{1,2}$	9.4 ± 0.2	6.86 ± 0.13
Filling factor	$\mathcal{F}$	-12.8	-7.3
Masses ($M_\odot$)	$M_{1,2}$	0.754 ± 0.006	0.628 ± 0.005
Radii ($R_\odot$)	$R_{1,2}$	0.650 ± 0.018	0.809 ± 0.018
Temperatures (K)	$T_{1,2}$	4500 ± 250	3800 ± 100
Surface gravity	$\log g_{1,2}$	4.69	4.42
Bolometric luminosities	$M_{bol_{1,2}}$	6.81	7.07
Flux contribution (V)	$l/(l_1 + l_2 + l_3)$	0.34	0.17
Flux contribution (B)	$l/(l_1 + l_2 + l_3)$	0.36	0.14

Table 11.1: System and stellar component parameters for J093010A

$M_{1,2}$ were found using the formula prescribed in the PHOEBE manual:

$$\sigma_{M_1} = M_1 \left(3\frac{\sigma_a}{a} + 2\frac{\sigma_P}{P} + \frac{\sigma_q}{q+1} \right)$$
$$\sigma_{M_2} = M_2 \left(3\frac{\sigma_a}{a} + 2\frac{\sigma_P}{P} + \frac{\sigma_q}{q(q+1)} \right).$$

11.5.2 J093010B

J093010B was simpler to model. We started with the assumptions that it is a contact system (i.e. $T_1 = T_2$ =4500 K, $\Omega_1 = \Omega_2$) in a circular orbit seen nearly edge-on, with $M_1 > M_2$, $R_1 > R_2$ and no third light. The period was set to 0.2277138 d, and the starting HJD to 2456288.87879 (a well-determined nearby primary eclipse from Koo *et al.*'s photometry). We first fitted the radial velocity curves alone for $a \sin i$, q and γ_0, as for J093010A, and found the best fit shown in Fig. 11.26 ($\chi^2 = 1.92$ for the primary and 3.44 for the secondary), which gave $a \sin i = 1.74 \pm 0.03 R_\odot$, $q = 0.389 \pm 0.012$ and $\gamma_0 = -7.8 \pm 1.7$ km s^{-1}. Again, we may note that the system velocity found for J093010B is the same as that found for J093010A within its uncertainties.

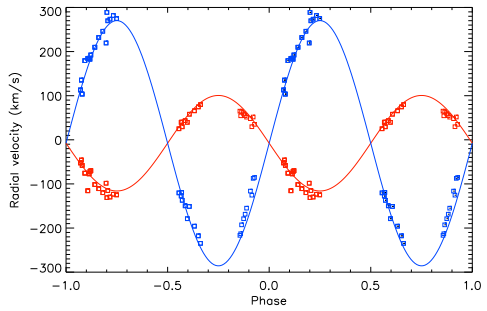

Figure 11.26: Best radial velocity curve PHOEBE fits for J093010B based on our WHT data. The primary curve is in red and the secondary in blue.

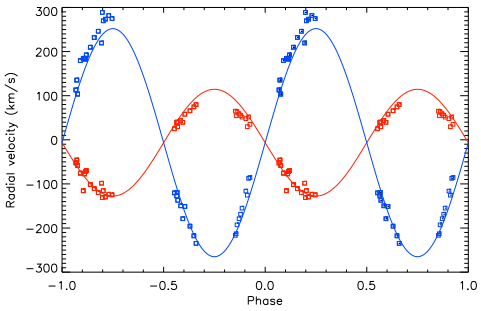

Figure 11.27: Radial velocity curve PHOEBE fits for J093010B implied by Koo *et al.*'s preferred model.

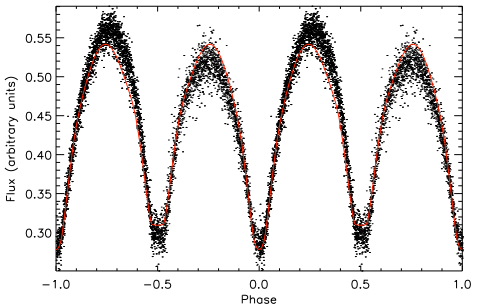

Figure 11.28: Best light curve PHOEBE fit for J093010B in V (unspotted model).

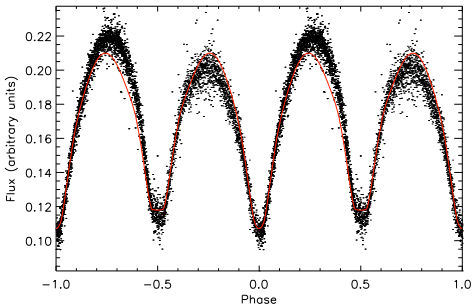

Figure 11.29: Best light curve PHOEBE fit for J093010B in B (unspotted model).

Koo *et al.* also advanced a model for J093010B based purely on its light curve, which used a value for the mass ratio of 0.468 ± 0.005 found via the "q-search" method: very far from the value found here. We reproduced their model in PHOEBE from their preferred parameters to see how well it matched the radial velocity curves (a and γ_0 were allowed to vary freely to reach optimal values given the other fixed parameters). Fig. 11.27 shows the poorer match of their model to the RV curves ($\chi^2 = 3.71$ and 4.99).

Then, using the BV light curves as well, i and Ω were allowed to reach their optima simultaneously (the continuous variation of the light curve meant that the approach taken to find J093010A's radii was impossible here). The best fits

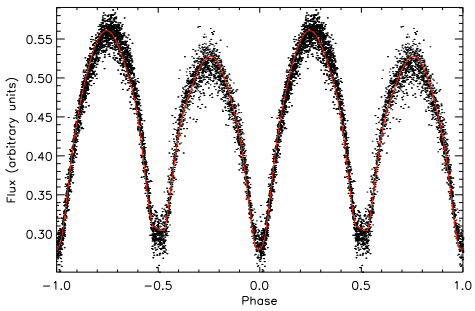

Figure 11.30: Best light curve PHOEBE fit for J093010B in V (spotted model).

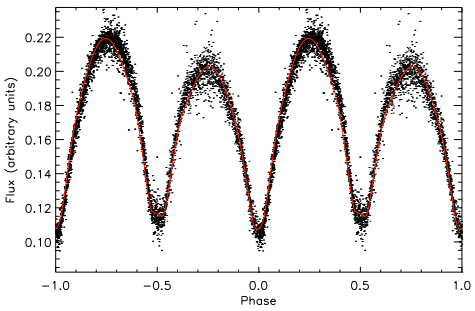

Figure 11.31: Best light curve PHOEBE fit for J093010B in B (spotted model).

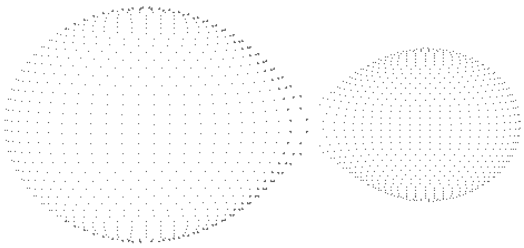

Figure 11.32: Image of best-fit PHOEBE spotted model for J093010B at phase 0.25. The large cool spot is visible at the limb of the primary.

are shown in Figs. 11.28 and 11.29. The Kopal potential corresponding to this fit indicates a filling factor of 0.19 as expected for a contact system.

Again, a better fit can be achieved if a spot is modelled, to account for the different heights of the maxima. An example spotted model is shown in Figs. 11.30 to 11.32; this uses a spot on the primary with colatitude 90°, longitude 80°, radius 100° and temperature 0.987 × mean primary temperature. As with J093010A, we emphasize that this is only one of several possible ways to model the light variations using a single spot; Koo *et al.* used a cool spot on the primary and a hot spot on the secondary instead. Our resulting parameters for the system, shown in Table 11.5.2, are not affected by the presence of the spot. The uncertainties on a, q, γ_0, i, T and $M_{1,2}$ were found as for J093010A; those for Ω and $R_{1,2}$ were found by setting a and q to their extrema in all combinations, and optimizing for Ω to find the lower and upper limits of these three parameters,

		Primary	Secondary
Semi-major axis ($R_\odot$)	a	1.74 ± 0.03	
Mass ratio	q	0.389 ± 0.012	
System velocity (km s^{-1})	γ_0	-7.8 ± 1.7	
Angle of incl. (°)	i	88 ± 2	
Kopal potential	Ω	2.61 ± 0.03	
Filling factor	$\mathcal{F}$	0.19	
Masses ($M_\odot$)	$M_{1,2}$	0.98 ± 0.06	0.38 ± 0.03
Radii ($R_\odot$)	$R_{1,2}$	$0.829^{+0.010}_{-0.005}$	$0.545^{+0.014}_{-0.009}$
Temperatures (K)	T	4500 ± 250	
Surface gravity	$\log g_{1,2}$	4.59	4.55
Bolometric luminosities	$M_{bol_{1,2}}$	6.28	7.21
Flux contribution (V)	$l/(l_1 + l_2)$	0.67	0.33
Flux contribution (B)	$l/(l_1 + l_2)$	0.64	0.36

Table 11.2: System and stellar component parameters for J093010B

consistent with an adequate fit to the data.

For both systems, distances were estimated by a similar method to that mentioned in Koo *et al.*: absolute bolometric magnitudes were outputs from PHOEBE, with uncertainties given by varying the components' temperatures within their own errors (for J093010A, the temperature ratio was kept constant, however). Absolute V magnitudes were then found using bolometric corrections as tabulated in Flower (1996), and apparent V magnitudes of the individual components determined from Koo *et al.*'s V light curves at their maxima in combination with the component light ratios obtained during analysis. The formula:

$$d = 10^{(M_{app}+5-M_{abs})/5}$$

was then used to obtain distance estimates in parsecs (extinction was ignored since it was expected to be insignificant in comparison with the uncertainties). For J093010A, $d = 45 \pm 12$ pc was found, and for J093010B, $d = 66 \pm 13$ pc; the uncertainties overlap at around 55 pc, further supporting the reality of the association between the two binaries. (Koo *et al.* found distances of 66±7 pc and 77±9 pc for J093010A and B respectively, also with overlapping uncertain-

ties though with different absolute values owing to their different models of the systems; crucially, they found higher temperatures for all components.)

11.6 Conclusion

After our initial discovery of J093010 as a probable doubly-eclipsing quadruple system, and Koo *et al.*'s follow-up observations which confirmed J093010A as a spectroscopic binary and revealed the presence of a fifth component of the system, we have carried out further spectroscopic and photometric observations of the whole system. We have confirmed J093010B as a spectroscopic binary also, and confirmed the location of the fifth component near J093010A. After modelling of both eclipsing systems we have obtained parameters for them which agree with those of Koo *et al.* in some areas, but disagree in several others, due to different modelling approaches and available data. The consistent distances and system velocities of both binaries, and of the fifth star, strongly support all five stars being gravitationally bound in a single system; their equivalent angles of inclination also suggest that both binary orbits lie in a single plane, implying probable formation from a single protostellar disk.

In future, we hope to disentangle the three spectra of J093010A and the two of J093010B (as described in e.g. Hadrava (2012)), and thus obtain better estimates of their individual effective temperatures. This will constrain the modelling further, and allow improved distance estimates for the system.

Table 11.3: Spectroscopic observations and radial velocities for J093010.

HJD	Exp. time /s	Prim. RV (A) /km s^{-1}	δ Prim. RV (A) /km s^{-1}	Sec. RV (A) /km s^{-1}	δ Sec. RV (A) /km s^{-1}	Ter. RV (A) /km s^{-1}	δ Ter. RV (A) /km s^{-1}	Prim. RV (B) /km s^{-1}	δ Prim. RV (B) /km s^{-1}	Sec. RV (B) /km s^{-1}	δ Sec. RV (B) /km s^{-1}
2456283.7679	5	91.6	4.5	-129.6	8.0	-6.2	1.1	25	19	-120	183
2456283.7704	30	89.4	4.0	-126.7	6.4	-8.1	1.2	39	16	-127	48
2456283.7710	30	90.8	4.0	-123.9	5.8	-5.8	1.0	40	16	-119	32
2456283.7716	30	90.5	4.0	-123.9	6.1	-7.8	1.1	29	21	-137	40
2456283.7749	180	92.0	3.7	-125.4	5.7	-7.0	1.1	43	17	-149	37
2456283.7773	180	91.0	3.8	-125.9	5.8	-7.0	1.1	39	22	-178	22
2456283.7796	180	90.4	3.7	-126.5	5.8	-7.5	1.1	57	19	-151	36
2456283.7853	360	90.2	3.5	-126.2	5.9	-8.3	1.1	65	19	-195	28
2456283.7897	180	90.7	3.5	-125.8	5.5	-7.8	1.1	74	19	-217	25
2456283.7921	180	91.3	3.6	-126.3	5.5	-7.4	1.2	79	20	-234	26
2456283.7979	360	86.6	5.3	-133.0	9.6	-8.3	0.8				
2456292.7661	60	58.8	3.5	-92.9	6.2	-6.0	1.1	-52	18	112	70
2456292.7671	60	57.2	3.6	-94.6	5.6	-8.1	1.2	-45	18	135	72
2456292.7680	60	60.3	3.5	-92.3	6.5	-5.4	0.9	-58	18	103	52
2456292.7710	10	61.2	4.2	-95.6	7.8	-7.2	1.7	-75	27	179	11
2456292.7743	10	63.0	4.5	-95.2	5.3	-0.5	2.0	-115	63	184	109
2456292.7758	60	63.5	3.7	-95.4	5.4	-3.6	1.0	-77	17	184	26
2456292.7767	60	65.0	3.9	-92.2	5.9	-1.5	1.0	-72	15	182	25
2456292.7777	60	64.9	3.5	-93.6	6.0	-2.2	1.0	-70	19	192	35
2456292.7822	360	66.2	3.5	-94.8	5.5	-3.0	1.0	-101	14	209	27
2456292.7866	360	67.5	3.5	-95.7	5.6	-3.1	1.1	-110	17	231	33
2456292.7911	360	69.7	3.6	-97.3	5.4	-2.5	1.1	-119	16	246	24
2456292.7948	60	74.0	4.8	-100.5	5.6	-1.2	1.5	-98	25	219	48

Table 11.3: (continued)

HJD	Exp. time /s	Prim. RV (A) /km s^{-1}	δ Prim. RV (A) /km s^{-1}	Sec. RV (A) /km s^{-1}	δ Sec. RV (A) /km s^{-1}	Ter. RV (A) /km s^{-1}	δ Ter. RV (A) /km s^{-1}	Prim. RV (B) /km s^{-1}	δ Prim. RV (B) /km s^{-1}	Sec. RV (B) /km s^{-1}	δ Sec. RV (B) /km s^{-1}
2456292.7957	60	72.3	4.1	-99.3	6.8	-2.7	1.5	-131	22	288	24
2456292.7967	60	71.9	3.6	-99.1	6.0	-4.9	1.1	-115	22	269	27
2456292.7992	300	73.2	3.4	-97.8	5.6	-2.4	1.1	-129	16	273	32
2456292.8029	300	74.0	3.7	-97.6	5.6	-1.8	1.1	-123	15	281	26
2456292.8066	300	75.9	3.6	-98.7	6.2	-2.2	1.2	-124	17	274	29
2456294.7665	60	-91.5	3.2	85.5	6.0	-11.3	1.1	64	18	-216	26
2456294.7674	60	-91.3	3.0	86.3	5.6	-11.5	1.1	54	24	-212	33
2456294.7684	60	-90.0	2.9	89.0	5.8	-8.9	1.1	63	20	-192	29
2456294.7707	120	-90.2	3.2	90.5	5.7	-8.8	1.0	58	24	-178	29
2456294.7724	120	-89.9	3.1	92.4	5.6	-8.4	0.9	54	21	-168	23
2456294.7740	120	-88.5	3.3	93.3	5.8	-6.9	0.9	51	21	-154	35
2456294.7783	110	-91.5	3.3	93.5	5.8	-8.0	1.0	47	24	-116	33
2456294.7799	110	-90.3	3.3	95.3	5.6	-6.8	1.0	29	20	-125	37
2456294.7814	110	-91.4	3.4	93.5	5.6	-7.7	1.0	51	22	-87	25
2456294.7829	110	-90.3	3.4	97.1	5.7	-6.2	0.9	35	19	-85	23
2456294.7845	110	-90.8	3.3	95.8	5.5	-7.2	1.0				
2456294.7860	110	-90.7	3.4	96.5	6.0	-6.2	0.9				
2456294.7885	110	-91.0	3.3	98.7	6.1	-5.1	1.0	-13.8[1]	4.3		
2456294.7901	110	-91.5	3.4	97.7	6.0	-6.1	1.1	-11.4	6.1		
2456294.7916	110	-92.9	3.4	99.1	5.9	-6.4	1.1	-13.0	5.3		
2456294.7931	110	-91.7	3.3	100.0	6.0	-4.7	1.0	-11.7	4.7		
2456294.7947	110	-93.4	3.5	97.7	6.7	-6.5	1.1	-11.6	4.7		

[1]This and subsequent radial velocities for J093010B are joint measurements for both spectral components combined, near phase 0.

Table 11.3: (continued)

HJD	Exp. time /s	Prim. RV (A) /km s^{-1}	δ Prim. RV (A) /km s^{-1}	Sec. RV (A) /km s^{-1}	δ Sec. RV (A) /km s^{-1}	Ter. RV (A) /km s^{-1}	δ Ter. RV (A) /km s^{-1}	Prim. RV (B) /km s^{-1}	δ Prim. RV (B) /km s^{-1}	Sec. RV (B) /km s^{-1}	δ Sec. RV (B) /km s^{-1}
2456294.7962	110	-91.7	3.5	103.6	6.0	-3.9	1.0	-9.3	4.4		
2456294.7986	60	-93.2	3.3	100.5	5.6	-6.5	1.0	-14.9	5.6		
2456294.7996	60	-93.9	3.5	100.1	6.2	-6.4	1.0	-14.0	4.5		
2456294.8005	60	-92.4	3.7	105.0	5.9	-3.5	0.9	-11.1	4.9		

Chapter 12

Circumbinary planets in post-common-envelope binaries?

After our investigation of very short-period contact binary candidates, and follow-up of individual interesting systems discovered in the course of the research, we applied the latest version of our period change detection techniques to a different subgroup of SuperWASP eclipsing binaries. This chapter is an extended version of Lohr *et al.* (2014b), including some background details cut for reasons of length at the referee's recommendation.

12.1 Introduction

Since the discovery of planetary-mass objects around the millisecond pulsar PSR B1257+12 (Wolszczan and Frail, 1992), exoplanets have been detected in a range of surprising environments. Numerous hot Jupiters present a challenge to planetary system formation models (e.g. Mayor and Queloz (1995)); planets have been found orbiting single members of binary and higher-order multiple star systems (e.g. Butler *et al.* (1997); Anglada-Escudé *et al.* (2012)); and recently a number of circumbinary planets have been observed (e.g. Doyle *et al.* (2011)). In

the last few years, claims of planets in post-common-envelope binaries (PCEBs) have proved especially controversial, and here we aim to add to the evidence needed to evaluate models for such systems, using archival survey data.

A notable class of binary star systems have passed through a phase of common envelope evolution. As originally outlined by Paczyński (1976), after an initially more massive component evolves off the main sequence and becomes a giant, it may overflow its Roche lobe and transfer mass to its companion on a dynamic timescale. If the companion then overflows its own Roche lobe, a short-lived non-corotating common envelope can surround the secondary and the core of the primary, creating a frictional drag force upon them. Orbital energy will be transferred from the binary components to the envelope as they spiral in towards each other, undergoing a dramatic reduction in orbital separation and period, and eventually the envelope will become unbound and be ejected from the system.

The details of the process and its various possible outcomes, including binary merger, are not yet fully understood (for a recent review see Ivanova *et al.* (2013)). However, one observed outcome is the formation of a PCEB consisting of a hot subdwarf B (sdB) or OB stellar core (Heber, 2009) and a low-mass main sequence star or brown dwarf companion, in a close but detached orbital configuration. The primaries of these sdB+dM systems would have overflowed their Roche lobes near the tip of the red giant branch and undergone a helium (He) core-flash; they typically have He core masses around 0.45–0.5 $M_{\odot}$. Other related types of PCEB contain white dwarf (WD) primaries, which may be the evolved remnants of sdB stars; lower-mass He WDs which were never able to burn He; or carbon/oxygen WDs resulting from Roche-lobe overflow on the asymptotic giant branch. The last type would be expected to be more massive.

Eclipsing PCEBs of these types are especially valuable for understanding common envelope evolution and subsequent system behaviours, since their parameters can be determined with high precision. Their photometric light curves are

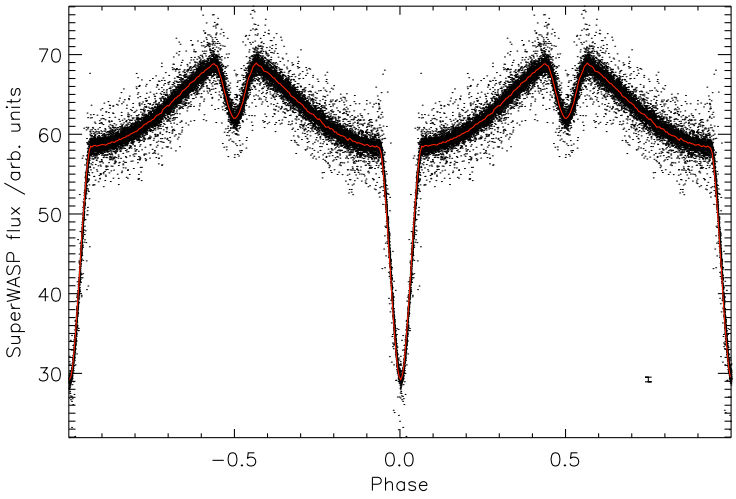

Figure 12.1: SuperWASP light curve for HW Vir, the prototype eclipsing sdB binary, phase-folded at period 10084.5643±0.0006 s, with binned mean curve overplotted in red. A typical point's uncertainty is shown (bottom right); the pseudo-V magnitude at quadrature is 10.52.

also highly distinctive, often exhibiting well-defined very deep primary eclipses and strong reflection effects (e.g. Fig. 12.1). Together with their short orbital periods (usually a few hours), these features facilitate accurate measurement of timings of minimum light, and thereby the construction of O−C diagrams to reveal any changes in orbital period over time. Zorotovic and Schreiber (2013) compiled a list of currently known eclipsing PCEBs, including 13 with an sdB primary and 43 with a WD primary, and noted that for five sdB systems and four WD systems apparent period changes had been observed: a surprisingly high proportion of those which have been well-studied over long time bases.

Many researchers have seen these period changes as evidence for the presence of additional massive bodies in the system: circumbinary giant planets[1] or brown dwarfs e.g. Lee *et al.* (2009); Beuermann *et al.* (2010). Such objects would be expected to create a light time effect (LITE), delaying or advancing the observed time of mid-eclipse of the binary components by gravitational attraction. This

[1]Planets might also in principle be detected through sinusoidal variations of an sdB star's pulsation period, as suggested for isolated pulsator V391 Peg (Silvotti *et al.*, 2007)

LITE will create a sinusoidal variation in the system's O−C diagram (in the case of a single additional mass in the binary's orbital plane), with a period corresponding to the third body's orbital period around the binary (P_3). For the simplest case of an edge-on circular orbit, Pribulla *et al.* (2012) give a formula relating the peak-to-peak amplitude of this sinusoidal variation ΔT to the three masses involved ($M_{1,2,3}$), P_3, the speed of light c and the universal gravitational constant G:

$$\Delta T \approx \frac{2M_3 G^{1/3}}{c} \left[\frac{P_3}{2\pi(M_1 + M_2)}\right]^{2/3}. \tag{12.1}$$

Roughly sinusoidal variations in light curve amplitude would also be expected if a circumbinary planet's orbit is not coplanar with the eclipsing binary's orbit, causing nodal precession of the binary (Söderhjelm, 1975). (Zasche and Wolf (2013) describe a relatively dramatic example of this phenomenon, which would usually only be detectable over many decades of observations.)

The reality of such PCEB planets is, as noted before, somewhat controversial. Where multiple circumbinary planets have been proposed in a single system, the long-term dynamical stability of their orbits has often been questioned e.g. Horner *et al.* (2013); Wittenmyer *et al.* (2013), though the dynamical stability analyses used have also been criticized on methodological grounds (Marsh *et al.*, 2014). Zorotovic and Schreiber (2013) carried out binary population syntheses which suggested that giant planets should be rare in the progenitors of PCEBs, leaving secondary planet formation (Völschow *et al.*, 2014) or a non-planetary cause such as the Applegate mechanism as the most likely explanations for the observed period changes.

Distinguishing between different proposed architectures for circumbinary planetary systems, and indeed determining whether planets are plausible in PCEBs at all, relies largely upon the quality of the eclipse timing observations: ideally, we would have a large number of precise measurements of light curve minima,

evenly covering a long time-base. In practice, many systems for which period changes indicative of circumbinary planets have been claimed, fall far short of this ideal. Therefore, here we search the archive of the SuperWASP project for evidence of period changes in those PCEBs from Zorotovic and Schreiber's Table 1 which have been observed by SuperWASP. The archive contains high-cadence photometric light curves for bright sources over almost the whole sky, stretching back to 2004 in many cases, and so should be capable of filling in gaps or extending the coverage of O−C diagrams for many of these systems. We have previously observed and measured period changes in short-period main sequence eclipsing binary candidates using SuperWASP data (Lohr *et al.*, 2012, 2013b); here, we develop our analytical method to improve the precision and robustness of its period change measurements, and to search for variations in light curve amplitude as well. It is hoped that the results may shed light on future investigations of this intriguing group of eclipsing binary systems.

12.2 Method

The SuperWASP archive was first searched for objects within 1 arcmin of the coordinates of known bright eclipsing PCEB systems. Matching light curves were downloaded, and checked visually for evidence of the expected variability. In marginal cases, and where sources neighbouring each other on the sky exhibited a similar pattern of variability, the IDL code *ah3* (Ch. 4) was used to determine objectively whether the eclipsing signal was detectable in the data, or to select the source with the strongest signal amongst near neighbours. Once the set of usable SuperWASP eclipsing PCEBs had been established, their Sys-Rem-corrected fluxes, from a 3.5 pixel-radius aperture, formed the basis of further analysis.

The code *ah3* was then used to determine optimum orbital periods for the

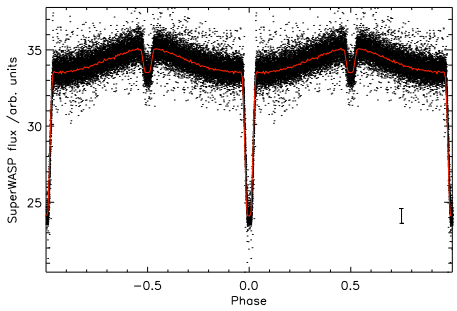

Figure 12.2: Light curve for AA Dor phase-folded at period 22597.030±0.003 s (pseudo-V magnitude at quadrature is 11.17). (For further figure explanations, see caption to Fig. 12.1.)

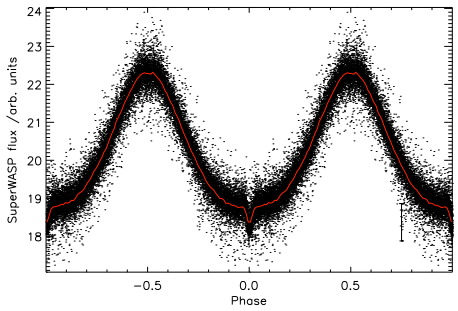

Figure 12.3: Light curve for ASAS 10232 phase-folded at period 12032.8839±0.0009 s (pseudo-V magnitude at quadrature is 11.76).

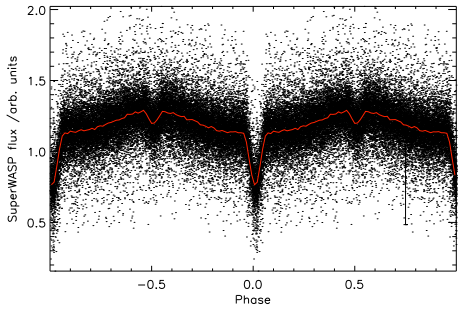

Figure 12.4: Light curve for EC 10246−2707 phase-folded at period 10239.0898±0.0003 s (pseudo-V magnitude at quadrature is 14.81).

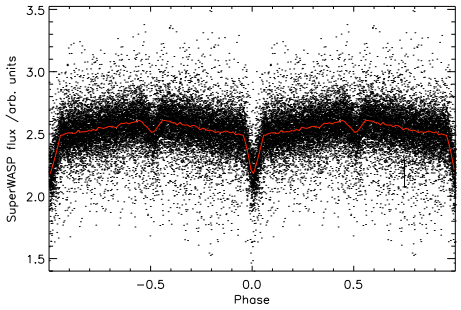

Figure 12.5: Light curve for HS 2231+2441 phase-folded at period 9554.789±0.002 s (pseudo-V magnitude at quadrature is 13.99).

eclipsing binaries (Ch. 4) and search for evidence of period change (Ch. 5). Statistical tests were also run to check the probability of finding such evidence by chance, and to assess the sensitivity of the method to genuine period changes of varying magnitudes (Ch. 6).

12.3 Results

Of Zorotovic and Schreiber's collected eclipsing PCEBs, twelve were bright enough to have usable observations in the SuperWASP archive, of which nine were

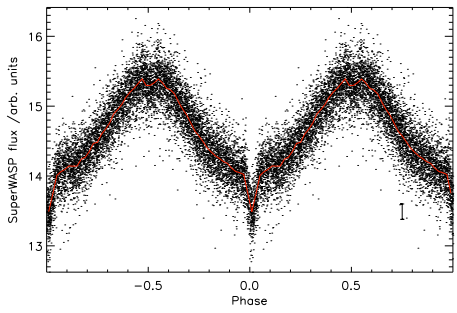

Figure 12.6: Light curve for 2M 1938+4603 phase-folded at period 10866.1147±0.0017 s (pseudo-V magnitude at quadrature is 12.09).

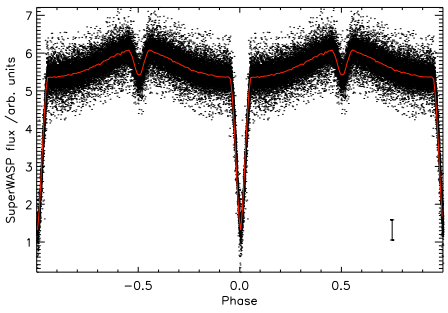

Figure 12.7: Light curve for NSVS 07826147 phase-folded at period 13976.9668±0.0004 s (pseudo-V magnitude at quadrature is 13.13).

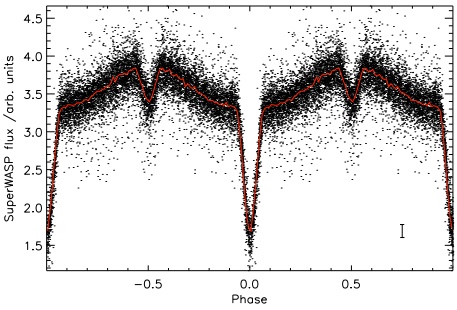

Figure 12.8: Light curve for NSVS 14256825 phase-folded at period 9536.3263±0.0005 s (pseudo-V magnitude at quadrature is 13.63).

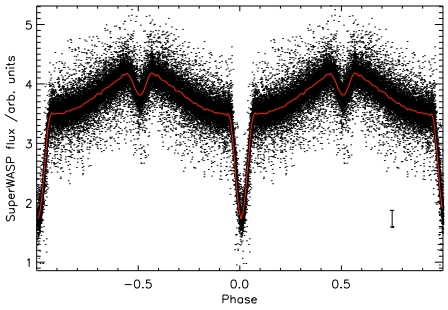

Figure 12.9: Light curve for NY Vir phase-folded at period 8727.7761±0.0007 s (pseudo-V magnitude at quadrature is 13.57).

HW Vir-type systems (sdB or sdOB primary with an M dwarf or brown dwarf companion), and three contained a WD with a low-mass main sequence companion (Table 12.5). In the case of QS Vir, two nearby sources fell within the SuperWASP aperture, resulting in a pair of very similar archive light curves containing the eclipsing signal of the same system. One curve was slightly brighter and had a larger amplitude, and was selected for further analysis here.

Orbital periods were determined for the twelve objects accurate to between 7 and 9 significant figures (see Table 12.5, which also gives the date ranges during which they were observed by SuperWASP). Their light curves, phase-

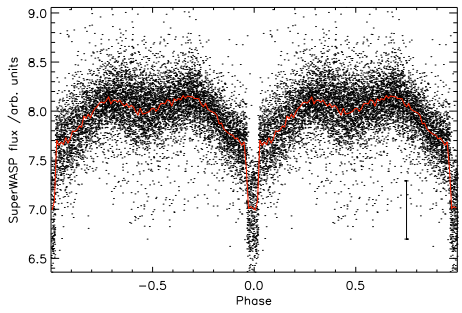

Figure 12.10: Light curve for DE CVn phase-folded at period 31461.639±0.008 s (pseudo-V magnitude at quadrature is 12.73).

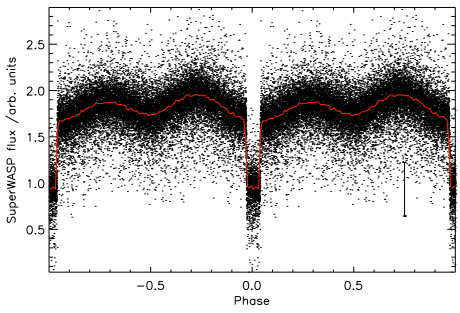

Figure 12.11: Light curve for QS Vir phase-folded at period 13025.4555±0.0008 s (pseudo-V magnitude at quadrature is 14.30).

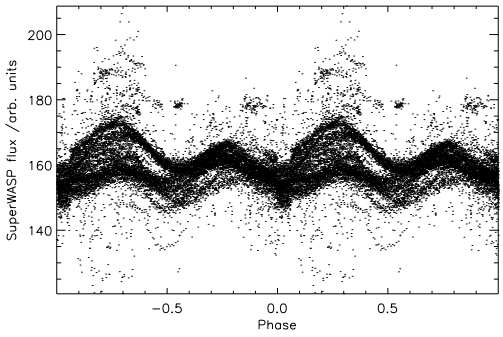

Figure 12.12: Light curve for V471 Tau phase-folded at period 45030.05±0.04 s (pseudo-V magnitude at quadrature is 9.46). The curve amplitude and shape are evidently highly variable on a fairly short timescale.

folded using these periods, are shown in Figs. 12.1 and 12.2–12.12. All exhibit a strong reflection effect; in ASAS 10232 (Fig. 12.3) and 2M 1938+4603 (Fig. 12.6) this dominates the light curve shape. The other systems all show deep, well-defined primary eclipses, which are flat-bottomed in the cases of the WD systems (Figs. 12.10–12.12) and AA Dor (Fig. 12.2). V471 Tau (Fig. 12.12) exhibited extreme short-term variability in light curve shape and amplitude, which prevented further analysis of possible period changes since no typical template curve could be determined for it. It therefore plays no further part in this study, though an individual customized analysis of its SuperWASP archive data might yield useful results in future.

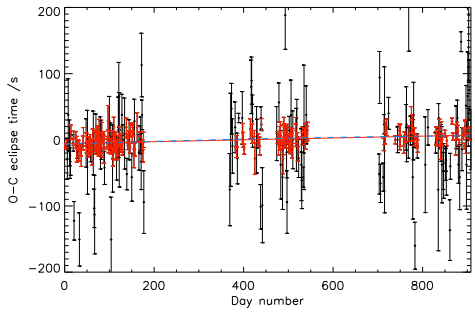

Figure 12.13: SuperWASP-only O−C diagram for AA Dor; no period change is indicated. (For further figure explanations, see caption to Fig. 5.5.)

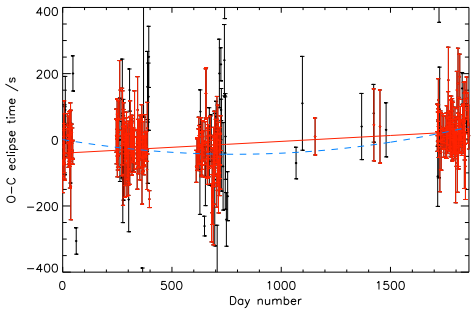

Figure 12.14: SuperWASP-only O−C diagram for ASAS 10232; the preferred quadratic fit indicates period increase of 0.0073±0.0012 s yr^{-1}, significant at p=0.02.

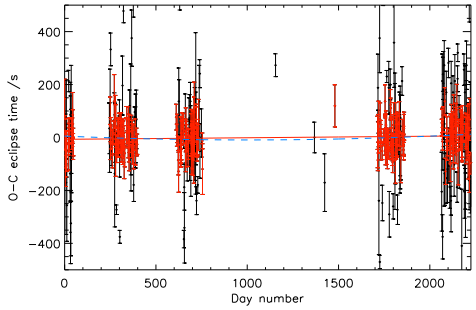

Figure 12.15: SuperWASP-only O−C diagram for EC 10246−2707; non-significant period increase is marginally preferred (p=0.36).

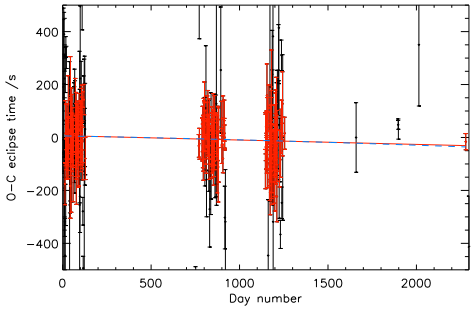

Figure 12.16: SuperWASP-only O−C diagram for HS 2231+2441; no period change is indicated.

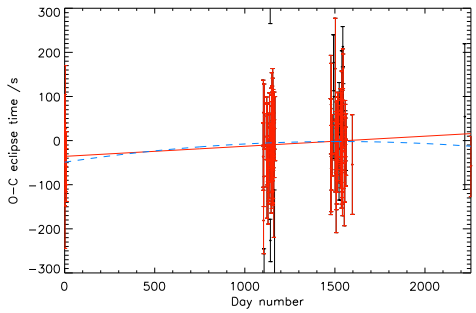

Figure 12.17: SuperWASP-only O−C diagram for 2M 1938+4603; no period change is indicated.

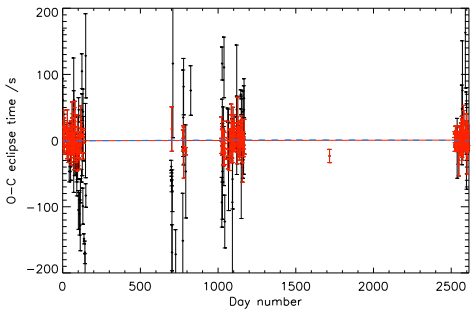

Figure 12.18: SuperWASP-only O−C diagram for NSVS 07826147; no period change is indicated.

The remaining eleven objects were searched for evidence of period change, and their O−C diagrams are given in Figs. 5.5 and 12.13–12.22. In six cases,

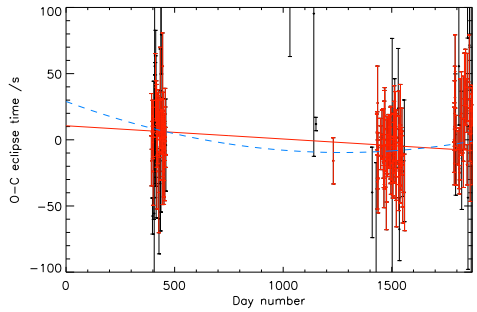

Figure 12.19: SuperWASP-only O−C diagram for NSVS 14256825; the preferred quadratic fit supports non-significant (p=0.28) period increase of 0.0019±0.0008 s yr^{-1}.

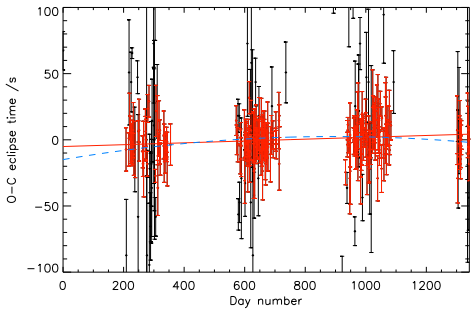

Figure 12.20: SuperWASP-only O−C diagram for NY Vir; the preferred quadratic fit indicates marginally significant (p=0.06) period decrease of −0.0016±0.0006 s yr^{-1}.

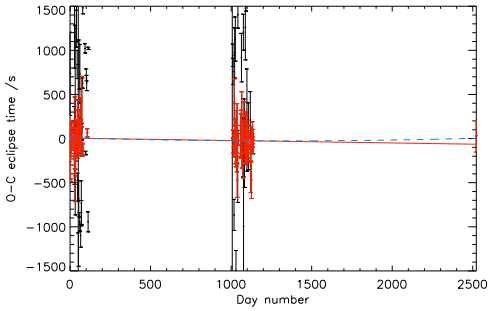

Figure 12.21: SuperWASP-only O−C diagram for DE CVn; no period change is indicated.

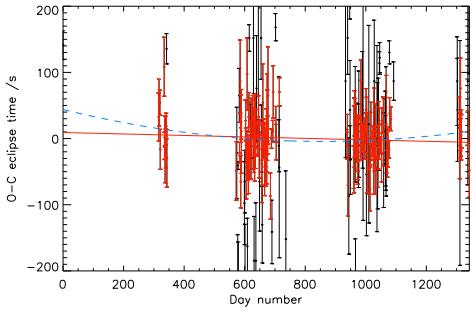

Figure 12.22: SuperWASP-only O−C diagram for QS Vir; the preferred quadratic fit supports non-significant (p=0.22) period increase of −0.007±0.003 s yr^{-1}.

the best fit to the data following outlier removal was quadratic (ASAS 10232, EC 10246−2707, HW Vir, NSVS 14256825, NY Vir and QS Vir), so the significance of the period change implied was tested for these objects. HW Vir (Fig. 5.5) exhibited highly significant period increase over the observed time base (p-value of 0.002 i.e. 0.2% of "background" tests provided equally strong or stronger evidence for period change, purely by chance). ASAS 10232 (Fig. 12.14) and NY Vir (Fig. 12.20) showed very plausible evidence for period change (p-values of 0.02 and 0.06 respectively). Even considering that eleven trials were

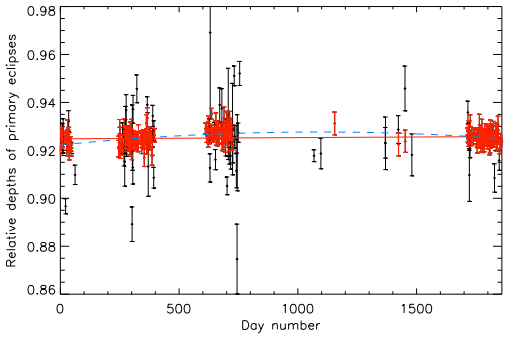

Figure 12.23: Amplitude-time diagram for ASAS 10232; excluded data points are in black and included ones in red (online only). A quadratic fit to the data (blue dashed line) appears somewhat superior to a linear fit (red solid line), and may indicate some long-term variation in light curve amplitude.

run, we would expect to find three or more results with $p \leq 0.06$ by accident only $\sim$2.5% of the time. QS Vir (Fig. 12.22), NSVS 14256825 (Fig. 12.19) and EC 10246−2707 (Fig. 12.15) provided increasingly weak and non-significant support for period change (p-values of 0.22, 0.28 and 0.36 respectively); however, we note that the direction and approximate magnitude of the changes suggested for QS Vir and NSVS 14256825 accord with the findings of other researchers (see Subsects. 12.4.11 and 12.4.8 below). The other five objects did not show evidence of period change over the time bases considered.

The first of these reference minima, converted to heliocentric Julian date (HJD-UTC), is given for each object in the final column of Table 12.5; in combination with the given periods, this provides SuperWASP linear ephemerides.

The full set of SuperWASP light curves had widely-varying sensitivities to genuine change: for DE CVn changes of up to 0.03 s yr^{-1} would not have been detectable, while for NSVS 07826147, any changes would have to be slower than 0.0003 s yr^{-1} to be missed. Table 12.5 gives the measured period changes ($\dot{P}$) and the limits of expected period change detectability ($\dot{P}$ limit).

No clear evidence of change in light curve amplitudes was observed, though there was a possible suggestion of curvature in ASAS 10232's amplitude-time

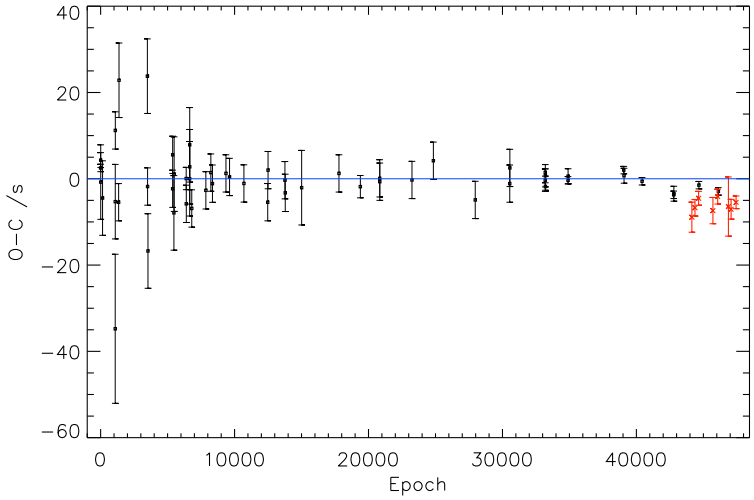

Figure 12.24: O−C diagram for AA Dor according to ephemeris of Kilkenny (2011), with points in black from previously published eclipse timings. Points in red are from new SuperWASP timings, binned on a seasonal basis.

diagram (Fig. 12.23), which might repay further investigation.

12.4 Discussion

For easier comparison with others' findings, previously-published eclipse timings were collected for each object, and converted to barycentric Julian date (BJD-TDB) where necessary[2]. O−C diagrams were then compiled relative to a recent or widely-used ephemeris, and the new SuperWASP values (also converted to BJD-TDB) were included after binning to improve the clarity of the trends they indicate. Objects are discussed individually.

12.4.1 AA Dor

AA Dor was discovered, identified as an eclipsing sdB binary, and given an initial solution in a series of papers by Kilkenny *et al.* (1978, 1979, 1981), and eclipse timings have been published for it covering the period 1977–2010 (Kilkenny,

[2]http://astroutils.astronomy.ohio-state.edu/time/hjd2bjd.html (see also Eastman *et al.* (2010)).

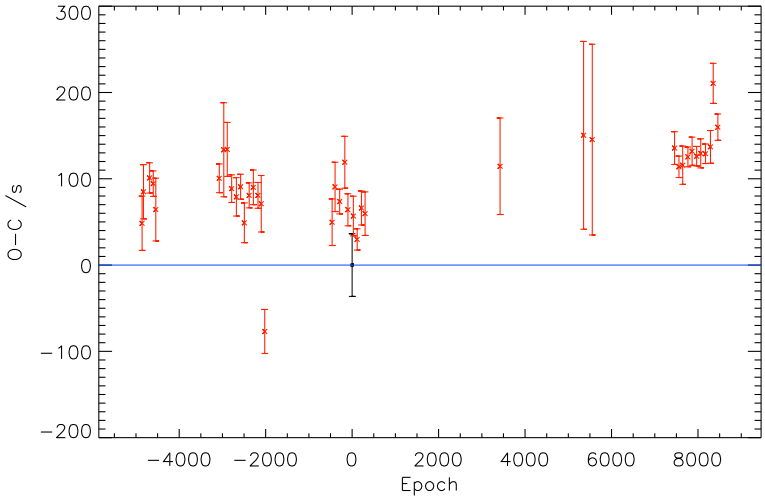

Figure 12.25: O−C diagram for ASAS 10232 according to ephemeris of Schaffenroth *et al.* (2013) combined with period found here. Black square indicates single previously published eclipse time from Schaffenroth *et al.*. Points in red are from new SuperWASP timings, binned on a fortnightly basis.

1986; Kilkenny *et al.*, 1991, 2000; Kilkenny, 2011). The ephemeris used here is from Kilkenny (2011):

$$\text{BJD} \quad 2443196.34925 + 0.2615397362E. \tag{12.2}$$

They conclude that a linear ephemeris is sufficient to explain the observations to date, and the addition of our partially-overlapping timings, extending coverage to March 2011 (Fig. 12.24), does not contradict this. They suggest that any change greater than about 3×10^{-7} s yr^{-1} would be ruled out. AA Dor is notable within the set of objects because, as Zorotovic and Schreiber point out, 'it is so far the only PCEB with continuous high-precision eclipse time measurements that does not show any signs of apparent period variations'.

12.4.2 ASAS 10232

The discovery paper for ASAS 10232 as an eclipsing sdB binary is Schaffenroth *et al.* (2013), which also provides an orbital solution, but only a single time of

minimum obtained from Carnes Hill Observatory BVI light curves from March 2008: HJD 2454538.99689±0.00042 (or possibly 0.000042). They determine a period from the first three years of SuperWASP archived observations, covering May 2006–January 2009; since our data points used here form a superset of their data, extending coverage to June 2011, we prefer our period (Table 12.5) with their cycle zero to form the ephemeris:

$$\text{BJD} \quad 2454538.99765 + 0.139269490E. \tag{12.3}$$

Schaffenroth *et al.* also measured individual eclipse times from their SuperWASP data, by a similar method to that used here (fitting a mean light curve to night-by-night data), to produce an O−C diagram (their Fig. 7), to which they fit a downward-opening parabola. On the basis of this they suggest a possible period decrease in the system, but note that it requires more observations to confirm. The fitting method used here is able to benefit from a longer time-base and hence a better-defined mean light curve; thus we have apparently been able to measure the times of eclipse more precisely from the same source of data. Although their point uncertainties are not shown, the majority of their O−C values seem to fall within ∼400 s of the fitted curve; ours (Fig. 12.14) fall mostly within ∼100 s of the preferred quadratic fit. After binning every two weeks' O−C values together (Fig. 12.25) the trend is even more clearly indicated: over six years, the system appears to be increasing, rather than decreasing in period. Of course, the variation may be more complex e.g. sinusoidal, on a still longer timescale, and further independent observations are needed to help clarify the behaviour of this system.

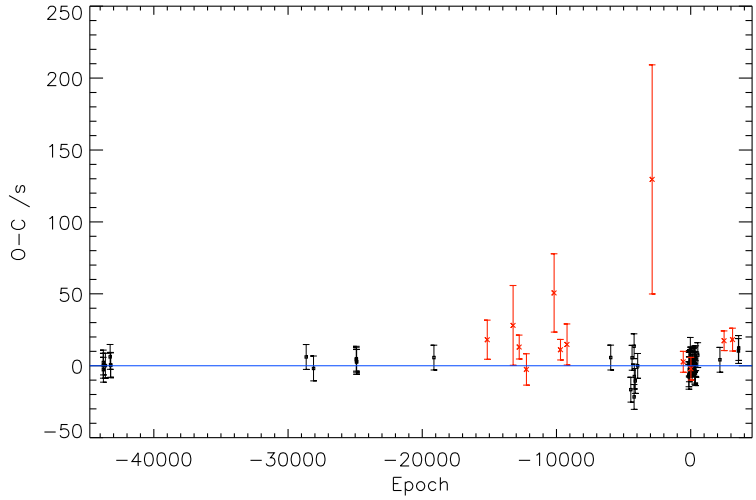

Figure 12.26: O−C diagram for EC 10246−2707 according to ephemeris of Barlow *et al.* (2013) and with their eclipse timings in black. Points in red are from new SuperWASP timings, binned on a seasonal basis.

12.4.3 EC 10246−2707

Although previously known to contain an sdB star, EC 10246−2707 was not described as an eclipsing binary until Barlow *et al.* (2013), which also estimates the system parameters and provides eclipse timings between February 1997 and June 2012. We use their ephemeris:

$$\text{BJD} \quad 2455680.562160 + 0.1185079936E. \tag{12.4}$$

They find no evidence for period change on the basis of their data, and determine a limit on detectability of change of 0.0003 s yr^{-1}. Our results here support this non-detection of change, and help to fill a gap in their coverage of the system's behaviour during 2006–2008.

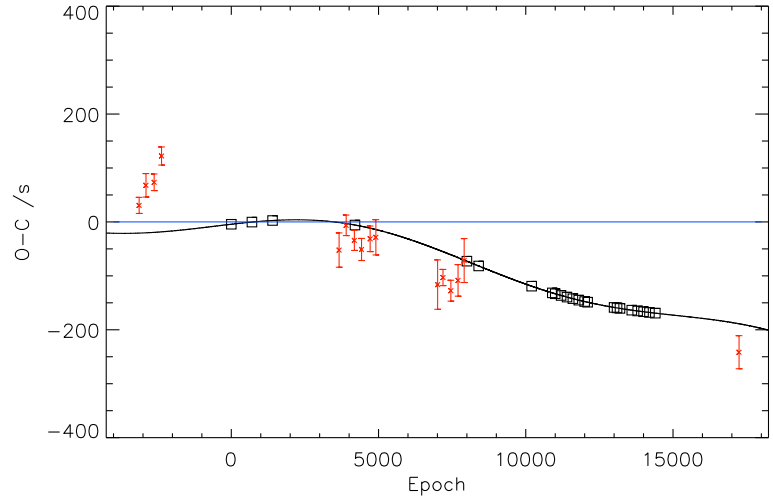

Figure 12.27: O−C diagram for HS 2231+2441 according to ephemeris of Østensen *et al.* (2007). Points in red are from new SuperWASP timings, binned on a monthly basis. Black squares indicate approximate locations of observations of Qian *et al.* (2010b), with their fitted curve overplotted as solid line.

12.4.4 HS 2231+2441

The discovery paper for HS 2231+2441 is Østensen *et al.* (2007), who determine system parameters and provide the ephemeris:

$$\text{BJD} \quad 2453522.669493 + 0.1105880E. \tag{12.5}$$

Qian *et al.* (2010b) describe observations of the system between 2005 and 2009, and provide an O−C diagram (their Fig. 4), which they fit with a function including both a quadratic and a sinusoidal term. Therefore, they suggest the presence of a secular decrease in orbital period, associated with magnetic braking, and a tertiary companion responsible for the sinusoidal variation. Since their times of minima do not appear to have been published yet, we compare our SuperWASP eclipse timings with their fitted curve, and estimate the epochs of their observations from their O−C diagram (Fig. 12.27). Although fairly close to their fit during 2006 and 2007, our observations do not strongly support it outside their original data range i.e. during 2004 and 2012, and a linear function

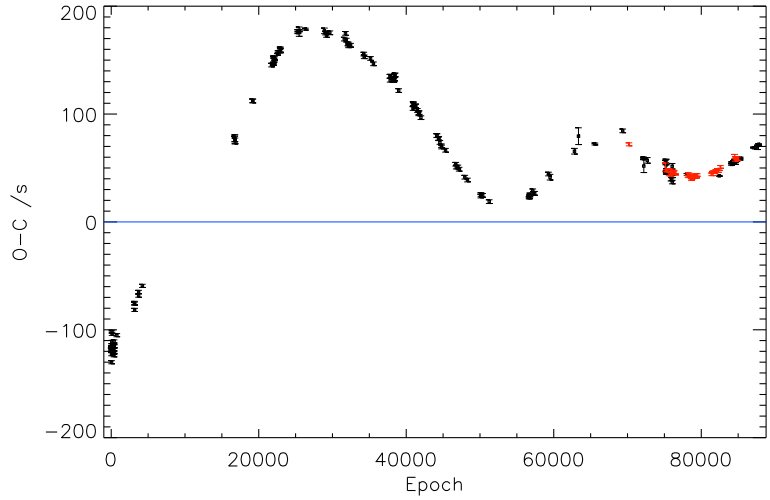

Figure 12.28: O−C diagram for HW Vir according to ephemeris of Lee *et al.* (2009). Data points in black are from previously-published primary eclipse timings, largely reproducing those included in Fig. 1 of Beuermann *et al.* (2012b). Points in red are from new SuperWASP timings, binned on a fortnightly basis.

might provide a better fit to the full data set. A straight-line fit with negative slope would be expected in an O−C diagram if the period used to construct it were too long; we note that Østensen *et al.*'s period, based on just three nights of observations during June and September 2005, is fractionally longer than ours (0.11058784 d), and quoted to lower precision, and this may be a cause for the apparent long-term downward trend seen here.

12.4.5 HW Vir

The prototype for eclipsing sdB binaries, HW Vir was discovered by Menzies and Marang (1986), and its times of minima were documented between 1984 and 2002 by a group at the South African Astronomical Observatory (Marang and Kilkenny, 1989; Kilkenny *et al.*, 1991, 1994, 2000, 2003), who also studied AA Dor and NY Vir over many years. Following Beuermann *et al.* (2012b), we include their eclipse timings in Fig. 12.28 along with others having a quoted error $\leq$0.0001 d (Wood *et al.*, 1993; Lee *et al.*, 2009; Brát *et al.*, 2011), and

Beuermann *et al.*'s own results, up to February 2012. For clearer comparison of our results with the recent models of Lee *et al.* and Beuermann *et al.*, we use their ephemeris:

$$\text{BJD} \quad 2445730.55803 + 0.1167195E. \tag{12.6}$$

Lee *et al.* interpreted the O−C diagram up to 2009 (epoch ∼76000; their Fig. 5 top panel) as the sum of a downward-opening parabola (secular period decrease caused by magnetic braking) and two sinusoidal terms (LITE associated with two substellar circumbinary companions). However, Beuermann *et al.* pointed out that the proposed companions' orbits crossed, indicating a probable near-encounter or collision within 2000 y; moreover, the O−C values after 2009 diverge substantially from Lee *et al.*'s fit, curving upwards rather than following the proposed quadratic decline. They argue for an alternative model without the long-term period decrease, and involving two circumbinary low-mass objects in orbits which they found to be stable for more than 10^8 y. We note that our new SuperWASP eclipse timings, covering July 2006 to March 2011, strongly support Beuermann *et al.*'s model over that of Lee *et al.*, in that a significant period increase is clear, and several previously undocumented parts of the general trend during this time are now well covered. HW Vir is also the system in which the contribution of SuperWASP archival data is most readily apparent: some 180 primary eclipse timings could be measured with uncertainties below 0.00006 d, covering about six years.

12.4.6 2M 1938+4603

2M 1938+4603, a *Kepler*-field object (Borucki *et al.*, 2010) known to contain an sdB star, was observed to possess shallow primary and secondary eclipses, in addition to its substantial reflection effect, by Østensen *et al.* (2010) (who also discovered HS 2231+2441). On the basis of 13 supplementary ground-based

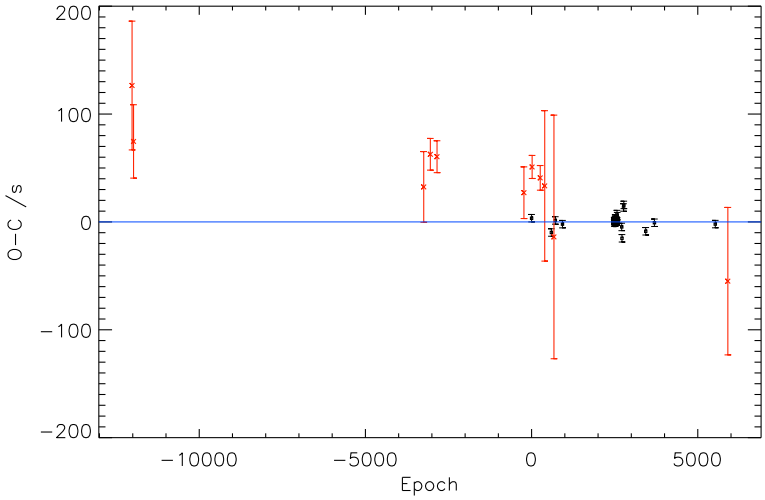

Figure 12.29: O−C diagram for 2M 1938+4603 according to ephemeris of Østensen *et al.* (2010). Points in red are from new SuperWASP timings, binned on a monthly basis.

timings covering June 2008–May 2010, they provide the ephemeris

$$\text{BJD} \quad 2454640.86416 + 0.12576530E. \tag{12.7}$$

Our SuperWASP timings extend coverage back to May 2004, and although they are individually not very precise, when binned together they suggest a long-term negative linear trend (Fig. 12.29). As with HS 2231+2441, we suspect Østensen *et al.*'s period is fractionally too long (ours is 0.12576522 d), creating a downward slope in the O−C diagram (their timing uncertainties may also be underestimated, given the scatter of their observations about the mean). Allowing for this, our data set does not seem to suggest any period change in this system. It is interesting to note that Østensen *et al.* also provide 77 extremely precise consecutive eclipse timings from *Kepler* observations (around epoch 2500); when the full continuous space-based light curve for this object is made available, it should be possible to determine whether 2M 1938+4603 is undergoing period variations with unprecedented confidence and precision.

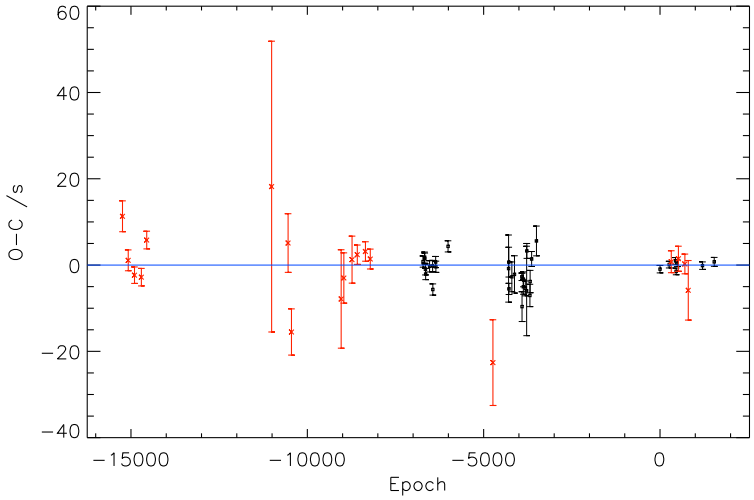

Figure 12.30: O−C diagram for NSVS 07826147 according to ephemeris of Backhaus *et al.* (2012). Points in red are from new SuperWASP timings, binned on a monthly basis.

12.4.7 NSVS 07826147

NSVS 07826147 was discovered by Kelley and Shaw (2007), and primary eclipse timings have been published for it by For *et al.* (2010); Liying and Shengbang (2010); Backhaus *et al.* (2012). We use Backhaus *et al.*'s ephemeris to construct our O−C diagram:

$$\text{BJD} \quad 2455611.926580 + 0.1617704531E. \tag{12.8}$$

No period change has been claimed yet for this system, though the previously-published timings only covered February 2008–October 2011; the addition of our SuperWASP timings (Fig. 12.30) extends the coverage back to May 2004, and provides stronger support for a constant orbital period. Indeed, our results suggest an upper limit on any period variation of about 0.0003 s yr^{-1}.

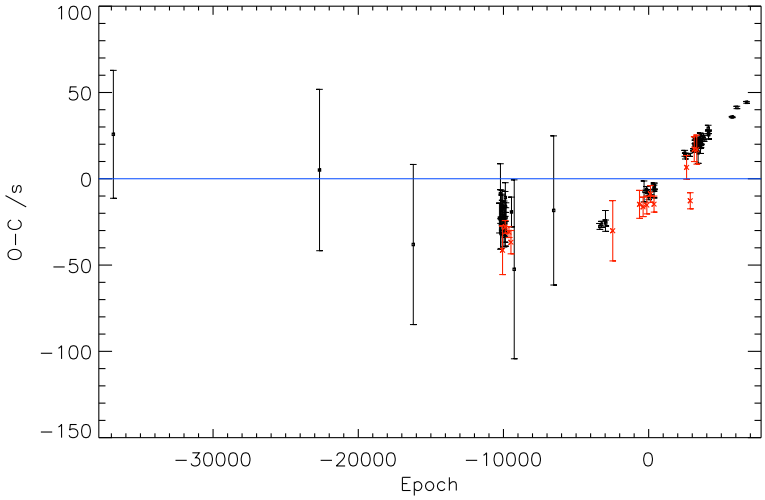

Figure 12.31: O−C diagram for NSVS 14256825 according to ephemeris of Hinse *et al.* (2014). Points in red are from new SuperWASP timings, binned on a monthly basis.

12.4.8 NSVS 14256825

NSVS 14256825 was identified as an eclipsing sdB binary by Wils *et al.* (2007), who published some eclipse timings; others have been provided by Kilkenny and Koen (2012); Beuermann *et al.* (2012a); Almeida *et al.* (2013). Qian *et al.* (2010b) report observations of the system since 2006, and claim evidence for a cyclic variation, but have not yet published supporting timing measurements. Here, we use the ephemeris of the most recent analysis of the system, Hinse *et al.* (2014):

$$\text{BJD} \quad 2455408.74454 + 0.11037411E. \tag{12.9}$$

On the basis of very similar O−C variations (Fig. 12.31), Beuermann *et al.* (2012a) argue for a single circumbinary low-mass companion in an elliptical orbit, while Almeida *et al.* (2013) prefer a two-planet model. Hinse *et al.* (2014), however, find that the data are insufficient to constrain any particular one-planet model, and provide no convincing evidence for a second circumbinary companion. Unfortunately, while our new timings are quite consistent with previous measure-

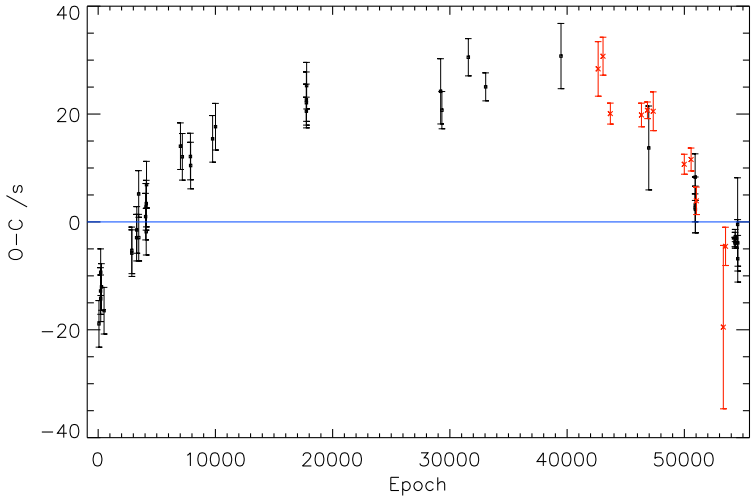

Figure 12.32: O−C diagram for NY Vir according to ephemeris of Qian *et al.* (2012). Points in red are from new SuperWASP timings, binned on a two-monthly basis.

ments, and independently support period increase over June 2006–August 2011, they do not add much to the coverage or clarify the longer-term trends of period variation for this particular system.

12.4.9 NY Vir

Kilkenny *et al.* (1998) published the discovery paper for NY Vir, and provided eclipse timings and an ephemeris for it between 1996 and 2010 (Kilkenny *et al.*, 2000; Kilkenny, 2011). Additional times are given in Çamurdan *et al.* (2012) and Qian *et al.* (2012); the latter also provides the revised ephemeris:

$$\text{BJD} \quad 2450223.362213 + 0.1010159673E. \tag{12.10}$$

A steady period decrease was observed in the O−C diagram (Fig. 12.32) by Kilkenny (2011); Çamurdan *et al.* (2012); Qian *et al.* (2012), and is independently supported by our new SuperWASP timings. Qian *et al.* argue that this is unlikely to be caused by the Applegate mechanism, gravitational radiation or magnetic

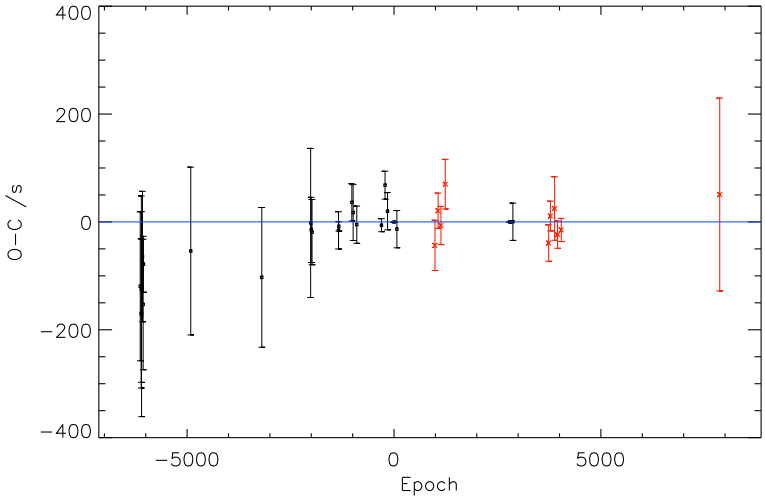

Figure 12.33: O−C diagram for DE CVn according to ephemeris of Parsons *et al.* (2010). Points in red are from new SuperWASP timings, binned on a monthly basis.

braking, due to its magnitude and the fully convective nature of the stars, and suggest instead that it is part of a long-term (>15 y) cyclic variation associated with a circumbinary planet; furthermore, they claim that the O−C diagram provides evidence for a shorter-period fourth body in the system.

12.4.10 DE CVn

DE CVn was identified as an X-ray source in the ROSAT catalogue (Voges *et al.*, 1999), and as an eclipsing binary containing a WD by Robb and Greimel (1997), who also published several times of minima. Other timings are provided by van den Besselaar *et al.* (2007); Tas *et al.* (2004); Parsons *et al.* (2010), and Parsons *et al.* also give the ephemeris we use for Fig. 12.33:

$$\text{BJD} \quad 2452784.554043 + 0.3641393156E. \tag{12.11}$$

Although the previously-published eclipse timings of DE CVn cover 1997–2006, Parsons *et al.* feel that most are too uncertain to allow any claims regarding

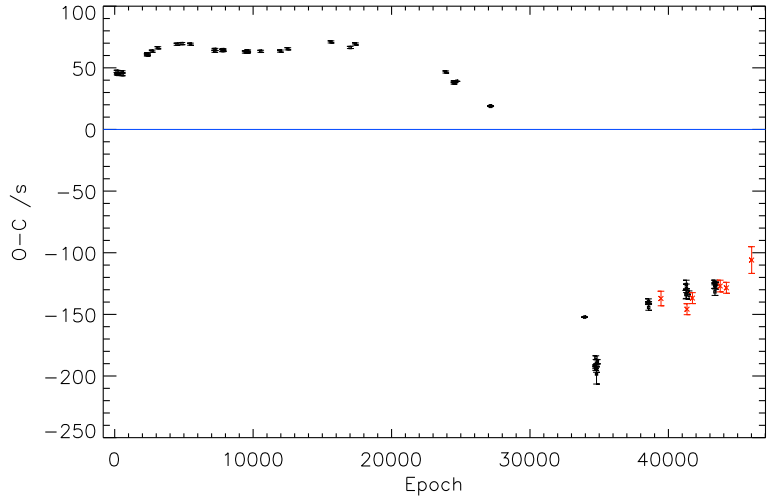

Figure 12.34: O−C diagram for QS Vir according to ephemeris of Parsons *et al.* (2010). Points in red are from new SuperWASP timings, binned on a four-monthly basis.

period change to be made. Our new timings extend coverage to March 2011, and although they also have large uncertainties, we may note at least that the whole O−C diagram is fully consistent with a constant period for this system, over about 14 years.

12.4.11 QS Vir

QS Vir was discovered and later identified as an eclipsing WD binary by Kilkenny *et al.* (1997); O'Donoghue *et al.* (2003). They and Kawka *et al.* (2002); Qian *et al.* (2010a); Parsons *et al.* (2010) provide eclipse timings for it, and here we use the ephemeris of Parsons *et al.*:

$$\text{BJD} \quad 2448689.64062 + 0.150757525E. \tag{12.12}$$

(Almeida and Jablonski (2011) also refer to new timings for the system, but have not yet published them.) The substantial period changes evident in Fig. 12.34 are demonstrated by Parsons *et al.* to be an order of magnitude too large to be

caused by the Applegate mechanism; however, they are also doubtful about the plausibility of a third body in the system, while noting that it "remains the only mechanism able to produce such a large period variation". The data set available to them covered April 1992–February 2010; Almeida and Jablonski (2011) add a few more points extending it to August 2010, and argue on this basis for a system containing two circumstellar low-mass bodies. Our partly-overlapping new timings extend the time base to March 2011, and provide independent, if weak, support for a recent increase in QS Vir's orbital period.

12.5 Conclusions

Twelve PCEBs with observations covering between three and seven years in the SuperWASP archive were analysed here for evidence of period and/or light curve amplitude change, potentially indicating the presence of circumbinary planets. Their periods were found to high precision, agreeing very closely with those found in previous studies. Hundreds of primary eclipse timings were also determined for the objects, in many cases for previously unobserved epochs, and are made available online[3], for future study of these systems' period variations.

Period changes found in much previous work were strongly confirmed here for HW Vir, as was the stability of the periods of AA Dor and NSVS 07826147. New eclipse timings of NSVS 14256825, NY Vir and QS Vir, previously suggested as hosts for third bodies, provided some support for period change, while claims of period variations for HS 2231+2441 were not supported by our data. V471 Tau could not be analysed for period variations due to its dramatic and apparently irregular amplitude changes. For 2M 1938+4603 and DE CVn, previously published eclipse timings had not been sufficient to make strong claims; we found no plausible evidence for period changes in these systems. However,

[3] `vizier.cfa.harvard.edu/viz-bin/VizieR?-source=J/A+A/566/A128`

for ASAS 10232, our data provided fairly strong evidence for period increase between May 2006 and June 2011, and perhaps for systematic amplitude changes as well, which might suggest this system as a further candidate for containing a circumbinary third body.

Table 12.1: PCEBs observable in SuperWASP archive

System short name	SuperWASP ID (Jhhmmss.ss±ddmmss.s)	Type	Time base MM/(20)YY	P (s)	$\dot{P}$ (s yr^{-1})	$\dot{P}$ limit (s yr^{-1})	Ref. min. (HJD-2450000)
AA Dor	J053140.34−695302.1	sdOB+dM/BD	09/08–03/11	22597.030(3)		0.01	4738.35858(3)
ASAS 10232[1]	J102321.90−373659.9	sdB+dM	05/06–06/11	12032.8839(9)	0.0073(12)	0.003	3860.198595(14)
EC 10246−2707	J102656.50−272256.7	sdB+dM	05/06–06/12	10239.0898(3)	0.0012(8)	0.003	3860.160327(12)
HS 2231+2441	J223421.48+245657.5	sdB+BD(?)	05/04–09/10	9554.789(2)		0.03	3150.651562(11)
HW Vir	J124420.23−084016.8	sdB+dM	07/06–03/11	10084.5643(6)	0.00287(9)	0.0003	3924.150031(12)
2M 1938+4603[2]	J193832.60+460359.1	sdB+dM	05/04–07/10	10866.1147(17)		0.01	3128.537206(13)
NSVS 07826147[3]	J153349.46+375928.2	sdB+dM	05/04–06/11	13976.9668(4)		0.0003	3128.425870(16)
NSVS 14256825	J202000.46+043756.4	sdOB+dM	06/06–08/11	9536.3263(5)	0.0019(8)	0.003	3904.675222(11)
NY Vir	J133848.16−020149.3	sdB+dM	07/07–03/11	8727.7761(7)	−0.0016(6)	0.003	4307.134430(10)
DE CVn	J132653.28+453246.9	WD+dM	05/04–03/11	31461.639(8)		0.03	3128.30088(4)
QS Vir	J134952.07−131337.3[4]	WD+dM	07/07–03/11	13025.4555(8)	0.007(3)	0.01	4307.164866(15)
V471 Tau	J035024.96+171447.4	WD+dK2	09/06–11/11	45030.05(4)			

[1] ASAS J102322−3737.0

[2] 2MASS J19383260+4603591

[3] Listed as NSVS 07826247 in Zorotovic and Schreiber (2013).

[4] Archive also contains slightly poorer quality observations of this object under the identifier 1SWASP J134952.00−131336.9.

Chapter 13

The multiplicity fraction of SuperWASP stars

13.1 Introduction

The importance of multiplicity for an understanding of stellar evolution is hard to overestimate. Single stars now appear to be in a minority, especially at higher masses (the recent review of Duchêne and Kraus (2013) indicated a multiplicity fraction for intermediate-mass stars $\geq$50%, rising to $\geq$80% for the most massive stars), and binary interactions are probably responsible for creating several different types of supernovae, novae and unusual star types such as blue stragglers. Amongst binaries, a significant proportion appear to be part of higher-order multiple systems (Tokovinin (2014a,b) estimated 29% for F and G dwarfs in a distance-limited sample), and such triples, quadruples etc. also have much to tell us about the formation and stability of stellar systems (see e.g. Michaely and Perets (2014); Naoz and Fabrycky (2014)).

Higher-order multiple star systems can be detected by a range of methods including direct resolution, radial velocity and proper motion analysis. For a survey like SuperWASP, additional eclipses in a binary light curve may occasion-

ally reveal further bodies in a system, as in Ch. 11, but a more widely applicable technique will be the detection of eclipse timing variations producing an approximately sinusoidal curve in an O−C diagram, as in Ch. 10 and 12. (This approach was used by Rappaport *et al.* (2013) to search for candidate triples in the Kepler eclipsing binary catalogue.) Here, we use a preliminary catalogue of candidate SuperWASP eclipsing binaries to search for orbital period changes potentially indicative of third bodies. These statistics can then be used to suggest a lower limit to the higher-order multiplicity fraction of SuperWASP stars.

13.2 Method

A provisional catalogue of SuperWASP eclipsing binary candidates was produced by Payne (2013), using a neural net classification method for all objects listed in the database with periods found by the method described in Norton *et al.* (2007, 2011). The catalogue contained 2875 objects classified as EW-type binaries, 5226 EB-type, 5826 EA-type exhibiting two eclipses per cycle, and 7056 potential EA-type systems in which only a single eclipse was visible. Owing to the large number of false positives expected in the last group, only the first three groups of sources were considered here for further analysis.

13927 light curves were downloaded from the archive, and a form of the *ah3* code (Ch. 4 and 5), modified for large numbers, was run on them. This checked and refined the orbital period associated with each object identifier, searching within a range centered on the catalogue period (itself derived from the archive database); produced a phase-folded light curve and mean fitting curve (with 100 bins); generated O−C, amplitude change and absolute flux change diagrams; and determined a rate of period change where this was supported by the O−C diagram. The output for each identifier was an image file allowing visual checking of the light curve, O−C diagram etc., and a log file line summarizing key statistics

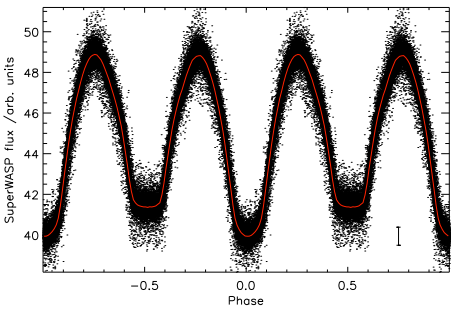

Figure 13.1: Light curve for J171747 (automatically classified as EW-type) folded at $P = 38649.224 \pm 0.006$ s, with binned mean curve overplotted in red. A representative error bar for a single observation is shown in the lower corner.

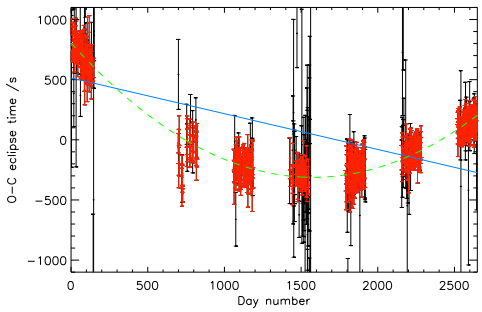

Figure 13.2: O−C diagram for J171747 spanning eight years. Red points and their adjusted uncertainties were automatically selected for period change determination; black points and uncertainties were excluded as outliers (a few additional more extreme outliers fall outside the bounds of the plot). Blue solid line shows best linear fit (reduced $\chi^2 = 13.58$, 548 d.f.); green dashed line shows best quadratic fit ($\chi^2 = 1.03$, 547 d.f.), strongly supporting a secular period increase, with rate 0.1466 ± 0.0018 s yr^{-1}.

such as number of data points in the light curve, mean flux, period, period change etc.

The log file revealed a number of objects clustered near particular periods: 1/4, 1/3, 2/5 and 2/3 of a sidereal day in particular. Visual checks of these objects (mainly on the EA list) confirmed that they were spurious periodic variables, with the variability resulting from temperature-related instrumental effects occurring daily e.g. peaks or troughs in the light curve at the start of each night's observations. These identifiers were removed from the list. For some objects, no significant period could be found in the given range, or no O−C diagram could be constructed (due to insufficient successful fits to nightly observations), and these objects were also removed from further consideration. These preliminary checks left 2844 EW-type, 5073 EB-type and 5323 EA-type objects.

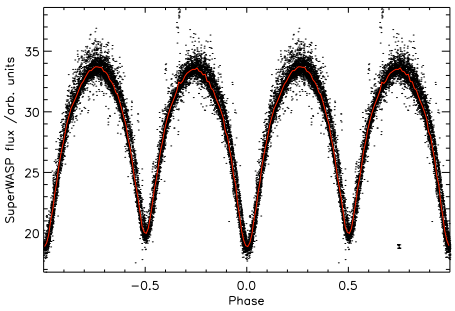

Figure 13.3: Light curve for J014933 (automatically classified as EW-type) folded at $P = 29445.863 \pm 0.005$ s.

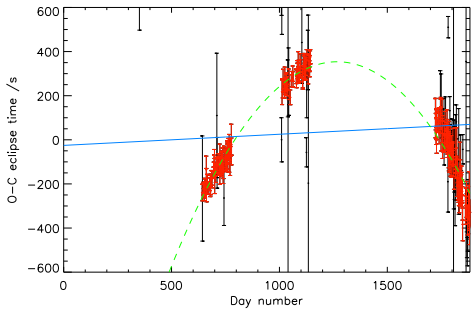

Figure 13.4: O−C diagram for J014933 covering about three years. Blue solid line shows best linear fit ($\chi^2 = 32.05$, 203 d.f.); green dashed line shows best quadratic fit ($\chi^2 = 1.00$, 202 d.f.), strongly supporting a secular period decrease, with rate -0.392 ± 0.005 s yr^{-1}.

For the remaining objects, where period change had been found by the code, the ratio between best linear and quadratic fit (reduced, modified) χ^2 values for the O−C diagram was used to select a sample for visual checking. (See Ch. 6 for more detail on how the significance of such ratios could be tested in individual cases; the number of degrees of freedom had a negligible impact on the difference between the two fits for each object.) All output files were checked down to a ratio of 1.25, below which it was hard to judge the classification by eye; the tests applied to PCEBs in Ch. 12 had also indicated that ratios below 1.05 did not generally indicate statistically significant period change. This meant that 679 EW-type, 436 EB-type and 806 EA-type objects were checked visually, and assigned a classification: plausible quadratic variation in the O−C diagram (supporting secular period change); plausible sinusoidal variation (supporting alternating period increases and decreases); no apparent period change (usually due to erratic time sampling misleading the program's fitting algorithm); erroneous period found (usually due to the original input period being significantly wrong); or unclear (usually when the time sampling was very sparse or the time

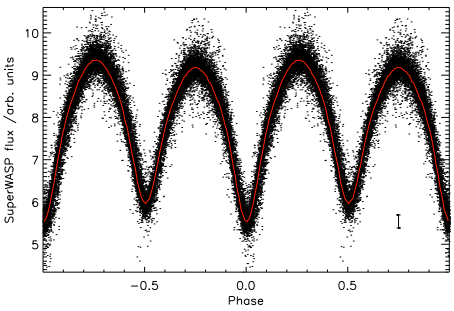

Figure 13.5: Light curve for J030313 (automatically classified as EW-type) folded at $P = 28942.582 \pm 0.003$ s.

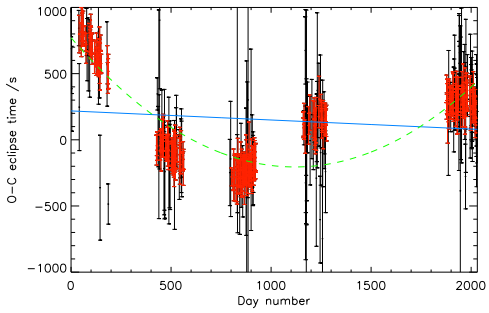

Figure 13.6: O−C diagram for J030313 spanning six years. Blue solid line shows best linear fit ($\chi^2 = 11.74$, 265 d.f.); green dashed line shows best quadratic fit ($\chi^2 = 3.01$, 264 d.f.), neither of which matches the data well. A sinusoidal variation is supported.

basis very limited).

13.3 Results

Period change was indicated by *ah3* for 2305/2844 EW-type, 3227/5073 EB-type and 3076/5323 EA-type objects. However, these fractions cannot be taken at face value: large numbers of these apparent changes involved very small differences between the best linear fit and the best quadratic fit to the O−C diagram, which would probably not have been statistically significant; many of the EA-type objects exhibiting apparent period change also turned out to have erroneous periods - usually very long periods which were likely multiples of the true period - and this could create the illusion of quadratic period change.

480/679 EW-type visually-checked objects were classified as exhibiting plausible period change, of which 388 showed quadratic and 92 sinusoidal behaviour (see Appendix B Tables B.1 and B.2 for complete list). Figs. 13.1 to 13.4 illustrate clear cases of period increase and decrease respectively, in this type, while Fig. 13.6 shows a more sinusoidal variation. Extending this proportion to all

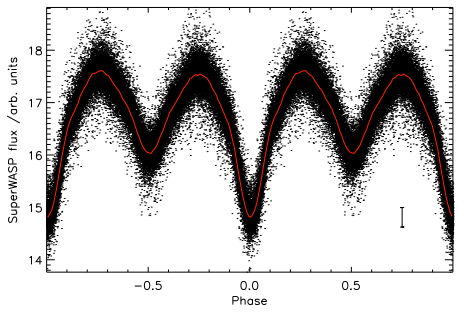

Figure 13.7: Light curve for J064024 (automatically classified as EB-type) folded at $P = 44851.164 \pm 0.007$ s.

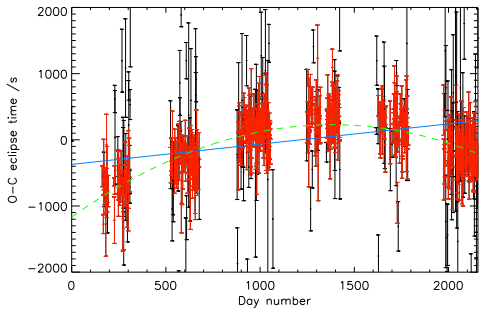

Figure 13.8: O−C diagram for J064024 covering six years. Blue solid line shows best linear fit ($\chi^2 = 2.96$, 466 d.f.); green dashed line shows best quadratic fit ($\chi^2 = 1.01$, 465 d.f.), strongly supporting a secular period decrease, with rate -0.277 ± 0.009 s yr^{-1}.

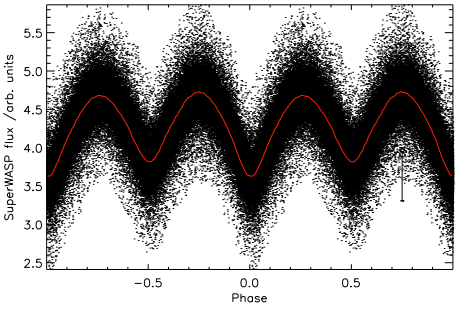

Figure 13.9: Light curve for J165649 (automatically classified as EB-type) folded at $P = 23775.304 \pm 0.003$ s. The short period and light curve shape would probably support EW-type classification instead.

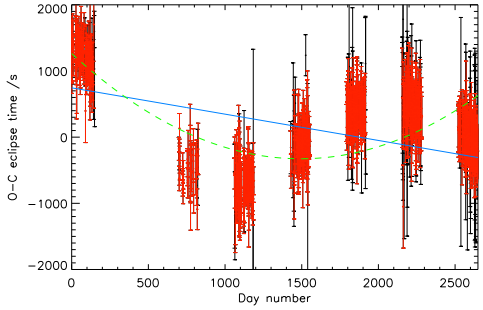

Figure 13.10: O−C diagram for J165649 spanning eight years. Blue solid line shows best linear fit ($\chi^2 = 4.51$, 582 d.f.); green dashed line shows best quadratic fit ($\chi^2 = 2.14$, 581 d.f.), which are similarly poor matches to the data. A sinusoidal variation is strongly supported.

the objects with linear-quadratic fit ratios above 1.05, and adjusting the whole sample size to account for expected numbers of erroneous periods and uncertain cases, we can estimate that about 41% of the EW-type objects are undergoing period change (see Table 13.5 for the full figures used in this calculation).

167/436 EB-type objects were classified as exhibiting plausible period change,

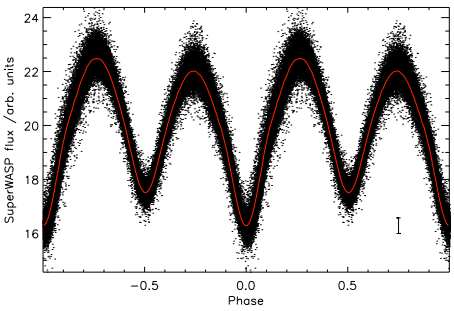

Figure 13.11: Light curve for J172023 (automatically classified as EB-type, but more plausibly EW-type) folded at $P = 27251.304 \pm 0.002$ s.

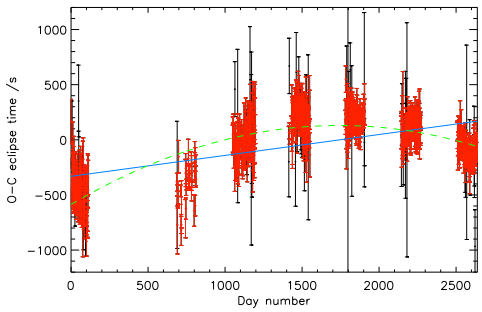

Figure 13.12: O−C diagram for J172023 spanning eight years. Blue solid line shows best linear fit ($\chi^2 = 4.34$, 627 d.f.); green dashed line shows best quadratic fit ($\chi^2 = 2.08$, 626 d.f.), both poor matches to the data. A sinusoidal variation is supported.

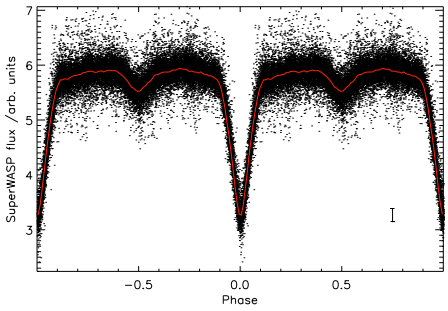

Figure 13.13: Light curve for J133349 (automatically classified as EA-type) folded at $P = 151475.59 \pm 0.07$ s.

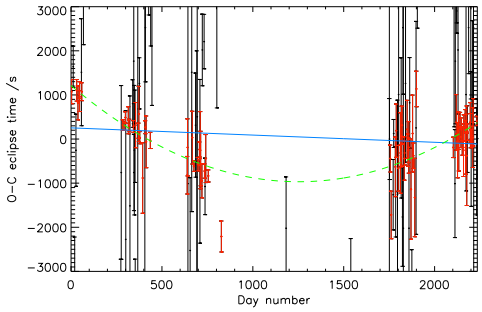

Figure 13.14: O−C diagram for J133349 spanning seven years. Blue solid line shows best linear fit ($\chi^2 = 5.94$, 75 d.f.); green dashed line shows best quadratic fit ($\chi^2 = 1.04$, 74 d.f.), strongly supporting a secular period increase, with rate 1.78 ± 0.09 s yr^{-1}.

137 quadratic and 30 sinusoidal (see Appendix B Tables B.3 and B.4 for complete list). Fig. 13.8 illustrates secular period change in this type, while Figs. 13.9 to 13.12 show clear sinusoidal variation (though these might be better described as EW-type systems). Scaling up the numbers as before (Table 13.5), we can estimate that about 19% of the EB-type objects are undergoing period change.

189/806 EA-type objects were classified as exhibiting plausible period change,

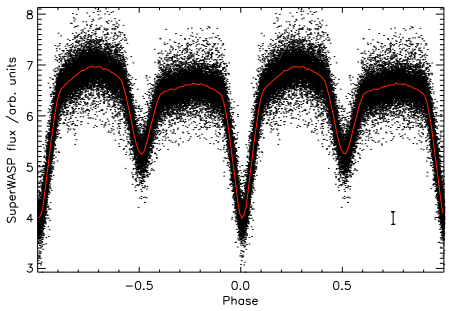

Figure 13.15: Light curve for J161253 (automatically classified as EA-type) folded at $P = 35162.816 \pm 0.007$ s.

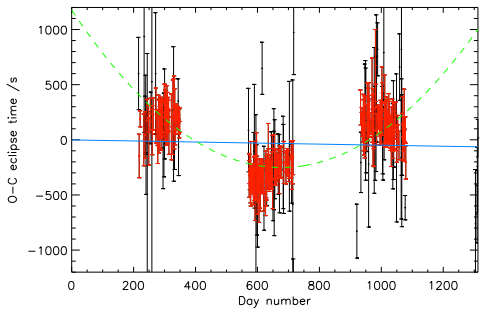

Figure 13.16: O−C diagram for J161253 covering just over three years. Blue solid line shows best linear fit ($\chi^2 = 4.15$, 235 d.f.); green dashed line shows best quadratic fit ($\chi^2 = 1.10$, 234 d.f.). Although a reasonable quadratic fit to the first three years of data has been achieved, the O−C trends within each year and the location of the partial data from year 4 on the diagram lend more support to a sinusoidal variation of notably short duration (modulating period ~ 2 y).

171 quadratic and 18 sinusoidal (see Appendix B Tables B.5 and B.6 for complete list). Fig. 13.14 illustrates secular period change in this type, while Fig. 13.16 shows probable sinusoidal variation. Scaling up the numbers as before (Table 13.5), we can estimate that about 14% of the EA-type objects are undergoing period change.

Plotting (quadratic) period change measurements against periods (Fig. 13.17) for the three types of eclipsing systems, we may note that the most rapid changes are found in the long-period EA-type binaries, while the short-period EWs all have period changes below 1 s yr^{-1} in magnitude. The shortest $P/\dot{P}$ timescale (i.e. a time to merger, if the period decrease continued at this rate) is seen in EB/EW-type object J051927 (Figs. 13.21 and 13.22), at ∼24000 years.

The period change distributions for the three types (Figs. 13.18 to 13.20) are very similar in shape: peaked strongly at small values on each side of zero,

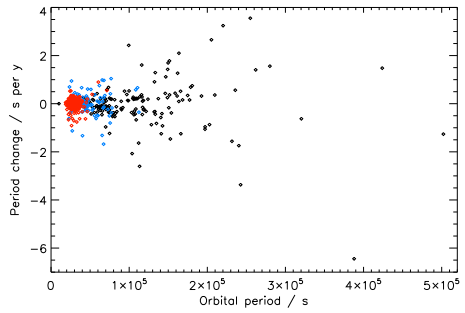

Figure 13.17: Period change measurements for 638 distinct sources exhibiting apparent quadratic variation in their O−C diagrams, plotted against their orbital periods. EW-type binaries are shown in red, EB-types in blue, and EA-types in black.

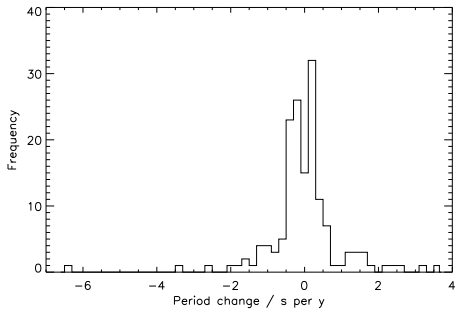

Figure 13.18: Period change distribution for EA-type eclipsing binaries.

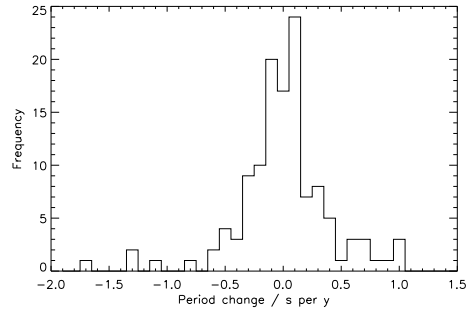

Figure 13.19: Period change distribution for EB-type eclipsing binaries.

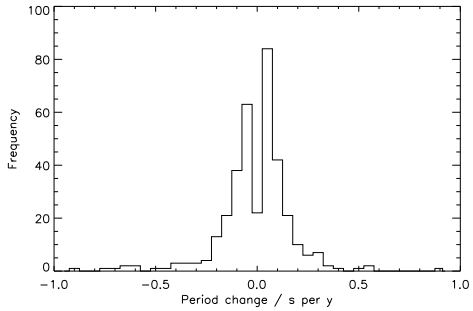

Figure 13.20: Period change distribution for EW-type eclipsing binaries.

with approximately Gaussian tails at larger values, and a gap around zero itself, where genuine period changes are very hard to detect. A Kolmogorov-Smirnov test of the positive values of each distribution against the negative values does not support any significant difference between them i.e. they are symmetric in a statistical sense. However, when all three distributions are considered simultaneously, the K-S test provides near-significant support for the two sides being drawn from different underlying distributions (P=0.07), and we may note that the peak on the positive side is slightly higher than the peak on the negative side in all three histograms.

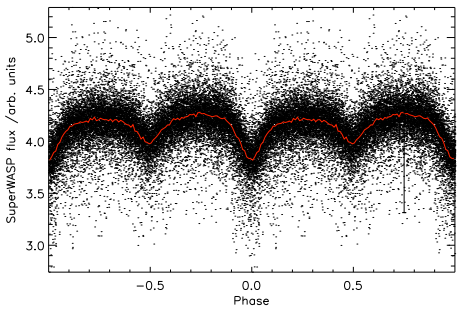

Figure 13.21: Light curve for J051927 (automatically classified as EB-type, but more likely EW-type) folded at $P = 27112.04 \pm 0.02$ s.

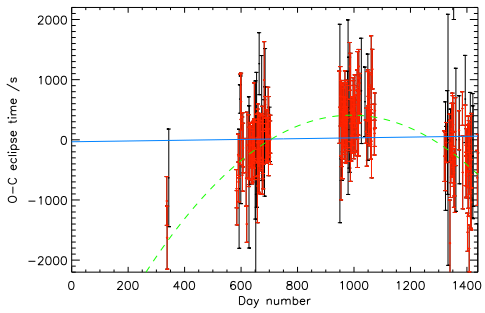

Figure 13.22: O−C diagram for J051927 covering just over three years. Blue solid line shows best linear fit ($\chi^2 = 2.06$, 174 d.f.); green dashed line shows best quadratic fit ($\chi^2 = 1.06$, 173 d.f.), strongly supporting a secular period decrease, with rate -1.13 ± 0.09 s yr^{-1}.

13.4 Discussion

As in Ch. 8, it is notable that the (quadratic) period change distributions found here are all broadly symmetric, with binary systems of all three light curve classes apparently as likely to increase in orbital period as to decrease. This would not necessarily be expected given the usual model of main sequence binaries tending to evolve from wider to smaller separations, primarily due to magnetic braking.

An explanation might be found by considering the sinusoidal period changes clearly seen in some of the O−C diagrams with long baselines e.g. J165649. In Fig. 13.10, if we only had the first five or six year of observations, the data would be well-fitted by a quadratic opening upwards, and we should conclude that the system was undergoing rapid period increase; conversely, if we only had the last five years of data, the diagram would support a quadratic opening downwards, and the system would appear to be undergoing steady period decrease. Given this, it seems plausible that many of the apparent quadratic changes detected here would prove to be part of longer-term sinusoidal variations if we continued to observe the systems. If the majority of period changes in our data set are

actually short sections of sinusoidal variations, this would neatly explain the symmetric distributions seen in Figs. 13.18 to 13.20, since the sections would be equally likely to be drawn from any part of the underlying sinusoid, implying equal numbers of apparent positive and negative period changes, on average, for a large sample.

There are two plausible causes for such widespread sinusoidal period variations. The Applegate mechanism could produce semi-sinusoidal modulations, of amplitude $\Delta P/P \sim 10^{-5}$ on a time scale of decades, in close binaries containing at least one active, convective star; luminosity variations would also be expected to be observed with the same period as the O−C modulation. However, it is unlikely that this mechanism is responsible for most of the cases seen here, which include widely-separated long-period binaries as well as W UMa-type systems, systems not exhibiting obvious luminosity changes of the correct period (e.g. J165649), systems exhibiting modulation on quite short time scales (e.g. J161253) and O−C amplitudes substantially too large (e.g. J051927).

A more straightforward explanation, which would be applicable to nearly all types of eclipsing systems seen here, would be the influence of a third body inducing sinusoidal period modulation through the Roemer (light travel time) delay and/or the physical delay for a third star in an eccentric or inclined-plane orbit (Rappaport *et al.* (2013) gives further details of the expected contributions of each effect in systems of different configurations). Further support for this cause is provided by the greater frequency of period changes seen in short-period EW-type systems compared with long-period EBs and EAs (Fig. 13.17): the modulation amplitude may be expected to be greater, and the modulation period shorter, in closer systems containing low-mass binaries. Moreover, a third star may have actually driven a binary to shorter orbital periods and towards contact configuration through Kozai cycles (Kozai, 1962). Additionally, higher-order multiplicity in some eclipsing SuperWASP binaries has been strongly supported

by other techniques (see Ch. 10 and 11), so these systems are not inherently unlikely.

If the majority of period changes measured here are associated with third bodies, their frequency within the sample of SuperWASP eclipsing binary candidates allows us to estimate the frequency of triples amongst binaries more generally, as around 24%. This lies between Tokovinin's slightly higher figure of 29% for F and G dwarfs (taking into account detection biases), and Rappaport *et al.*'s estimate of "at least 20% of all close binaries".

13.5 Conclusion

A neural-net-based catalogue of ∼14000 candidate SuperWASP eclipsing binaries was searched to check their orbital periods and classification, and to search for evidence of period change. Numerous clear cases of quadratic and sinusoidal variation in O−C diagrams were observed; interpreting the quadratic variation as sections of longer-period sinusoidal variation would explain the symmetrical period change distributions observed in all three classes of binaries. If this period modulation is caused by third bodies, this allows us to estimate a lower limit for the higher-order multiplicity fraction among local galactic binaries of around 24%, which tallies well with other estimates.

Table 13.1: Object statistics used in multiplicity calculations

	EW-type	EB-type	EA-type
Total objects considered	2844	5073	5323
Period change found by *ah3*	2305	3227	3076
Objects with χ^2 ratio $\geq$1.05[1]	1414	1395	1797
Objects without apparent period change[2]	1430	3678	3526
Objects checked visually	679	436	806
Period change confirmed visually	480	167	189
Period change rejected visually	88	50	48
Wrong period detected visually	24	33	340
Unclear cases on visual check	87	186	229
Expected genuine period change[3]	1000	534	421
Expected wrong periods[4]	50	106	758
Expected unclear cases[5]	364	2164	1512
Expected valid objects[6]	2430	2803	3053
Expected period change percentage[7]	41.2%	19.1%	13.8%

[1]See Section 13.2 for explanation of this ratio.

[2]I.e. row 1 - row 3.

[3]Obtained by extending the confirmed period change ratio (row 6 / row 5) to all objects with plausibly-significant χ^2 ratios (row 3).

[4]Obtained by extending the detected wrong period ratio (row 8 / row 5) to all objects with plausibly-significant χ^2 ratios (row 3).

[5]Obtained by extending the unclear cases ratio (row 9 / row 5) to all objects considered (row 1).

[6]I.e. total objects considered minus expected objects with wrong periods or unclear cases (row 1 - (row 11 + row 12)).

[7]I.e. (row 10 / row 13) $\times$ 100%.

Conclusion

This research project had as its primary aim the investigation of variable stars exhibiting varying periods using SuperWASP data, and it quickly came to focus primarily upon eclipsing binaries in the archive. Techniques suited to analyzing large quantities of high-cadence but often low signal-to-noise photometric observations were developed incrementally (IDL codes *handle*, *autohandle*, *ah2* and *ah3*), and proved successful in measuring orbital periods precisely, and detecting and quantifying period changes, both in real and synthetic test data.

Original results were achieved in seven main areas. First, in a "proof of concept" that eclipsing binary period changes could be detected in SuperWASP archival data, 53 very short-period candidate W UMa-type binaries previously identified by Norton *et al.* (2011) were searched for evidence of period change; several of their period measurements were corrected, and highly significant period change was observed in three objects, one of which (J234401) appeared to be a candidate for stellar merger on a relatively short timescale. This collection of SuperWASP binary candidates near the short-period limit (P <20000 s) was then expanded to 143 following a semi-automated search of the archive, 97 of which were new discoveries; their smooth period distribution seemed to support an explanation for the short-period limit involving binaries reaching critical configurations and evolving rapidly towards merger, rather than it being a mere observational consequence of the current age of the Universe. Significant period changes were observed in many of these binaries, though surprisingly with

a nearly symmetrical distribution about zero.

Several individual candidate binaries from these collections were subsequently followed up spectroscopically, and with further photometric observations. For J150822 and J160156, this enabled confirmation of their status as spectroscopic and eclipsing binaries; their light and radial velocity curves were then modelled to determine their system and component parameters, contributing to fundamental knowledge in the relatively under-studied fields of low-mass stars and short-period contact systems. However, J234401 proved more mysterious: high-resolution spectra did not exhibit the expected evidence for line splitting and shifting; moreover, its O−C curve over a longer time base supported an approximately sinusoidal variation in period length. After exploring rotational modulation and brown dwarf companion explanations, we favoured a triple system model in which a low-mass contact eclipsing binary orbited a more massive star dominating the combined spectrum; multicolour photometric follow-up by C. Koen subsequently supported this theory.

Another multiple system emerged from the short-period binary samples: J093010, whose erratic O−C diagram alerted our attention to additional eclipses in its (contact binary) light curve, associated with a second, longer-period detached eclipsing binary at the same location. Spectroscopic and multicolour photometric follow-up observations by ourselves and Koo *et al.* (2014) strongly supported these two binaries being gravitationally bound together, and revealed the existence of a fifth star associated with the detached binary. Only five other doubly-eclipsing quadruple systems had been discovered at that time; that this is apparently a doubly-eclipsing quintuple system makes it even more unusual and intriguing. Our modelling of the components of the system indicated that they are all fairly low-mass late G to early M stars in a single orbital plane, and probably fragmented from a single protostellar disk. This nearby, bright system thus has the potential to tell us much about the formation and stability

of hierarchical multiples.

Another group of unusual eclipsing binaries was also studied for evidence of orbital period variation, potentially (but controversially) associated with planetary-mass companions: post-common-envelope eclipsing systems like the prototype HW Vir. Eleven such objects have long-term light curves in the SuperWASP archive, and were studied using the most sensitive version of my code; we were able to confirm at high significance the period changes previously observed by other researchers in HW Vir, and at lower significance changes in NSVS 14256825, NY Vir and QS Vir; in ASAS 10232 we found significant evidence for period increase not previously claimed by others. Our hundreds of new SuperWASP eclipse timings for these much-studied systems should provide useful evidence in the current debate over the existence of circumbinary planets in such extreme environments.

Finally, a collection of $\sim$14000 candidate SuperWASP eclipsing binaries found by Payne (2013) was explored for evidence of period changes, with similar results to the earlier and smaller study of very short-period binaries: period change distributions for EA, EB and EW-type eclipsing systems at a wide range of periods were broadly symmetric about zero. We propose as explanation for this surprising finding that the majority of the period changes observed are caused by third bodies: if a long enough time-base were considered, the quadratic variations in their O$-$C diagrams might prove to be short sections of sinusoidal variations. This idea is supported by the clear observation of sinusoidal variations in some of the O$-$C diagrams. If correct, this would allow us to estimate a lower limit for the fraction of SuperWASP binaries in triple systems as around 24%, which tallies well with other estimates for the higher-order multiplicity fraction of lower-mass binaries.

These results have only scratched the surface of the valuable evidence on variable stars hidden in the SuperWASP archive. Many of the systems investigated

here have already proved to be of interest for the wider astronomical community and would repay further study: as examples of low-mass stars whose physical parameters are accessible through joint photometric and spectroscopic observations; as short-period contact binaries potentially close to a poorly-understood merger stage of (main-sequence) stellar evolution; as unusual higher-order multiple systems which challenge current models for star formation. Specifically, our tentative argument that around a quarter of binaries may have additional stellar companions could provide input and constraints for stellar population synthesis models and numerical simulations of cluster formation. In light of this, it would be highly desirable to follow up promising candidates for triple systems such as J165649 (Fig. 13.10), to confirm their status, perhaps by direct resolution of a third body, and so derive information on component masses, brightnesses, separations and relative orbital inclinations. It would also be interesting to run a form of my period and period change-searching code on the entire SuperWASP database of $\sim$30 million objects to look for eclipsing binary candidates potentially missed in Payne's work - perhaps exploiting the flux distribution idea outlined in Sect. 4.5. And finally, somewhere in the archive, a binary approaching imminent merger may still be waiting to be discovered.

Appendix A

Light curves and O−C diagrams for 143 objects

The following figures show folded light curves (left) and O−C diagrams (right) for 143 objects. On the O−C diagrams, the dotted lines represent the best linear fit to the data, and the solid lines the best quadratic fit. Note that many O−C diagrams represent non-significant period change, or were disregarded due to paucity of data: see Table 8.1 for significant results.

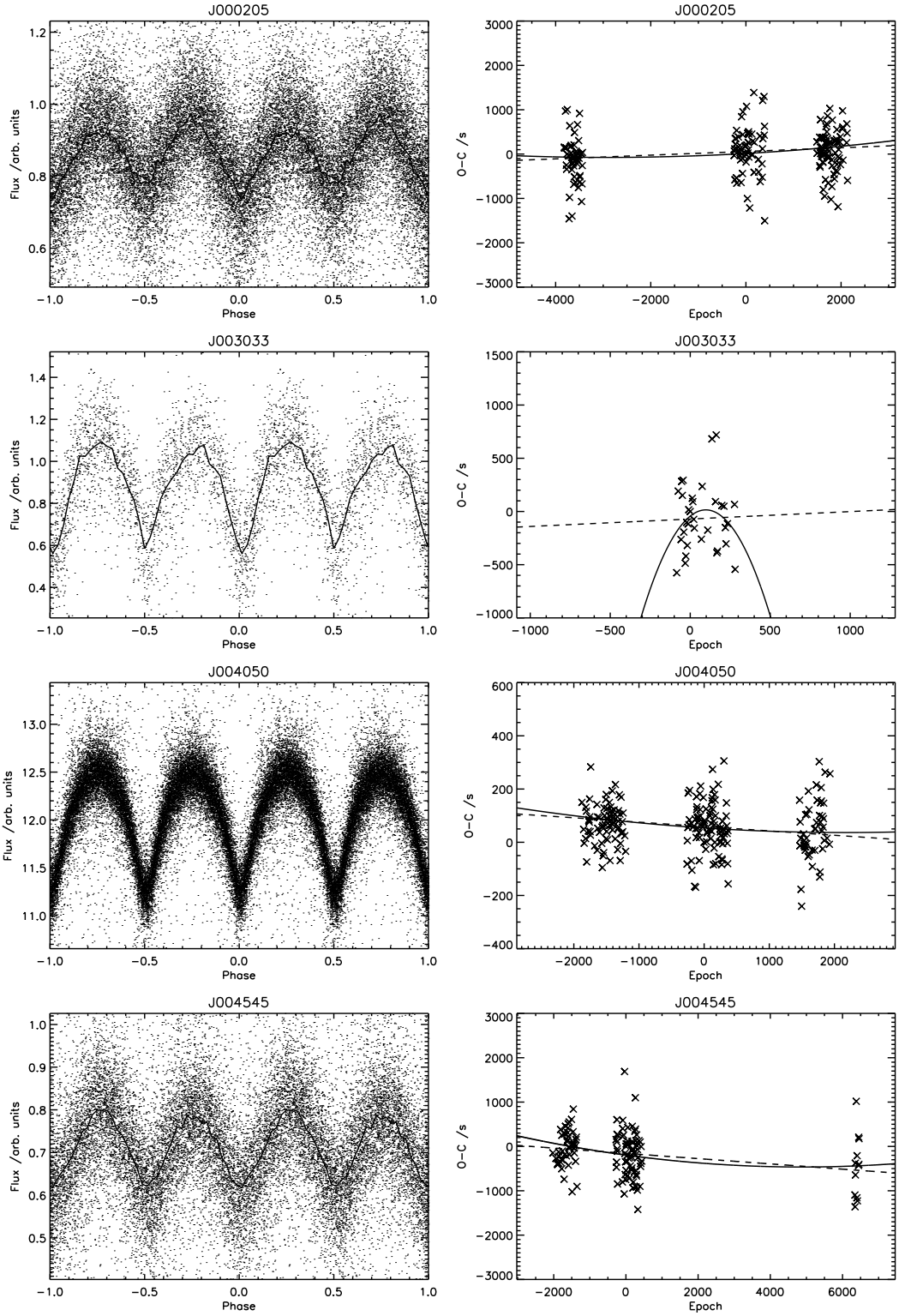

Figure A.1: Light curves and O−C diagrams for 143 objects

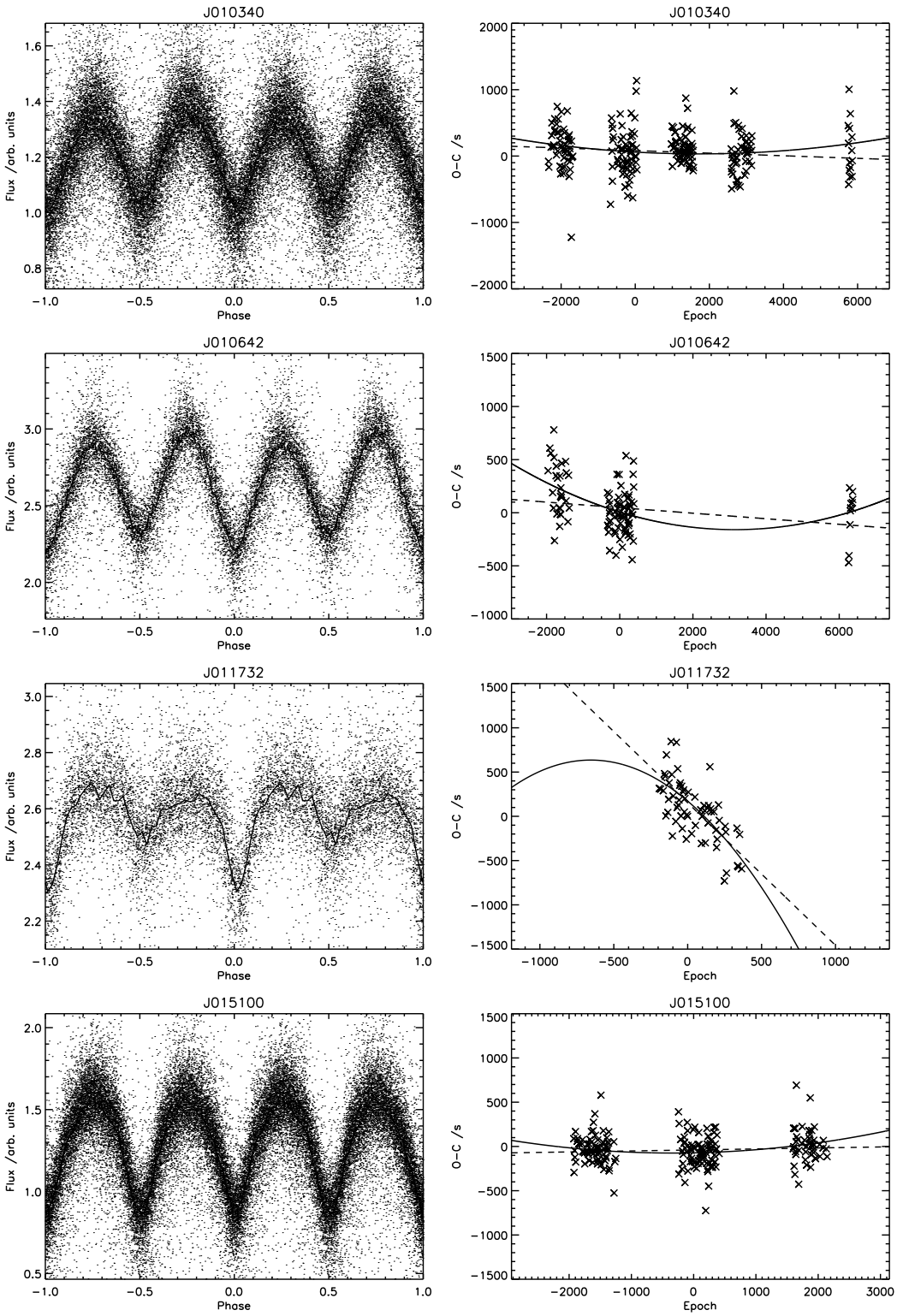
J010340
Flux /arb. units
Phase
J010340
O−C /s
Epoch
J010642
Flux /arb. units
Phase
J010642
O−C /s
Epoch
J011732
Flux /arb. units
Phase
J011732
O−C /s
Epoch
J015100
Flux /arb. units
Phase
J015100
O−C /s
Epoch

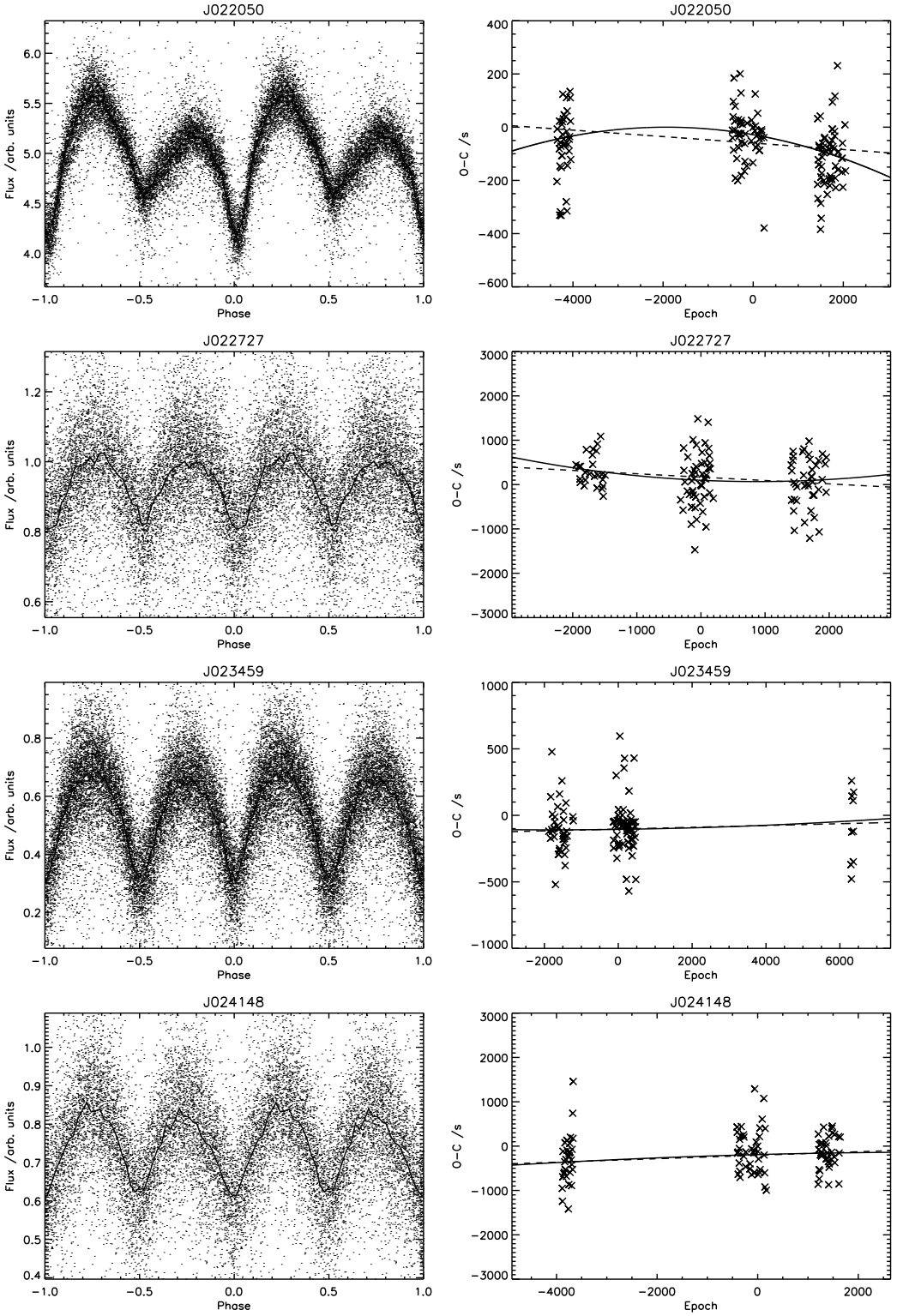
J022050
Flux /arb. units
Phase
J022050
O−C /s
Epoch
J022727
Flux /arb. units
Phase
J022727
O−C /s
Epoch
J023459
Flux /arb. units
Phase
J023459
O−C /s
Epoch
J024148
Flux /arb. units
Phase
J024148
O−C /s
Epoch

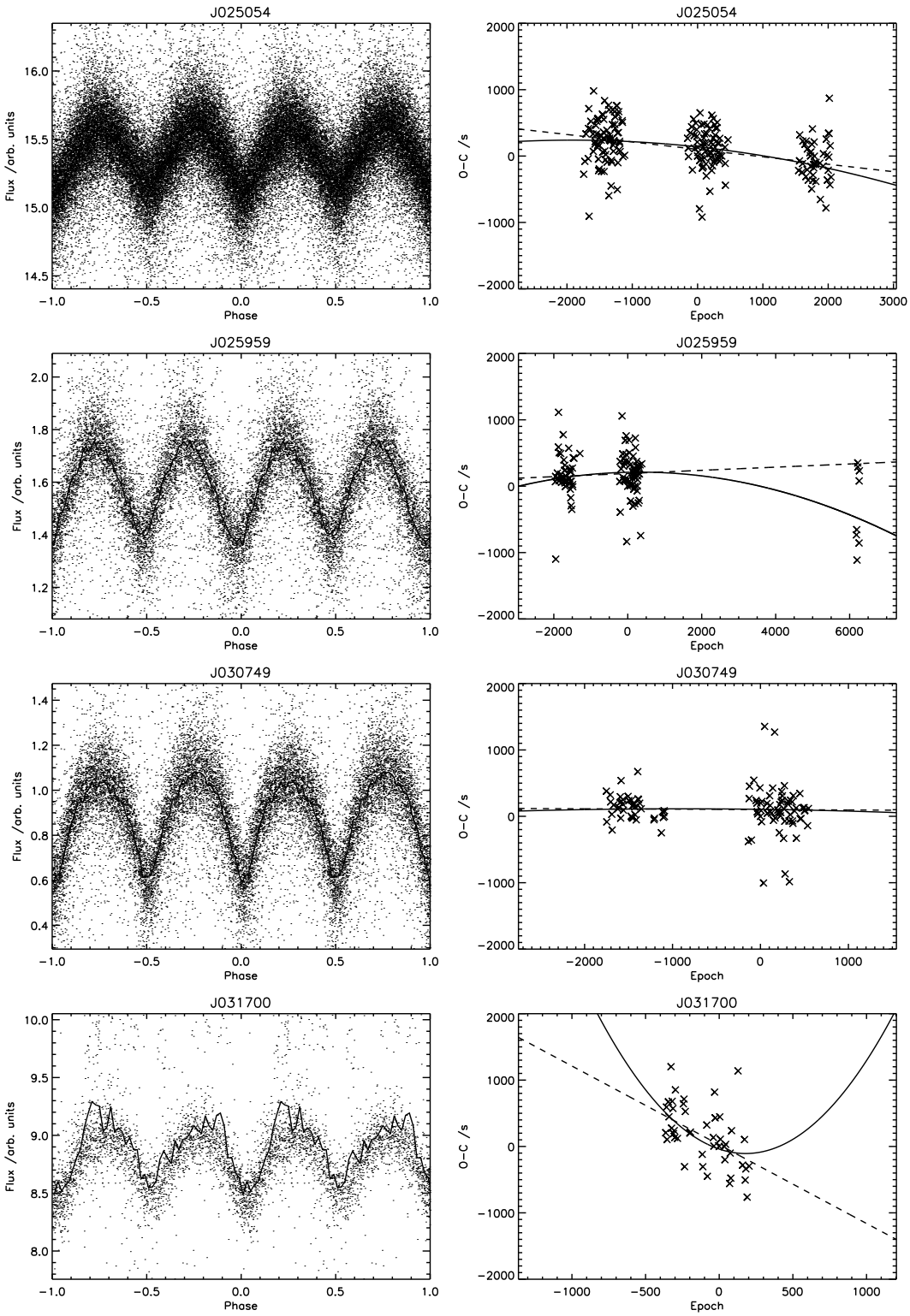
J025054
Flux /orb. units
Phase
J025054
O−C /s
Epoch
J025959
Flux /orb. units
Phase
J025959
O−C /s
Epoch
J030749
Flux /orb. units
Phase
J030749
O−C /s
Epoch
J031700
Flux /orb. units
Phase
J031700
O−C /s
Epoch

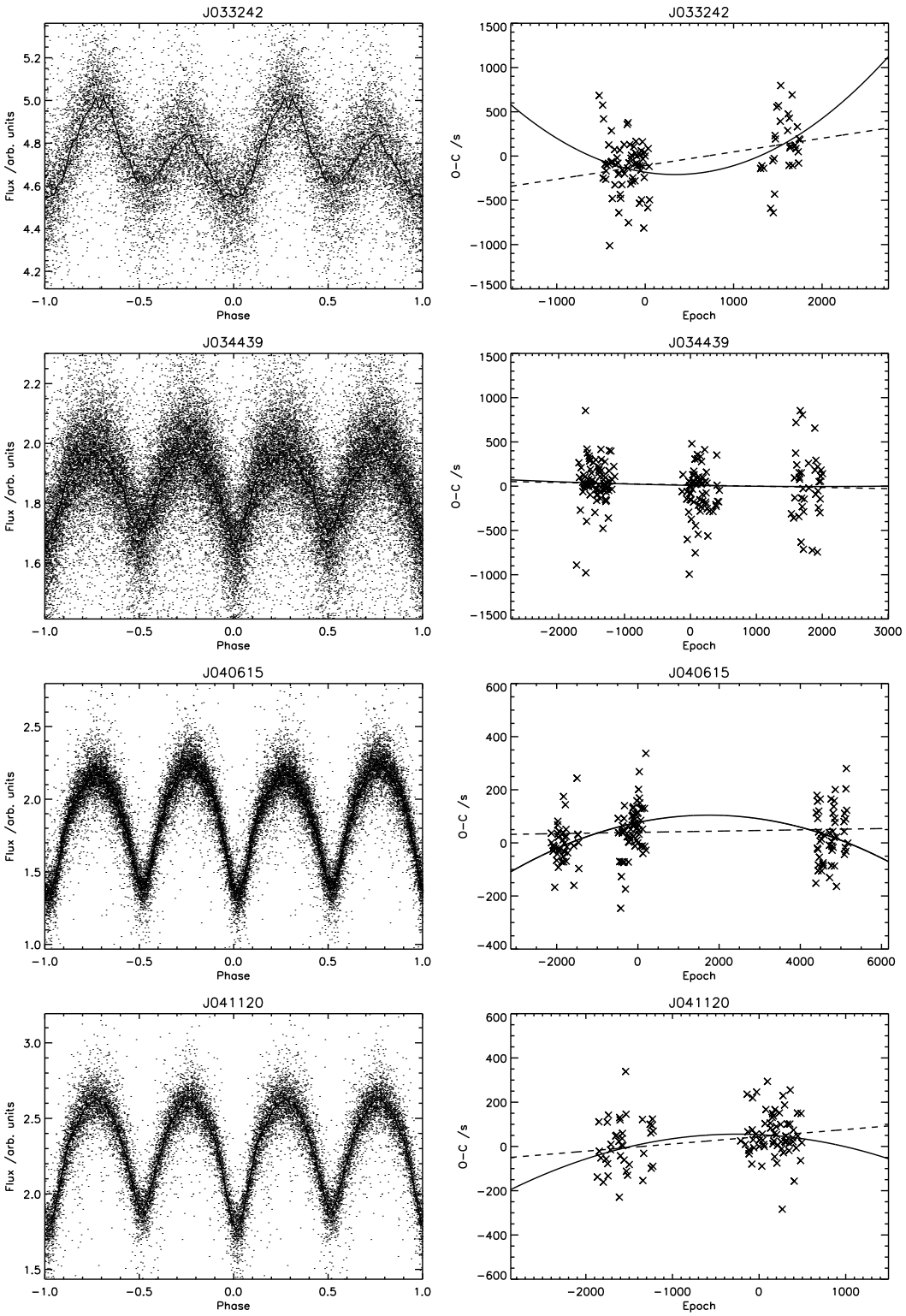
J033242
Flux /arb. units
Phase
J033242
O−C /s
Epoch
J034439
Flux /arb. units
Phase
J034439
O−C /s
Epoch
J040615
Flux /arb. units
Phase
J040615
O−C /s
Epoch
J041120
Flux /arb. units
Phase
J041120
O−C /s
Epoch

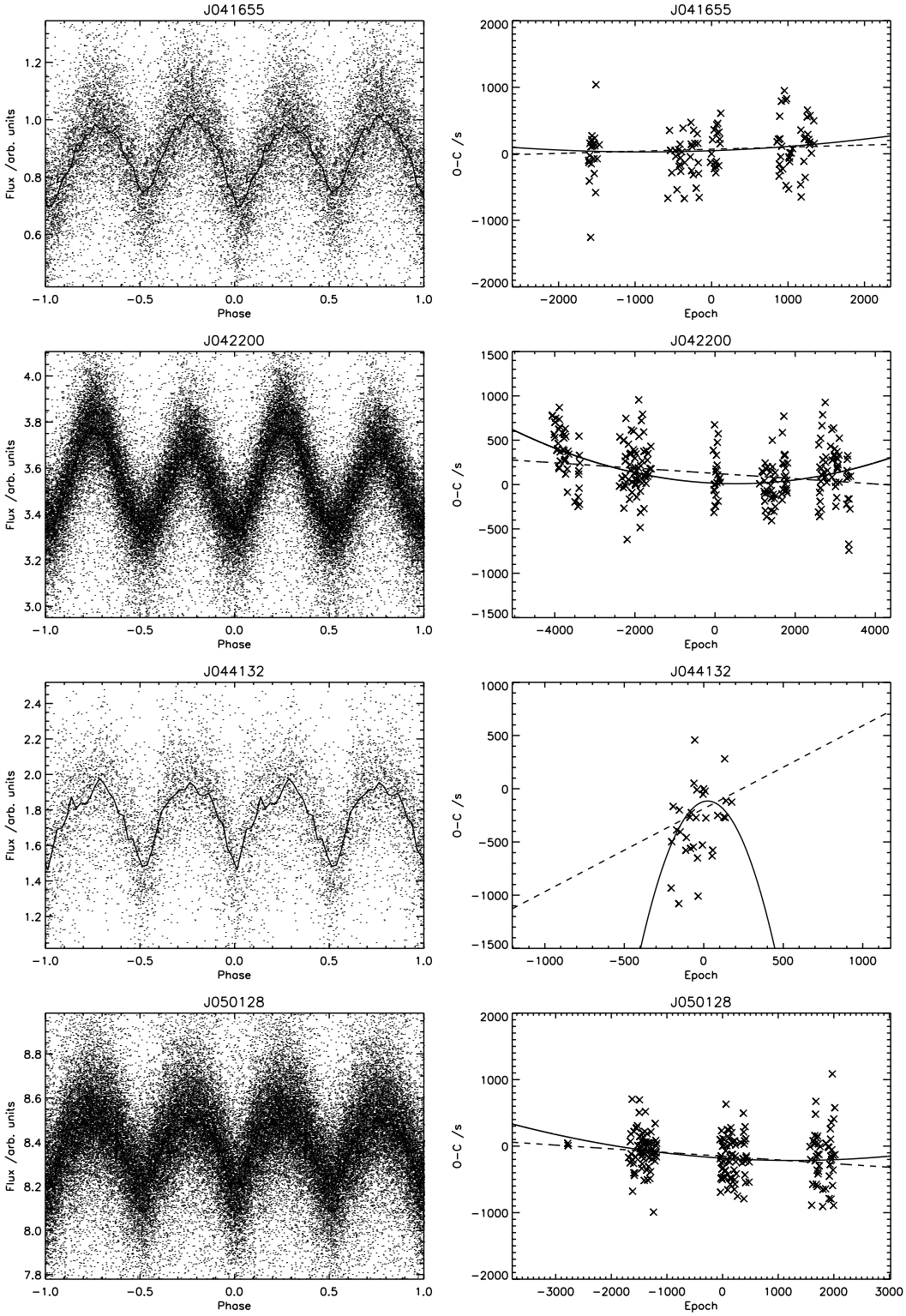
J041655
Flux /arb. units
Phase
J041655
O−C /s
Epoch
J042200
Flux /arb. units
Phase
J042200
O−C /s
Epoch
J044132
Flux /arb. units
Phase
J044132
O−C /s
Epoch
J050128
Flux /arb. units
Phase
J050128
O−C /s
Epoch

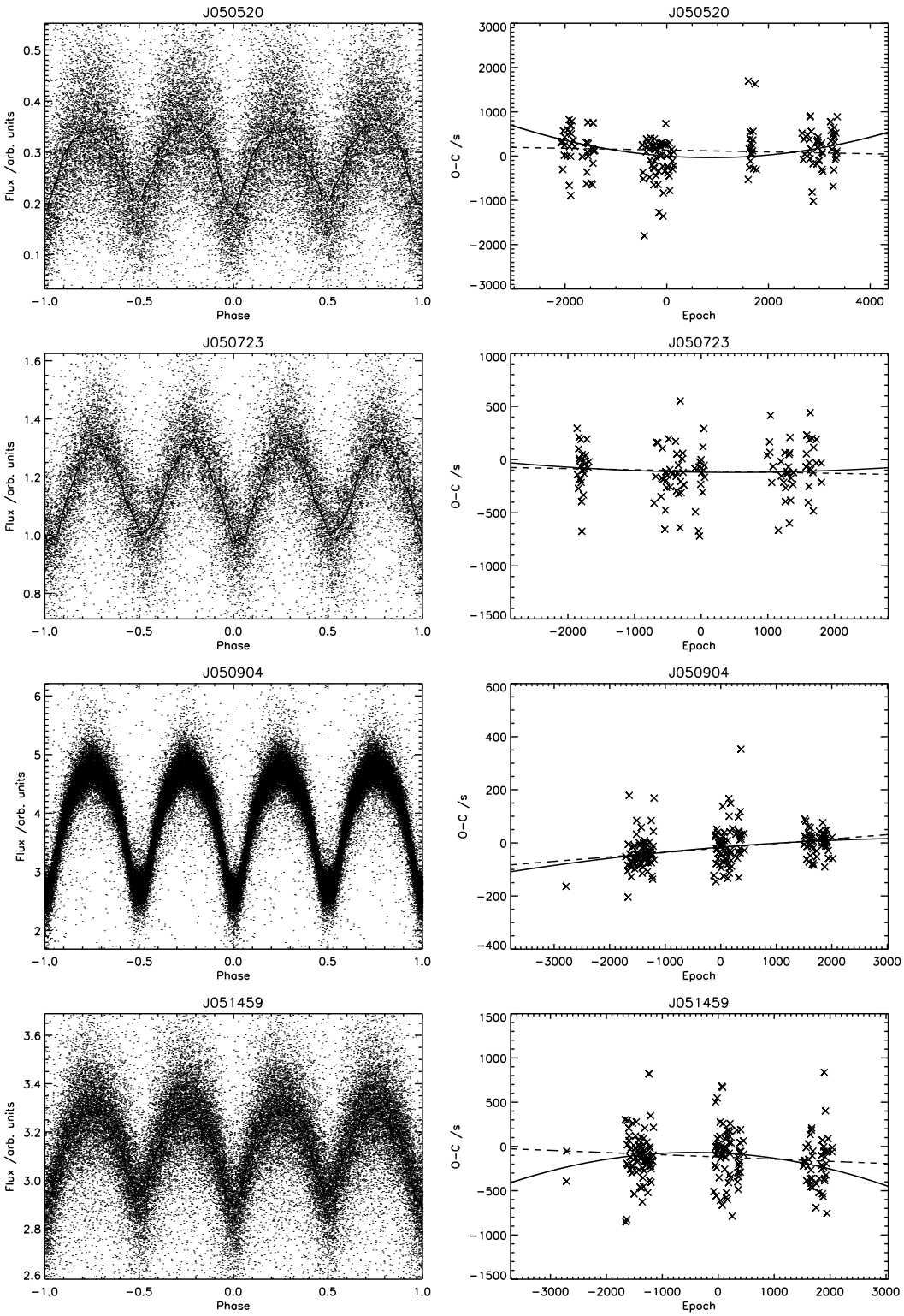
J050520
Flux /arb. units
Phase
J050520
O−C /s
Epoch
J050723
Flux /arb. units
Phase
J050723
O−C /s
Epoch
J050904
Flux /arb. units
Phase
J050904
O−C /s
Epoch
J051459
Flux /arb. units
Phase
J051459
O−C /s
Epoch

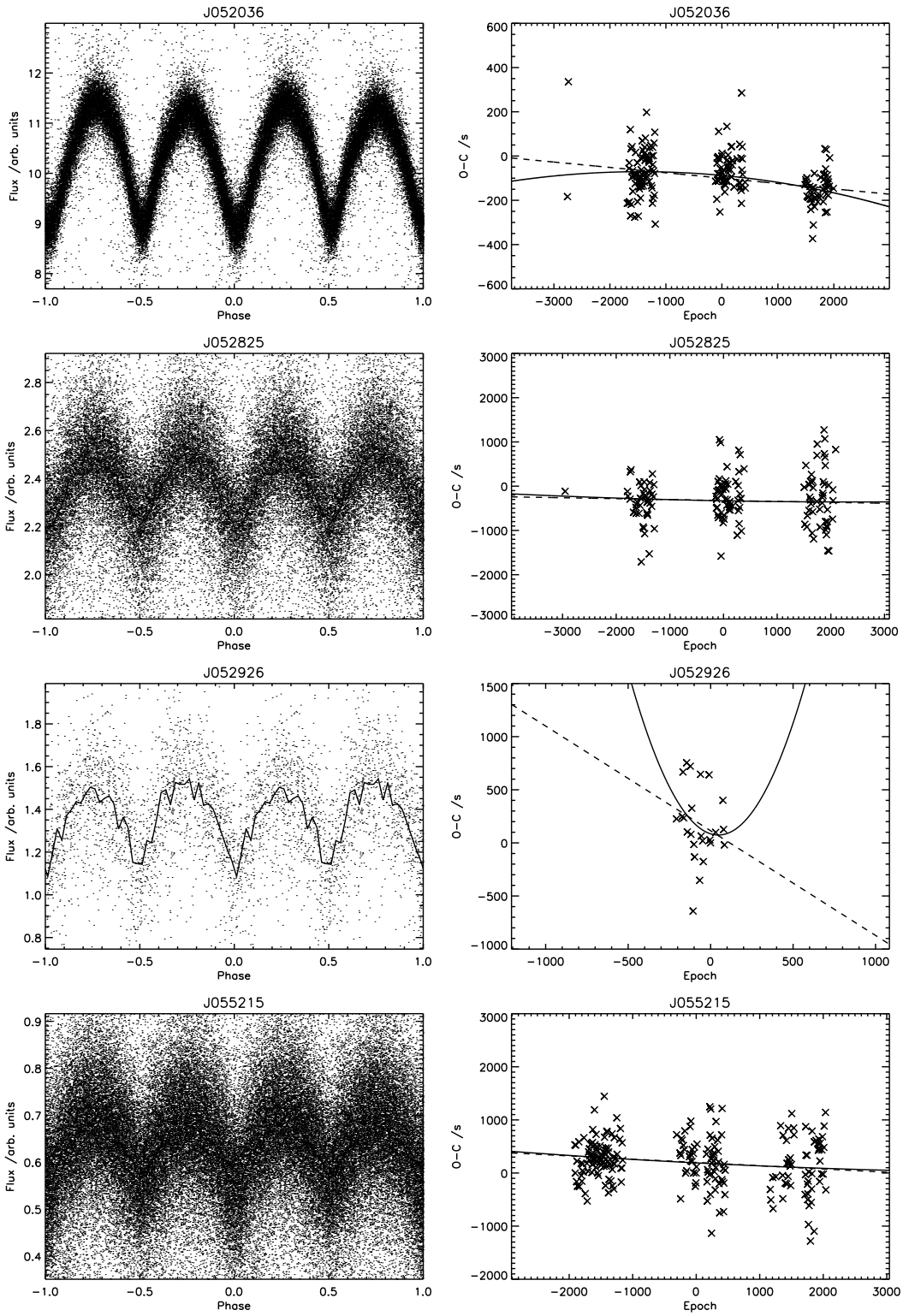
J052036
Flux /arb. units
Phase
J052036
O−C /s
Epoch
J052825
Flux /arb. units
Phase
J052825
O−C /s
Epoch
J052926
Flux /arb. units
Phase
J052926
O−C /s
Epoch
J055215
Flux /arb. units
Phase
J055215
O−C /s
Epoch

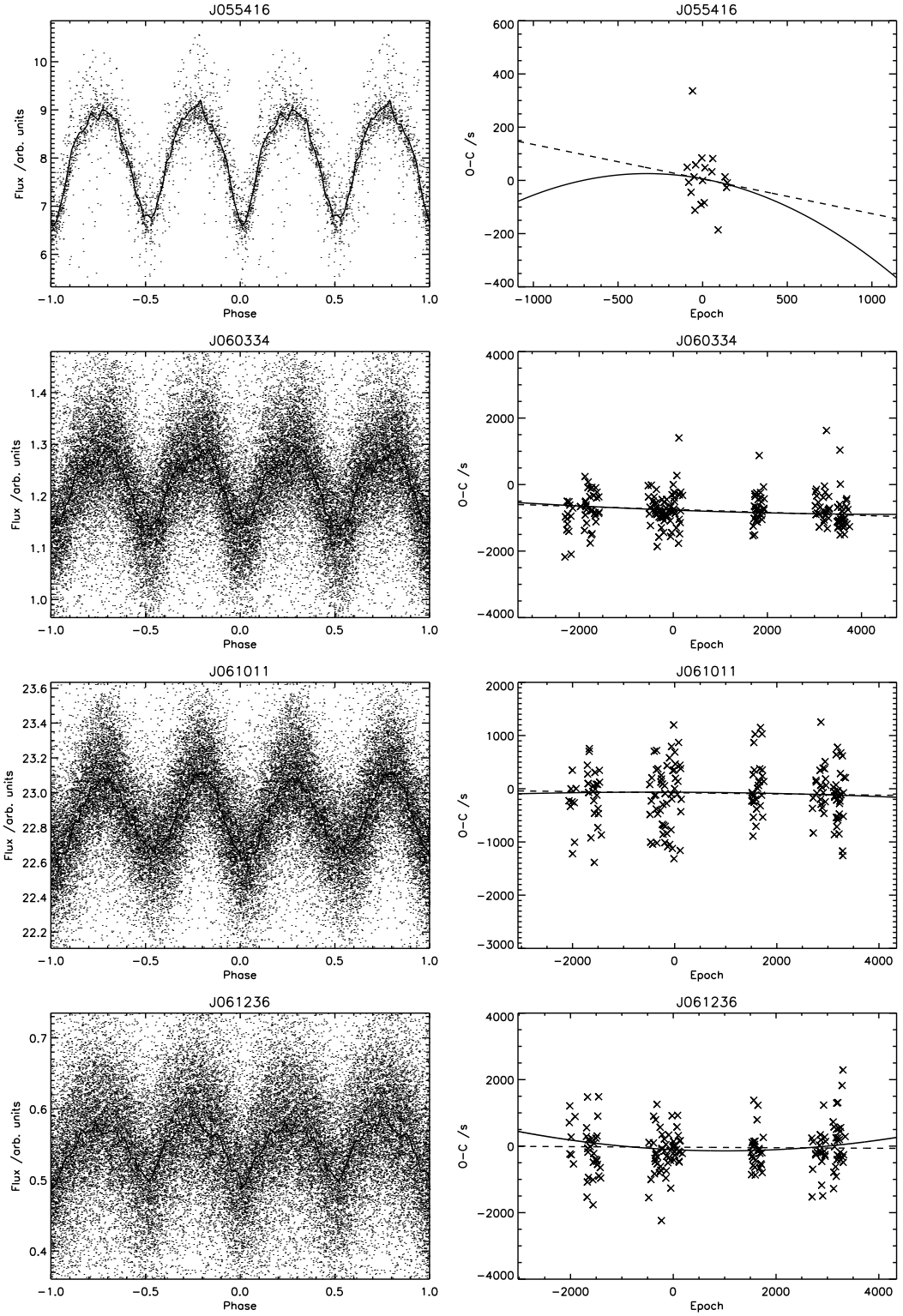
J055416
Flux /arb. units
Phase
J055416
O−C /s
Epoch
J060334
Flux /arb. units
Phase
J060334
O−C /s
Epoch
J061011
Flux /arb. units
Phase
J061011
O−C /s
Epoch
J061236
Flux /arb. units
Phase
J061236
O−C /s
Epoch

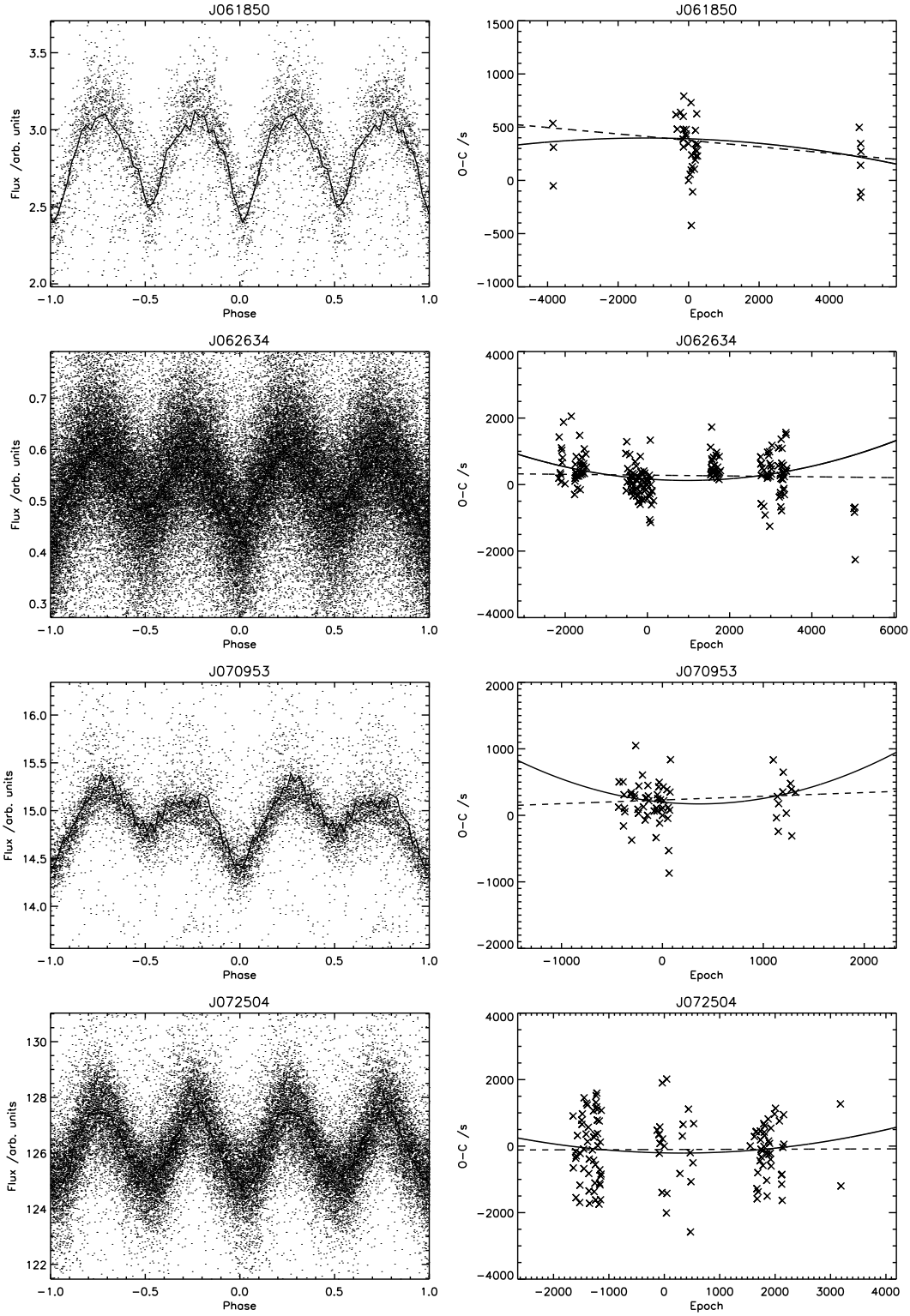
J061850
Flux /arb. units
Phase
J061850
O−C /s
Epoch
J062634
Flux /arb. units
Phase
J062634
O−C /s
Epoch
J070953
Flux /arb. units
Phase
J070953
O−C /s
Epoch
J072504
Flux /arb. units
Phase
J072504
O−C /s
Epoch

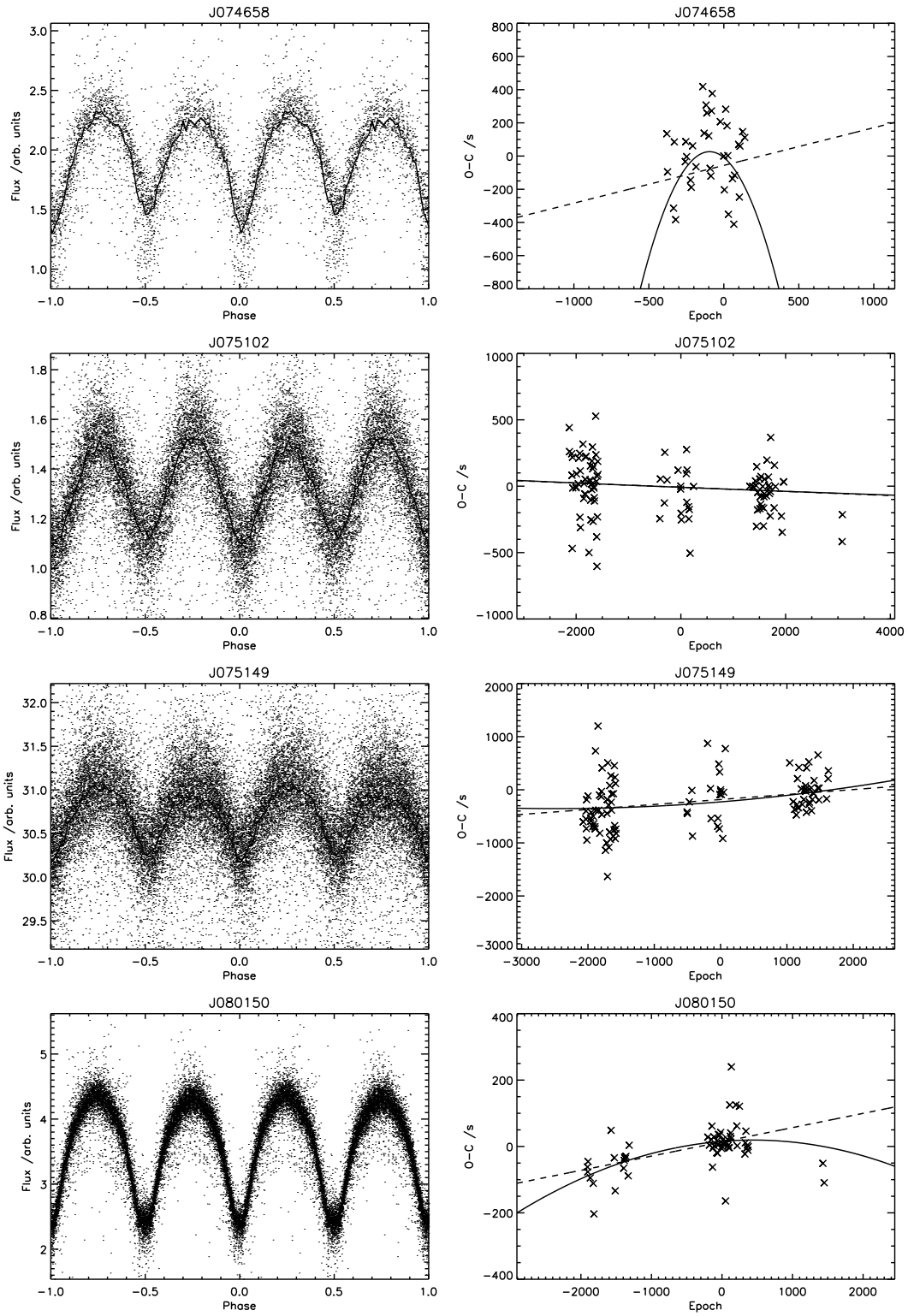
J074658
Flux /arb. units
Phase
J074658
O−C /s
Epoch
J075102
Flux /arb. units
Phase
J075102
O−C /s
Epoch
J075149
Flux /arb. units
Phase
J075149
O−C /s
Epoch
J080150
Flux /arb. units
Phase
J080150
O−C /s
Epoch

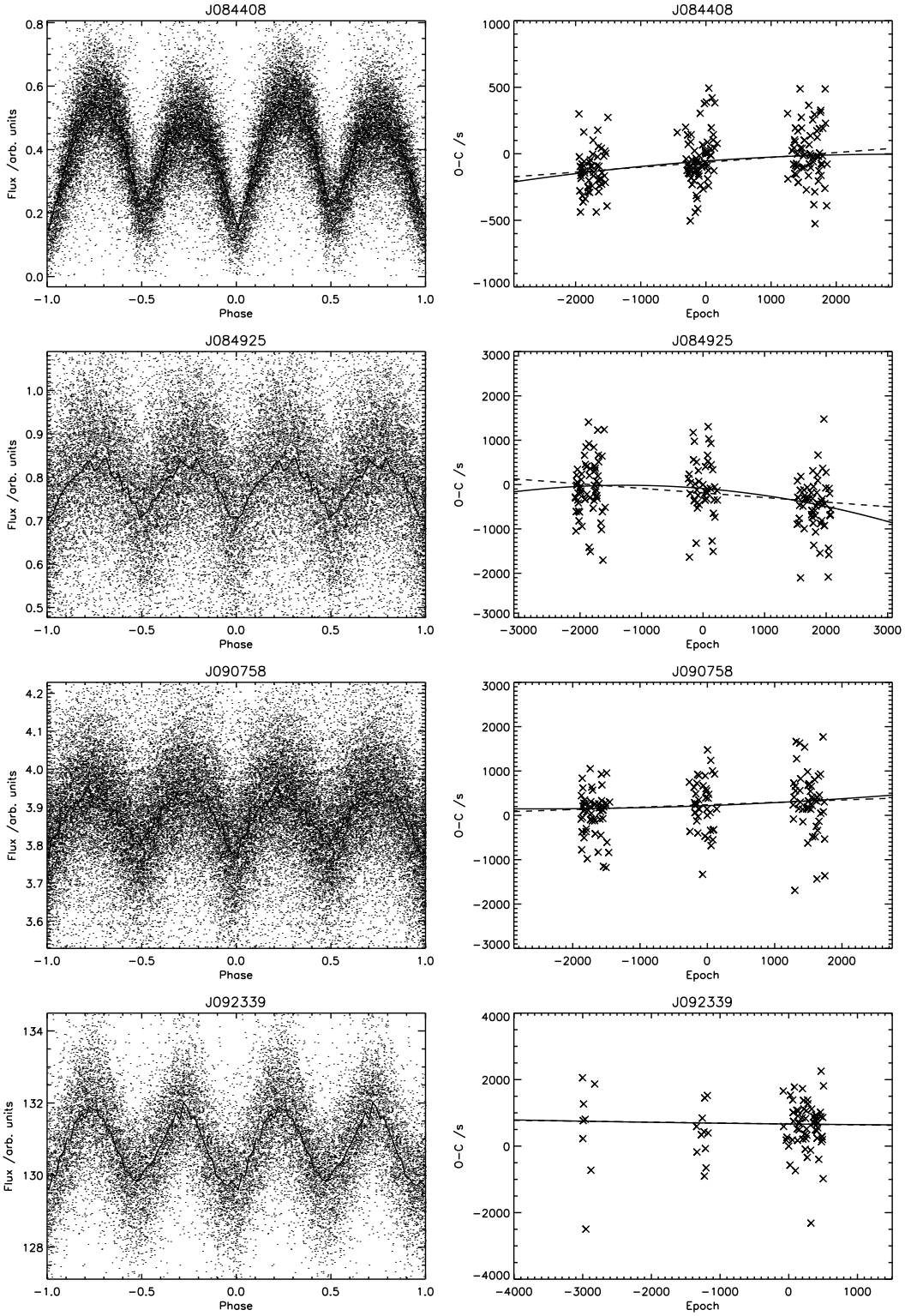
J084408
Flux /arb. units
Phase
J084408
O−C /s
Epoch
J084925
Flux /arb. units
Phase
J084925
O−C /s
Epoch
J090758
Flux /arb. units
Phase
J090758
O−C /s
Epoch
J092339
Flux /arb. units
Phase
J092339
O−C /s
Epoch

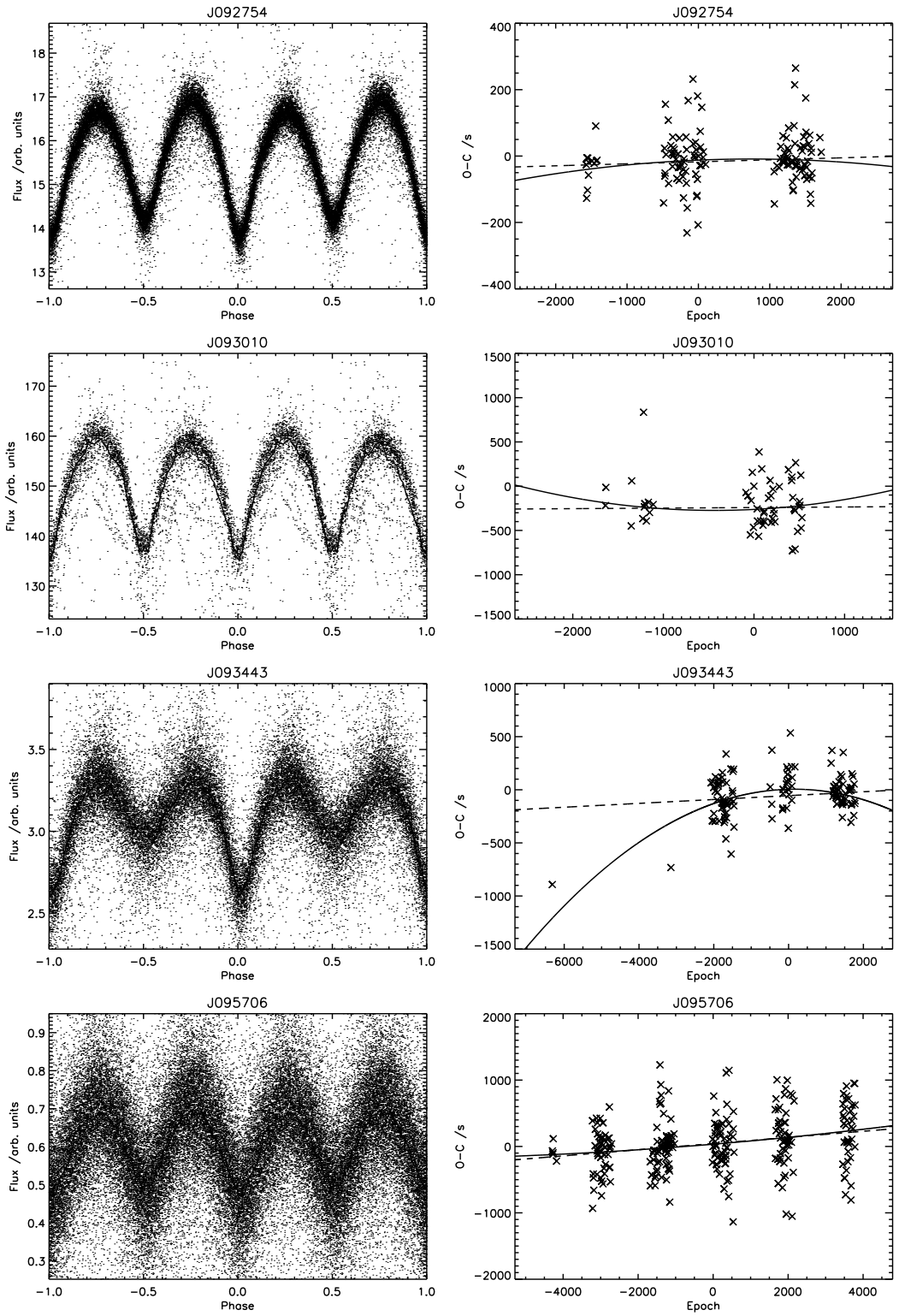
J092754
Flux /arb. units
Phase
J092754
O−C /s
Epoch
J093010
Flux /arb. units
Phase
J093010
O−C /s
Epoch
J093443
Flux /arb. units
Phase
J093443
O−C /s
Epoch
J095706
Flux /arb. units
Phase
J095706
O−C /s
Epoch

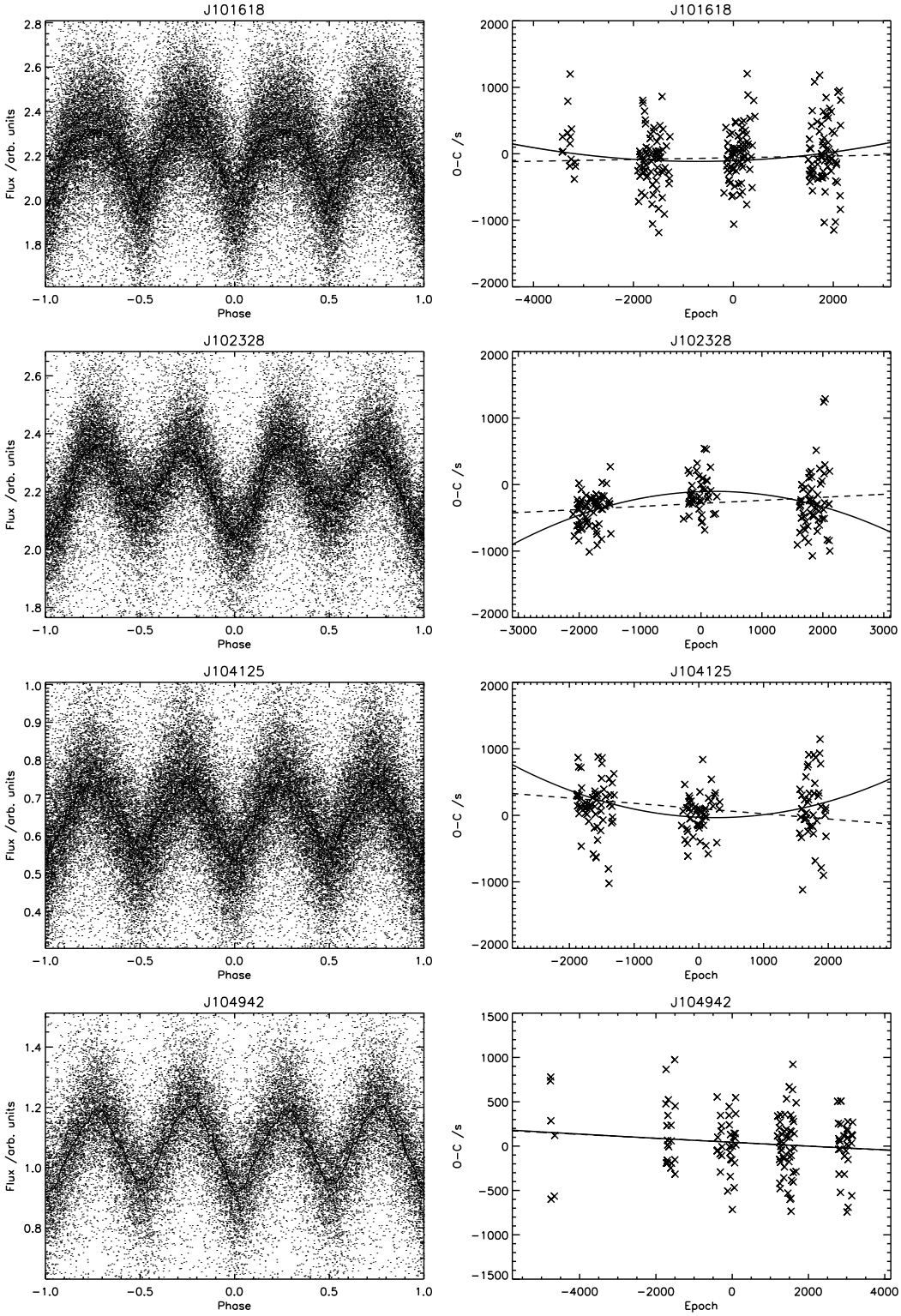
J101618
Flux /arb. units
Phase
J101618
O−C /s
Epoch
J102328
Flux /arb. units
Phase
J102328
O−C /s
Epoch
J104125
Flux /arb. units
Phase
J104125
O−C /s
Epoch
J104942
Flux /arb. units
Phase
J104942
O−C /s
Epoch

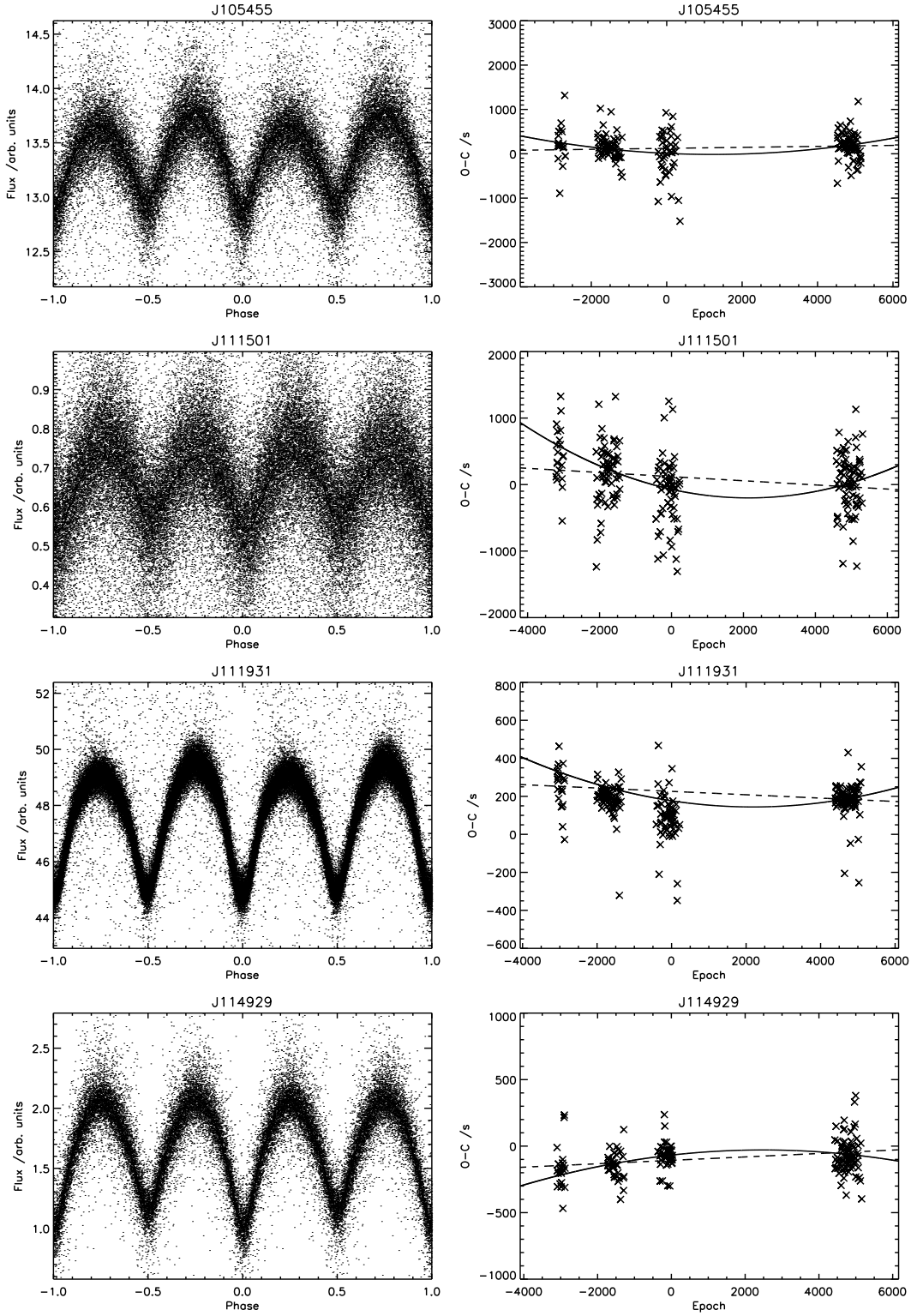
J105455
Flux /arb. units
Phase
J105455
O−C /s
Epoch
J111501
Flux /arb. units
Phase
J111501
O−C /s
Epoch
J111931
Flux /arb. units
Phase
J111931
O−C /s
Epoch
J114929
Flux /arb. units
Phase
J114929
O−C /s
Epoch

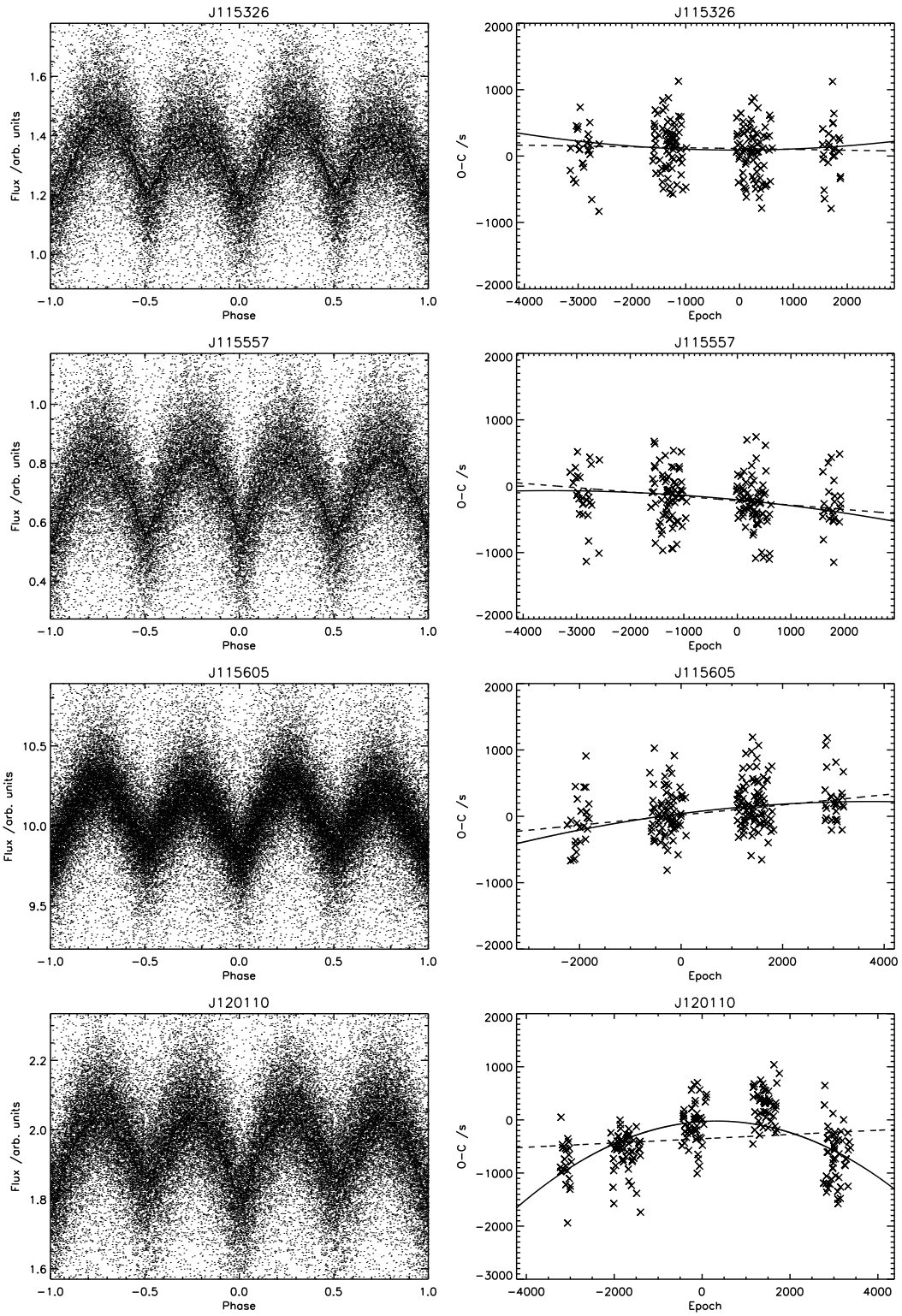
J115326
Flux /arb. units
Phase
J115326
O−C /s
Epoch
J115557
Flux /arb. units
Phase
J115557
O−C /s
Epoch
J115605
Flux /arb. units
Phase
J115605
O−C /s
Epoch
J120110
Flux /arb. units
Phase
J120110
O−C /s
Epoch

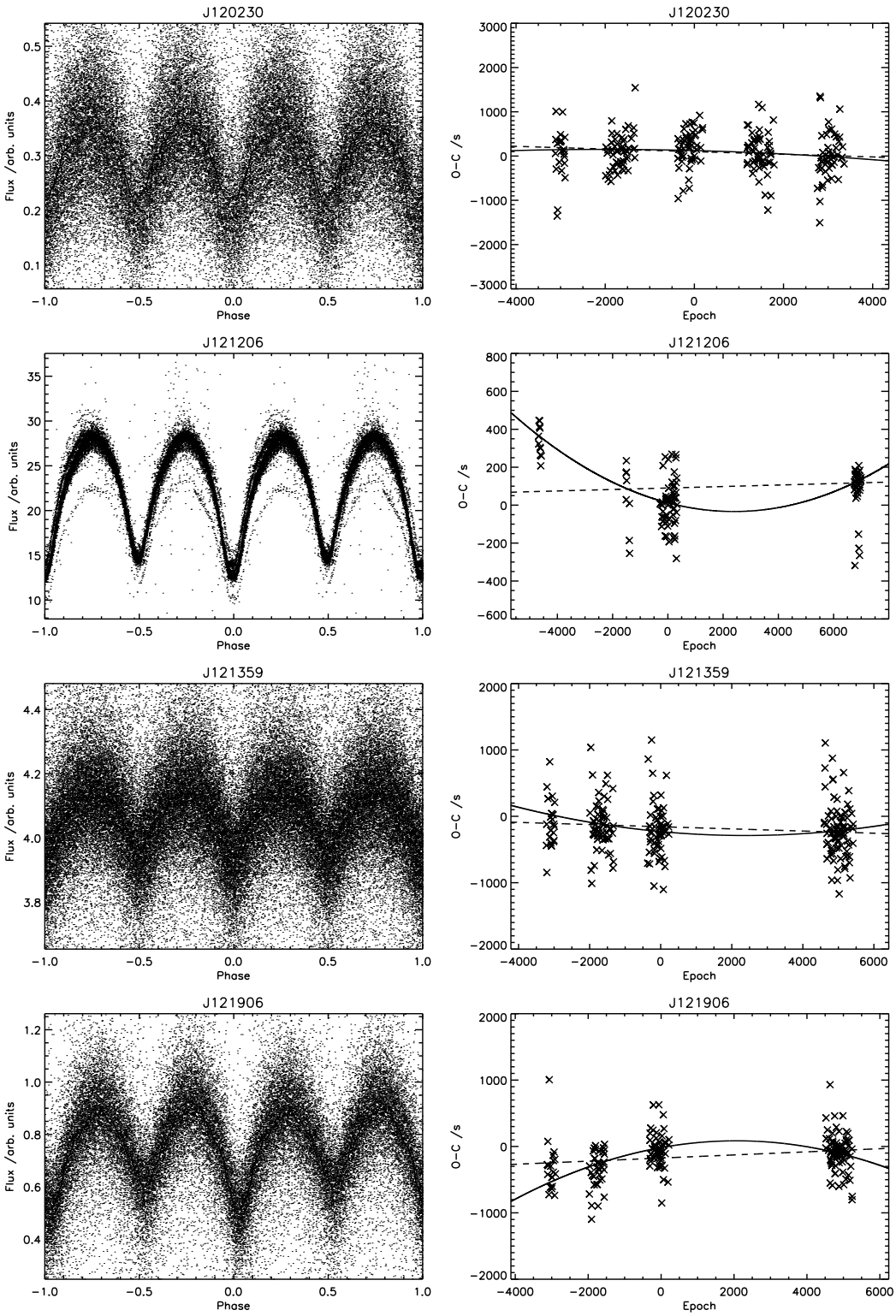
J120230
Flux /arb. units
Phase
J120230
O−C /s
Epoch
J121206
Flux /arb. units
Phase
J121206
O−C /s
Epoch
J121359
Flux /arb. units
Phase
J121359
O−C /s
Epoch
J121906
Flux /arb. units
Phase
J121906
O−C /s
Epoch

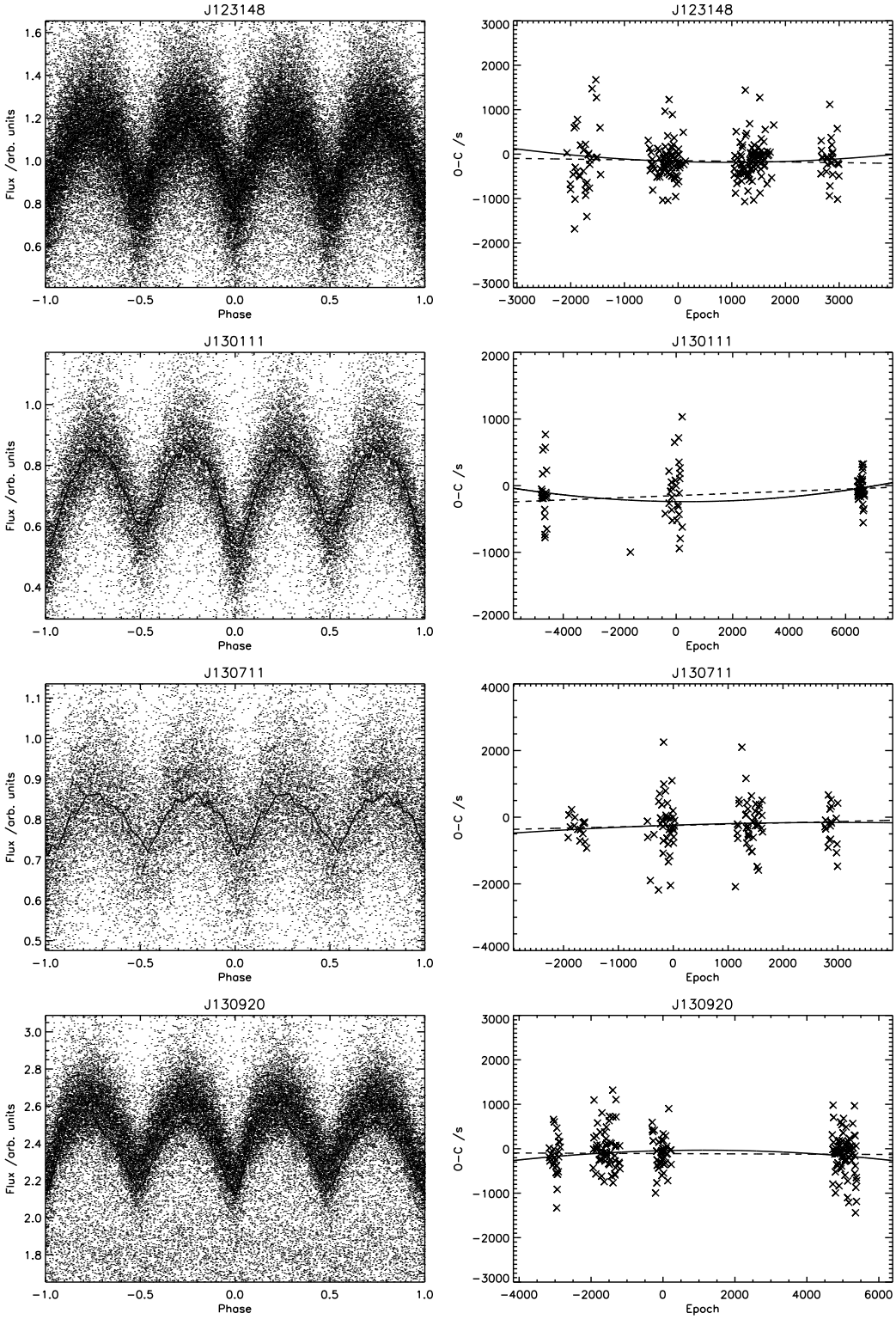
J123148
Flux /arb. units
Phase
J123148
O−C /s
Epoch
J130111
Flux /arb. units
Phase
J130111
O−C /s
Epoch
J130711
Flux /arb. units
Phase
J130711
O−C /s
Epoch
J130920
Flux /arb. units
Phase
J130920
O−C /s
Epoch

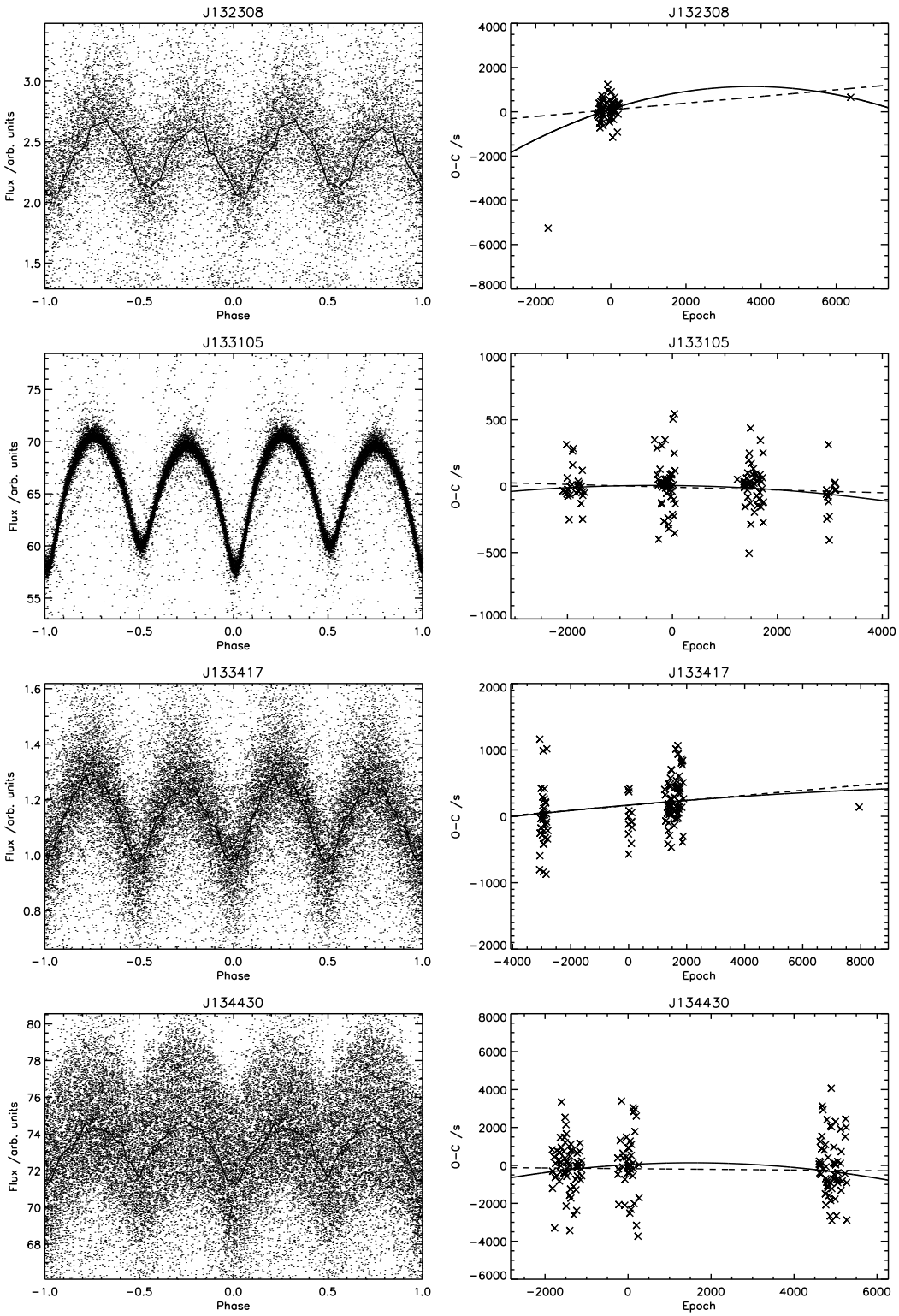
J132308
Flux /arb. units
Phase
J132308
O−C /s
Epoch
J133105
Flux /arb. units
Phase
J133105
O−C /s
Epoch
J133417
Flux /arb. units
Phase
J133417
O−C /s
Epoch
J134430
Flux /arb. units
Phase
J134430
O−C /s
Epoch

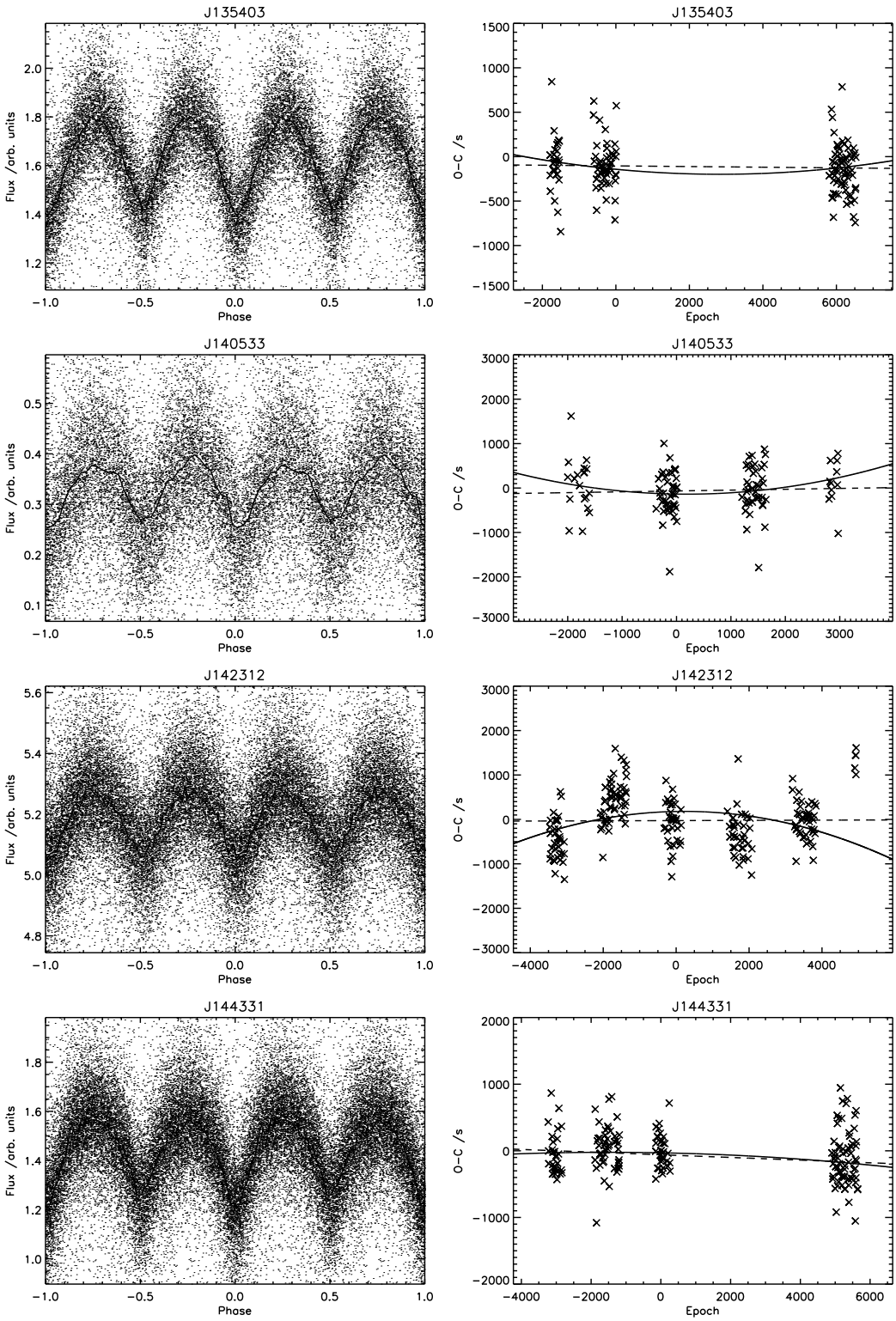
J135403
Flux /arb. units
Phase
J135403
O−C /s
Epoch
J140533
Flux /arb. units
Phase
J140533
O−C /s
Epoch
J142312
Flux /arb. units
Phase
J142312
O−C /s
Epoch
J144331
Flux /arb. units
Phase
J144331
O−C /s
Epoch

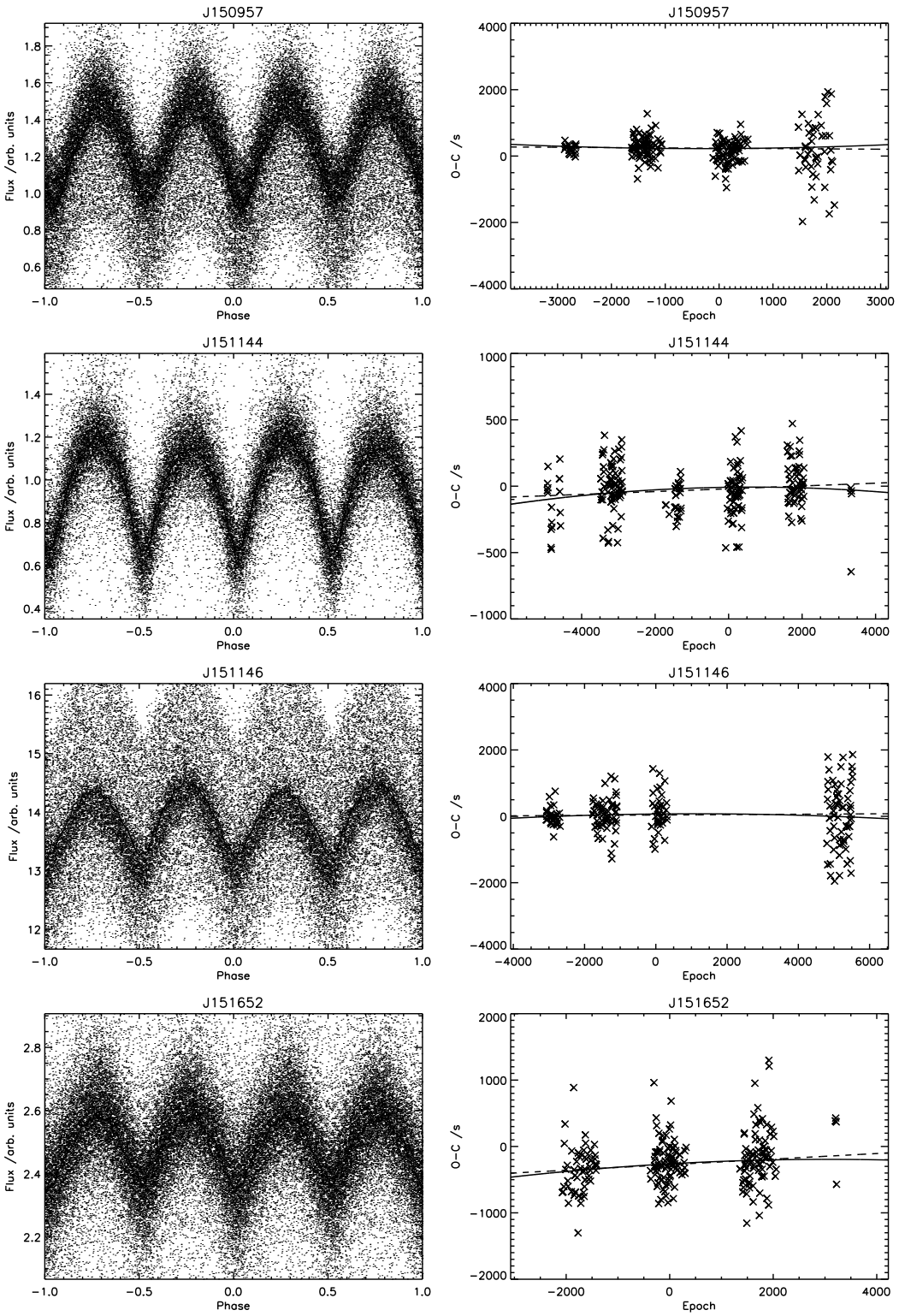
J150957
Flux /arb. units
Phase
J150957
O−C /s
Epoch
J151144
Flux /arb. units
Phase
J151144
O−C /s
Epoch
J151146
Flux /arb. units
Phase
J151146
O−C /s
Epoch
J151652
Flux /arb. units
Phase
J151652
O−C /s
Epoch

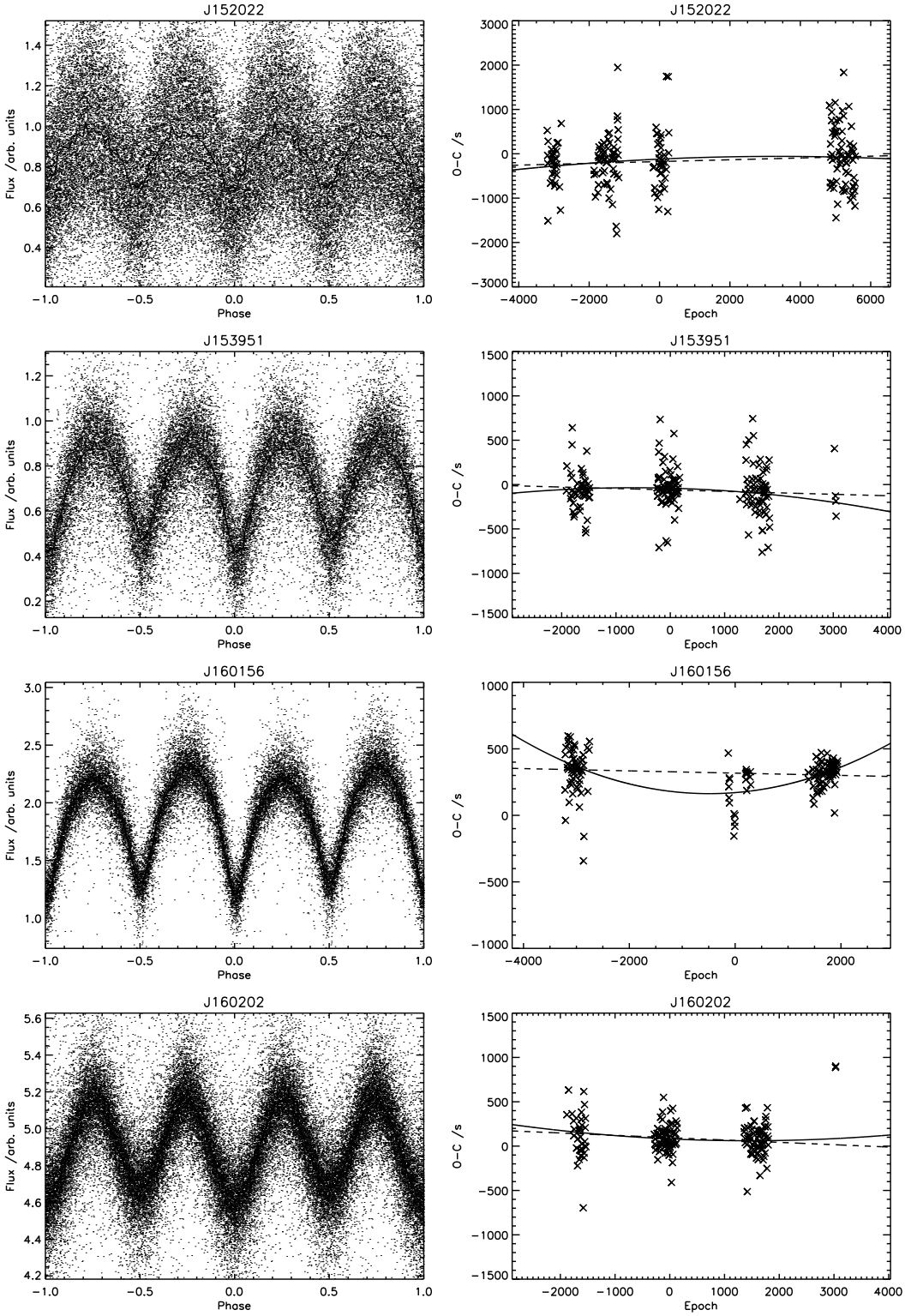
J152022
Flux /arb. units
Phase
J152022
O−C /s
Epoch
J153951
Flux /arb. units
Phase
J153951
O−C /s
Epoch
J160156
Flux /arb. units
Phase
J160156
O−C /s
Epoch
J160202
Flux /arb. units
Phase
J160202
O−C /s
Epoch

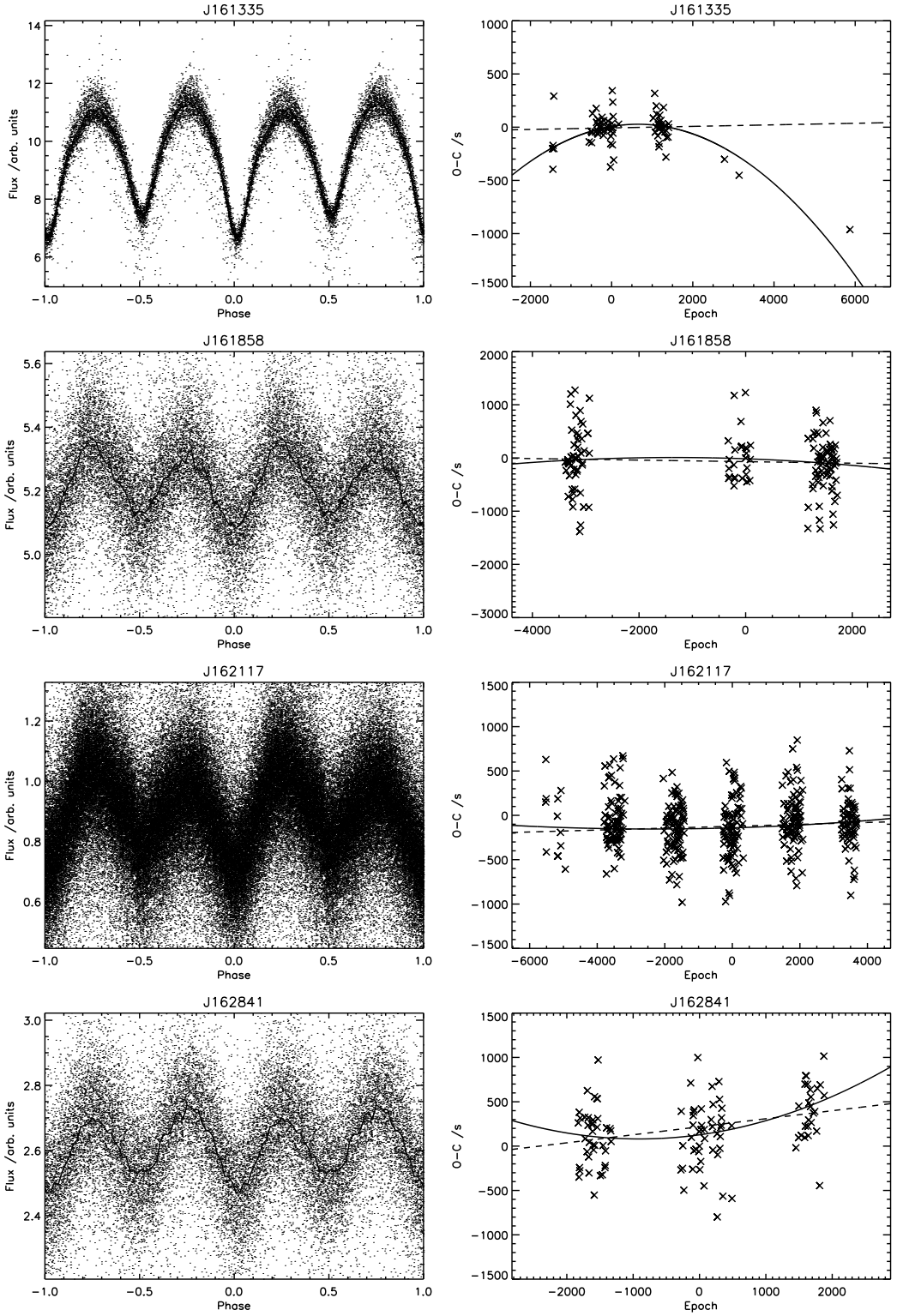
J161335
Flux /arb. units
Phase
J161335
O−C /s
Epoch
J161858
Flux /arb. units
Phase
J161858
O−C /s
Epoch
J162117
Flux /arb. units
Phase
J162117
O−C /s
Epoch
J162841
Flux /arb. units
Phase
J162841
O−C /s
Epoch

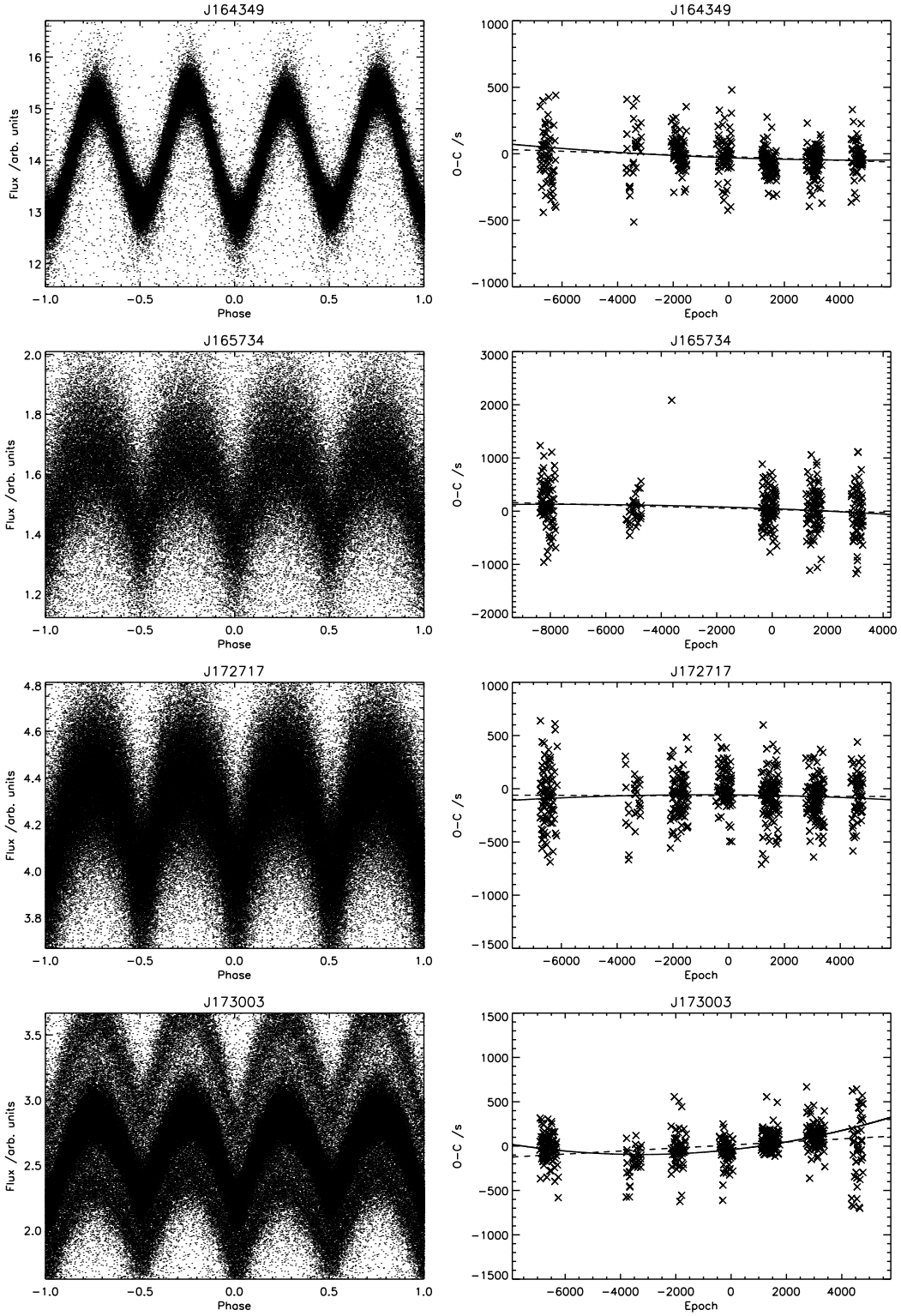
J164349
Flux /arb. units
Phase
J164349
O−C /s
Epoch
J165734
Flux /arb. units
Phase
J165734
O−C /s
Epoch
J172717
Flux /arb. units
Phase
J172717
O−C /s
Epoch
J173003
Flux /arb. units
Phase
J173003
O−C /s
Epoch

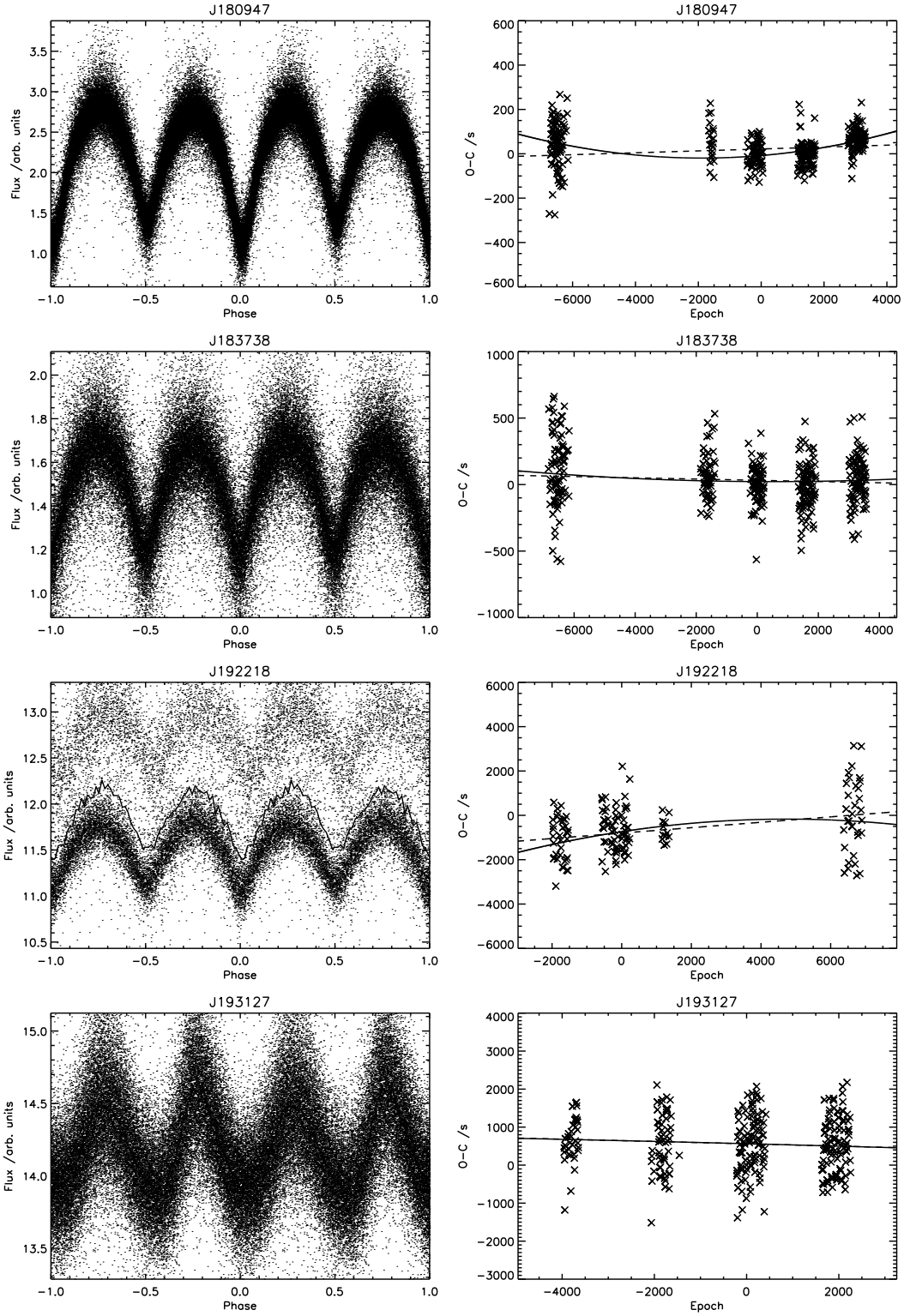
J180947
Flux /arb. units
Phase
J180947
O−C /s
Epoch
J183738
Flux /arb. units
Phase
J183738
O−C /s
Epoch
J192218
Flux /arb. units
Phase
J192218
O−C /s
Epoch
J193127
Flux /arb. units
Phase
J193127
O−C /s
Epoch

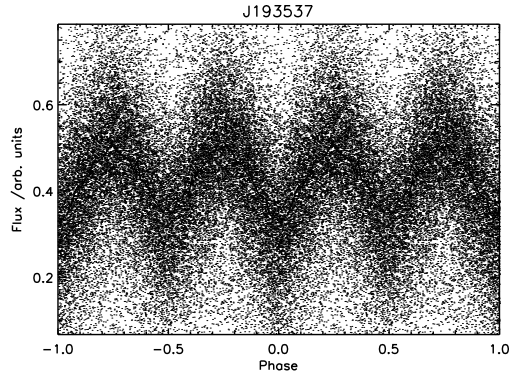
J193537
Flux /arb. units
Phase

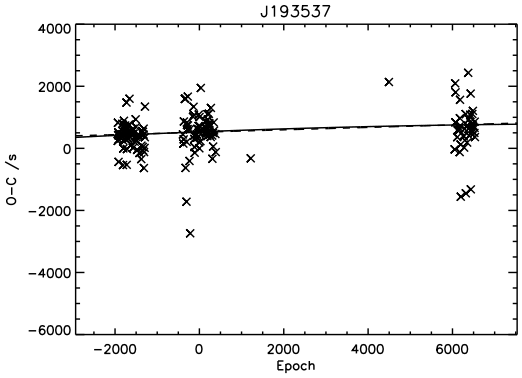
J193537
O−C /s
Epoch

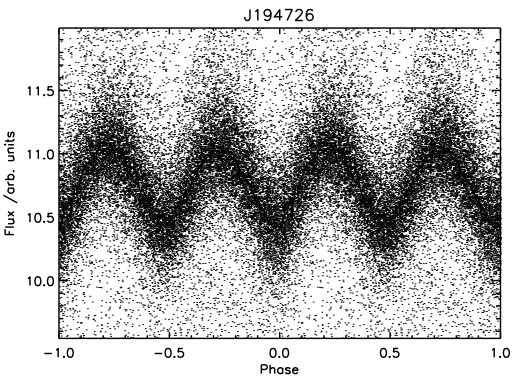
J194726
Flux /arb. units
Phase

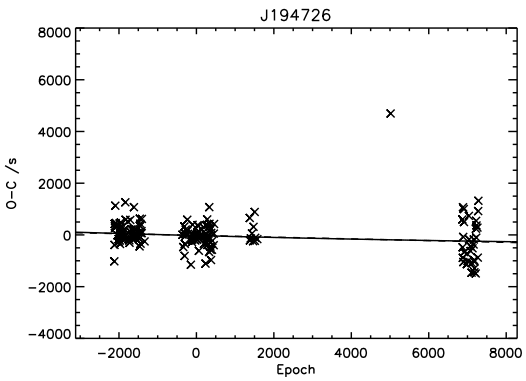
J194726
O−C /s
Epoch

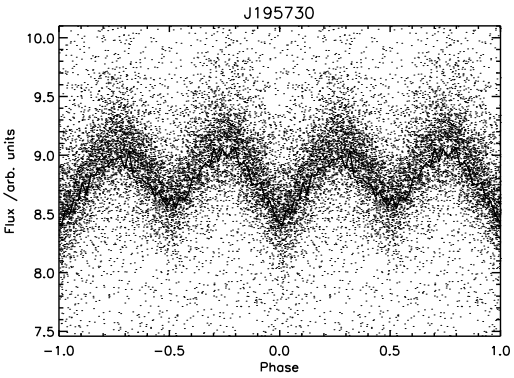
J195730
Flux /arb. units
Phase

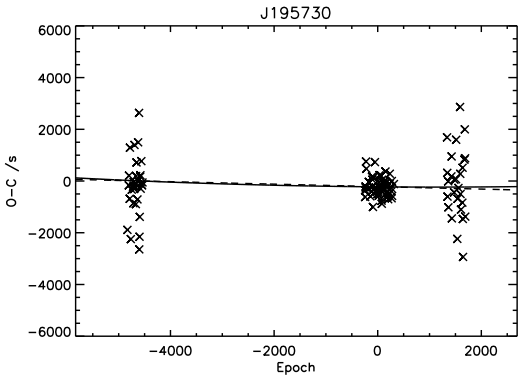
J195730
O−C /s
Epoch

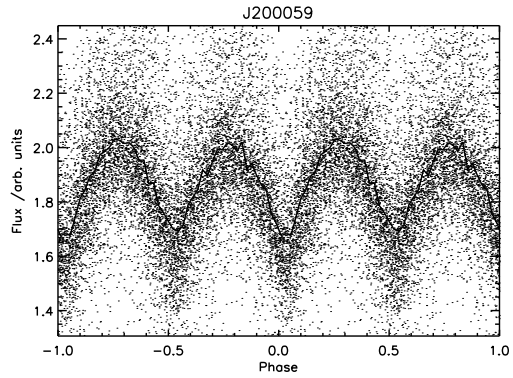
J200059
Flux /arb. units
Phase

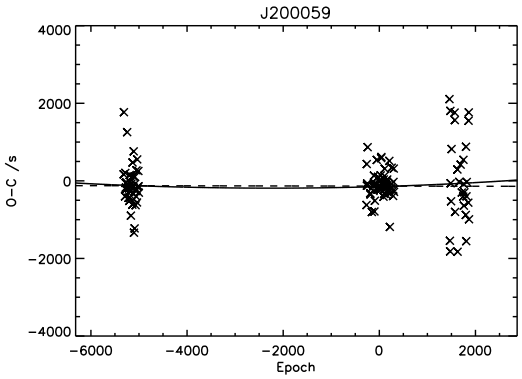
J200059
O−C /s
Epoch

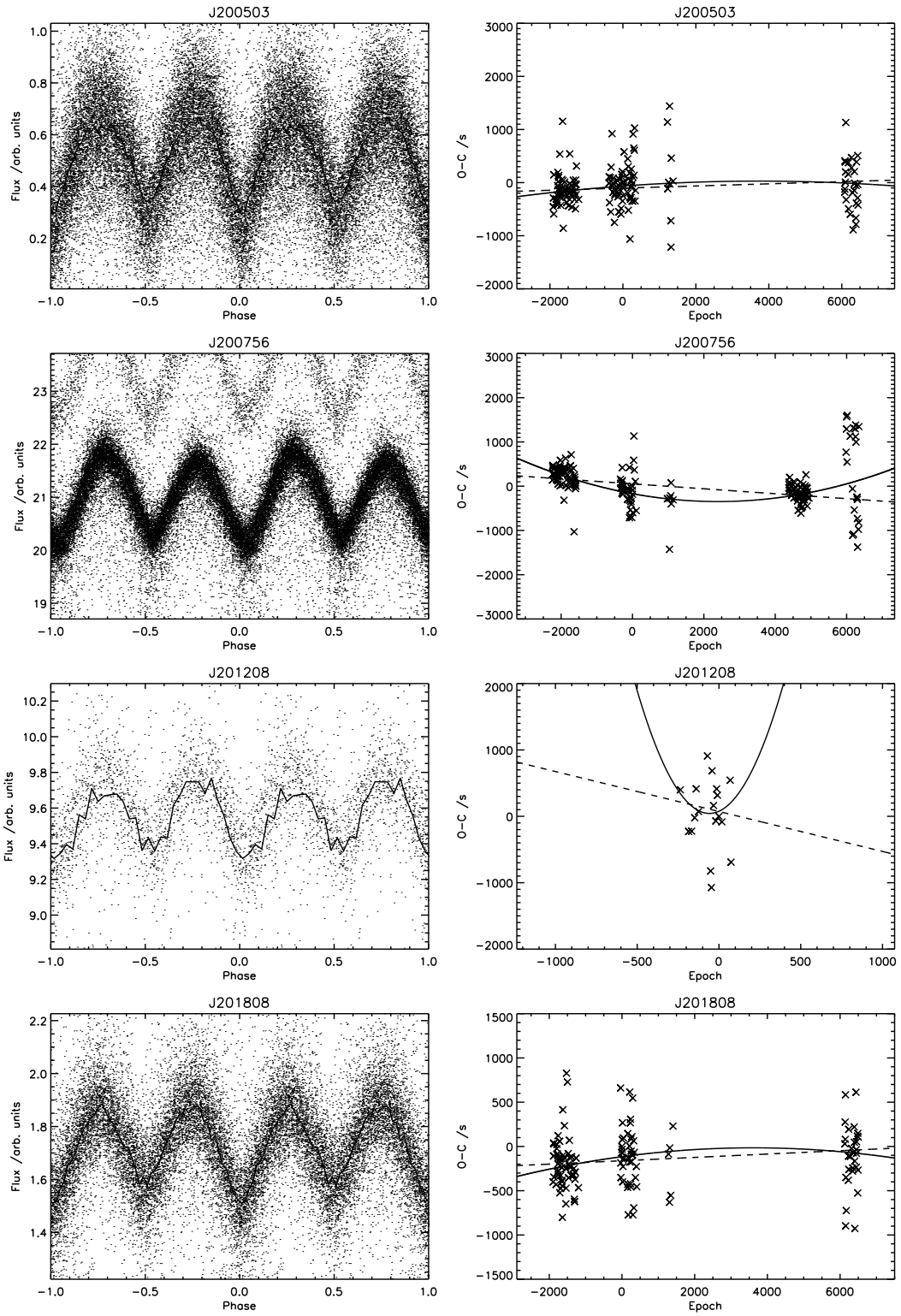
J200503
Flux /arb. units
Phase
J200503
O−C /s
Epoch
J200756
Flux /arb. units
Phase
J200756
O−C /s
Epoch
J201208
Flux /arb. units
Phase
J201208
O−C /s
Epoch
J201808
Flux /arb. units
Phase
J201808
O−C /s
Epoch

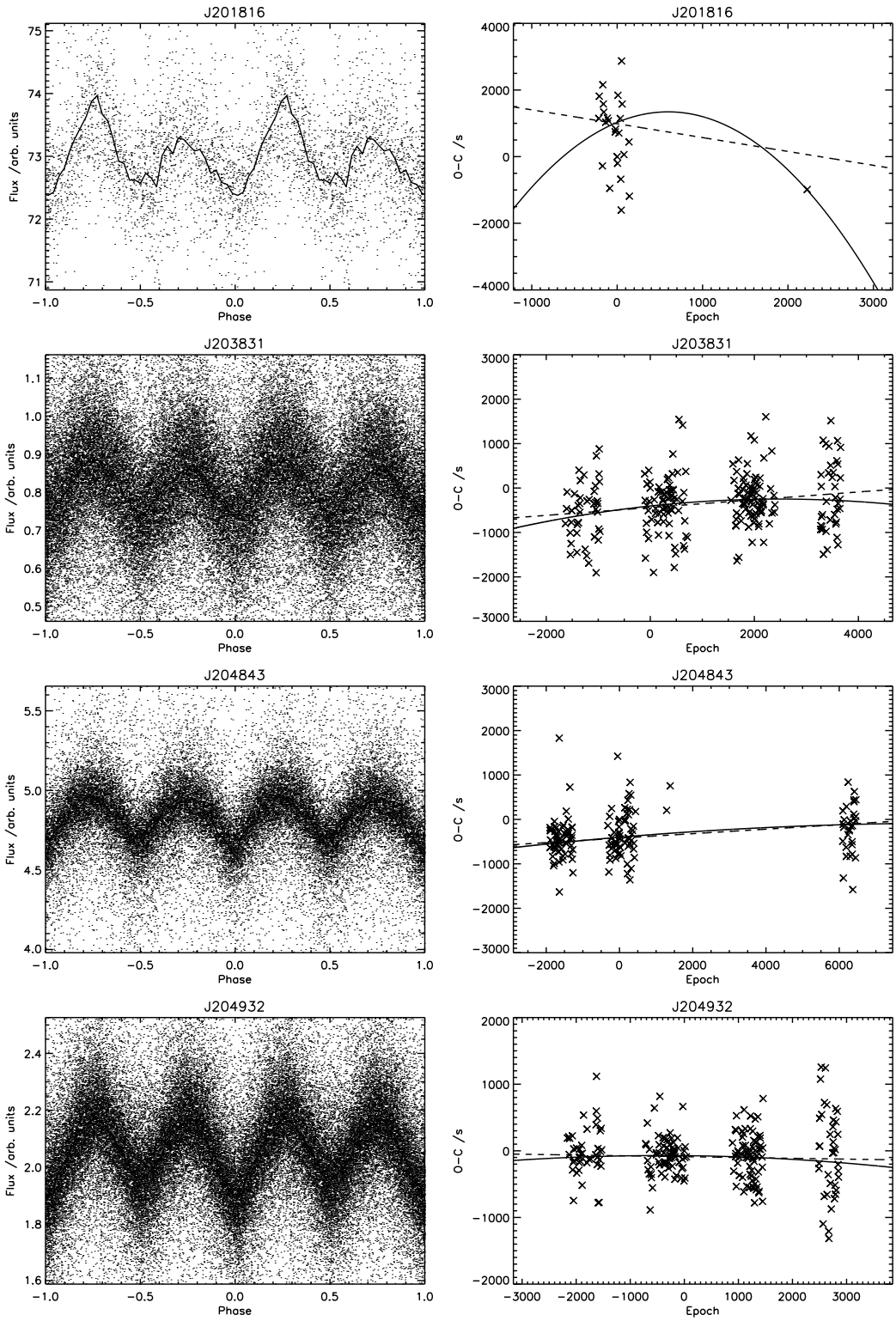
J201816
Flux /arb. units
Phase
J201816
O−C /s
Epoch
J203831
Flux /arb. units
Phase
J203831
O−C /s
Epoch
J204843
Flux /arb. units
Phase
J204843
O−C /s
Epoch
J204932
Flux /arb. units
Phase
J204932
O−C /s
Epoch

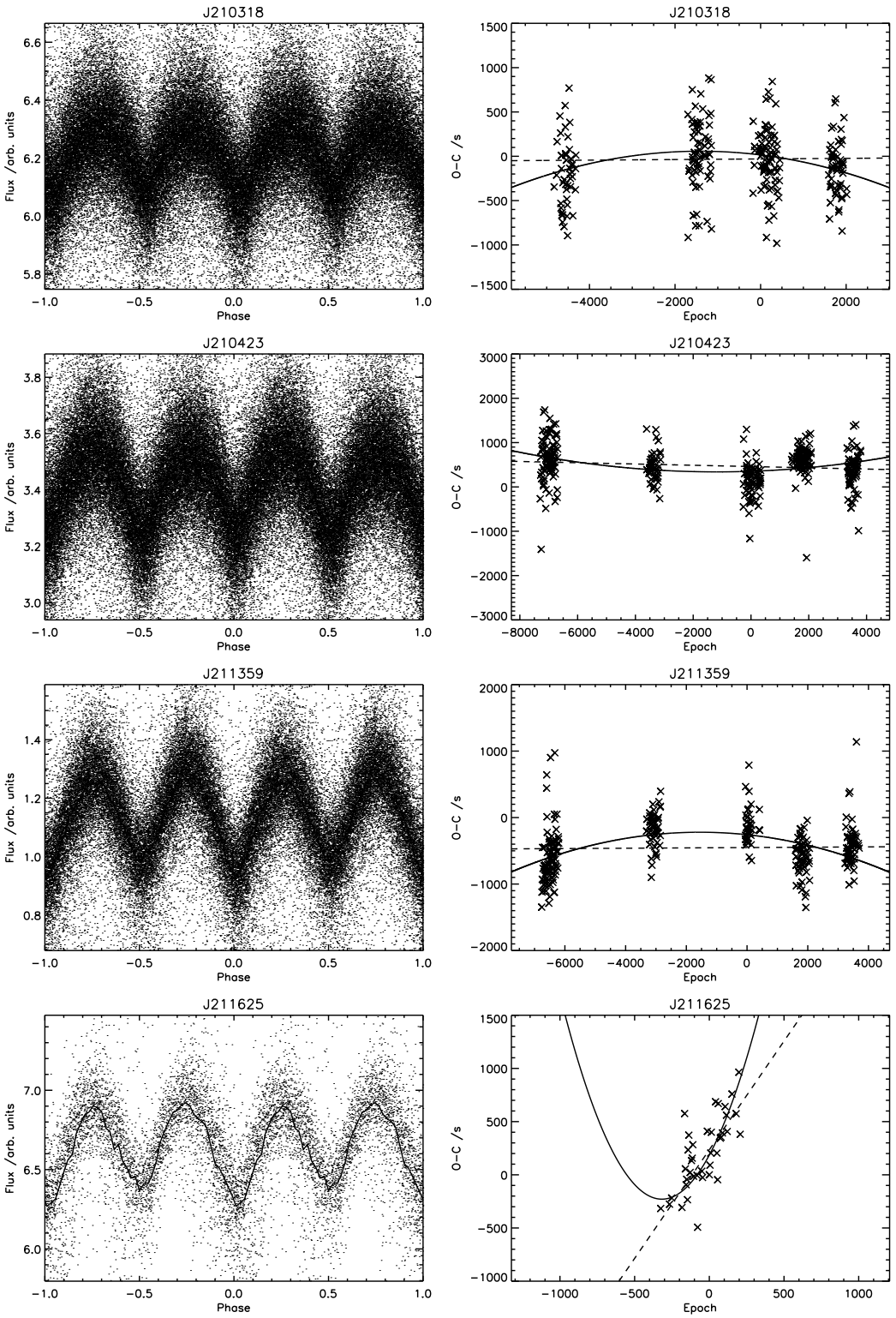
J210318
Flux /arb. units
Phase
J210318
O−C /s
Epoch
J210423
Flux /arb. units
Phase
J210423
O−C /s
Epoch
J211359
Flux /arb. units
Phase
J211359
O−C /s
Epoch
J211625
Flux /arb. units
Phase
J211625
O−C /s
Epoch

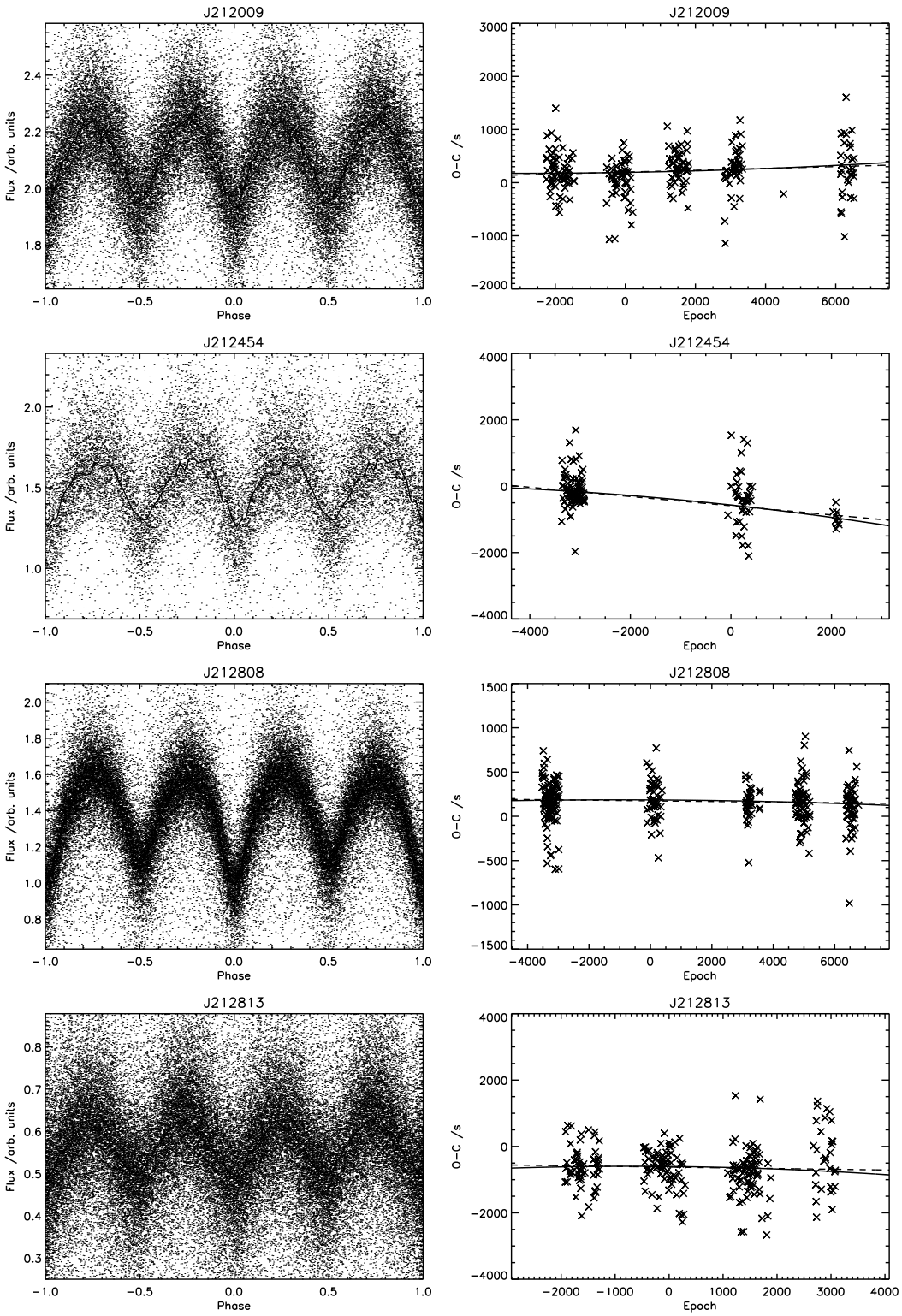
J212009
Flux /arb. units
Phase
J212009
O−C /s
Epoch
J212454
Flux /arb. units
Phase
J212454
O−C /s
Epoch
J212808
Flux /arb. units
Phase
J212808
O−C /s
Epoch
J212813
Flux /arb. units
Phase
J212813
O−C /s
Epoch

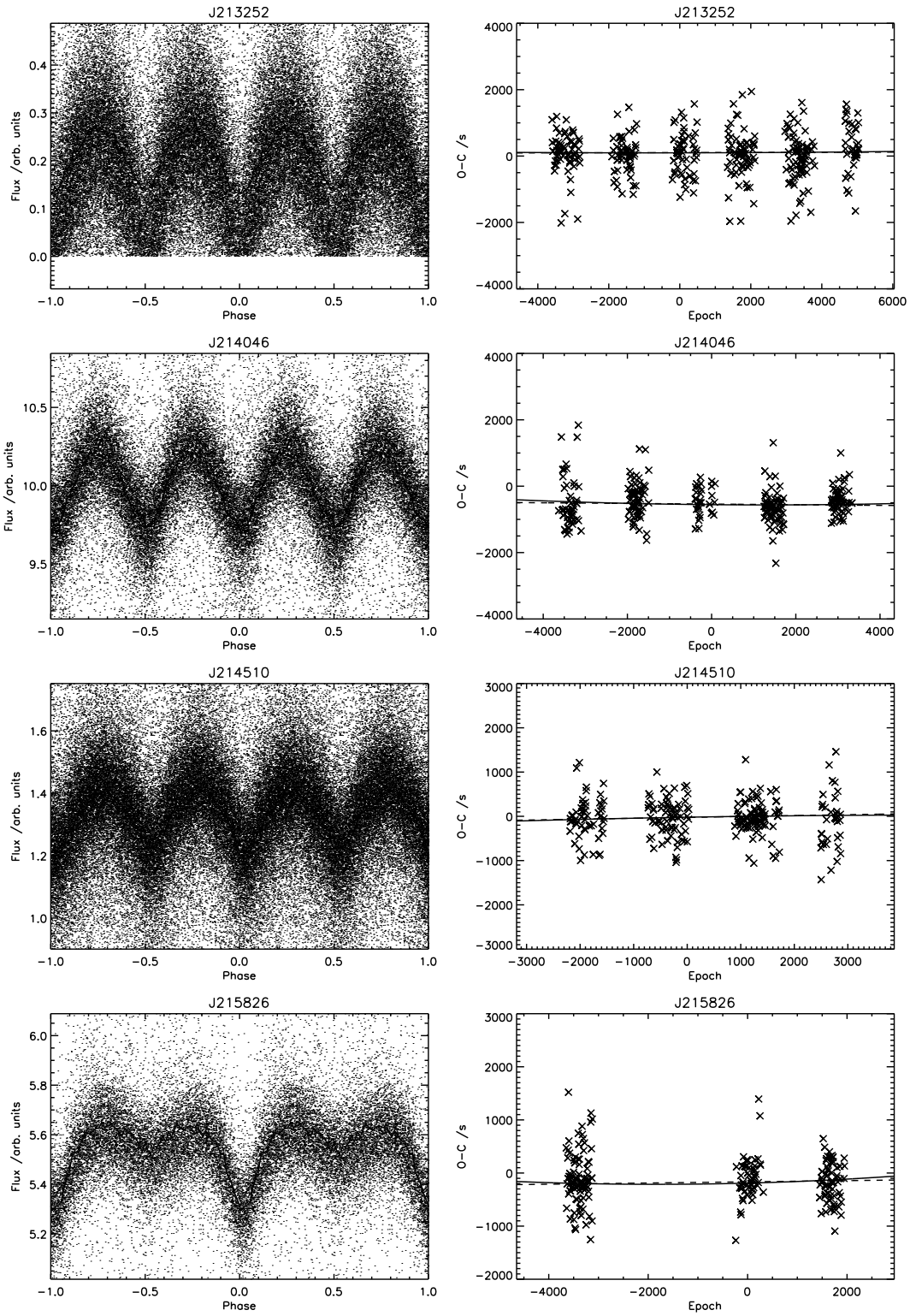
J213252
Flux /arb. units
Phase
J213252
O−C /s
Epoch
J214046
Flux /arb. units
Phase
J214046
O−C /s
Epoch
J214510
Flux /arb. units
Phase
J214510
O−C /s
Epoch
J215826
Flux /arb. units
Phase
J215826
O−C /s
Epoch

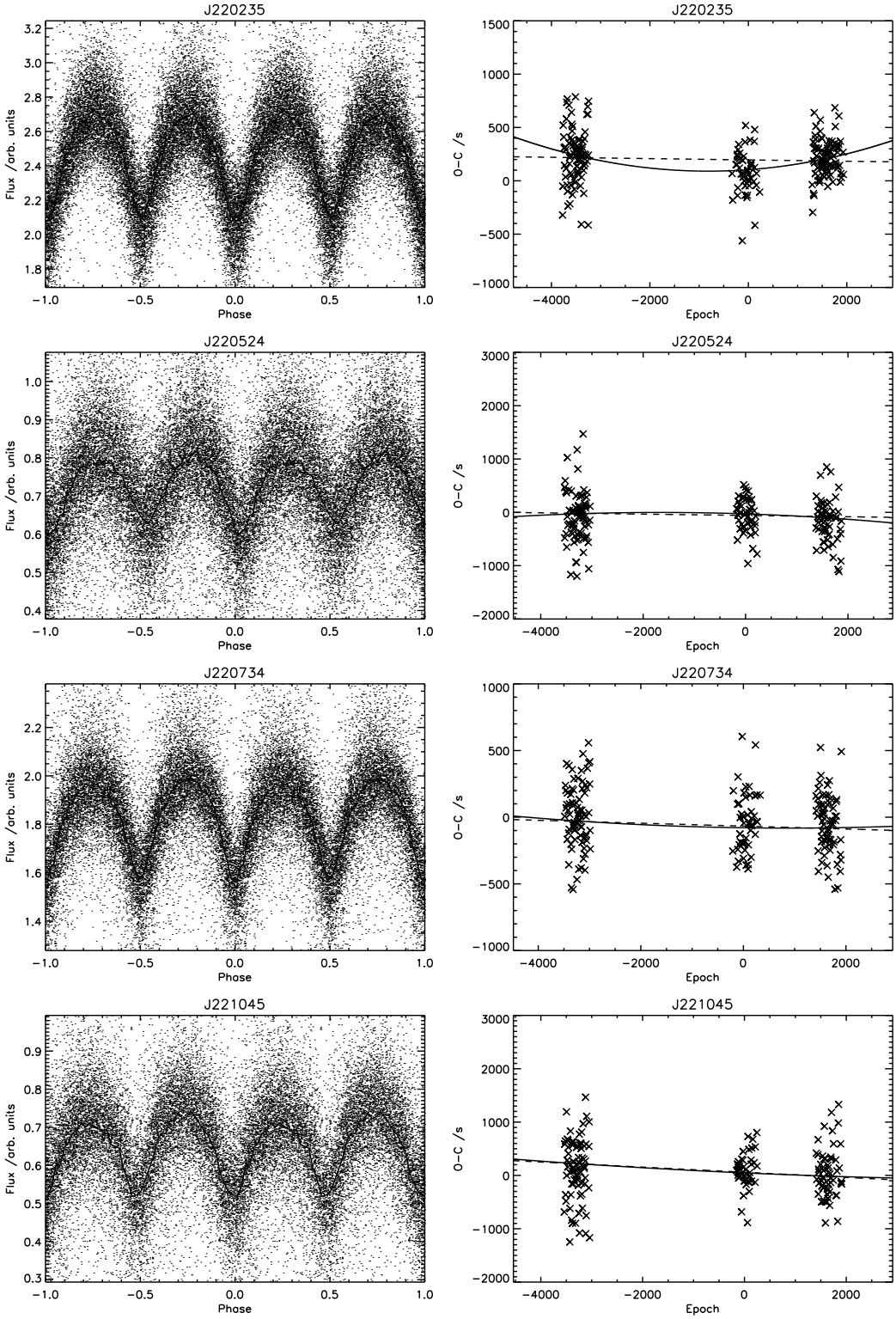
J220235
Flux /arb. units
Phase
J220235
O−C /s
Epoch
J220524
Flux /arb. units
Phase
J220524
O−C /s
Epoch
J220734
Flux /arb. units
Phase
J220734
O−C /s
Epoch
J221045
Flux /arb. units
Phase
J221045
O−C /s
Epoch

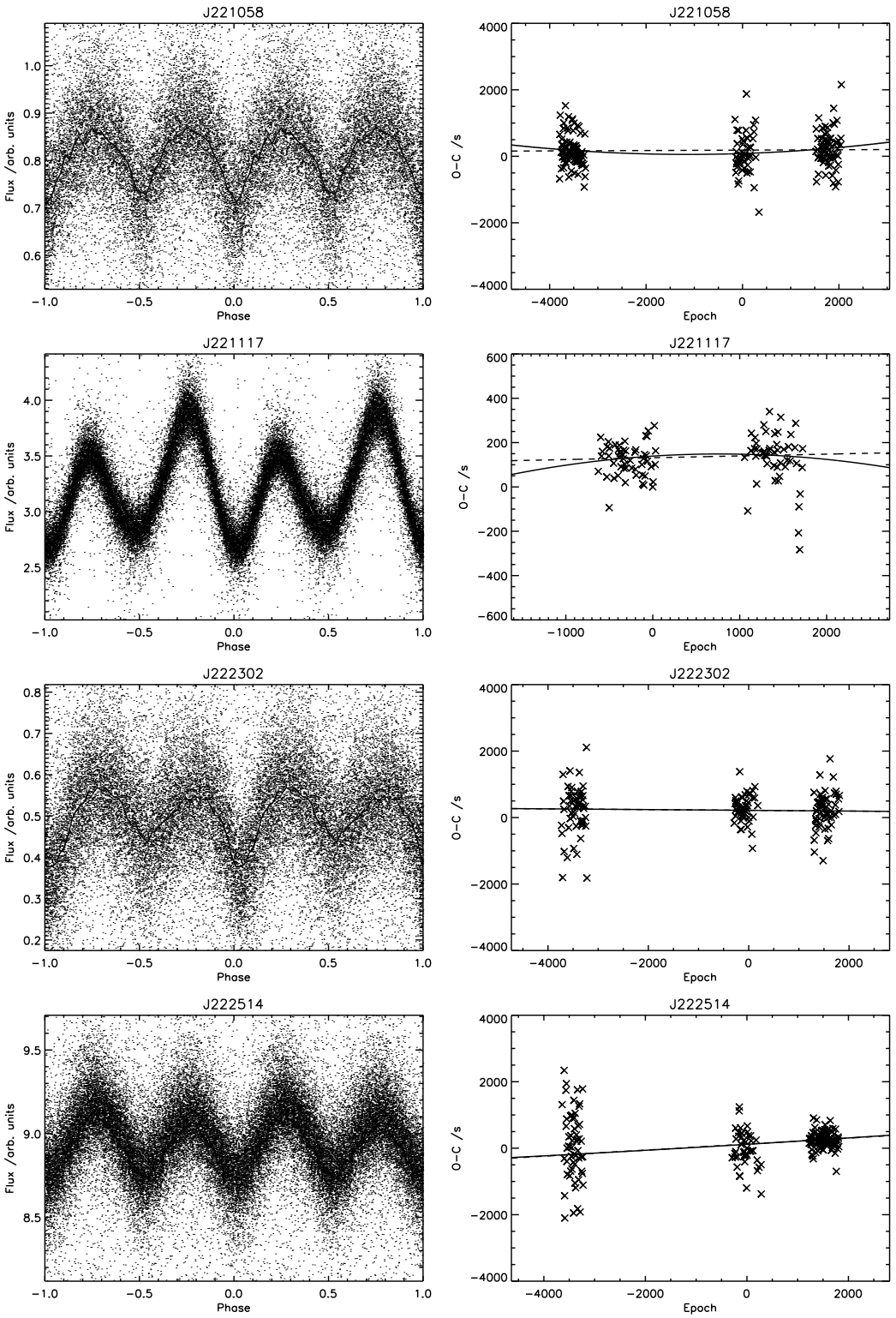
J221058
Flux /arb. units
Phase
J221058
O−C /s
Epoch
J221117
Flux /arb. units
Phase
J221117
O−C /s
Epoch
J222302
Flux /arb. units
Phase
J222302
O−C /s
Epoch
J222514
Flux /arb. units
Phase
J222514
O−C /s
Epoch

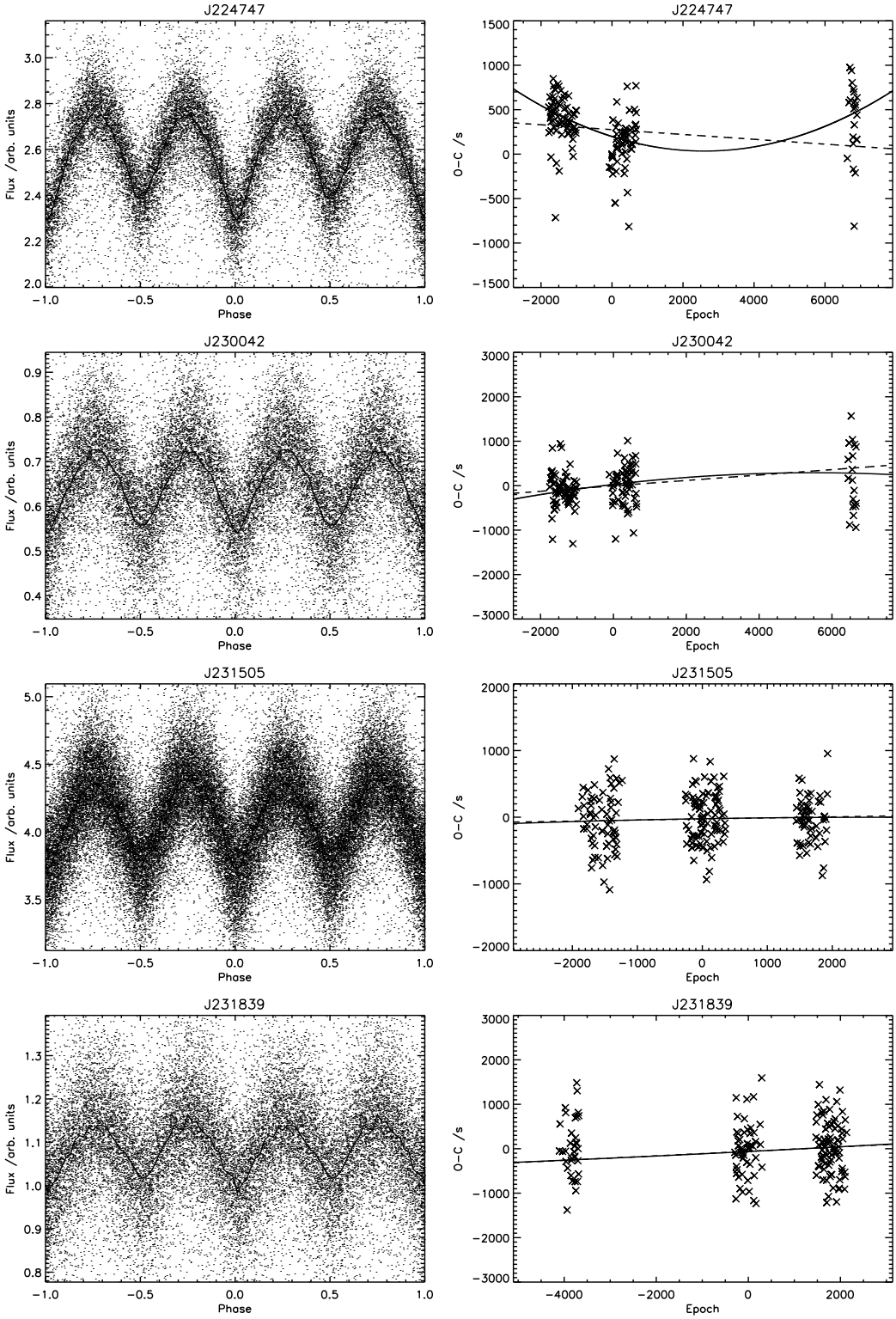
J224747
Flux /arb. units
Phase
J224747
O−C /s
Epoch
J230042
Flux /arb. units
Phase
J230042
O−C /s
Epoch
J231505
Flux /arb. units
Phase
J231505
O−C /s
Epoch
J231839
Flux /arb. units
Phase
J231839
O−C /s
Epoch

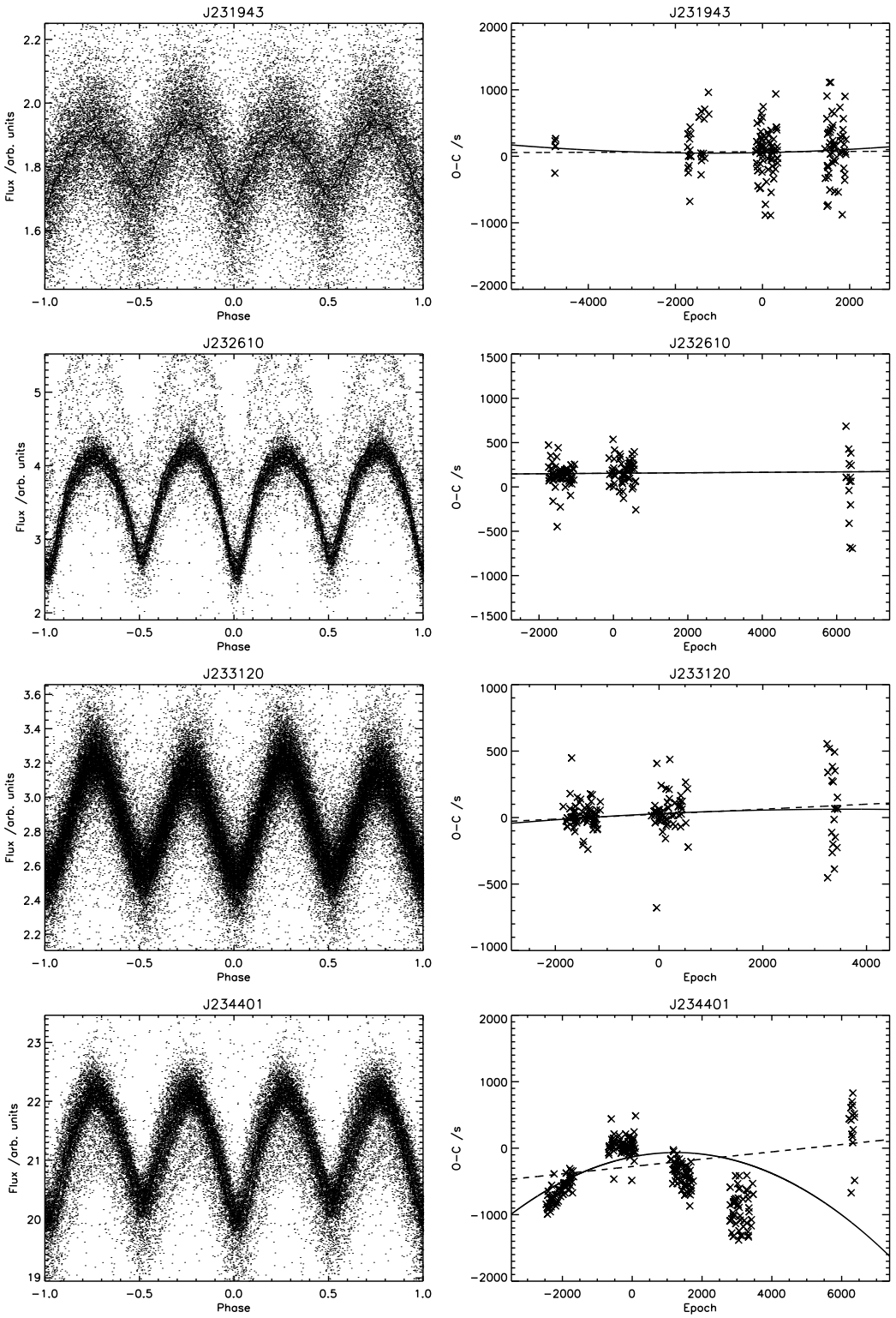
J231943
Flux /arb. units
Phase
J231943
O−C /s
Epoch
J232610
Flux /arb. units
Phase
J232610
O−C /s
Epoch
J233120
Flux /arb. units
Phase
J233120
O−C /s
Epoch
J234401
Flux /arb. units
Phase
J234401
O−C /s
Epoch

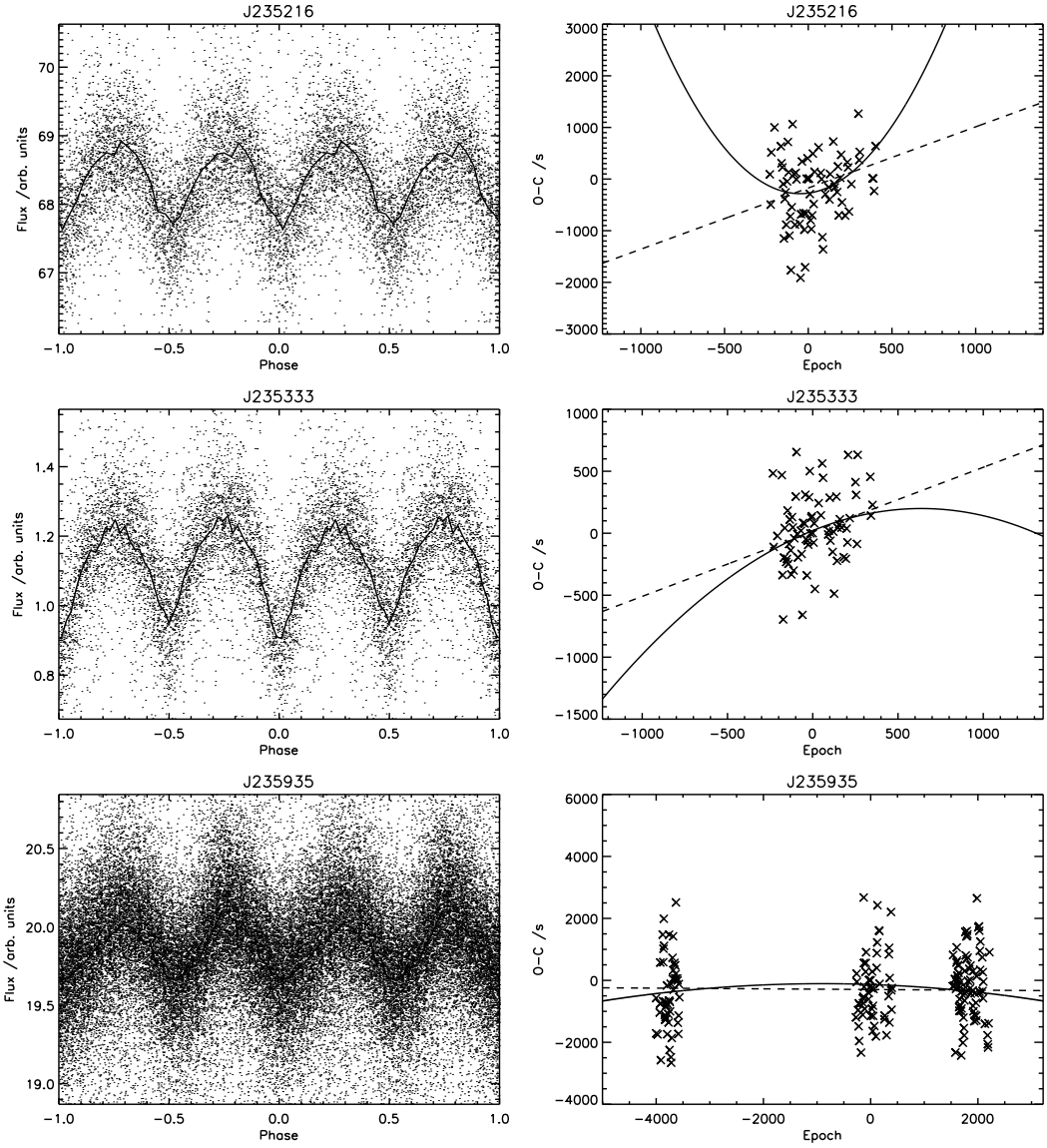
J235216
Flux /arb. units
Phase
J235216
O−C /s
Epoch
J235333
Flux /arb. units
Phase
J235333
O−C /s
Epoch
J235935
Flux /arb. units
Phase
J235935
O−C /s
Epoch

Appendix B

Lists of SuperWASP EBs exhibiting period changes

Table B.1: Periods and quadratic period change determinations for 388 EW-type eclipsing binary candidates.

WASP ID (1SWASP Jhhmmss.ss±ddmmss.s)	P /s	δP /s	$\dot{P}$ /s yr^{-1}	$\delta\dot{P}$ /s yr^{-1}	Lin. fit χ^2	Quad. fit χ^2
J000139.04-362125.6	23055.9526	0.0035	0.10153	0.01084	1.41	1.02
J000309.18-345618.4	22931.8584	0.0024	0.03004	0.00312	1.41	1.00
J001259.92+141858.3	28468.7719	0.0047	0.16307	0.01053	2.37	1.08
J001536.38+312111.8[1]	26700.2768	0.0050	0.11666	0.01319	1.40	1.01
J001537.75+312045.4[1]	26700.2626	0.0050	0.11709	0.01377	1.43	1.05
J002328.00-204150.0	35829.8821	0.0073	0.21826	0.00243	0.75	7.23
J002446.47+192503.1	34684.7733	0.0036	0.06151	0.00638	1.70	1.02
J002449.36-274418.9	27100.4861	0.0029	0.10369	0.00627	3.01	1.39
J002540.75-344942.8	23210.3472	0.0043	0.03466	0.00334	1.44	1.01
J002828.13+262749.9	28027.8361	0.0062	0.10126	0.00360	5.22	1.03
J003033.53+392722.9	36040.0447	0.0041	0.03444	0.00309	1.49	1.01
J004240.46-295638.3	26065.7641	0.0030	0.16061	0.00320	2.34	2.54
J004633.78-333058.0	25845.7152	0.0027	0.02974	0.00334	1.36	1.03
J004637.72+315117.4	29674.0043	0.0031	0.04501	0.00273	2.14	1.01
J004920.20+232516.8	31037.5712	0.0020	0.07318	0.00385	3.35	1.06
J005101.52+283749.3	25141.5830	0.0021	0.05593	0.00503	1.74	1.00
J005408.45+385402.4	25582.1462	0.0018	0.02136	0.00186	1.61	1.00
J010642.20-330857.9	19187.5812	0.0024	0.05851	0.00693	1.36	1.00

[1]This "object" and its neighbour(s) at similar coordinates are duplicates of a single astrophysical object.

Table B.1: (continued)

WASP ID (1SWASP Jhhmmss.ss±ddmmss.s)	P /s	δP /s	$\dot{P}$ /s yr^{-1}	$\delta\dot{P}$ /s yr^{-1}	Lin. fit χ^2	Quad. fit χ^2
J010705.03+321208.9	36353.2310	0.0060	0.10231	0.00382	5.11	1.09
J010857.78+214640.2	26618.9627	0.0035	0.06599	0.00306	4.30	1.01
J012655.03+305219.6	32237.0103	0.0023	0.04150	0.00158	4.37	1.05
J013015.91+333918.5	35108.4868	0.0065	0.09971	0.00504	3.61	1.87
J013200.97-220217.0[1]	28278.9545	0.0045	0.04683	0.00273	1.90	1.06
J013201.00-220225.1[1]	28278.9529	0.0024	0.04661	0.00278	1.84	1.05
J013629.46+015020.8	23080.2017	0.0079	0.15775	0.01072	2.01	1.01
J014431.77-134956.4	22963.5012	0.0086	0.22716	0.02414	1.46	1.00
J014933.69-193729.2	29445.8626	0.0048	0.39174	0.00493	2.05	1.00
J015437.68-040908.1[1]	33492.9996	0.0140	0.12377	0.01235	1.52	1.02
J015438.89-040920.2[1]	33493.0274	0.0157	0.13047	0.01284	1.55	1.02
J020759.54-285841.4	36464.1647	0.0070	0.15275	0.00927	2.43	1.04
J020921.37+142358.4	24007.1559	0.0028	0.16642	0.00814	3.37	1.06
J021544.21-202410.2	25134.4635	0.0028	0.04088	0.00269	1.81	1.02
J021547.14-045208.2	24878.2912	0.0085	0.18038	0.01942	1.42	1.00
J022531.17-185947.3	32301.0483	0.0036	0.05981	0.00408	1.72	1.00
J022758.57-125932.0	24163.6986	0.0104	0.52411	0.05853	1.74	1.06
J023129.78-125221.9	22339.8286	0.0111	0.44133	0.06492	1.38	1.02
J025203.36+093116.5	25701.5310	0.0092	0.34546	0.04807	1.33	1.00
J025305.48-203139.3	39645.4547	0.0042	0.08046	0.00483	2.04	1.00
J030155.78-391442.8	26997.6296	0.0040	0.16712	0.01365	1.67	1.00
J030314.81-231112.0	39451.3788	0.0052	0.11707	0.00886	1.97	1.02
J031751.34-361530.3	34135.4342	0.0026	0.04354	0.00400	1.59	1.01
J032810.22-250400.4[1]	27259.6772	0.0026	0.08928	0.00705	1.68	1.00
J032811.87-250330.0[1]	27259.6801	0.0023	0.08415	0.00396	2.80	1.02
J033531.91+055850.3	27540.4049	0.0081	0.14727	0.02206	1.26	1.00
J033609.51-183826.6	24410.0097	0.0046	0.12775	0.00653	2.41	1.07
J034927.54+125432.3	26384.1149	0.0047	0.02585	0.00376	1.27	1.01
J035212.51-343325.8	27357.8370	0.0043	0.04581	0.00641	1.25	1.00
J035422.58-360538.4	25094.6166	0.0024	0.05866	0.00639	1.47	1.08
J035546.30+070816.2	32457.1878	0.0067	0.14795	0.01776	1.37	1.01
J041036.33+340258.6	23369.3663	0.0047	0.07502	0.00662	2.03	1.00
J041120.40-230232.3	18690.4686	0.0021	0.04659	0.00447	1.58	1.03
J041418.36-462657.1	26925.5386	0.0012	0.01631	0.00154	1.37	1.01
J041651.90-045351.9	24782.5942	0.0062	0.11603	0.01535	1.32	1.00
J041711.37+015851.0	23720.9411	0.0023	0.08107	0.00869	1.41	1.03
J041813.35-061534.0	28317.9685	0.0132	0.28679	0.02431	1.71	1.00
J043424.83+082201.8	36619.5424	0.0344	0.62464	0.02290	5.39	1.07
J043935.24-301034.3	22885.1316	0.0019	0.05043	0.00391	1.64	1.04
J044622.57+044054.3	22356.0914	0.0054	0.66685	0.04150	2.40	1.03
J045657.16-092952.9	22517.4106	0.0064	0.15060	0.02224	1.28	1.02
J050203.72-024807.5	27819.6332	0.0054	0.07488	0.00865	1.39	1.03

Table B.1: (continued)

WASP ID (1SWASP Jhhmmss.ss±ddmmss.s)	P /s	δP /s	$\dot{P}$ /s yr^{-1}	$\delta\dot{P}$ /s yr^{-1}	Lin. fit χ^2	Quad. fit χ^2
J050225.71-152514.0	27088.7500	0.0044	0.61057	0.02231	4.82	1.05
J050317.30-344940.0	24952.5803	0.0026	0.08743	0.00441	2.40	1.05
J050333.59-252155.7	35776.1467	0.0061	0.27766	0.00561	0.64	1.04
J050416.72-192247.7	24789.6923	0.0027	0.11957	0.00365	4.73	1.56
J050734.80-212930.1	25031.4042	0.0042	0.11110	0.00920	1.55	1.00
J050922.02-193233.5	23400.7929	0.0021	0.04971	0.00260	2.18	1.04
J051146.32+043612.9	32992.3657	0.0246	0.75979	0.06914	1.69	1.05
J051359.39-454655.2	25328.4951	0.0026	0.17592	0.00825	2.30	1.06
J051842.33+142505.3	29759.2820	0.0057	0.10690	0.00530	3.32	1.05
J052354.95+164744.4[1]	29674.3935	0.0081	0.06412	0.00757	1.44	1.00
J052357.13+164810.4[1]	29674.4103	0.0069	0.04959	0.00690	1.32	1.00
J052449.39-280900.5	23827.0325	0.0017	0.05664	0.00242	3.60	1.76
J052623.59-335404.7	36878.9163	0.0046	0.28730	0.00830	4.72	1.01
J053002.84-013005.7	23728.0040	0.0056	0.04851	0.00527	1.31	1.01
J054137.57-382224.9	30198.5348	0.0046	0.10952	0.00485	3.84	2.28
J054905.38-255424.1	27048.7962	0.0022	0.05847	0.00335	2.34	1.42
J054911.37-190234.4	27150.1740	0.0020	0.04844	0.00319	1.90	1.04
J055302.53-401849.3	35022.3590	0.0110	0.17521	0.01181	1.64	1.06
J055707.88-273831.0	25645.9971	0.0030	0.03816	0.00242	1.80	1.02
J060556.82-534251.9	40058.9404	0.0076	0.32627	0.01445	2.53	1.06
J060759.31-340929.0	26225.3831	0.0015	0.03292	0.00181	2.05	1.01
J061150.72-451944.8	30805.7819	0.0028	0.06998	0.00214	3.75	1.59
J061512.11-401319.4	24726.3784	0.0027	0.06375	0.00206	3.04	1.03
J061537.07-452833.9	28346.6878	0.0042	0.06906	0.00499	1.47	1.05
J061624.13-461943.4	25621.6913	0.0014	0.08450	0.00313	2.64	1.02
J061855.12-253840.0	30188.6740	0.0068	0.07139	0.00632	1.50	1.01
J061916.96-464237.2	30294.6061	0.0071	0.15356	0.01264	1.54	1.04
J062155.28-430715.5	32498.1687	0.0051	0.07901	0.00486	1.59	1.03
J062909.20-435426.9	30862.9827	0.0042	0.09705	0.00296	3.25	1.03
J063019.95-443827.6	34837.4364	0.0050	0.09199	0.00318	2.90	1.04
J063641.97-370337.2	30038.2093	0.0033	0.11197	0.00674	2.02	1.07
J064341.20+375333.2	24991.2764	0.0172	0.13982	0.00834	2.65	1.01
J064427.46+294110.1	24995.6947	0.0122	0.07268	0.00315	4.90	1.00
J075521.21+334946.5	26201.9016	0.0046	0.03904	0.00494	1.48	1.01
J081516.14+405331.9[1]	24760.0067	0.0025	0.09146	0.00528	3.69	1.24
J081518.82+405254.2[1]	24760.0095	0.0049	0.06435	0.00819	1.54	1.00
J082211.83+390147.7	27384.7442	0.0054	0.23506	0.00647	1.86	3.15
J083321.24-082812.4	27524.5441	0.0048	0.08734	0.00843	1.50	1.04
J083355.99-120408.2	60518.3686	0.0181	0.90000	0.08250	1.56	1.01
J084303.35-034239.8[1]	30115.5669	0.0045	0.19877	0.00819	3.17	1.04
J084303.58-034333.6[1]	30115.6064	0.0062	0.19969	0.01429	1.71	1.00
J084303.97-034252.5[1]	30115.5752	0.0032	0.19866	0.00661	4.37	1.02

Table B.1: (continued)

WASP ID (1SWASP Jhhmmss.ss±ddmmss.s)	P /s	δP /s	$\dot{P}$ /s yr^{-1}	$\delta\dot{P}$ /s yr^{-1}	Lin. fit χ^2	Quad. fit χ^2
J084348.79+031638.7	25507.7987	0.0032	0.05582	0.00610	1.38	1.04
J090823.62-142253.2	27058.3137	0.0093	0.12744	0.01273	1.45	1.02
J091243.24-080852.8	29659.9419	0.0114	0.09967	0.01100	1.41	1.08
J091705.40-024737.1	27261.9611	0.0089	0.20891	0.01046	2.57	1.01
J091831.82-032026.0	29776.8529	0.0092	0.13341	0.01414	1.42	1.09
J092100.49-173234.9	25998.0625	0.0027	0.05768	0.00410	1.55	1.01
J095332.59-183407.1	37536.6198	0.0047	0.07672	0.00358	2.27	1.02
J095550.69-140934.9	20860.7266	0.0044	0.08577	0.00832	1.43	1.02
J100247.96+010540.3	36272.5545	0.0159	0.10612	0.00818	1.84	1.01
J101257.33+101655.2	30204.8562	0.0080	0.16796	0.01552	1.87	1.01
J102108.91-374909.8	26413.7076	0.0054	0.24352	0.00978	2.74	1.01
J102528.13-191054.9	22831.5515	0.0025	0.06100	0.00443	1.79	1.05
J103611.60-373726.1	46327.2451	0.0127	0.32522	0.01485	2.58	1.02
J104921.71-414044.4[1]	29134.8355	0.0045	0.06307	0.00472	1.64	1.01
J104923.65-414108.3[1]	29134.8386	0.0039	0.05606	0.00490	1.47	1.00
J105140.12-212440.5	24593.6251	0.0028	0.21326	0.00462	5.97	1.03
J105225.72-025919.3	25387.8518	0.0036	0.53388	0.02678	2.87	1.00
J105743.98-463334.2	37236.2227	0.0056	0.13070	0.00645	2.22	1.01
J110002.08+044206.5	25134.6343	0.0081	0.09380	0.00817	1.64	1.05
J111145.22-425459.7	29774.6720	0.0014	0.03222	0.00179	1.87	1.00
J111222.16-364056.5	45035.0673	0.0068	0.05032	0.00451	1.41	1.02
J112047.99-401142.8	32280.4463	0.0068	0.38600	0.00780	8.08	1.02
J112342.75-322002.0[1]	22931.3401	0.0023	0.03283	0.00184	1.89	1.01
J112343.20-321942.9[1]	22931.3374	0.0014	0.02991	0.00158	2.02	1.03
J113139.00-433217.4	32300.9349	0.0052	0.12681	0.00575	2.34	1.00
J113139.68-325540.5	25787.3042	0.0042	0.10023	0.00546	2.05	1.06
J113211.99-395459.5[1]	29135.8924	0.0024	0.05023	0.00315	1.74	1.00
J113212.54-395531.0[1]	29135.8871	0.0019	0.04517	0.00268	1.87	1.00
J114248.08-354857.5	31988.0439	0.0029	0.04379	0.00156	4.30	1.79
J114412.80-404650.1	29888.3967	0.0025	0.05223	0.00298	2.23	1.06
J114538.75-362254.0	35126.1024	0.0046	0.10517	0.00604	4.01	3.12
J115048.46-242321.8[1]	30617.2588	0.0020	0.04223	0.00269	1.76	1.02
J115049.18-242303.1[1]	30617.2567	0.0019	0.05177	0.00275	2.07	1.01
J115620.05-352844.8	25378.9201	0.0027	0.05774	0.00240	2.91	1.01
J115936.86-433130.5	23968.5980	0.0031	0.02613	0.00316	1.36	1.08
J120458.54+065536.9	27244.3477	0.0066	0.10206	0.00814	1.73	1.01
J120519.86-075606.3	29181.2555	0.0049	0.10092	0.01144	1.44	1.06
J120746.20-060202.3	22823.3528	0.0041	0.20136	0.01040	2.91	1.00
J120929.91-355556.8	30610.9392	0.0059	0.09082	0.00827	1.45	1.08
J121507.29-234352.3	30031.9203	0.0028	0.05000	0.00413	1.54	1.06
J121947.28-353242.9	29241.9904	0.0033	0.05391	0.00492	1.48	1.04
J122741.36-215102.8	26225.9542	0.0046	0.06890	0.00879	1.36	1.04

Table B.1: (continued)

WASP ID (1SWASP Jhhmmss.ss±ddmmss.s)	P /s	δP /s	$\dot{P}$ /s yr^{-1}	$\delta\dot{P}$ /s yr^{-1}	Lin. fit χ^2	Quad. fit χ^2
J123242.36-384854.3	20648.4422	0.0023	0.09102	0.00485	2.20	1.03
J123300.28+264258.3	20506.7991	0.0009	0.01611	0.00085	3.57	1.79
J123305.52+270803.6	29197.4618	0.0027	0.03711	0.00469	1.35	1.02
J124015.04-184800.9	27355.9652	0.0080	0.17013	0.00637	8.67	4.48
J124337.23+384415.6	28243.7890	0.0025	0.02285	0.00151	3.80	2.35
J124446.27+411049.7	38327.1618	0.0037	0.02397	0.00321	1.42	1.01
J124858.67-305155.3	22978.8109	0.0015	0.05057	0.00580	1.28	1.00
J125121.44+271346.8	23041.6019	0.0027	0.04258	0.00205	9.24	6.79
J130450.15+072432.1	22990.8531	0.0070	0.10838	0.01462	1.28	1.01
J130625.40+342916.9	29608.1205	0.0035	0.05196	0.00297	2.63	1.01
J131032.21-040932.6	26891.6308	0.0083	0.21213	0.00394	5.44	1.13
J131150.67-423655.8	40089.0373	0.0061	0.11437	0.00674	2.08	1.06
J131531.04-142655.3	28223.5332	0.0079	0.30266	0.03044	1.59	1.02
J132253.52-405327.3	33876.9795	0.0075	0.22450	0.02131	1.47	1.04
J132801.70-272947.5	26141.2665	0.0026	0.15153	0.00404	7.40	2.08
J132844.14-214206.5	31464.0102	0.0070	0.30221	0.01377	2.88	1.03
J133105.91+121538.0	18836.3665	0.0080	0.03096	0.00346	1.61	1.02
J133229.87-300756.1	26792.3433	0.0019	0.03663	0.00427	1.32	1.03
J133246.14-174532.3	35376.1994	0.0078	0.18508	0.01075	3.97	2.10
J134005.59-021956.0	29880.9582	0.0071	0.24478	0.01457	2.27	1.01
J134247.31-185307.3	35336.9437	0.0074	0.22525	0.00564	8.39	1.47
J134615.95-221531.9	44053.8540	0.0098	0.62994	0.02444	3.91	1.02
J134713.10-351625.2	30344.3341	0.0031	0.05726	0.00591	1.41	1.05
J134738.72-213540.3	22578.3050	0.0035	0.14185	0.00667	3.29	1.01
J135105.28-110129.5	24360.9092	0.0064	0.22603	0.01532	2.18	1.00
J135150.82-021230.3	27719.3367	0.0040	0.06834	0.00798	1.38	1.04
J135250.67-181330.6	31143.2747	0.0036	0.09286	0.00563	2.28	1.02
J135835.27-334041.1	30831.5636	0.0022	0.04824	0.00402	1.52	1.02
J141203.55-365515.4	28565.5201	0.0044	0.17066	0.01170	2.09	1.12
J141844.85+020021.5	25242.8862	0.0113	0.48450	0.04844	1.50	1.02
J142144.07+464159.2	27532.7134	0.0028	0.05220	0.00185	7.53	2.38
J142344.98+374744.0	34323.3173	0.0029	0.07723	0.00529	1.95	1.00
J142443.22-261758.9	30667.9195	0.0033	0.06143	0.00416	1.85	1.00
J143009.36-185138.5	27951.9921	0.0020	0.02606	0.00223	1.37	1.02
J143415.01-193319.8	27678.8274	0.0034	0.02300	0.00166	1.54	1.05
J143515.00-042347.4	25375.0955	0.0102	0.29648	0.04032	1.28	1.01
J143642.70-203755.6	26015.5481	0.0022	0.14829	0.00291	8.42	1.09
J144338.24-332721.1	26174.6198	0.0049	0.24757	0.00817	4.95	1.06
J144618.02-300423.0	30387.0044	0.0067	0.13185	0.01327	1.42	1.01
J144618.27-194004.6	32225.5421	0.0083	0.06060	0.00607	1.28	1.01
J144621.23-300501.0	30387.0058	0.0047	0.12309	0.01162	1.45	1.02
J144813.07-211242.7	22579.3946	0.0017	0.06211	0.00191	3.99	1.02

Table B.1: (continued)

WASP ID (1SWASP Jhhmmss.ss±ddmmss.s)	P /s	δP /s	$\dot{P}$ /s yr^{-1}	$\delta\dot{P}$ /s yr^{-1}	Lin. fit χ^2	Quad. fit χ^2
J145117.49+251215.9	26897.5111	0.0042	0.13617	0.00537	3.96	1.02
J145230.63-093907.0	28846.8080	0.0034	0.33714	0.00687	8.41	1.03
J145414.77-252457.7	34984.5557	0.0043	0.21348	0.02267	1.50	1.08
J145614.28-261748.0	29719.5204	0.0033	0.03019	0.00394	1.27	1.00
J145828.44+110554.9	30821.5898	0.0092	0.19315	0.02574	1.38	1.00
J150022.39-072654.4	24601.2138	0.0115	0.13449	0.00750	2.07	1.07
J150452.17-375739.0	32325.1884	0.0028	0.01589	0.00165	1.59	1.22
J150518.70+310308.8	26079.7292	0.0039	0.03757	0.00409	1.36	1.00
J150737.19+145509.3	27413.7898	0.0034	0.10585	0.00595	2.23	1.01
J151335.43-372546.2	21203.8749	0.0043	0.02200	0.00256	1.34	1.03
J151507.74-361806.4	22396.2570	0.0019	0.02924	0.00188	1.92	1.03
J151701.45+141023.2	28095.3438	0.0041	0.16591	0.00716	3.49	1.62
J151712.32-190322.5	26411.1233	0.0067	0.05052	0.00360	1.62	1.03
J152109.95-192941.1	29493.6960	0.0057	0.27987	0.01236	3.31	1.03
J152235.78+310803.4	39785.2796	0.0047	0.10126	0.00552	2.45	1.02
J152519.47+254259.1	34319.1321	0.0028	0.13630	0.00767	2.42	1.02
J154254.80-211525.2	24684.6690	0.0033	0.04584	0.00392	1.35	1.00
J154554.26-324113.8	42735.5930	0.0084	0.13557	0.00978	2.02	1.03
J154957.83-182437.9	28366.5990	0.0061	0.17653	0.00768	3.08	1.02
J155510.85+074146.8	26247.4750	0.0160	0.91080	0.09022	1.50	1.08
J155516.59-125730.4	20373.7404	0.0062	0.23818	0.01444	2.21	1.00
J161512.99-153227.4	35322.2624	0.0092	0.37012	0.04371	1.48	1.02
J162003.20+070728.7	23784.0653	0.0063	0.38570	0.00888	8.82	1.49
J162240.75+430108.1	35777.0890	0.0023	0.08138	0.00326	2.31	1.04
J162406.56+344241.9	36513.7552	0.0052	0.05781	0.00392	1.41	1.02
J163547.40+452458.6	29272.3826	0.0025	0.05384	0.00329	1.59	1.01
J164148.76+562234.7	30585.7751	0.0111	0.25232	0.03616	1.28	1.01
J164313.22+384539.2	33299.3766	0.0587	0.06319	0.00505	1.33	1.04
J164425.58+415809.2	36613.8563	0.0026	0.07810	0.00207	3.62	1.03
J164452.80+302816.7	20460.2343	0.0015	0.09470	0.00253	3.58	1.04
J164534.64+300748.3	25621.6811	0.0022	0.01426	0.00083	1.56	1.01
J165029.58+341856.3	28044.7983	0.0020	0.11182	0.00201	6.17	1.06
J165039.92+274423.8	25751.6575	0.0020	0.01991	0.00112	1.72	1.01
J165112.79+411758.3	29776.0995	0.0020	0.04688	0.00180	2.16	1.02
J170121.84+420949.9	31981.0904	0.0038	0.06619	0.00069	8.76	2.76
J170437.99+330348.7	36472.6505	0.0042	0.03006	0.00152	1.70	1.02
J170837.95+401421.0	25180.0648	0.0019	0.07409	0.00373	1.84	1.03
J171747.03+313601.9	38649.2241	0.0063	0.14663	0.00177	3.58	1.03
J171836.71+355408.6[1]	24865.5887	0.0025	0.02641	0.00169	1.53	1.03
J171839.93+355426.2[1]	24865.5857	0.0027	0.02940	0.00135	1.99	1.00
J172132.38+295145.0	32250.7103	0.0023	0.02643	0.00132	1.74	1.00
J172430.45+290650.2	34198.9545	0.0062	0.03546	0.00306	1.30	1.03

Table B.1: (continued)

WASP ID (1SWASP Jhhmmss.ss±ddmmss.s)	P /s	δP /s	$\dot{P}$ /s yr^{-1}	$\delta\dot{P}$ /s yr^{-1}	Lin. fit χ^2	Quad. fit χ^2
J172621.82+534959.7	27380.7082	0.0034	0.02626	0.00203	1.29	1.00
J172630.75+350042.4[1]	33879.1512	0.0026	0.12057	0.00282	3.89	1.02
J172631.34+350115.4[1]	33879.1569	0.0034	0.12387	0.00259	4.88	1.07
J172800.35+380716.5	28143.6527	0.0024	0.02876	0.00163	1.50	1.02
J173046.12+440433.1[1]	23388.4046	0.0023	0.01653	0.00106	1.40	1.03
J173048.26+440452.0[1]	23388.3998	0.0026	0.01959	0.00106	1.56	1.04
J173329.70+355638.3	24962.3650	0.0045	0.09185	0.00339	2.28	1.00
J173413.54+440117.9	20765.0324	0.0042	0.04775	0.00155	2.63	1.07
J173920.60+354210.5	29648.2199	0.0041	0.16895	0.00270	1.42	2.12
J174241.53+385654.3	31040.6232	0.0023	0.14377	0.00661	2.11	1.04
J174353.45+313146.9	35217.0851	0.0034	0.10038	0.00438	2.36	1.03
J174509.72+332714.8[1]	29018.9561	0.0032	0.02474	0.00199	1.40	1.00
J174511.09+332706.7[1]	29018.9561	0.0033	0.02554	0.00187	1.50	1.02
J174641.37+340856.8	22629.1969	0.0033	0.07468	0.00441	1.74	1.02
J175238.97+434942.1[1]	27327.3058	0.0021	0.03559	0.00232	1.57	1.00
J175239.07+434931.5[1]	27327.3065	0.0027	0.03124	0.00240	1.40	1.00
J175239.54+434901.7[1]	27327.3039	0.0029	0.03808	0.00354	1.28	1.00
J180025.61+401104.2	30962.4873	0.0051	0.13660	0.00401	3.79	1.04
J180328.64+475728.6	27639.8236	0.0024	0.05104	0.00273	1.84	1.00
J180733.25+465435.1	33061.6706	0.0033	0.08902	0.00239	4.40	1.04
J180818.61+343436.2	25172.8769	0.0019	0.06680	0.00184	4.10	1.09
J180947.64+490255.0	19688.4827	0.0015	0.01074	0.00092	1.34	1.02
J181033.53+421623.2	29245.4896	0.0034	0.04082	0.00193	2.09	1.01
J181125.92+431316.5[1]	27066.9938	0.0015	0.02462	0.00166	1.62	1.05
J181126.34+431255.5[1]	27066.9982	0.0022	0.02418	0.00154	1.71	1.06
J181127.16+431233.8[1]	27066.9969	0.0015	0.02629	0.00160	1.67	1.02
J181152.45+373845.8	28181.2260	0.0027	0.03153	0.00277	1.38	1.08
J181630.80+371102.9[1]	34709.7502	0.0027	0.09459	0.00189	7.53	1.00
J181632.07+371114.2[1]	34709.7470	0.0040	0.09099	0.00211	5.79	1.01
J182013.98+465527.2	31616.7158	0.0035	0.03234	0.00276	1.40	1.07
J182345.47+410548.0	31860.0860	0.0024	0.06085	0.00198	3.02	1.01
J182358.52+351518.2	26403.7718	0.0042	0.17988	0.00588	3.22	1.08
J183053.08+485848.6	30036.2211	0.0037	0.14167	0.00370	4.11	1.02
J183454.44+372710.0	32371.7762	0.0043	0.06478	0.00623	1.28	1.01
J183823.68+423624.1	29452.0923	0.0044	0.03083	0.00191	1.59	1.00
J190122.57-454523.4	32536.8377	0.0057	0.27583	0.00795	6.18	1.06
J190755.84+495222.2	23662.2190	0.0057	0.21634	0.02520	1.25	1.00
J191525.86+424844.8[1]	24292.5410	0.0023	0.05955	0.00287	2.57	1.03
J191525.89+424830.9[1]	24292.5442	0.0028	0.06839	0.00288	3.16	1.04
J191844.50-332459.3	23707.0236	0.0020	0.05246	0.00474	1.65	1.00
J192104.48+561941.9	28883.5447	0.0034	0.05377	0.00498	1.38	1.00
J193731.58+494819.9	32374.7372	0.0050	0.27770	0.02871	1.46	1.05

Table B.1: (continued)

WASP ID (1SWASP Jhhmmss.ss±ddmmss.s)	P /s	δP /s	$\dot{P}$ /s yr^{-1}	$\delta\dot{P}$ /s yr^{-1}	Lin. fit χ^2	Quad. fit χ^2
J194009.64-430251.7	31733.9991	0.0052	0.29871	0.00760	6.46	1.00
J194722.46+535234.7	27317.1355	0.0019	0.10396	0.00789	1.92	1.00
J195855.76-452122.0	30639.1600	0.0039	0.07903	0.00948	1.32	1.01
J200058.88-255843.8	26917.7636	0.0031	0.02472	0.00271	1.44	1.05
J200951.27-335118.4	29350.5957	0.0026	0.03379	0.00211	2.09	1.00
J201118.05-315504.5	29567.2873	0.0057	0.04943	0.00583	1.32	1.00
J201633.24-384103.7[1]	23684.1681	0.0020	0.03107	0.00192	2.09	1.02
J201634.12-384100.4[1]	23684.1644	0.0016	0.03349	0.00198	2.14	1.00
J201833.56-363456.3	33082.1626	0.0026	0.04668	0.00508	1.35	1.00
J201933.56-272648.2	35202.8987	0.0050	0.09114	0.01009	1.51	1.09
J202111.03+014556.9	23561.4001	0.0026	0.04372	0.00451	1.58	1.08
J202558.23-380008.5	24309.2998	0.0044	0.08430	0.01025	1.32	1.00
J202920.15-071324.5	22522.1888	0.0073	0.21189	0.01134	2.49	1.18
J202932.37-544850.2	24435.7615	0.0042	0.08314	0.00804	1.33	1.00
J203253.21-145950.0	71442.0706	0.0570	0.55097	0.04249	1.86	1.00
J203612.16+061218.9	22111.7831	0.0038	0.04777	0.00156	3.91	1.01
J203746.96+161900.9	26815.6470	0.0031	0.17755	0.01324	1.92	1.01
J203845.24-213719.8	27780.2731	0.0031	0.02427	0.00193	1.51	1.00
J203940.48-201532.1	25350.8442	0.0065	0.08626	0.00500	2.01	1.01
J204120.52-270526.0	28546.2034	0.0031	0.10044	0.00500	3.23	1.03
J204455.32+092628.4	26000.5343	0.0032	0.04318	0.00295	1.83	1.03
J205028.98+090149.8[1]	31983.6985	0.0045	0.04565	0.00489	1.37	1.03
J205029.01+090135.0[1]	31983.7062	0.0050	0.04553	0.00493	1.34	1.02
J205249.37+002213.0	25006.5742	0.0054	0.12481	0.00809	2.02	1.01
J205427.96+101157.8[1]	23009.1643	0.0039	0.04005	0.00312	1.60	1.00
J205428.29+101233.8[1]	23009.1679	0.0021	0.04396	0.00311	1.74	1.02
J205558.14-362654.6	28297.7137	0.0027	0.09471	0.00430	3.11	1.04
J205744.03+074723.6[1]	24553.1468	0.0039	0.06340	0.00537	1.44	1.00
J205745.41+074732.1[1]	24553.1417	0.0042	0.05329	0.00476	1.40	1.00
J205845.63-423730.6[1]	23624.6060	0.0028	0.04863	0.00371	1.36	1.02
J205847.01-423704.4[1]	23624.6121	0.0025	0.05286	0.00397	1.35	1.01
J205914.34-290042.8	29569.5306	0.0032	0.02368	0.00265	1.35	1.00
J210227.76-211256.2	31687.0901	0.0065	0.12000	0.00861	1.66	1.03
J210332.19-211719.6	27579.5826	0.0242	0.13085	0.01141	1.39	1.01
J210405.59-052221.2	24577.3034	0.0043	0.09087	0.01237	1.33	1.02
J210421.11-214246.5	34141.6330	0.0077	0.04604	0.00363	1.56	1.04
J210500.92-403325.4	28022.4922	0.0040	0.06734	0.00304	2.04	1.01
J210548.49-253537.6	30660.6220	0.0181	0.11398	0.01478	1.25	1.00
J210553.39-164744.8	30913.9892	0.0062	0.10276	0.00558	2.16	1.06
J210816.24+013918.5	28007.1809	0.0043	0.13180	0.00709	2.58	1.12
J211233.74-265811.4	29517.9764	0.0027	0.03731	0.00456	1.38	1.06
J211618.59+071146.8	32084.9590	0.0037	0.02609	0.00251	1.42	1.07

Table B.1: (continued)

WASP ID (1SWASP Jhhmmss.ss±ddmmss.s)	P /s	δP /s	$\dot{P}$ /s yr^{-1}	$\delta\dot{P}$ /s yr^{-1}	Lin. fit χ^2	Quad. fit χ^2
J211712.82-002102.7	32117.3451	0.0061	0.04067	0.00383	1.52	1.02
J211845.75-625303.0	23664.4271	0.0029	0.08664	0.00608	1.56	1.00
J211848.65-174924.9	30924.2848	0.0033	0.02422	0.00222	1.38	1.02
J211848.97-625248.7	23664.4257	0.0037	0.08790	0.00584	1.69	1.02
J211850.78-190935.7	26568.7097	0.0034	0.10108	0.00321	4.24	1.03
J211940.57+040632.8	32817.2277	0.0116	0.10097	0.01159	1.39	1.03
J212012.55+155700.1	46458.8277	0.0072	0.19524	0.01566	1.54	1.02
J212023.09-214611.4	30596.9798	0.0043	0.04514	0.00383	1.51	1.01
J212318.85-462224.1	25581.1741	0.0023	0.05343	0.00212	2.43	1.06
J212445.29-212826.5	21517.6759	0.0023	0.04980	0.00146	4.73	1.01
J212725.69+194432.5[1]	33323.7619	0.0092	0.06184	0.00375	1.97	1.05
J212725.75+194446.8[1]	33323.8131	0.0066	0.05992	0.00375	1.93	1.07
J212737.32+113357.1	30000.8831	0.0041	0.08618	0.00304	3.97	1.02
J212742.11+350515.5	28939.8792	0.0014	0.03267	0.00134	2.82	1.02
J212821.54+333602.3	24459.7183	0.0015	0.01418	0.00161	1.34	1.07
J212849.75-312932.3	32587.7839	0.0044	0.16727	0.01023	2.05	1.03
J212915.04+160454.5	24447.9308	0.0037	0.05899	0.00101	2.41	2.34
J213000.95+293252.1	27120.7502	0.0032	0.13195	0.00370	5.05	1.02
J213005.09+204438.9	27514.9484	0.0045	0.05427	0.00262	2.70	1.06
J213031.21+354147.2	32422.6022	0.0053	0.19324	0.00921	2.56	1.00
J213104.20-520823.2[1]	25005.3683	0.0043	0.19060	0.00964	2.14	1.01
J213106.00-520756.3[1]	25005.3430	0.0062	0.19399	0.01241	1.72	1.03
J213209.35-344251.4	32538.5281	0.0031	0.05068	0.00203	3.85	1.01
J213353.51-034247.0	24243.2199	0.0098	0.16331	0.01540	1.56	1.00
J213437.52-522921.0	23403.4025	0.0021	0.17007	0.00408	5.49	1.01
J213519.13-272249.3	31873.4974	0.0048	0.09125	0.00614	2.05	1.01
J213530.64+181350.3	23110.6445	0.0037	0.03568	0.00448	1.29	1.03
J213643.78+300741.3	23691.7410	0.0049	0.05583	0.00595	1.38	1.05
J213654.55+333445.3	37999.5018	0.0038	0.07580	0.00172	9.17	2.68
J213852.12+280545.1	29543.4639	0.0017	0.02509	0.00132	2.37	1.10
J214411.77+332533.0	25344.0233	0.0016	0.04649	0.00137	4.62	1.07
J214609.97-010647.2	24636.2830	0.0040	0.10277	0.01023	1.50	1.02
J214956.37+205822.6	25545.3851	0.0041	0.04325	0.00511	1.46	1.06
J215027.43-402158.4	25902.1680	0.0037	0.05456	0.00418	1.51	1.00
J215214.08+344232.5	31960.2696	0.0033	0.05206	0.00316	2.02	1.04
J215231.21+095541.9	26086.2038	0.0032	0.03174	0.00324	1.34	1.01
J215248.61+272720.0	31873.9693	0.0029	0.07466	0.00222	5.40	1.09
J215511.89+294406.1[1]	25531.3281	0.0023	0.02007	0.00151	1.54	1.00
J215512.35+294334.7[1]	25531.3248	0.0019	0.02009	0.00106	2.14	1.03
J215513.58+294321.5[1]	25531.3322	0.0023	0.01908	0.00086	2.54	1.01
J215711.19+224010.6	36462.9916	0.0053	0.06295	0.00144	0.37	4.06
J220125.40+295459.8	28100.8204	0.0029	0.05857	0.00236	2.83	1.02

Table B.1: (continued)

WASP ID (1SWASP Jhhmmss.ss±ddmmss.s)	P /s	δP /s	$\dot{P}$ /s yr^{-1}	$\delta\dot{P}$ /s yr^{-1}	Lin. fit χ^2	Quad. fit χ^2
J220158.63+333702.2	24685.8062	0.0012	0.02686	0.00122	2.53	1.01
J220344.41+245432.3	24209.2065	0.0056	0.17781	0.00932	2.67	1.00
J220344.46+294835.9	25440.9706	0.0037	0.03266	0.00330	1.43	1.00
J220541.82+195510.8	26232.8137	0.0037	0.01031	0.00099	1.53	1.11
J220621.44+125607.0	36318.2026	0.0071	0.11464	0.00704	1.81	1.09
J220742.30+305002.0	31178.6894	0.0030	0.02429	0.00182	1.83	1.08
J221107.43-193133.2	32291.0518	0.0056	0.05820	0.00821	1.33	1.06
J221604.06+255835.9	26347.0722	0.0031	0.06527	0.00294	2.85	1.03
J221925.74-180646.9	29422.3145	0.0040	0.02717	0.00296	1.29	1.01
J222306.39+371936.7	34550.6943	0.0086	0.10253	0.00798	1.80	1.00
J222338.65+085923.2	29262.6142	0.0093	0.07724	0.00859	1.42	1.02
J222654.39-410644.8	32408.3674	0.0039	0.06530	0.00311	2.43	1.03
J222700.96+312439.8	30130.5329	0.0028	0.02027	0.00254	1.25	1.00
J222810.73-294742.4	24156.1713	0.0026	0.02314	0.00278	1.34	1.03
J223615.49+060051.3	26730.8104	0.0079	0.21978	0.01134	2.79	1.02
J223616.76+331856.7	27907.8032	0.0023	0.02819	0.00085	5.19	1.52
J225355.35-343210.0	26337.0903	0.0047	0.04063	0.00354	1.60	1.02
J225625.94-360050.0	38862.1490	0.0035	0.07672	0.00278	4.61	1.01
J225825.84-260337.4	28308.4259	0.0069	0.13027	0.00655	3.23	1.01
J225840.47+343746.2	52499.7922	0.0111	0.38989	0.04059	1.50	1.04
J225849.64+134917.9	26737.2971	0.0215	0.10070	0.00736	2.12	1.09
J225911.06+362117.9[1]	29211.4959	0.0044	0.70833	0.02698	4.11	1.07
J225911.81+362043.4[1]	29211.5004	0.0050	0.70132	0.03238	2.93	1.00
J230823.75-194214.0	27925.3389	0.0045	0.07377	0.00305	2.92	1.05
J231147.41+014427.2	26358.8090	0.0100	0.17266	0.02305	1.30	1.02
J231405.38-452026.1	25068.0283	0.0041	0.10807	0.00970	1.38	1.00
J231709.20-003547.0	28701.6456	0.0073	0.09560	0.00637	2.03	1.00
J232016.64-440354.7	31543.6683	0.0032	0.07084	0.00450	1.73	1.02
J232314.32-373056.0	29032.9907	0.0030	0.04346	0.00135	8.92	4.05
J232629.30+312040.9	24494.1403	0.0027	0.04781	0.00498	1.84	1.47
J233420.61-432952.4	27697.8216	0.0016	0.05373	0.00306	2.03	1.06
J234557.74-211338.0	26239.3483	0.0031	0.08253	0.00195	8.16	2.74
J235324.37-435052.1	30543.6186	0.0064	0.23307	0.01084	2.63	1.05
J235956.13-371901.3	20922.6329	0.0026	0.05383	0.00386	1.89	1.00

Table B.2: Periods for 92 EW-type eclipsing binary candidates exhibiting sinusoidal period change.

SuperWASP ID (1SWASP Jhhmmss.ss±ddmmss.s)	P /s	δP /s	Linear fit χ^2	Quadratic fit χ^2
J000326.28-163119.6	26964.3004	0.0035	1.77	1.22
J000653.04+164621.7	23994.2856	0.0027	1.93	1.27
J001527.97-022821.8	21791.2432	0.0111	1.30	1.01
J004403.66-023850.7	24174.6406	0.0029	1.85	1.09
J010321.75+023040.2	24611.0539	0.0107	2.22	1.07
J011611.78-065936.8	28058.0934	0.0095	1.70	1.07
J012124.43+031002.9	23051.7087	0.0040	1.69	1.03
J012450.31-324123.7	26694.9375	0.0022	4.23	2.52
J013436.73-392811.0	25088.1674	0.0050	1.56	1.00
J030313.42-203651.7	28942.5823	0.0027	1.74	3.01
J034214.72-200845.9	24368.4482	0.0041	3.32	1.73
J035947.51+151810.7	20321.6227	0.0024	1.69	1.00
J041002.85-082739.4	33784.2602	0.0114	5.06	1.07
J043856.65-334552.0	26625.0185	0.0048	1.95	1.46
J045358.91+040113.4	27163.2578	0.0076	2.15	1.07
J045923.15-175907.3	27245.4999	0.0048	1.48	1.01
J050040.60-142252.6	38303.1958	0.0129	1.30	1.04
J051244.85+101510.6	23928.1268	0.0059	1.69	1.02
J060334.68-212558.6	30723.8251	0.0030	2.37	1.01
J090714.86-382809.1	25414.0838	0.0100	4.58	8.15
J091440.54-140937.6	30347.4737	0.0082	3.74	1.03
J092816.62+052143.6	23482.8060	0.0105	1.40	1.02
J093214.30+023852.3	22849.9584	0.0047	1.27	1.01
J095045.09-081948.6	26476.0702	0.0048	1.74	1.11
J110019.07-404720.2	32259.3663	0.0031	1.86	1.27
J115941.63-201844.6	45654.7244	0.0284	1.42	1.01
J130310.90-350601.8	23800.5220	0.0016	1.33	1.06
J132229.10+154301.6	21264.1561	0.0041	3.32	2.52
J132946.36-322001.9	24188.4542	0.0033	3.02	2.36
J133356.89-315320.2	27952.6363	0.0020	1.27	1.00
J135354.48-204849.8	25526.7106	0.0042	1.69	1.10
J135511.41-454842.9	24439.0112	0.0014	7.03	2.46
J140726.61-383538.8[2]	22694.6536	0.0014	1.59	1.02
J140727.90-383500.6[2]	22694.6577	0.0033	2.15	1.01
J142357.42-172147.6	31909.7272	0.0047	1.32	1.02
J142508.85-221536.1	21568.1410	0.0020	1.28	1.01
J142807.46-193934.2	27422.4458	0.0052	7.78	1.76
J143103.05-241743.6	24871.1663	0.0018	2.20	1.04
J143750.20-385113.5[2]	25262.7712	0.0026	2.57	4.16

[2]This "object" and its neighbour(s) at similar coordinates are duplicates of a single astrophysical object.

Table B.2: (continued)

SuperWASP ID (1SWASP Jhhmmss.ss±ddmmss.s)	P /s	δP /s	Linear fit χ^2	Quadratic fit χ^2
J143750.76-385044.2[2]	25262.7643	0.0039	1.15	5.79
J144226.37-455807.1	21735.0430	0.0011	3.29	1.26
J150413.11+044809.7	25262.7909	0.0076	1.27	1.00
J150822.80-054236.9	22469.1685	0.0022	4.76	1.04
J160153.56+245217.5	23218.1860	0.0026	8.15	6.15
J160711.35+143740.5	24416.6688	0.0115	1.31	1.04
J162337.21+155720.4	20404.8976	0.0024	2.59	1.02
J165631.99+302222.5	35519.9678	0.0039	2.54	1.00
J165749.20+442513.3	22621.5690	0.0032	1.77	1.03
J165819.77+334021.5	23170.7380	0.0011	1.66	1.04
J165852.46+391423.3[2]	26835.2475	0.0019	1.35	1.04
J165854.11+391408.2[2]	26835.2451	0.0021	1.37	1.03
J171159.64+513347.1	32960.2022	0.0053	1.51	1.02
J171239.43+330800.8	27711.7054	0.0024	1.49	1.01
J171408.32+353051.0	35321.9106	0.0051	2.18	1.08
J172004.77+365156.0	23404.2186	0.0052	2.13	1.03
J172551.78+472104.9	21279.4935	0.0067	2.02	1.05
J172554.97+383452.7	24194.2975	0.0023	1.62	1.05
J172844.98+434813.6	20858.4460	0.0017	1.68	1.01
J172931.63+401030.5[2]	31314.0792	0.0058	3.65	1.06
J172934.79+401004.0[2]	31314.0858	0.0039	2.32	1.01
J173601.67+470218.0	25153.6225	0.0017	2.71	1.06
J173834.25+452719.0	24049.3984	0.0010	1.55	1.00
J174310.98+432709.6	22300.5177	0.0023	4.35	1.06
J174736.99+450215.1	30173.9437	0.0062	3.50	2.07
J175306.53+423432.4[2]	31999.5788	0.0028	1.76	1.03
J175308.08+423438.5[2]	31999.5759	0.0039	1.87	1.04
J180849.93+423112.3	26437.5313	0.0043	1.57	1.09
J182416.12+351428.1	23786.9640	0.0029	2.31	1.00
J190525.37-450202.1[2]	25122.7956	0.0022	2.92	1.02
J190526.42-450140.2[2]	25122.7961	0.0018	2.66	1.12
J194705.51-375117.1	27284.0071	0.0034	1.39	1.04
J200029.89-450927.6	27169.9991	0.0117	2.35	1.78
J200445.46-180450.1[2]	37712.7114	0.0047	1.56	1.05
J200445.65-180426.0[2]	37712.7319	0.0062	1.50	1.03
J201045.52-624834.3	29677.8092	0.0072	1.59	1.02
J201900.18+563607.3	26891.9950	0.0054	6.40	2.78
J203227.89-084306.8	29805.5231	0.0084	1.56	1.00
J205300.55+054050.5	29041.6393	0.0036	4.36	1.99
J211418.53-135322.6	36233.0865	0.0277	3.09	1.59
J212052.50+060508.0	24592.9634	0.0062	1.95	1.01
J212417.25-445503.3	28368.8967	0.0024	1.91	1.06

Table B.2: (continued)

SuperWASP ID (1SWASP Jhhmmss.ss±ddmmss.s)	P /s	δP /s	Linear fit χ^2	Quadratic fit χ^2
J212606.24+002242.7	35681.9935	0.0087	8.89	2.57
J212707.11+170132.7	22268.9160	0.0012	1.35	1.04
J213325.34-181259.9	28004.1224	0.0019	2.40	1.04
J214718.43-184649.1	26583.7251	0.0035	1.64	1.03
J215144.82-173012.8	26038.4737	0.0049	1.28	1.00
J223041.03+220321.9	25403.7615	0.0032	1.52	1.00
J223105.82-194104.6	20166.3986	0.0019	1.70	1.09
J223539.58+025255.7	30595.2229	0.0096	4.28	2.71
J224046.86-281802.2	30917.9669	0.0043	1.49	1.00
J231107.24-353514.4	23248.2880	0.0022	3.91	1.03
J232246.97-424839.3	22540.3507	0.0011	1.73	1.02

Table B.3: Periods and quadratic period change determinations for 137 EB-type eclipsing binary candidates.

WASP ID (1SWASP Jhhmmss.ss±ddmmss.s)	P /s	δP /s	$\dot{P}$ /s yr^{-1}	$\delta\dot{P}$ /s yr^{-1}	Lin. fit χ^2	Quad. fit χ^2
J001311.15+053540.1	26657.5999	0.0060	0.22048	0.01356	2.56	1.23
J002035.20+400415.8	25666.2288	0.0053	0.09488	0.00645	2.06	1.00
J002439.13+245522.7	36526.1109	0.0046	0.02151	0.00200	1.68	1.00
J003512.87-325603.5	43663.8649	0.0072	0.09966	0.00677	3.32	2.48
J010313.78+352903.7	38643.6699	0.0049	0.05079	0.00367	2.01	1.00
J010655.30-194334.5	29782.3384	0.0042	0.04943	0.00394	1.49	1.00
J011529.82+045222.6	65381.7361	0.0332	1.31450	0.09737	1.98	1.01
J011915.76+301338.9	25077.4957	0.0037	0.02525	0.00292	1.43	1.08
J012605.25+052409.8	26203.3693	0.0100	0.94489	0.11020	1.46	1.12
J012652.34-215327.1	27563.1003	0.0098	0.35775	0.01266	3.39	1.02
J012755.25-230141.1	50649.3928	0.0046	0.04925	0.00693	1.29	1.02
J014725.33-170359.5	24444.1154	0.0037	0.05732	0.00337	2.28	1.48
J015106.39+151004.5	40488.7803	0.0068	0.27184	0.02202	1.82	1.01
J015657.69-273831.7	59333.6127	0.0199	0.47996	0.04769	1.51	1.00
J020009.68-243302.7	56043.2456	0.0153	0.37118	0.03258	1.68	1.03
J020118.74-370452.1	26622.2034	0.0030	0.06910	0.00239	6.65	3.02
J023316.35+030807.5	47463.8890	0.0230	0.27131	0.03681	1.27	1.00
J025936.73-170309.9[3]	40192.9453	0.0132	0.15858	0.01367	1.46	1.00
J025937.42-170328.1[3]	40193.0076	0.0163	0.16060	0.01609	1.35	1.03
J030027.05+021100.3	46303.1283	0.0480	0.25224	0.03095	1.41	1.05
J030135.18-155219.7	24982.3294	0.0089	0.37191	0.03472	1.61	1.01
J031612.03-220530.8	66697.0052	0.0147	0.17923	0.01866	1.42	1.01
J033809.13-191323.6	29509.7908	0.0049	0.02582	0.00230	1.51	1.05
J034448.99-030443.0	67283.8448	0.0449	1.67823	0.16579	1.60	1.01
J035447.18+293417.7	59143.8256	0.0246	0.10954	0.01339	1.47	1.03
J041148.18-114726.9	36022.2120	0.0099	0.36462	0.02086	2.66	1.04
J041352.58-375233.2	45205.9001	0.0122	0.32103	0.02769	1.75	1.00
J043324.85-235619.7	53877.7316	0.0209	0.21638	0.01008	7.91	6.00
J050123.14-213338.7	25123.6969	0.0092	0.20878	0.02106	1.39	1.00
J050233.35-235904.4	27696.3439	0.0112	0.25559	0.03306	1.55	1.12
J050851.75+024915.8	25548.9197	0.0145	0.07786	0.00986	1.30	1.01
J051501.69-180353.3[3]	47130.7574	0.0078	0.07924	0.00762	1.41	1.00
J051501.70-180356.1[3]	47130.7438	0.0086	0.07699	0.00791	1.36	1.00
J051927.38-092222.2	27112.0427	0.0228	1.12859	0.08535	2.06	1.06
J053502.16-315436.4	60182.0982	0.0245	0.49111	0.03661	1.61	1.02
J064024.57-454037.4	44851.1635	0.0070	0.27714	0.00919	2.96	1.01
J065825.96+222055.0[3]	23957.8207	0.0096	0.09673	0.00472	3.58	1.00
J065826.46+222121.6[3]	23957.8336	0.0052	0.09731	0.00426	4.42	1.02
J080741.57+414801.7	55647.3479	0.0230	0.49700	0.02376	4.30	7.30

[3]This "object" and its neighbour(s) at similar coordinates are duplicates of a single astrophysical object.

Table B.3: (continued)

WASP ID (1SWASP Jhhmmss.ss±ddmmss.s)	P /s	δP /s	$\dot{P}$ /s yr^{-1}	$\delta\dot{P}$ /s yr^{-1}	Lin. fit χ^2	Quad. fit χ^2
J082822.13+481402.7	48168.3001	0.0183	0.17093	0.03334	1.35	1.05
J083522.32-135021.4	52715.2700	0.0090	0.26598	0.02852	1.42	1.00
J085246.55-203052.7	40706.6776	0.0139	0.32423	0.03644	1.43	1.00
J090642.73-080134.5	65424.9639	0.1193	0.98631	0.08844	1.57	1.00
J091241.57-351514.1	39891.9215	0.0073	0.08184	0.00762	1.57	1.00
J092820.11-125052.1	43361.2290	0.0079	0.15234	0.01652	1.33	1.01
J093001.60-102202.5	46897.7916	0.0127	0.60976	0.02574	3.32	1.03
J095943.27-190756.1	40569.7349	0.0072	0.03335	0.00270	1.46	1.00
J100035.48-180131.9	72707.9721	0.0226	0.23605	0.02164	1.52	1.08
J101131.65-001757.7	75956.7554	0.0966	0.41323	0.06368	1.31	1.02
J101617.40-075540.1	30955.2013	0.0093	0.05220	0.00603	1.29	1.03
J102710.92-084448.6	23591.3540	0.0109	0.69705	0.05525	1.98	1.02
J110544.26-382057.0	67753.5849	0.0144	0.13616	0.01643	1.26	1.00
J121925.17+212059.1	47909.8403	0.0084	0.08958	0.01262	1.43	1.01
J122108.33-435213.7	30384.4412	0.0038	0.19013	0.01205	1.81	1.01
J124942.21-452013.0	25777.6922	0.0020	0.07896	0.00606	1.54	1.02
J125035.02+005700.7[3]	30487.2006	0.0054	0.44670	0.02198	2.91	1.03
J125035.29+005656.3[3]	30487.2089	0.0057	0.45515	0.02296	2.94	1.01
J131150.47-423728.2[3]	40089.0390	0.0024	0.10664	0.00807	1.66	1.02
J131151.73-423705.1[3]	40089.0381	0.0061	0.10928	0.00675	1.95	1.01
J131649.36-454901.1[3]	35398.8728	0.0022	0.03791	0.00217	2.23	1.02
J131650.51-454853.0[3]	35398.8736	0.0022	0.03812	0.00246	2.02	1.06
J133755.61-324531.4	37329.5334	0.0056	0.09899	0.01249	1.25	1.00
J134004.45-370606.2	44210.6820	0.0094	0.22169	0.01942	1.51	1.00
J141152.31-303010.7	28172.0402	0.0043	0.05902	0.00644	1.34	1.02
J144006.44+070942.7	75609.0857	0.0323	0.80130	0.10651	1.34	1.00
J144154.38-032446.1	39634.4495	0.0114	0.34247	0.02699	1.74	1.02
J144515.30-350320.6	68874.6989	0.0200	0.34331	0.01883	2.31	1.01
J145123.85-374047.0	112473.1233	0.0290	0.35062	0.04131	1.53	1.00
J145127.35+290553.3	26862.4152	0.0028	0.09715	0.00800	2.57	1.93
J150309.05-200922.1	46529.2575	0.0073	0.04661	0.00445	1.39	1.05
J152331.11-161926.4	108449.6833	0.0496	0.57831	0.07363	1.52	1.02
J152813.19+100756.5	34031.0526	0.0194	0.40020	0.02673	2.38	1.01
J152916.75-142606.3	110667.7975	0.0741	0.66525	0.08378	1.44	1.01
J160158.84-193541.8	28483.8850	0.0064	0.09779	0.00728	1.71	1.05
J161608.14+144503.0	34841.8165	0.0073	0.13090	0.00998	1.67	1.01
J164815.55+444429.4	26094.2845	0.0024	0.10653	0.00237	5.24	1.26
J165659.02+494647.6[3]	32858.8940	0.0033	0.10834	0.00851	1.38	1.00
J165704.05+494655.8[3]	32858.8986	0.0043	0.16698	0.01295	1.47	1.01
J170308.96+343457.1	45132.8900	0.0049	0.07161	0.00242	2.70	1.04
J173606.09+411841.3	38810.4300	0.0091	0.04758	0.00300	1.44	1.02
J174323.10+475141.4	34067.9160	0.0031	0.02359	0.00186	1.25	1.00

Table B.3: (continued)

WASP ID (1SWASP Jhhmmss.ss±ddmmss.s)	P /s	δP /s	$\dot{P}$ /s yr^{-1}	$\delta\dot{P}$ /s yr^{-1}	Lin. fit χ^2	Quad. fit χ^2
J174401.90+421825.6	26916.4165	0.0053	0.09091	0.00531	1.51	1.02
J175821.87+354152.2[3]	45064.6033	0.0076	0.07960	0.00515	1.65	1.02
J175823.86+354207.1[3]	45064.6054	0.0068	0.07755	0.00471	1.74	1.04
J180612.83+485829.5	42334.6267	0.0088	0.06392	0.00586	1.31	1.02
J181549.67+410637.8	45690.6329	0.0060	0.02557	0.00257	1.27	1.00
J181631.52+430000.6	31562.4249	0.0061	0.09536	0.00383	2.54	1.02
J191432.02-423246.6	67119.6466	0.0191	0.25102	0.03139	1.37	1.00
J191601.56+560055.3	27822.5455	0.0057	0.07357	0.00783	1.29	1.01
J193623.93-405317.5	40782.0055	0.0096	0.05189	0.00569	1.37	1.00
J193827.36+534444.9	51034.2863	0.0162	0.59809	0.05961	1.53	1.01
J200646.19-403057.1	78050.0989	0.0199	0.17604	0.02359	1.37	1.06
J201316.80+032427.9[3]	40366.5133	0.0079	0.06126	0.00836	1.37	1.05
J201317.68+032401.8[3]	40366.5091	0.0068	0.05721	0.00506	1.85	1.01
J201355.55-414719.0	32788.5051	0.0073	0.14594	0.01570	1.38	1.01
J201751.07-164339.1	63068.6025	0.0167	0.25375	0.01776	1.78	1.00
J201828.56-191729.4	46023.1836	0.0076	0.08150	0.00544	3.64	2.62
J202019.01-183504.2	77120.2930	0.0209	0.37396	0.03583	1.49	1.00
J202653.65-235017.9	31209.4771	0.0049	0.19385	0.02247	1.36	1.00
J202935.94-164629.7	26809.5583	0.0119	0.18642	0.01748	1.35	1.00
J204512.38+182522.2	82250.7489	0.2514	4.56608	0.27269	7.17	5.06
J204926.24-430855.9	27373.2504	0.0036	0.07059	0.00228	3.22	1.02
J205217.98-025936.7	27639.5653	0.0406	0.33365	0.02178	2.23	1.00
J205802.10-460400.3	61526.7256	0.0097	0.06865	0.00626	1.35	1.04
J210245.41+115952.6	41170.4880	0.0089	0.07756	0.00763	1.37	1.02
J210445.26-352546.5[3]	32027.4109	0.0038	0.04760	0.00514	1.40	1.00
J210445.74-352543.4[3]	32027.4170	0.0034	0.04836	0.00543	1.38	1.00
J210743.76-023812.8	31357.9637	0.0161	0.15194	0.01236	1.77	1.03
J211249.61-043241.2	40270.4050	0.0163	1.32974	0.05232	4.44	1.00
J212100.60-370342.2	29293.2884	0.0034	0.07504	0.00484	1.99	1.00
J212459.04-213924.0	61824.8018	0.0466	0.75583	0.02314	0.96	7.32
J213339.02+295713.4	65961.9745	0.0139	0.09463	0.01041	1.44	1.14
J213939.20+282331.3	52323.6985	0.0075	0.04558	0.00513	1.35	1.01
J214448.94-552447.7	23608.7593	0.0031	0.12088	0.00747	1.79	1.04
J214757.80+314218.8	67718.1312	0.0855	0.97366	0.07373	3.25	2.39
J215112.10+350502.9	45910.4853	0.0088	0.14477	0.01253	1.52	1.02
J215920.91+264115.1	23757.2055	0.0070	0.13801	0.00168	2.21	1.00
J220052.88+203349.0[3]	47607.9111	0.0324	0.32165	0.03074	1.55	1.10
J220054.61+203310.9[3]	47607.7961	0.0113	0.29160	0.01987	1.88	1.01
J220124.23+352040.7	28119.3775	0.0035	0.02656	0.00289	1.32	1.00
J220209.63-014758.2	24002.1543	0.0125	0.15519	0.02015	1.31	1.02
J220310.93+223207.1	61760.2153	0.0133	0.04821	0.00570	1.30	1.01
J220359.55+193307.4	41781.6348	0.0031	0.03822	0.00326	1.61	1.02

Table B.3: (continued)

WASP ID (1SWASP Jhhmmss.ss±ddmmss.s)	P /s	δP /s	$\dot{P}$ /s yr^{-1}	$\delta\dot{P}$ /s yr^{-1}	Lin. fit χ^2	Quad. fit χ^2
J220616.40-453943.1	37037.2172	0.0096	0.16386	0.01528	1.39	1.00
J220837.88+183744.2	37472.9665	0.0082	0.11051	0.00483	3.18	1.00
J221352.24-065817.4	22909.1169	0.0150	0.61323	0.04412	1.93	1.01
J221621.13+293307.4	30262.6096	0.0036	0.07965	0.00516	2.16	1.20
J221900.50+303848.2	28010.8993	0.0024	0.05350	0.00177	4.65	1.02
J225854.49+145145.4	57660.6230	0.0364	0.61513	0.05571	2.16	1.46
J230255.03+311954.5	39152.6962	0.0155	0.66717	0.06169	1.61	1.00
J230501.90-435608.2	42653.9166	0.0071	0.02281	0.00192	1.48	1.00
J230637.08+103359.4	26069.9742	0.0120	0.29654	0.04450	1.31	1.01
J231135.24-010909.2	26802.6773	0.0306	0.26306	0.02738	1.51	1.01
J231158.42-052605.3	74601.3546	0.0514	0.50424	0.06717	1.31	1.00
J232226.60-093527.0	76860.3575	0.0473	1.04409	0.09238	1.92	1.09
J234020.56-253007.2	33516.9902	0.0031	0.07469	0.00594	1.76	1.04
J235102.70-005546.6	45064.8306	0.0140	0.27633	0.03684	1.37	1.03

Table B.4: Periods for 30 EB-type eclipsing binary candidates exhibiting sinusoidal period change.

SuperWASP ID (1SWASP Jhhmmss.ss±ddmmss.s)	P /s	δP /s	Linear fit χ^2	Quadratic fit χ^2
J004716.03-194143.7	42233.1360	0.0094	1.43	2.95
J010006.57-074430.5	60863.1903	0.0594	3.07	1.08
J023948.86-261804.7	42754.9359	0.0067	1.76	1.19
J043127.71-004352.0	40229.2524	0.0234	1.62	1.02
J043536.13-005226.5	32505.8435	0.0468	2.27	1.06
J090358.97-213218.5[4]	40644.4700	0.0095	1.34	1.03
J090401.71-213238.5[4]	40644.4622	0.0103	1.52	1.02
J091816.12-184818.8	24490.6721	0.0105	2.42	1.67
J093609.79-181008.2	60075.1198	0.0119	1.60	1.01
J094212.53-362912.6	59666.0398	0.0091	1.25	1.00
J104933.20-165751.1	43630.0075	0.0183	2.16	1.00
J133233.71-253439.5	51989.7255	0.0119	1.39	1.04
J143209.99-174257.1	22421.0854	0.0018	2.56	1.05
J145920.96+012448.0	29817.3958	0.0351	1.46	1.07
J151210.90+175124.1	23678.2093	0.0078	6.51	5.11
J153336.78-215811.1	60888.3593	0.0228	1.35	1.01
J162410.43+455526.7	22950.3614	0.0021	9.28	4.55
J165649.13+402738.4	23775.3036	0.0031	4.51	2.14
J172023.92+411512.7	27251.3042	0.0023	4.34	2.08
J201144.64+570512.7	46345.5543	0.0197	3.50	1.02
J203341.88-205838.4	24928.4306	0.0031	1.40	1.01
J211359.46+122712.4	19190.1240	0.0026	1.43	1.01
J212456.58-213909.0	61824.7961	0.0364	3.39	2.47
J215746.18-661432.0	28148.3045	0.0085	1.35	1.00
J220210.22-014819.9	24002.1257	0.0101	1.43	1.00
J220215.40+094552.4	69338.0593	0.0391	1.38	1.04
J221449.81-213020.5	24810.6553	0.0065	1.55	1.05
J221652.14+222934.4	29933.5192	0.0016	1.96	1.10
J223537.37+025328.3	30595.2128	0.0070	1.86	1.07
J225913.78-082932.6	25034.2317	0.0423	2.82	1.08

[4]This "object" and its neighbour(s) at similar coordinates are duplicates of a single astrophysical object.

Table B.5: Periods and quadratic period change determinations for 171 EA-type eclipsing binary candidates.

WASP ID (1SWASP Jhhmmss.ss±ddmmss.s)	P /s	δP /s	$\dot{P}$ /s yr^{-1}	$\delta\dot{P}$ /s yr^{-1}	Lin. fit χ^2	Quad. fit χ^2
J002717.28-233642.0	132393.9737	0.0703	0.90936	0.04890	8.76	1.10
J003518.16+404547.6	149296.3079	0.0778	1.42926	0.09536	5.23	1.01
J004345.09+305619.6[5]	128416.8238	0.0322	0.87129	0.03805	9.82	1.10
J004346.91+305603.8[5]	128416.7300	0.0336	0.82979	0.04481	6.35	1.01
J005015.63+310004.9	148976.7937	0.0756	0.25266	0.04421	1.61	1.00
J005147.36+264032.1	116414.1095	0.0649	0.28170	0.03874	2.10	1.00
J005156.72-044304.5	146859.7518	0.1080	1.11732	0.27649	1.40	1.02
J005543.22+153749.0	105194.4528	0.0804	0.27323	0.04344	1.34	1.01
J010319.14-374513.9	96993.8405	0.0253	0.38453	0.02358	3.73	1.08
J010512.40+274603.1	61915.3376	0.0166	0.16260	0.01220	2.92	1.21
J011416.27+224537.6	119041.9879	0.0467	0.22763	0.04636	1.58	1.25
J012546.35-395610.6	108937.6523	0.0308	0.67112	0.03212	9.43	1.06
J014219.31+162950.8	113337.4219	0.1107	2.59979	0.74277	1.61	1.08
J014225.32+375524.7	80038.6659	0.0208	0.37472	0.04089	2.21	1.03
J015326.78-315822.2	69515.3391	0.0186	0.20071	0.03181	1.29	1.01
J021521.43-121226.7	84257.1033	0.0983	0.32581	0.05543	1.36	1.02
J021559.07+144920.0	161333.3957	0.1101	0.32097	0.09190	1.47	1.12
J022941.61-054714.9	58871.3953	0.0255	0.42254	0.06030	1.38	1.00
J023018.20-333539.6	65716.7771	0.0142	0.30045	0.01496	3.23	1.01
J025911.05-185839.3	197087.8901	0.1341	1.05788	0.14398	1.96	1.03
J034413.03-411646.8	62414.5652	0.0179	0.10158	0.00769	2.69	1.63
J035525.61+313047.9	41956.5689	0.0102	0.12224	0.01830	1.45	1.03
J040014.48-074559.8	55336.8643	0.0196	0.36832	0.02600	2.21	1.02
J040259.25+271855.3	180715.6138	0.1247	0.74769	0.14422	1.82	1.10
J041456.76+312714.6	192548.4053	0.0912	0.32032	0.05040	2.34	1.11
J041944.93-321008.6[5]	55571.0449	0.0272	0.16702	0.01219	2.08	1.00
J041946.84-321006.3[5]	55571.0563	0.0174	0.11985	0.01255	1.56	1.01
J044601.99-293247.1	72647.9214	0.0169	0.23204	0.01266	3.28	1.02
J045232.36+061935.9	70263.5126	0.0280	0.23457	0.03979	1.45	1.06
J050011.67-380150.0	165760.9268	0.0955	0.51973	0.10663	1.42	1.01
J050205.46-284245.5	142667.1017	0.0649	0.92004	0.06978	4.65	1.78
J053450.76-302514.6	44308.2169	0.0068	0.10257	0.00819	2.26	1.69
J054017.61-431819.1	78673.1074	0.0256	0.52843	0.05909	1.27	1.00
J060630.95-262651.1	117105.5380	0.0411	0.10592	0.02546	1.28	1.00
J060730.26-330736.5	254977.5816	0.1618	3.55581	0.55600	1.80	1.04
J061727.55-213628.9	158788.8422	0.0577	0.43825	0.06411	2.45	1.19
J063051.52-320833.4	74752.0454	0.0152	0.25844	0.02790	1.52	1.00
J063807.68-294323.4	63430.7580	0.0171	0.20248	0.02329	1.34	1.00
J065343.99-430921.1	231568.9715	0.1566	1.55783	0.21984	1.83	1.00

[5]This "object" and its neighbour(s) at similar coordinates are duplicates of a single astrophysical object.

Table B.5: (continued)

WASP ID (1SWASP Jhhmmss.ss±ddmmss.s)	P /s	δP /s	$\dot{P}$ /s yr^{-1}	$\delta\dot{P}$ /s yr^{-1}	Lin. fit χ^2	Quad. fit χ^2
J065530.28-403623.5	94027.2428	0.0330	0.52254	0.03115	2.71	1.06
J084421.88-022002.0[5]	73503.7197	0.0343	0.34451	0.03487	1.70	1.00
J084422.29-022027.4[5]	73503.7189	0.0377	0.37819	0.04251	1.55	1.00
J090932.65-013539.3	152667.3426	0.1243	1.46543	0.34362	1.36	1.03
J091428.94-134138.6	163674.5458	0.1319	2.10124	0.26915	2.23	1.13
J091649.26+051759.3	116116.8393	0.0571	1.60859	0.10288	5.12	1.13
J093046.79-185614.1	91894.7169	0.0183	0.15880	0.01240	2.67	1.16
J093921.15-204517.0[5]	141928.2906	0.0759	0.41022	0.04201	2.23	1.05
J093921.40-204536.2[5]	141928.1343	0.0387	0.36312	0.04190	1.99	1.02
J095144.05-102331.8	387900.1816	0.2394	6.44426	0.99669	2.69	1.12
J100532.02-144420.7	205246.7068	0.2287	2.65681	0.63056	1.61	1.04
J100721.56-221857.3	104793.7580	0.0368	0.21890	0.01948	2.51	1.10
J102157.55-034329.7	132868.9516	0.1633	0.32143	0.10077	1.42	1.07
J103128.30-411425.2	240367.2799	0.1565	1.74203	0.23442	2.59	1.04
J104619.94-455759.5	280109.4715	0.1441	1.56214	0.36075	1.34	1.00
J110818.29-231335.7	118260.1848	0.0335	0.24998	0.03332	2.03	1.15
J111701.40-401011.4	64620.3240	0.0085	0.09740	0.01181	1.26	1.00
J111909.11-425706.2	124039.5216	0.0482	0.19047	0.03565	1.46	1.10
J112105.65-260738.3	62738.0366	0.0116	0.27584	0.01772	2.17	1.00
J112618.04-233309.5	98059.5421	0.0218	0.13991	0.02112	1.35	1.01
J120951.49-322757.4	153966.5708	0.0311	0.38251	0.08557	1.53	1.16
J121935.63-273836.7	242636.0323	0.0462	3.36834	0.32560	3.20	1.03
J123601.48-435859.2	67677.4497	0.0167	0.23432	0.01579	2.30	1.04
J124109.78-050500.6	59088.0409	0.0315	0.34885	0.03964	1.46	1.00
J124128.16+354643.6	60616.9893	0.0094	0.12687	0.02032	1.33	1.00
J124420.23-084016.8	10084.5643	0.0006	0.00281	0.00009	6.20	1.00
J124551.60-200656.0	133348.9706	0.0524	0.43455	0.06801	1.86	1.09
J131124.02+375954.4	197162.9657	0.0328	0.96122	0.15379	2.52	1.00
J132228.82-392554.3	502167.8392	0.4272	1.26231	0.54505	1.36	1.00
J132640.58-160616.5	220195.8207	0.0820	3.24448	0.76300	1.63	1.00
J132710.24-041020.6	65162.2966	0.0539	0.45735	0.04443	1.74	1.03
J132856.21-224333.4	48634.9625	0.0065	0.09510	0.01304	1.38	1.01
J133024.89+134932.0	44638.0692	0.0125	0.13592	0.01106	2.21	1.03
J133349.56-455000.1[5]	151475.5918	0.0739	1.77946	0.09271	5.94	1.04
J133351.32-455029.6[5]	151475.6005	0.0763	1.87456	0.12982	3.95	1.03
J133353.43-455016.0[5]	151475.6362	0.0657	2.25330	0.19633	2.84	1.00
J134225.06-450554.0	65449.2149	0.0076	0.05992	0.00522	1.72	1.00
J134754.90-304934.6[5]	54420.0744	0.0136	0.11367	0.01463	1.28	1.00
J134755.89-304905.2[5]	54420.0784	0.0137	0.14553	0.01612	1.37	1.00
J135441.76-220452.4	70564.6769	0.0105	0.11983	0.01825	1.26	1.00
J140632.28+411535.6	41544.5209	0.0098	0.24825	0.03640	1.45	1.02
J140658.98+112609.7	60760.5856	0.0620	0.22027	0.03663	1.32	1.00

Table B.5: (continued)

WASP ID (1SWASP Jhhmmss.ss±ddmmss.s)	P /s	δP /s	$\dot{P}$ /s yr^{-1}	$\delta\dot{P}$ /s yr^{-1}	Lin. fit χ^2	Quad. fit χ^2
J141254.20-054750.2	99440.7241	0.0870	2.42815	0.21107	2.20	1.00
J141412.22-210227.5	75994.7674	0.0221	0.20134	0.01276	2.30	1.00
J141825.56-310926.8	113673.8533	0.0409	0.28568	0.03705	1.78	1.00
J141850.78+435001.9	68503.5707	0.0138	0.16502	0.02476	1.58	1.14
J142920.96+320803.7	134891.7353	0.0493	0.81717	0.02265	8.17	1.06
J144228.84-100808.1	74891.2442	0.0711	1.23239	0.12818	2.01	1.08
J150029.60+334022.1	108588.3868	0.0326	0.21960	0.01277	6.13	1.30
J150753.03+153330.1	52682.2289	0.0130	0.12846	0.01997	1.56	1.09
J154643.40-230747.4	110761.7951	0.0287	0.21720	0.02820	2.28	1.29
J154853.06-241701.2	140520.3358	0.0771	0.57122	0.12711	1.43	1.02
J155440.39-191526.5	82532.8914	0.0328	0.39813	0.04016	1.84	1.00
J155559.84-171138.6	107026.8617	0.0353	0.20066	0.03798	1.29	1.00
J161605.83+142549.4	174854.3595	0.1386	0.34688	0.10005	1.43	1.11
J161738.89+085602.6	149822.9842	0.1047	1.69590	0.33786	1.90	1.00
J161813.25-191814.8	112156.1920	0.0663	1.63486	0.11876	3.01	1.00
J162209.63-164832.7	54883.5951	0.0214	0.36409	0.04303	1.32	1.00
J162649.35+511036.2	79597.5788	0.0284	0.48560	0.05071	1.27	1.00
J163020.99+381910.3	64490.1709	0.0460	0.18950	0.01400	1.83	1.00
J163307.64+333125.4	423871.3410	0.1143	1.48019	0.23145	1.58	1.00
J164357.76+261744.4	45319.3228	0.0084	0.17350	0.00797	2.18	1.00
J164403.77+392332.9	105694.0969	0.0192	0.18685	0.01217	3.19	1.15
J165628.71+373918.9	151698.8438	0.0454	0.36679	0.03476	2.50	1.42
J165656.95+291906.3	68046.9498	0.0167	0.06061	0.00479	1.50	1.00
J170823.63+395749.6	53242.5877	0.0079	0.17769	0.01034	1.85	1.00
J172531.62+311917.3	177297.0709	0.0506	0.15585	0.01910	2.09	1.18
J173059.32+432449.6	81384.5771	0.0134	0.16790	0.00671	4.49	1.17
J173935.42+325628.2[5]	70683.6744	0.0157	0.08580	0.00561	3.18	1.88
J173936.81+325646.7[5]	70683.6557	0.0115	0.09853	0.00438	4.99	2.20
J175050.71+500249.8	202828.7813	0.0922	0.86811	0.08918	3.75	1.97
J180311.93+321113.8	320385.0727	0.1734	0.62549	0.08907	2.79	1.00
J181513.49+381805.3	74475.7465	0.0175	0.08583	0.01046	1.30	1.00
J182211.67+473407.9	74825.1032	0.0436	0.23318	0.01986	1.96	1.37
J183315.61+374512.8	168370.1742	0.0504	0.15792	0.02378	1.62	1.00
J184833.70+511255.9	71540.0279	0.0213	0.58252	0.06384	1.44	1.00
J190756.71+592351.9	103061.1361	0.0484	0.36528	0.08877	1.31	1.02
J191842.53+485705.5	99849.4124	0.0645	0.53140	0.08940	1.32	1.01
J193447.30-405505.6	146153.8169	0.0575	0.43185	0.05452	2.08	1.03
J193839.34-445955.2[5]	116803.6461	0.0295	0.45348	0.06904	1.48	1.02
J193839.47-450036.8[5]	116803.6143	0.0292	0.44729	0.03586	3.49	1.00
J194237.47-383921.9[5]	178749.0344	0.0964	0.90230	0.13321	2.18	1.03
J194237.49-383955.0[5]	178749.0884	0.0565	0.68910	0.08085	3.02	1.03
J195132.38-432249.4	261961.8568	0.1584	1.40644	0.18315	3.21	1.07

Table B.5: (continued)

WASP ID (1SWASP Jhhmmss.ss±ddmmss.s)	P /s	δP /s	$\dot{P}$ /s yr^{-1}	$\delta\dot{P}$ /s yr^{-1}	Lin. fit χ^2	Quad. fit χ^2
J195606.05-425712.8	121625.0639	0.0556	0.31482	0.04856	1.99	1.30
J200616.91-285128.2[5]	79610.1180	0.0304	0.39522	0.03445	1.93	1.00
J200618.36-285203.3[5]	79610.0745	0.0331	0.37437	0.03072	2.09	1.02
J200945.62+485149.1[5]	103769.2640	0.0584	1.91330	0.17632	2.26	1.00
J200945.67+485207.3[5]	103769.2237	0.0559	2.07126	0.14721	4.36	1.02
J201956.50+020134.3	73531.4942	0.0292	0.68143	0.06794	1.74	1.00
J203521.94-610346.1	63547.1729	0.0188	0.12521	0.00882	1.86	1.03
J203615.68-313025.3[5]	74573.0655	0.0204	0.35499	0.02222	2.99	1.00
J203616.56-313047.9[5]	74573.0187	0.0136	0.37162	0.01964	3.36	1.00
J203718.08-383047.2[5]	89784.8842	0.0395	0.29254	0.05789	1.27	1.00
J203722.39-383015.5[5]	89784.8399	0.0306	0.10367	0.01742	1.52	1.14
J204327.63-550257.8	69971.1809	0.0324	0.96476	0.04045	3.32	1.04
J204829.85+203805.0	162031.0374	0.0945	1.26976	0.12705	4.59	1.19
J205001.34-623355.5	89782.5379	0.0385	0.19735	0.01553	1.86	1.01
J205332.50+043849.5	67669.5632	0.0273	0.05502	0.00627	1.87	1.02
J210444.88-352550.8	32027.4178	0.0049	0.04870	0.00487	1.48	1.00
J210459.79-205219.2	132043.4830	0.0921	0.34032	0.03661	1.93	1.08
J210604.30+021702.2	51268.1071	0.0338	0.42434	0.01915	3.31	1.00
J210734.75+042417.9	99010.3898	0.0343	0.12955	0.02238	1.73	1.07
J212818.11-440917.3	69266.3380	0.0138	0.10092	0.00378	3.30	1.01
J212859.72+195220.1	150757.9302	0.1170	0.16795	0.01698	3.29	1.04
J213942.42+262116.7	108688.5992	0.0217	0.20186	0.01247	4.84	1.11
J213956.15-051352.1	133370.3987	0.1266	1.29370	0.21918	2.14	1.18
J214156.25+084248.8	58443.7965	0.0212	0.07957	0.00751	1.80	1.03
J214421.05+352314.3	106107.5241	0.0280	0.45840	0.05188	1.63	1.02
J214711.73-325347.2	137301.2754	0.0295	0.21129	0.05424	1.40	1.08
J214749.02-201353.5[5]	141014.8289	0.1091	1.24746	0.06880	7.01	1.05
J214749.89-201406.3[5]	141014.6333	0.0832	1.19421	0.07196	5.73	1.00
J215125.19+072024.3	83515.1465	0.0497	0.12438	0.01792	1.37	1.01
J220140.75+103718.4	235778.3793	0.1329	0.56398	0.09081	1.87	1.00
J220600.10+193549.6	50097.3847	0.0095	0.02831	0.00142	2.76	1.02
J220844.67-310920.0	115863.6500	0.0431	0.36937	0.08434	1.32	1.01
J221055.15+071513.5	77573.1200	0.0515	0.19080	0.02633	1.73	1.05
J222128.29+333002.6[5]	81707.7420	0.0316	0.39172	0.04258	1.55	1.01
J222128.41+333020.9[5]	81707.7491	0.0318	0.53403	0.02232	4.28	1.01
J222453.27+275559.6	209650.4559	0.0873	0.36216	0.05921	1.91	1.00
J222523.60-443539.3	106616.4214	0.0236	0.30444	0.02056	4.26	1.18
J222533.85+280448.8	34258.7906	0.0043	0.02874	0.00317	1.31	1.00
J222615.03+211301.7	117206.3933	0.0253	0.14777	0.01195	3.01	1.01
J222700.55-371118.1	163572.1181	0.0739	0.09689	0.02514	1.54	1.11
J224204.77-301655.0	107653.0892	0.0428	0.42700	0.04722	2.21	1.25
J224734.87-390831.7	72931.2954	0.0307	0.13729	0.02174	1.26	1.00

Table B.5: (continued)

WASP ID (1SWASP Jhhmmss.ss±ddmmss.s)	P /s	δP /s	$\dot{P}$ /s yr^{-1}	$\delta\dot{P}$ /s yr^{-1}	Lin. fit χ^2	Quad. fit χ^2
J225001.27-204506.9	58551.1334	0.0096	0.09802	0.01090	1.33	1.01
J225203.88-125643.6	90262.2813	0.0705	0.24784	0.04934	1.40	1.00
J225831.95-421716.8	60549.1311	0.0098	0.08688	0.00516	3.11	1.09
J230311.15-391418.2	118210.4112	0.0511	0.13911	0.03683	1.28	1.00
J231519.78+164719.1	166173.7498	0.1305	1.24791	0.19784	1.95	1.03
J233319.32+222233.4	108959.8514	0.0806	0.22714	0.05071	1.56	1.00

Table B.6: Periods for 18 EA-type eclipsing binary candidates exhibiting sinusoidal period change.

SuperWASP ID (1SWASP Jhhmmss.ss±ddmmss.s)	P /s	δP /s	Linear fit χ^2	Quadratic fit χ^2
J012449.35-074004.9	48166.4372	0.0106	1.73	1.00
J065342.87-430911.9	231569.1013	0.1861	1.72	1.11
J103820.77+141603.6	51847.5434	0.0130	3.63	2.10
J154429.44-150320.4	153000.8339	0.1163	1.69	1.09
J154946.55-204150.7	31539.3276	0.0092	2.28	1.54
J161253.63-022042.2	35162.8162	0.0071	4.15	1.10
J165954.85+542803.3	17704.2415	0.0041	1.41	1.11
J171335.36+304236.0	195863.4824	0.0602	3.36	2.04
J173329.02+403315.2	85462.0986	0.0215	1.29	1.00
J174615.04+452331.8	68011.5823	0.0091	4.37	3.21
J182625.19+412014.5	223985.1555	0.0854	1.94	1.00
J210421.98+131253.4	102913.9002	0.0303	2.10	1.03
J210935.08-225030.2	53947.1017	0.0128	6.08	4.78
J213148.77-450242.3	162475.5469	0.0851	3.92	2.41
J214614.83+122939.9	53129.3740	0.0076	1.46	1.00
J220643.31-434358.4	158330.0850	0.1138	1.67	1.01
J224452.75-420045.6	81623.9483	0.0213	2.22	1.16
J235755.28-415543.1	121213.2071	0.0462	1.52	1.14

References

Affer L, Micela G, Favata F and Flaccomio E (2012) 'The rotation of field stars from CoRoT data', *MNRAS*, 424, 11–22.

Akerlof C, Amrose S, Balsano R, Bloch J, Casperson D, Fletcher S, Gisler G, Hills J, Kehoe R, Lee B, Marshall S, McKay T, Pawl A, Schaefer J, Szymanski J and Wren J (2000) 'ROTSE All-Sky Surveys for Variable Stars. I. Test Fields', *AJ*, 119, 1901–1913.

Almeida L A and Jablonski F (2011) 'Two bodies with high eccentricity around the cataclysmic variable QS Vir', in *The Astrophysics of Planetary Systems: Formation, Structure, and Dynamical Evolution (IAU Symposium No. 276)*, edited by Sozzetti A, Lattanzi M G and Boss A P (IAU/CUP), pp. 495–496.

Almeida L A, Jablonski F and Rodrigues C V (2013) 'Two Possible Circumbinary Planets in the Eclipsing Post-common Envelope System NSVS 14256825', *ApJ*, 766, 11.

Anglada-Escudé G, Arriagada P, Vogt S S, Rivera E J, Butler R P, Crane J D, Shectman S A, Thompson I B, Minniti D, Haghighipour N, Carter B D, Tinney C G, Wittenmyer R A, Bailey J A, O'Toole S J, Jones H R A and Jenkins J S (2012) 'A Planetary System around the nearby M Dwarf GJ 667C with At Least One Super-Earth in Its Habitable Zone', *ApJ*, 751, L16.

Applegate J H (1992) 'A mechanism for orbital period modulation in close binaries', *ApJ*, 385, 621–629.

Auvergne M, Bodin P, Boisnard L, Buey J T, Chaintreuil S, Epstein G, Jouret M, Lam-Trong T, Levacher P, Magnan A, Perez R, Plasson P, Plesseria J, Peter G, Steller M, Tiphène D, Baglin A, Agogué P, Appourchaux T, Barbet D, Beaufort T, Bellenger R, Berlin R, Bernardi P, Blouin D, Boumier P, Bonneau F, Briet R, Butler B, Cautain R, Chiavassa F, Costes V, Cuvilho J, Cunha-Parro V, de Oliveira Fialho F, Decaudin M, Defise J M, Djalal S, Docclo A, Drummond R, Dupuis O, Exil G, Fauré C, Gaboriaud A, Gamet P, Gavalda P, Grolleau E, Gueguen L, Guivarc'h V, Guterman P, Hasiba J, Huntzinger G, Hustaix H, Imbert C, Jeanville G, Johlander B, Jorda L, Journoud P, Karioty F, Kerjean L, Lafond L, Lapeyrere V, Landiech P, Larqué T, Laudet P, Merrer J L, Leporati L, Leruyet B, Levieuge B, Llebaria A, Martin L, Mazy E, Mesnager J M, Michel J P, Moalic J P, Monjoin W, Naudet D, Neukirchner S, Nguyen-Kim K, Ollivier M, Orcesi J L, Ottacher H, Oulali A, Parisot J, Perruchot S, Piacentino A, da Silva L P, Platzer J, Pontet B, Pradines A, Quentin C, Rohbeck U, Rolland G, Rollenhagen F, Romagnan R, Russ N, Samadi R, Schmidt R, Schwartz N, Sebbag I, Smit H, Sunter W, Tello M, Toulouse P, Ulmer B, Vandermarcq O, Vergnault E, Wallner R, Waultier G and Zanatta P (2009) 'The CoRoT satellite in flight: description and performance', *A&A*, 506, 411–424.

Backhaus U, Bauer S, Beuermann K, Diese J, Dreizler S, Hessman F V, Husser T O, Klapdohr K H, Möllmanns J, Schünecke R, Dette J, Dubbert J, Miosga T, Vogel A L R, Simons S, Biriuk S, Debrah M, Griemens M, Hahn A, Möller T, Pawlowski M, Schweizer M, Speck A L, Zapros C, Bollmann T, Habermann F N, Haustovich N, Lauser M, Liebing F, Niederstadt F, Hoppen K, Kindermann D, Küppers F, Rauch B, Althoff F, Horstmann M, Kellerman J N, Kietz

R, Nienaber T, Sauer M, Secci A and Wüllner L (2012) 'The quest for companions to post-common envelope binaries. I. Searching a sample of stars from the CSS and SDSS', *A&A*, 538, A84.

Barclay T, Ramsay G, Hakala P, Napiwotzki R, Nelemans G, Potter S and Todd I (2011) 'Stellar variability on time-scales of minutes: results from the first 5 yr of the Rapid Temporal Survey', *MNRAS*, 413, 2696–2708.

Barlow B N, Kilkenny D, Drechsel H, Dunlap B H, O'Donoghue D, Geier S, O'Steen R G, Clemens J C, LaCluyze A P, Reichart D E, Haislip J B, Nysewander M C and Ivarsen K M (2013) 'EC 10246-2707: an eclipsing subdwarf B+M dwarf binary', *MNRAS*, 430, 22–31.

Batten A H and Hardie R H (1965) 'ADS 9537 - A pair of eclipsing binaries.', *AJ*, 70, 666–667.

Beuermann K, Breitenstein P, Debski B, Diese J, Dubovsky P A, Dreizler S, Hessman F V, Hornoch K, Husser T O, Pojmański G, Wolf M, Woźniak P R, Zasche P, Denk B, Langer M, Wagner C, Wahrenberg D, Bollmann T, Habermann F N, Haustovich N, Lauser M, Liebing F and Niederstadt F (2012a) 'The quest for companions to post-common envelope binaries. II. NSVS14256825 and HS0705+6700', *A&A*, 540, A8.

Beuermann K, Dreizler S, Hessman F V and Deller J (2012b) 'The quest for companions to post-common envelope binaries. III. A reexamination of HW Virginis', *A&A*, 543, 138.

Beuermann K, Hessman F V, Dreizler S, Marsh T R, Parsons S G, Winget D E, Miller G F, Schreiber M R, Kley W, Dhillon V S, Littlefair S P, Copperwheat C M and Hermes J J (2010) 'Two planets orbiting the recently formed post-common envelope binary NN Serpentis', *A&A*, 521, L60.

Binnendijk L (1970) 'The orbital elements of W Ursae Majoris systems', *Vistas in Astronomy*, 12, 217–256.

Blažko S (1907) 'Mitteilung über veränderliche Sterne', *Astron Nachr*, 175, 325–328.

Borucki W J, Koch D, Basri G, Batalha N, Brown T, Caldwell D, Caldwell J, Christensen-Dalsgaard J, Cochran W D, DeVore E, Dunham E W, Dupree A K, Gautier T N, Geary J C, Gilliland R, Gould A, Howell S B, Jenkins J M, Kondo Y, Latham D W, Marcy G W, Meibom S, Kjeldsen H, Lissauer J J, Monet D G, Morrison D, Sasselov D, Tarter J, Boss A, Brownlee D, Owen T, Buzasi D, Charbonneau D, Doyle L, Fortney J, Ford E B, Holman M J, Seager S, Steffen J H, Welsh W F, Rowe J, Anderson H, Buchhave L, Ciardi D, Walkowicz L, Sherry W, Horch E, Isaacson H, Everett M E, Fischer D, Torres G, Johnson J A, Endl M, MacQueen P, Bryson S T, Dotson J, Haas M, Kolodziejczak J, Cleve J V, Chandrasekaran H, Twicken J D, Quintana E V, Clarke B D, Allen C, Li J, Wu H, Tenenbaum P, Verner E, Bruhweiler F, Barnes J and Prša A (2010) 'Kepler Planet-Detection Mission: Introduction and First Results', *Sci*, 327, 977–980.

Bradstreet D H and Guinan E F (1994) 'Stellar Mergers and Acquisitions: The Formation and Evolution of W Ursae Majoris Binaries', in *Interacting Binary Stars*, edited by Shafter A W (Astronomical Society of the Pacific Conference Series, San Francisco, Calif.), pp. 228–243.

Brát L, Trnka J, Šmelcer L, Lehky M, Kucakova H, Lomoz F, Hanzl D, Vrastak M, Corfini G, Pribik V, Dreveny R, Ehrenberger R, Kocian R, Masek M, Polak J, Starzomski J, Marchi F, Poddany S, Zejda M, Cagas P, Klos M, Garofalo R, Klimentova J, Kliment P, Speil J, Magris M, Hladik B, Honkova K, Jurysek J, Smycka T, Moudra M, Naves R, Ruocco N, Zahajsky J, Audejean M, Pejcha

O, Uhlar R, Vieira J, Zasche P and Zambelli R (2011) 'B.R.N.O. Contributions #37 - Times of minima', *Open European Journal on Variable Stars*, 137, 1–57.

Buckley D A H, Swart G P and Meiring J G (2006) 'Completion and commissioning of the Southern African Large Telescope', in *Ground-based and Airborne Telescopes*, edited by Stepp L M, p. 32.

Burgh E B, Nordsieck K H, Kobulnicky H A, Williams T B, O'Donoghue D, Smith M P, Percival J W, Iye M and Moorwood A F M (2003) 'Prime Focus Imaging Spectrograph for the Southern African Large Telescope: optical design', in *Instrument Design and Performance for Optical/Infrared Ground-based Telescopes*, edited by Iye M and Moorwood A, pp. 1463–1471.

Butler R P, Marcy G W, Williams E, Hauser H and Shirts P (1997) 'Three New "51 Pegasi–Type" Planets', *ApJ*, 474, L115.

Cagaš P and Pejcha O (2012) 'Discovery of a double eclipsing binary with periods near a 3:2 ratio', *A&A*, 544, L3.

Çamurdan C M, Çamurdan D Z and Ibanoğlu C (2012) 'Photometric observations and orbital period variations of HS 0705 + 6700 and NY Vir', *New Astronomy*, 17, 325–330.

Chew Y G M (2010) *On the analysis of two low-mass, eclipsing binary systems in the young Orion Nebula cluster* (Vanderbilt University, unpublished PhD thesis).

Christopoulou P E, Papageorgiou A, Vasileiadis T and Tsantilas S (2012) 'A Holistic View of the W UMa Type TY Boo', *AJ*, 144, 149.

Clarkson W I, Charles P A, Coe M J, Laycock S, Tout M D and Wilson C A (2003) 'Long-term properties of accretion discs in X-ray binaries - I. The variable third period in SMC X-1', *MNRAS*, 339, 447–454.

Coughlin J L, López-Morales M, Harrison T E, Ule N and Hoffman D I (2011) 'Low-mass Eclipsing Binaries in the Initial Kepler Data Release', *AJ*, 141, 78.

Crawford S M, Still M, Schellart P, Balona L, Buckley D A H, Dugmore G, Gulbis A A S, Kniazev A, Kotze M, Loaring N, Nordsieck K H, Pickering T E, Potter S, Colmenero E R, Vaisanen P, Williams T and Zietsman E (2010) 'PySALT: the SALT science pipeline', in *Observatory Operations: Strategies, Processes, and Systems III*, edited by Silva D R, Peck A B and Soifer B T, p. 54.

Creevey O L, Grundahl F, Pallé P L, Jørgensen U G, Belmonte J A, Christensen-Dalsgaard J, Frandsen S, Kjeldsen H and Kjærgaard P (2011) 'The Observatorio del Teide welcomes SONG:the Stellar Observations Network Group', in *Highlights of Spanish Astrophysics VI: Proceedings of the IX Scientific Meeting of the Spanish Astronomical Society*, edited by Osorio M R Z, Gorgas J, Apellániz J M, Pardo J R and de Paz A G, pp. 686–692.

da Silva R, Maceroni C, Gandolfi D, Lehmann H and Hatzes A P (2014) 'CoRoT 105906206: a short-period and totally eclipsing binary with a delta Scuti type pulsator', *A&A*, 565, A55.

Davis P J, Kolb U, Willems B and Gänsicke B T (2008) 'How many cataclysmic variables are crossing the period gap? A test for the disruption of magnetic braking', *MNRAS*, 389, 1563–1576.

Deacon N R, Schlieder J E, Olofsson J, Johnston K G and Henning T (2013) 'A young hierarchical triple system harbouring a candidate debris disc', *MNRAS*, 434, 1117–1128.

Degroote P, Acke B, Samadi R, Aerts C, Kurtz D W, Noels A, Miglio A, Montalbán J, Bloemen S, Baglin A, Baudin F, Catala C, Michel E and Auvergne M (2011) 'CoRoT's view on variable B8/9 stars: spots versus pulsations. Evidence for differential rotation in HD 174648', *A&A*, 536, 82.

Dimitrov D P and Kjurkchieva D P (2010) 'GSC2314-0530: the shortest-period eclipsing system with dMe components', *MNRAS*, 406, 2559–2568.

Djorgovski S G, Mahabal A A, Drake A J, Graham M J and Donalek C (2013) 'Sky Surveys', in *Planets, Stars and Stellar Systems: Astronomical Techniques, Software, and Data*, edited by Oswalt T D and Bond H E (Springer Science+Business Media, Dordrecht), pp. 223–282.

Djorgovski S G, Mahabal A A, Drake A J, Graham M J, Donalek C and Williams R (2012) 'Exploring the Time Domain with Synoptic Sky Surveys', in *New Horizons in Time-Domain Astronomy*, edited by Griffin R E M, Hanisch R J and Seaman R (Cambridge University Press, Cambridge, UK), pp. 141–146.

Dotter A, Chaboyer B, Jevremović D, Kostov V, Baron E and Ferguson J W (2008) 'The Dartmouth Stellar Evolution Database', *ApJS*, 178, 89–101.

Doyle L R, Carter J A, Fabrycky D C, Slawson R W, Howell S B, Winn J N, Orosz J A, Prša A, Welsh W F, Quinn S N, Latham D, Torres G, Buchhave L A, Marcy G W, Fortney J J, Shporer A, Ford E B, Lissauer J J, Ragozzine D, Rucker M, Batalha N, Jenkins J M, Borucki W J, Koch D, Middour C K, Hall J R, McCauliff S, Fanelli M N, Quintana E V, Holman M J, Caldwell D A, Still M, Stefanik R P, Brown W R, Esquerdo G A, Tang S, Furesz G, Geary J C, Berlind P, Calkins M L, Short D R, Steffen J H, Sasselov D, Dunham E W, Cochran W D, Boss A, Haas M R, Buzasi D and Fischer D (2011) 'Kepler-16: A Transiting Circumbinary Planet', *Sci*, 333, 1602.

Drake A J, Djorgovski S G, García-Álvarez D, Graham M J, Catelan M, Mahabal A A, Donalek C, Prieto J L, Torrealba G, Abraham S, Williams R, Larson S and Christensen E (2014) 'Ultra-short Period Binaries from the Catalina Surveys', *ApJ*, 790, 157.

Duchêne G and Kraus A (2013) 'Stellar Multiplicity', *Annual Review of Astronomy and Astrophysics*, 51, 269–310.

Duerbeck H W (1996) 'W UMa type variables', in *Light Curves of Variable Stars. A Pictorial Atlas*, edited by Sterken C and Jaschek C (Cambridge University Press), pp. 183–187.

Eastman J, Siverd R and Gaudi B S (2010) 'Achieving Better Than 1 Minute Accuracy in the Heliocentric and Barycentric Julian Dates', *PASP*, 122, 935–946.

Eggleton P (2006) *Evolutionary Processes in Binary and Multiple Stars* (Cambridge University Press, Cambridge, UK).

Elkhateeb M M, Nouh M I, Saad S M and Zaid I (2014a) 'A CCD photometric study of the newly discovered short period eclipsing binary 1SWASP J210318.76 + 021002.2', *New Astronomy*, 32, 10–15.

Elkhateeb M M, Saad S M, Nouh M I and Shokry A (2014b) 'Photometric study of the newly discovered short period eclipsing binary 1SWASP J133105.91 + 121538.0', *New Astronomy*, 28, 85–90.

Essam A, Djurašević G, Ahmed N M and Jurković M (2014) 'A photometric study of the W UMa-type eclipsing binary system 1SWASP J160156.04 + 202821.6', *New Astronomy*, 32, 16–20.

Essam A, Mohamadien G F, Ahmed N M and Ali G B (2013) 'First CCD photometric observation of the W-UMa eclipsing binary system 1SWASP J064501.21+342154.9', *NRIAG Journal of Astronomy and Geophysics*, 2, 256–265.

Eyer L, Dubath P, Mowlavi N, North P, Triaud A, Barblan F, Siopis C, Guy L, Tingley B, Zucker S, Evans D W, Wyrzykowski L, Süveges M and Ivezic

Z (2012a) 'The Impact of Gaia and LSST on Binaries and Exoplanets', in *From Interacting Binaries to Exoplanets: Essential Modeling Tools*, edited by Richards M T and Hubeny I (Cambridge University Press), pp. 33–40.

Eyer L, Dubath P, Saesen S, Evans D W, Wyrzykowski L, Hodgkin S and Mowlavi N (2012b) 'From Hipparcos to Gaia', in *New Horizons in Time-Domain Astronomy*, edited by Griffin R E M, Hanisch R J and Seaman R (Cambridge University Press, Cambridge, UK), pp. 153–157.

Feast M W (1996a) 'Cepheid variables', in *Light Curves of Variable Stars. A Pictorial Atlas*, edited by Sterken C and Jaschek C (Cambridge University Press), pp. 86–91.

Feast M W (1996b) 'delta Scuti variables', in *Light Curves of Variable Stars. A Pictorial Atlas*, edited by Sterken C and Jaschek C (Cambridge University Press), pp. 81–83.

Feast M W (1996c) 'RR Lyrae variables', in *Light Curves of Variable Stars. A Pictorial Atlas*, edited by Sterken C and Jaschek C (Cambridge University Press), pp. 83–86.

Flower P J (1996) 'Transformations from Theoretical Hertzsprung-Russell Diagrams to Color-Magnitude Diagrams: Effective Temperatures, B-V Colors, and Bolometric Corrections', *ApJ*, 469, 355.

For B Q, Green E M, Fontaine G, Drechsel H, Shaw J S, Dittmann J A, Fay A G, Francoeur M, Laird J, Moriyama E, Morris M, Rodríguez-López C, Sierchio J M, Story S M, Strom A, Wang C, Adams S M, Bolin D E, Eskew M and Chayer P (2010) 'Modeling the System Parameters of 2M 1533+3759: A New Longer Period Low-Mass Eclipsing sdB+dM Binary', *ApJ*, 708, 253–267.

García R A (2013) 'Solar-Like Stars Observed by Kepler: An Incredible Adventure', in *Stellar Pulsations: Impact of New Instrumentation and New Insights*,

edited by Suárez J C, Garrido R, Balona L A and Christensen-Dalsgaard J (Springer-Verlag Berlin Heidelberg), pp. 171–175.

Gies D R, Williams S J, Matson R A, Guo Z, Thomas S M, Orosz J A and Peters G J (2012) 'A Search for Hierarchical Triples using Kepler Eclipse Timing', *AJ*, 143, 137.

Graczyk D, Soszyński I, Poleski R, Pietrzyński G, Udalski A, Szymański M K, Kubiak M, Wyrzykowski Ł and Ulaczyk K (2011) 'The Optical Gravitational Lensing Experiment. The OGLE-III Catalog of Variable Stars. XII. Eclipsing Binary Stars in the Large Magellanic Cloud', *Acta Astron*, 61, 103–122.

Green S F and Jones M H (2004) *An Introduction to the Sun and Stars* (Open University and Cambridge University Press, Cambridge, UK).

Griffin R E, Hanisch R J and Seaman R L (2012) *New Horizons in Time-Domain Astronomy: Proceedings of the 285th Symposium of the International Astronomical Union* (Cambridge University Press, Cambridge, UK).

Griffin R F (2012) 'Spectroscopic Binaries: Towards the 100-Year Time Domain', in *New Horizons in Time-Domain Astronomy*, edited by Griffin R E M, Hanisch R J and Seaman R (Cambridge University Press, Cambridge, UK), pp. 75–80.

Grindlay J, Tang S, Los E and Servillat M (2012) 'Opening the 100-Year Window for Time-Domain Astronomy', in *New Horizons in Time-Domain Astronomy*, edited by Griffin R E M, Hanisch R J and Seaman R (Cambridge University Press, Cambridge, UK), pp. 29–34.

Guinan E F and Bradstreet D H (1988) 'Kinematic Clues to the Origin and Evolution of Low Mass Contact Binaries', in *Formation and Evolution of Low Mass Stars*, edited by Dupree A K and Lago M T V T (Kluwer, Dordrecht), p. 345.

Hadrava P (2012) 'The Disentangling of Stellar Spectra', in *From Interacting Binaries to Exoplanets: Essential Modeling Tools*, edited by Richards M T and Hubeny I (IAU), pp. 351–358.

Hakala P, Ramsay G and Barclay T (2012) 'Contact Binary Population from the RATS Survey', in *New Horizons in Time-Domain Astronomy*, edited by Griffin R E, Hanisch R J and Seaman R L (Cambridge University Press, Cambridge, UK), p. 434.

Hall D S (1996a) 'Algol type eclipsing binaries', in *Light Curves of Variable Stars. A Pictorial Atlas*, edited by Sterken C and Jaschek C (Cambridge University Press), pp. 168–173.

Hall D S (1996b) 'beta Lyrae type eclipsing binaries', in *Light Curves of Variable Stars. A Pictorial Atlas*, edited by Sterken C and Jaschek C (Cambridge University Press), pp. 173–177.

Hall D S (1996c) 'BY Dra variables', in *Light Curves of Variable Stars. A Pictorial Atlas*, edited by Sterken C and Jaschek C (Cambridge University Press), pp. 120–122.

Harrison T E, Coughlin J L, Ule N M and López-Morales M (2012) 'Kepler Cycle 1 Observations of Low-mass Stars: New Eclipsing Binaries, Single Star Rotation Rates, and the Nature and Frequency of Starspots', *ApJ*, 143, 4.

Haswell C A (2010) *Transiting Exoplanets* (Cambridge University Press / Open University, Cambridge).

Heber U (2009) 'Hot Subdwarf Stars', *ARA&A*, 47, 211–251.

Henden A A, Levine S E, Terrell D, Smith T C and Welch D (2012) 'Data Release 3 of the AAVSO All-Sky Photometric Survey (APASS)', *Journal of the American Association of Variable Star Observers*, 40, 430.

Hilditch R W (2001) *An Introduction to Close Binary Stars* (Cambridge University Press, Cambridge, UK).

Hinse T C, Lee J W, Goździewski K, Horner J and Wittenmyer R A (2014) 'Revisiting the proposed circumbinary multiplanet system NSVS 14256825', *MNRAS*, 438, 307–317.

Holdsworth D L, Smalley B, Gillon M, Clubb K I, Southworth J, Maxted P F L, Anderson D R, Barros S C C, Cameron A C, Delrez L, Faedi F, Haswell C A, Hellier C, Horne K, Jehin E, Norton A J, Pollacco D, Skillen I, Smith A M S, West R G and Wheatley P J (2014) 'High-frequency A-type pulsators discovered using SuperWASP', *MNRAS*, 439, 2078–2095.

Holmes S, Kolb U, Haswell C A, Burwitz V, Lucas R J, Rodriguez J, Rolfe S M, Rostron J and Barker J (2011) 'PIRATE: A Remotely Operable Telescope Facility for Research and Education', *PASP*, 123, 1177–1187.

Horne J H and Baliunas S L (1986) 'A prescription for period analysis of unevenly sampled time series', *ApJ*, 302, 757–763.

Horner J, Wittenmyer R A, Tinney C G, Robertson P, Hinse T C and Marshall J P (2013) 'Dynamical Constraints on Multi-Planet Exoplanetary Systems', in *Proceedings of the 12th Australian Space Science Conference*, edited by Short W and Cairns I (National Space Society of Australia), pp. 103–115.

Huber K F, Wolter U, Czesla S, Schmitt J H M M, Esposito M, Ilyin I and González-Pérez J N (2009) 'Long-term stability of spotted regions and the activity-induced Rossiter-McLaughlin effect on V889 Herculis. A synergy of photometry, radial velocity measurements, and Doppler imaging', *A&A*, 501, 715–728.

Hurley J R, Tout C A and Pols O R (2002) 'Evolution of binary stars and the effect of tides on binary populations', *MNRAS*, 329, 897–928.

Ivanova N, Justham S, Chen X, Marco O D, Fryer C L, Gaburov E, Ge H, Glebbeek E, Han Z, Li X D, Lu G, Marsh T, Podsiadlowski P, Potter A, Soker N, Taam R, Tauris T M, van den Heuvel E P J and Webbink R F (2013) 'Common envelope evolution: where we stand and how we can move forward', *A&AR*, 21, 59.

Jiang D, Han Z, Ge H, Yang L and Li L (2012) 'The short-period limit of contact binaries', *MNRAS*, 421, 2769–2773.

Jones M H and Lambourne R J A (2004) *An Introduction to Galaxies and Cosmology* (Open University and Cambridge University Press, Cambridge, UK).

Kawka A, Vennes S, Koch R and Williams A (2002) 'Optical Observations and Orbital Parameters of the Close DA plus dMe Binaries BPM 71214, EUVE J0720-31.7, BPM 6502, and EC 13471-1258', *AJ*, 124, 2853–2867.

Kelley N and Shaw J S (2007) 'Combined NSVS/2MASS database search for Cool Algols and Eclipsing Subdwarf B Stars', *Journal of the Southeastern Association for Research in Astronomy*, 1, 13–16.

Kilkenny D (1986) 'Ephemeris for the sdOB eclipsing binary, AA DOR (LB3459)', *Observatory*, 106, 160–162.

Kilkenny D (2011) 'The orbital periods of AA Dor and NY Vir', *MNRAS*, 412, 487–491.

Kilkenny D, Harrop-Allin M and Marang F (1991) 'Recent Minima and Improved Ephemerides for the Eclipsing Hot Subdwarfs LB 3459 (= AA Dor) and BD -7 3477 (= HW Vir)', *Information Bulletin on Variable Stars*, 3569, 1.

Kilkenny D, Hilditch R W and Penfold J E (1978) 'LB 3459, a short-period eclipsing binary system containing two O-type subdwarfs', *MNRAS*, 183, 523–531.

Kilkenny D, Hilditch R W and Penfold J E (1979) 'LB3459, an O-type subdwarf eclipsing binary system. II - New photometry and an improved analysis', *MNRAS*, 187, 1–7.

Kilkenny D, Hill P W and Penfold J E (1981) 'LB 3459, an O-type subdwarf eclipsing binary system. III - Radial velocity curve and orbital solutions', *MNRAS*, 194, 429–437.

Kilkenny D, Keuris S, Marang F, Roberts G, van Wyk F and Ogloza W (2000) 'On the orbital periods of three close binaries with hot subdwarf primaries', *Observatory*, 120, 48–59.

Kilkenny D and Koen C (2012) 'Detection of an increasing orbital period in the subdwarf B eclipsing system NSVS 14256825', *MNRAS*, 421, 3238–3241.

Kilkenny D, Marang F and Menzies J W (1994) 'A Period Decrease in the Sdb Eclipsing Binary System Hw-Virginis', *MNRAS*, 267, 535.

Kilkenny D, O'Donoghue D, Koen C, Lynas-Gray A E and van Wyk F (1998) 'The EC 14026 stars - VIII. PG 1336-018: a pulsating sdB star in an HWVir-type eclipsing binary', *MNRAS*, 296, 329–338.

Kilkenny D, O'Donoghue D, Koen C, Stobie R S and Chen A (1997) 'The Edinburgh-Cape Blue Object Survey - II. Zone 1 - the North Galactic CAP', *MNRAS*, 287, 867–893.

Kilkenny D, van Wyk F and Marang F (2003) 'The sdB eclipsing system HW Vir: a substellar companion?', *Observatory*, 123, 31–36.

Kim C H, Kreiner J M and Nha L S (2003) 'Statistics of times of minimum light of 1140 eclipsing binary stars', in *Stellar Astrophysics - A Tribute to Helmut A. Abt*, edited by Cheng K S, Leung K C and Li T P (Kluwer Academic Publishers, Dordrecht), pp. 127–130.

Koen C (2014) 'Multicolour time series photometry of the variable star 1SWASP J234401.81-212229.1', *MNRAS*, 441, 3075–3082.

Kolb U (2010) *Extreme Environment Astrophysics* (Open University and Cambridge University Press, Cambridge, UK).

Koo J R, Lee J W, Lee B C, Kim S L, Lee C U, Hong K, Lee D J and Rey S C (2014) '1SWASP J093010.78+533859.5: A Possible Hierarchical Quintuple System', *AJ*, 147, 104.

Kopal Z (1955) 'The classification of close binary systems', *Annales d'Astrophysique*, 18, 379–430.

Kopal Z (1959) *Close binary systems* (Chapman & Hall, London).

Kopal Z and Kurth R (1957) 'The Relation between Period and Times of the Maxima or Minima of Variable Stars', *Zeitschrift fur Astrophysik*, 42, 90–100.

Kornilov V G, Lipunov V M, Gorbovskoy E S, Belinski A A, Kuvshinov D A, Tyurina N V, Shatsky N I, Sankovich A V, Krylov A V, Balanutsa P V, Chazov V V, Kuznetsov A S, Zimnuhov D S, Senik V A, Tlatov A G, Parkhomenko A V, Dormidontov D V, Krushinsky V V, Zalozhnyh I S, Popov A A, Yazev S A, Budnev N M, Ivanov K I, Konstantinov E N, Gress O A, Chvalaev O V, Yurkov V V, Sergienko Y P and Kudelina I P (2012) 'Robotic optical telescopes global network MASTER II. Equipment, structure, algorithms', *Experimental Astronomy*, 33, 173–196.

Kozai Y (1962) 'Secular perturbations of asteroids with high inclination and eccentricity', *AJ*, 67, 591.

Krautter J (1996a) 'Flare stars', in *Light Curves of Variable Stars. A Pictorial Atlas*, edited by Sterken C and Jaschek C (Cambridge University Press), pp. 53–59.

Krautter J (1996b) 'Pre-main sequence stars', in *Light Curves of Variable Stars. A Pictorial Atlas*, edited by Sterken C and Jaschek C (Cambridge University Press), pp. 45–53.

Kreiner J M, Kim C H and Nha I S (2001) *An Atlas of O-C Diagrams of Eclipsing Binary Stars* (Wydawnictwo Naukowe Akademii Pedagogicznej, Cracow, Poland).

Kubiak M, Udalski A and Szymański M K (2006) 'Period Changes of Contact Binaries in OGLE Database', *Acta Astron*, 56, 253–265.

Kwee K K and van Woerden H (1956) 'A method for computing accurately the epoch of minimum of an eclipsing variable', *Bulletin of the Astronomical Institutes of the Netherlands*, 12, 327–330.

Lafler J and Kinman T D (1965) 'An RR Lyrae Star Survey with Ihe Lick 20-INCH Astrograph II. The Calculation of RR Lyrae Periods by Electronic Computer.', *ApJS*, 11, 216–222.

Leavitt H S and Pickering E C (1912) 'Periods of 25 Variable Stars in the Small Magellanic Cloud.', *Harvard College Observatory Circular*, 173, 1–3.

Lee C U, Kim S L, Lee J W, Kim C H, Jeon Y B, Kim H I, Yoon J N and Humphrey A (2008) 'V994 Herculis: the multiple system with a quadruple-lined spectrum and a double eclipsing feature', *MNRAS*, 389, 1630–1636.

Lee J W, Kim S L, Kim C H, Koch R H, Lee C U, Kim H I and Park J H (2009) 'The sdB+M Eclipsing System HW Virginis and its Circumbinary Planets', *AJ*, 137, 3181–3190.

Lee J W, Lee C U, Kim S L, Kim H I and Park J H (2011) 'The Light and Period Variations of the Eclipsing Binary AA Ursae Majoris', *PASP*, 123, 34–43.

Lehmann H, Zechmeister M, Dreizler S, Schuh S and Kanzler R (2012) 'KIC 4247791: a SB4 system with two eclipsing binaries (2EBs). A quadruple system?', *A&A*, 541, A105.

Levenberg K (1944) 'A Method for the Solution of Certain Non-linear Problems in Least Squares', *Quarterly of Applied Mathematics*, 2(2), 164–168.

Liu N P, Qian S B, Soonthornthum B, Leung K C, Liao W P, Zhu L Y, He J J, Liu L and Zhao E G (2014) 'First Photometric Study of the Very Short Period K-type Contact Binary 1SWASP J064501.21+342154.9', *AJ*, 147, 41.

Liying Z and Shengbang Q (2010) 'A photometric study of a new short period eclipsing sdB binary NSVS 07826147', *Ap&SS*, 329, 107–112.

Lohr M E, Hodgkin S T, Norton A J and Kolb U C (2014a) 'Parameters of two low-mass contact eclipsing binaries near the short-period limit', *A&A*, 563, A34.

Lohr M E, Norton A J, Anderson D R, Cameron A C, Faedi F, Haswell C A, Hellier C, Hodgkin S T, Horne K, Kolb U C, Maxted P F L, Pollacco D, Skillen I, Smalley B, West R G and Wheatley P J (2014b) 'Period and amplitude variations in post-common-envelope eclipsing binaries observed with SuperWASP', *A&A*, 566, A128.

Lohr M E, Norton A J, Kolb U C, Anderson D R, Faedi F and West R G (2012) 'Period decrease in three SuperWASP eclipsing binary candidates near the short-period limit', *A&A*, 542, A124.

Lohr M E, Norton A J, Kolb U C and Boyd D R S (2013a) 'One, two, or three stars? An investigation of an unusual eclipsing binary candidate undergoing dramatic period changes', *A&A*, 558, A71.

Lohr M E, Norton A J, Kolb U C, Maxted P F L, Todd I and West R G (2013b) 'Period and period change measurements for 143 SuperWASP eclipsing binary candidates near the short-period limit and discovery of a doubly eclipsing quadruple system', *A&A*, 549, A86.

Lomb N R (1976) 'Least-squares frequency analysis of unequally spaced data', *Ap&SS*, 39, 447–462.

Mahabal A A, Djorgovski S G, Drake A J, Donalek C, Graham M J, Williams R D, Chen Y, Moghaddam B, Turmon M, Beshore E and Larson S (2011) 'Discovery, classification, and scientific exploration of transient events from the Catalina Real-time Transient Survey', *Bulletin of the Astronomical Society of India*, 39, 387–408.

Marang F and Kilkenny D (1989) 'Recent Minima of the Subdwarf Eclipsing Binary BD -7 3477 (=HW Vir)', *Information Bulletin on Variable Stars*, 3390, 1.

Marquardt D W (1963) 'An Algorithm for Least-Squares Estimation of Nonlinear Parameters', *SIAM Journal on Applied Mathematics*, 11(2), 431–441.

Marsh T R (2005) 'Doppler Tomography', *Ap&SS*, 296, 403–415.

Marsh T R and Horne K (1988) 'Images of accretion discs. II - Doppler tomography', *MNRAS*, 235, 269–286.

Marsh T R, Parsons S G, Bours M C P, Littlefair S P, Copperwheat C M, Dhillon V S, Breedt E, Caceres C and Schreiber M R (2014) 'The planets around NN Serpentis: still there', *MNRAS*, 437, 475–488.

Masci F J, Hoffman D I, Grillmair C J and Cutri R M (2014) 'Automated Classification of Periodic Variable Stars Detected by the Wide-field Infrared Survey Explorer', *AJ*, 148, 21.

Maxted P F L, Anderson D R, Burleigh M R, Cameron A C, Heber U, Gänsicke B T, Geier S, Kupfer T, Marsh T R, Nelemans G, O'Toole S J, Østensen R H, Smalley B, West R G and Bloemen S (2012) 'Discovery of a Stripped Red-giant Core in a Bright Eclipsing Binary Star', in *Fifth Meeting on Hot Subdwarf Stars and Related Objects*, edited by Kilkenny D, Jeffery C S and Koen C (San Francisco, CA: Astronomical Society of the Pacific), p. 137.

Mayor M and Queloz D (1995) 'A Jupiter-mass companion to a solar-type star', *Nat*, 378, 355–359.

Mazeh T, Tamuz O, Zucker S, Udalski A and the Wasp Consortium (2006) 'Sys-Rem – A new algorithm to remove systematic effects in large photometric datasets: application to OGLE and SuperWASP lightcurves', in *Tenth Anniversary of 51 Peg-b: Status of and prospects for hot Jupiter studies*, edited by Arnold L, Bouchy F and Moutou C (Frontier Group), pp. 165–172.

McLaughlin D B (1924) 'Some results of a spectrographic study of the Algol system', *ApJ*, 60, 22–31.

Menzies J W and Marang F (1986) 'A New B-Subdwarf Eclipsing Binary with an Extremely Short Period', in *Instrumentation and Research Programmes for Small Telescopes (IAU Symposium No. 118)*, edited by Hearnshaw J B and Cottrell P L (D. Reidel), pp. 305–306.

Michaely E and Perets H B (2014) 'Secular dynamics in hierarchical three-body systems with mass loss and mass transfer', *ArXiv e-prints*, 1406.3035.

Minniti D, Lucas P W, Emerson J P, Saito R K, Hempel M, Pietrukowicz P, Ahumada A V, Alonso M V, Alonso-Garcia J, Arias J I, Bandyopadhyay R M, Barbá R H, Barbuy B, Bedin L R, Bica E, Borissova J, Bronfman L, Carraro G, Catelan M, Clariá J J, Cross N, de Grijs R, Dékány I, Drew J E, na C F, Feinstein C, Lajús E F, Gamen R C, Geisler D, Gieren W, Goldman B,

Gonzalez O A, Gunthardt G, Gurovich S, Hambly N C, Irwin M J, Ivanov V D, Jordán A, Kerins E, Kinemuchi K, Kurtev R, López-Corredoira M, Maccarone T, Masetti N, Merlo D, Messineo M, Mirabel I F, Monaco L, Morelli L, Padilla N, Palma T, Parisi M C, Pignata G, Rejkuba M, Roman-Lopes A, Sale S E, Schreiber M R, Schröder A C, Smith M, Jr L S, Soto M, Tamura M, Tappert C, Thompson M A, Toledo I, Zoccali M and Pietrzynski G (2010) 'VISTA Variables in the Via Lactea (VVV): The public ESO near-IR variability survey of the Milky Way', *New Astronomy*, 15, 433–443.

Mislis D, Pyrzas S, Harlaftis E T, Street R A, Horne K, Pollacco D, Seiradakis J H, Kane S R, Lister T, Cameron C, Clarkson W I and Solomos N (2006) 'WASP0: A wide field CCD search for extra solar planets. Instrumentation, data analysis and preliminary results', in *Recent Advances in Astronomy and Astrophysics: 7th International Conference of the Hellenic Astronomical Society*, edited by Solomos N (AIP Conference Proceedings), pp. 810–815.

Monaghan J J (1968) 'The Precession of a Rotating Magnetic Star', *Zeitschrift fur Astrophysik*, 69, 154–159.

Naoz S and Fabrycky D C (2014) 'Mergers and Obliquities in Stellar Triples', *ArXiv e-prints*, 1405.5223.

Nefs S V, Birkby J L, Snellen I A G, Hodgkin S T, Pinfield D J, Sipocz B, Kovacs G, Mislis D, Saglia R P, Koppenhoefer J, Cruz P, Barrado D, Martin E L, Goulding N, Stoev H, Zendejas J, del Burgo C, Cappetta M and Pavlenko Y V (2012) 'Four ultra-short-period eclipsing M-dwarf binaries in the WFCAM Transit Survey', *MNRAS*, 425, 950–968.

Norton A J, Payne S G, Evans T, West R G, Wheatley P J, Anderson D R, Barros S C C, Butters O W, Cameron A C, Christian D J, Enoch B, Faedi F, Haswell C A, Hellier C, Holmes S, Horne K D, Kane S R, Lister T A, Maxted

P F L, Parley N, Pollacco D, Simpson E K, Skillen I, Smalley B, Southworth J and Street R A (2011) 'Short period eclipsing binary candidates identified using SuperWASP', *A&A*, 528, A90.

Norton A J, Wheatley P J, West R G, Haswell C A, Street R A, Cameron A C, Christian D J, Clarkson W I, Enoch B, Gallaway M, Hellier C, Horne K, Irwin J, Kane S R, Lister T A, Nicholas J P, Parley N, Pollacco D, Ryans R, Skillen I and Wilson D M (2007) 'New periodic variable stars coincident with ROSAT sources discovered using SuperWASP', *A&A*, 467, 785–905.

O'Connell D J K (1951) 'The so-called periastron effect in close eclipsing binaries ; New variable stars (fifth list)', *Publications of the Riverview College Observatory*, 2, 85–100.

O'Donoghue D, Koen C, Kilkenny D, Stobie R S, Koester D, Bessell M S, Hambly N and MacGillivray H (2003) 'The DA+dMe eclipsing binary EC13471-1258: its cup runneth over ... just', *MNRAS*, 345, 506–528.

Orosz J A, Welsh W F, Carter J A, Brugamyer E, Buchhave L A, Cochran W D, Endl M, Ford E B, MacQueen P, Short D R, Torres G, Windmiller G, Agol E, Barclay T, Caldwell D A, Clarke B D, Doyle L R, Fabrycky D C, Geary J C, Haghighipour N, Holman M J, Ibrahim K A, Jenkins J M, Kinemuchi K, Li J, Lissauer J J, Prša A, Ragozzine D, Shporer A, Still M and Wade R A (2012a) 'The Neptune-sized Circumbinary Planet Kepler-38b', *ApJ*, 758, 87.

Orosz J A, Welsh W F, Carter J A, Fabrycky D C, Cochran W D, Endl M, Ford E B, Haghighipour N, MacQueen P J, Mazeh T, Sanchis-Ojeda R, Short D R, Torres G, Agol E, Buchhave L A, Doyle L R, Isaacson H, Lissauer J J, Marcy G W, Shporer A, Windmiller G, Barclay T, Boss A P, Clarke B D, Fortney J, Geary J C, Holman M J, Huber D, Jenkins J M, Kinemuchi K, Kruse E, Ragozzine D, Sasselov D, Still M, Tenenbaum P, Uddin K, Winn J N, Koch D G

and Borucki W J (2012b) 'Kepler-47: A Transiting Circumbinary Multiplanet System', *Sci*, 337, 1511.

Østensen R, Oreiro R, Drechsel H, Heber U, Baran A, Pigulski A, Napiwotzki R and Burleigh M R (2007) 'HS 2231+2441: A New Eclipsing sdB Binary of the HW Vir Type', in *15th European Workshop on White Dwarfs (ASP Conference Series, Vol. 372)*, edited by Napiwotzki R and Burleigh M R (San Francisco: Astronomical Society of the Pacific), pp. 483–486.

Østensen R H, Green E M, Bloemen S, Marsh T R, Laird J B, Morris M, Moriyama E, Oreiro R, Reed M D, Kawaler S D, Aerts C, Vučković M, Degroote P, Telting J H, Kjeldsen H, Gilliland R L, Christensen-Dalsgaard J, Borucki W J and Koch D (2010) '2M1938+4603: a rich, multimode pulsating sdB star with an eclipsing dM companion observed with Kepler', *MNRAS*, 408, L51–L55.

Paczyński B (1976) 'Common Envelope Binaries', in *Structure and Evolution of Close Binary Systems (IAU Symposium No. 73)*, edited by Paczyński B, Eggleton P, Mitton S and Whelan J (D. Reidel), pp. 75–80.

Paczyński B (1997) 'The Future of Massive Variability Searches.', in *Variable Stars and the Astrophysical Returns of the Microlensing Surveys*, edited by Ferlet R, Maillard J P and Raban B (Gif-sur-Yvette, France : Editions Frontieres), p. 357.

Paczyński B, SzczygiełD M, Pilecki B and Pojmański G (2006) 'Eclipsing binaries in the All Sky Automated Survey catalogue', *MNRAS*, 368, 1311–1318.

Parley N R, Green S F, McBride N, Haswell C A, Cameron A C, Lister T A, West R G, Pollacco D L and Consortium S (2008) 'The SuperWASP Asteroid Light Curve and Phase Curve Survey', *LPI Contributions*, 1405, 8049.

Parley N R, McBride N, Green S F, Haswell C A, Clarkson W I, Christian D J, Collier-Cameron A, Evans N A, Fitzsimmons A, Hellier C, Hodgkin S T, Horne K, Irwin J, Kane S R, Keenan F P, Lister T A, Norton A J, Osborne J P, Pollacco D, Ryans R, Skillen I, Street R A, West R G and Wheatley P J (2005) 'Serendipitous Asteroid Lightcurve Survey Using SuperWASP', *Earth Moon and Planets*, 97, 261–268.

Parsons S G, Marsh T R, Copperwheat C M, Dhillon V S, Littlefair S P, Hickman R D G, Maxted P F L, Gänsicke B T, Unda-Sanzana E, Colque J P, Barraza N, Sánchez N and Monard L A G (2010) 'Orbital period variations in eclipsing post-common-envelope binaries', *MNRAS*, 407, 2362–2382.

Paunzen E, Wraight K T, Fossati L, Netopil M, White G J and Bewsher D (2013) 'A photometric study of chemically peculiar stars with the STEREO satellites - II. Non-magnetic chemically peculiar stars', *MNRAS*, 429, 119–125.

Payne S G (2013) *Catalogue of SuperWASP variable stars: PhD dissertation for the Open University* (unpublished).

Pepper J, Kuhn R B, Siverd R, James D and Stassun K (2012) 'The KELT-South Telescope', *PASP*, 124, 230–241.

Pigulski A, Pojmański G, Pilecki B and SzczygiełD M (2009) 'The All Sky Automated Survey. The Catalog of Variable Stars in the Kepler Field of View', *Acta Astron*, 59, 33–46.

Pojmański G (1997) 'The All Sky Automated Survey', *Acta Astron*, 47, 467–481.

Pojmański G (2002) 'The All Sky Automated Survey. Catalog of Variable Stars. I. 0 h - 6 h Quarter of the Southern Hemisphere', *Acta Astron*, 52, 397–427.

Pojmański G (2003) 'The All Sky Automated Survey. The Catalog of Variable

Stars. II. 6 h-12 h Quarter of the Southern Hemisphere', *Acta Astron*, 53, 341–369.

Pojmański G and Maciejewski G (2004) 'The All Sky Automated Survey. Catalog of Variable Stars. III. 12 h-18 h Quarter of the Southern Hemisphere', *Acta Astron*, 54, 153–179.

Pojmański G and Maciejewski G (2005) 'The All Sky Automated Survey. Catalog of Variable Stars. IV. 18 h-24 h Quarter of the Southern Hemisphere', *Acta Astron*, 55, 97–122.

Pojmański G, Pilecki B and SzczygiełD (2005) 'The All Sky Automated Survey. Catalog of Variable Stars. V. Declinations 0 arcd - +28 arcd of the Northern Hemisphere', *Acta Astron*, 55, 275–301.

Poleski R, Soszyński I, Udalski A, Szymański M K, Kubiak M, Pietrzyński G, Wyrzykowski Ł, Szewczyk O and Ulaczyk K (2010a) 'The Optical Gravitational Lensing Experiment. The OGLE-III Catalog of Variable Stars. VI. Delta Scuti Stars in the Large Magellanic Cloud', *Acta Astron*, 60, 1–16.

Poleski R, Soszyński I, Udalski A, Szymański M K, Kubiak M, Pietrzyński G, Wyrzykowski Ł and Ulaczyk K (2010b) 'The Optical Gravitational Lensing Experiment. The OGLE-III Catalog of Variable Stars. X. Enigmatic Class of Double Periodic Variables in the Large Magellanic Cloud', *Acta Astron*, 60, 179–196.

Pollacco D L, Skillen I, Cameron A C, Christian D J, Hellier C, Irwin J, Lister T A, Street R A, West R G, Anderson D, Clarkson W I, Deeg H, Enoch B, Evans A, Fitzsimmons A, Haswell C A, Hodgkin S, Horne K, Kane S R, Keenan F P, Maxted P F L, Norton A J, Osborne J, Parley N R, Ryans R S I, Smalley B, Wheatley P J and Wilson D M (2006) 'The WASP Project and the SuperWASP Cameras', *PASP*, 118(848), 1407–1418.

Press W H, Teukolsky S A, Vetterling W T and Flannery B P (2007) *Numerical Recipes: The Art of Scientific Computing* (Cambridge University Press, New York), 3 ed.

Pribulla T, Balud'anský D, Dubovský P, Kudzej I, Š Parimucha, Siwak M and Vaňko M (2008) 'VW LMi: tightest quadruple system known. Light-time effect and possible secular changes of orbits', *MNRAS*, 390, 798–806.

Pribulla T, Vaňko M, von Eiff M A, Andreev M, Aslantürk A, Awadalla N, Balud'anský D, Bonanno A, Božić H, Catanzaro G, Çelik L, Christopoulou P E, Covino E, Cusano F, Dimitrov D, Dubovský P, Esmer E M, Frasca A, Hambálek L, Hanna M, Hanslmeier A, Kalomeni B, Kjurkchieva D P, Krushevska V, Kudzej I, Kundra E, Kuznyetsova Y, Lee J W, Leitzinger M, Maciejewski G, Moldovan D, Morais M H M, Mugrauer M, Neuhäuser R, Niedzielski A, Odert P, Ohlert J, Özavci I, Papageorgiou A, Š Parimucha, Poddaný S, Pop A, Raetz M, Raetz S, Romanyuk Y, Ruždjak D, Schulz J, Senavci H V, Szalai T, Székely P, Sudar D, Tezcan C T, Törün M E, Turcu V, Vince O and Zejda M (2012) 'The Dwarf project: Eclipsing binaries - precise clocks to discover exoplanets', *Astron Nachr*, 333, 754–766.

Prša A and Zwitter T (2005) 'A Computational Guide to Physics of Eclipsing Binaries. I. Demonstrations and Perspectives', *ApJ*, 628, 426–438.

Qian S B, Liao W P, Zhu L Y, Dai Z B, Liu L, He J J, Zhao E G and Li L J (2010a) 'A giant planet in orbit around a magnetic-braking hibernating cataclysmic variable', *MNRAS*, 401, L34–L38.

Qian S B, Zhu L Y, Dai Z B, Fernández-Lajús E, Xiang F Y and He J J (2012) 'Circumbinary Planets Orbiting the Rapidly Pulsating Subdwarf B-type Binary NY Vir', *ApJ*, 745, L23.

Qian S B, Zhu L Y, Liu L, Dai Z B, He J J, Liao W P, Zhao E G, Zola S,

Kuligowska E and Winiarski M (2010b) 'Orbital period investigation of some short-period sdB-type eclipsing binaries', *Ap&SS*, 329, 113–117.

Ramsay G, Brooks A, Hakala P, Barclay T, Garcia-Alvarez D, Antoci V, Greiss S, Still M, Steeghs D, Gänsicke B and Reynolds M (2014) 'RATS-Kepler - a deep high-cadence survey of the Kepler field', *MNRAS*, 437, 132–146.

Ramsay G and Hakala P (2005) 'RApid Temporal Survey (RATS) - I. Overview and first results', *MNRAS*, 360, 314–321.

Rappaport S, Deck K, Levine A, Borkovits T, Carter J, Mellah I E, Sanchis-Ojeda R and Kalomeni B (2013) 'Triple-star Candidates among the Kepler Binaries', *ApJ*, 768, 33.

Rappaport S, Verbunt F and Joss P C (1983) 'A new technique for calculations of binary stellar evolution, with application to magnetic braking', *ApJ*, 275, 713–731.

Rasio F A (1995) 'The minimum mass ratio of W Ursae Majoris binaries', *ApJ*, 444, L41–L43.

Ripepi V, Moretti M I, Clementini G, Marconi M, Cioni M R, Marquette J B and Tisserand P (2012) 'Preliminary results for RR Lyrae stars and Classical Cepheids from the Vista Magellanic Cloud (VMC) survey', *Ap&SS*, 341, 51–56.

Robb R M and Greimel R (1997) 'The Eclipsing Binary RX J1326.9+4532', *Information Bulletin on Variable Stars*, 4486, 1.

Rossiter R A (1924) 'On the detection of an effect of rotation during eclipse in the velocity of the brigher component of beta Lyrae, and on the constancy of velocity of this system.', *ApJ*, 60, 15–21.

Rucinski S M (1992) 'Can full convection explain the observed short-period limit of the W UMa-type binaries?', *AJ*, 103, 960–966.

Rucinski S M (1998) 'Contact Binaries of the Galactic Disk: Comparison of the Baade's Window and Open Cluster Samples', *AJ*, 116, 2998–3017.

Ryan S G and Norton A J (2010) *Stellar Evolution and Nucleosynthesis* (Cambridge University Press, Cambridge, UK).

Saglia R P, Tonry J L, Bender R, Greisel N, Seitz S, Senger R, Snigula J, Phleps S, Wilman D, Bailer-Jones C A L, Klement R J, Rix H W, Smith K, Green P J, Burgett W S, Chambers K C, Heasley J N, Kaiser N, Magnier E A, Morgan J S, Price P A, Stubbs C W and Wainscoat R J (2012) 'The Photometric Classification Server for Pan-STARRS1', *ApJ*, 746, 128.

Samus N N, Goranskij V P, Durlevich O V, Kazarovets E V, Kireeva N N, Pastukhova E N and Zharova A V (2007-2013) *General Catalogue of Variable Stars (GCVS database, Version 2013 Apr.): VizieR On-line Data Catalog: B/gcvs* (Institute of Astronomy of Russian Academy of Sciences and Sternberg State Astronomical Institute of the Moscow State University).

Scargle J D (1982) 'Studies in astronomical time series analysis. II - Statistical aspects of spectral analysis of unevenly spaced data', *ApJ*, 263, 835–853.

Schaffenroth V, Geier S, Drechsel H, Heber U, Wils P, Østensen R H, Maxted P F L and di Scala G (2013) 'A new bright eclipsing hot subdwarf binary from the ASAS and SuperWASP surveys', *A&A*, 553, A18.

Schwamb M E, Orosz J A, Carter J A, Welsh W F, Fischer D A, Torres G, Howard A W, Crepp J R, Keel W C, Lintott C J, Kaib N A, Terrell D, Gagliano R, Jek K J, Parrish M, Smith A M, Lynn S, Simpson R J, Giguere M J and Schawinski K (2013) 'Planet Hunters: A Transiting Circumbinary Planet in a Quadruple Star System', *ApJ*, 768, 127.

Schwarzenberg-Czerny A (1996) 'Fast and Statistically Optimal Period Search in Uneven Sampled Observations', *ApJ*, 460, L107.

Schwarzenberg-Czerny A (2003) 'An astronomer's guide to period searching', in *Interplay of Periodic, Cyclic and Stochastic Variability in Selected Areas of the H-R Diagram*, edited by Sterken C (Astronomical Society of the Pacific, San Francisco), pp. 383–390.

Schwarzenberg-Czerny A (2012) 'On the Sensitivity of Period Searches', in *New Horizons in Time-Domain Astronomy*, edited by Griffin E, Hanisch R and Seaman R (Cambridge University Press), pp. 81–86.

Shin M S, Yi H, Kim D W, Chang S W and Byun Y I (2012) 'Detecting Variability in Massive Astronomical Time-series Data. II. Variable Candidates in the Northern Sky Variability Survey', *AJ*, 143, 65.

Silvotti R, Schuh S, Janulis R, Solheim J E, Bernabei S, Østensen R, Oswalt T D, Bruni I, Gualandi R, Bonanno A, Vauclair G, Reed M, Chen C W, Leibowitz E, Paparo M, Baran A, Charpinet S, Dolez N, Kawaler S, Kurtz D, Moskalik P, Riddle R and Zola S (2007) 'A giant planet orbiting the 'extreme horizontal branch' star V391 Pegasi', *Nat*, 449, 189–191.

Siudek M, Batsch T, Castro-Tirado A J, Czyrkowski H, Cwiok M, Dabrowski R, Jelínek M, Kasprowicz G, Majcher A, Majczyna A, Malek K, Mankiewicz L, Nawrocki K, Opiela R, Piotrowski L W, Sokolowski M, Wawrzaszek R, Wrochna G, Zaremba M and Zarnecki A F (2011) 'Pi of the Sky Telescopes in Spain and Chile', *Acta Polytechnica*, 51, 64.

Smalley B, Kurtz D W, Smith A M S, Fossati L, Anderson D R, Barros S C C, Butters O W, Cameron A C, Christian D J, Enoch B, Faedi F, Haswell C A, Hellier C, Holmes S, Horne K, Kane S R, Lister T A, Maxted P F L, Norton A J, Parley N, Pollacco D, Simpson E K, Skillen I, Southworth J, Street R A, West R G, Wheatley P J and Wood P L (2011) 'SuperWASP observations of pulsating Am stars', *A&A*, 535, A3.

Smith A M S and WASP C (2014) 'The SuperWASP exoplanet transit survey', *Contributions of the Astronomical Observatory Skalnate Pleso*, 43, 500–512.

Söderhjelm S (1975) 'The three-body problem and eclipsing binaries - Application to algol and lambda Tauri', *A&A*, 42, 229–236.

Soszyński I, Dziembowski W A, Udalski A, Poleski R, Szymański M K, Kubiak M, Pietrzyński G, Wyrzykowski Ł, Ulaczyk K, Kozłowski S and Pietrukowicz P (2011a) 'The Optical Gravitational Lensing Experiment. The OGLE-III Catalog of Variable Stars. XI. RR Lyrae Stars in the Galactic Bulge', *Acta Astron*, 61, 1–23.

Soszyński I, Poleski R, Udalski A, Szymanski M K, Kubiak M, Pietrzynski G, Wyrzykowski L, Szewczyk O and Ulaczyk K (2008a) 'The Optical Gravitational Lensing Experiment. The OGLE-III Catalog of Variable Stars. I. Classical Cepheids in the Large Magellanic Cloud', *Acta Astron*, 58, 163–185.

Soszyński I, Poleski R, Udalski A, Szymański M K, Kubiak M, Pietrzyński G, Wyrzykowski Ł, Szewczyk O and Ulaczyk K (2010a) 'The Optical Gravitational Lensing Experiment. The OGLE-III Catalog of Variable Stars. VII. Classical Cepheids in the Small Magellanic Cloud', *Acta Astron*, 60, 17–39.

Soszyński I, Udalski A, Pietrukowicz P, Szymański M K, Kubiak M, Pietrzyński G, Wyrzykowski Ł, Ulaczyk K, Poleski R and Kozłowski S (2011b) 'The Optical Gravitational Lensing Experiment. The OGLE-III Catalog of Variable Stars. XIV. Classical and Type II Cepheids in the Galactic Bulge', *Acta Astron*, 61, 285–301.

Soszyński I, Udalski A, Pietrukowicz P, Szymański M K, Kubiak M, Pietrzyński G, Wyrzykowski Ł, Ulaczyk K, Poleski R and Kozłowski S (2013a) 'The Optical Gravitational Lensing Experiment. The OGLE-III Catalog of Variable Stars. Type II Cepheids in the Galactic Bulge - Supplement', *Acta Astron*, 63, 37–40.

Soszyński I, Udalski A, Szymański M K, Kubiak J, Pietrzyński G, Wyrzykowski Ł, Ulaczyk K and Poleski R (2010b) 'The Optical Gravitational Lensing Experiment. The OGLE-III Catalog of Variable Stars. IX. RR Lyr Stars in the Small Magellanic Cloud', *Acta Astron*, 60, 165–178.

Soszyński I, Udalski A, Szymański M K, Kubiak M, Pietrzyński G, Wyrzykowski Ł, Szewczyk O, Ulaczyk K and Poleski R (2008b) 'The Optical Gravitational Lensing Experiment. The OGLE-III Catalog of Variable Stars. II.Type II Cepheids and Anomalous Cepheids in the Large Magellanic Cloud', *Acta Astron*, 58, 293–312.

Soszyński I, Udalski A, Szymański M K, Kubiak M, Pietrzyński G, Wyrzykowski Ł, Szewczyk O, Ulaczyk K and Poleski R (2009a) 'The Optical Gravitational Lensing Experiment. The OGLE-III Catalog of Variable Stars. III. RR Lyrae Stars in the Large Magellanic Cloud', *Acta Astron*, 59, 1–18.

Soszyński I, Udalski A, Szymański M K, Kubiak M, Pietrzyński G, Wyrzykowski Ł, Szewczyk O, Ulaczyk K and Poleski R (2009b) 'The Optical Gravitational Lensing Experiment. The OGLE-III Catalog of Variable Stars. IV. Long-Period Variables in the Large Magellanic Cloud', *Acta Astron*, 59, 239–253.

Soszyński I, Udalski A, Szymański M K, Kubiak M, Pietrzyński G, Wyrzykowski Ł, Szewczyk O, Ulaczyk K and Poleski R (2009c) 'The Optical Gravitational Lensing Experiment. The OGLE-III Catalog of Variable Stars. V. R Coronae Borealis Stars in the Large Magellanic Cloud', *Acta Astron*, 59, 335–347.

Soszyński I, Udalski A, Szymański M K, Kubiak M, Pietrzyński G, Wyrzykowski Ł, Ulaczyk K and Poleski R (2010c) 'The Optical Gravitational Lensing Experiment. The OGLE-III Catalog of Variable Stars. VIII. Type II Cepheids in the Small Magellanic Cloud', *Acta Astron*, 60, 91–107.

Soszyński I, Udalski A, Szymański M K, Kubiak M, Pietrzyński G, Wyrzykowski

Ł, Ulaczyk K, Poleski R, Kozłowski S and Pietrukowicz P (2011c) 'The Optical Gravitational Lensing Experiment. The OGLE-III Catalog of Variable Stars. XIII. Long-Period Variables in the Small Magellanic Cloud', *Acta Astron*, 61, 217–230.

Soszyński I, Udalski A, Szymański M K, Kubiak M, Pietrzyński G, Wyrzykowski Ł, Ulaczyk K, Poleski R, Kozlowski S, Pietrukowicz P and Skowron J (2013b) 'The Optical Gravitational Lensing Experiment. The OGLE-III Catalog of Variable Stars. XV. Long-Period Variables in the Galactic Bulge', *Acta Astron*, 63, 21–36.

Stellingwerf R F (1978) 'Period determination using phase dispersion minimization', *ApJ*, 224, 953–960.

Stepień K (2006) 'The Low-Mass Limit for Total Mass of W UMa-type Binaries', *Acta Astron*, 56, 347–364.

Stepień K and Gazeas K (2012) 'Evolution of Low Mass Contact Binaries', *Acta Astron*, 62, 153–177.

Sterken C (1996a) 'Ap and roAp stars', in *Light Curves of Variable Stars. A Pictorial Atlas*, edited by Sterken C and Jaschek C (Cambridge University Press), pp. 112–117.

Sterken C (1996b) 'The classification of variable stars', in *Light Curves of Variable Stars. A Pictorial Atlas*, edited by Sterken C and Jaschek C (Cambridge University Press), pp. 8–20.

Sterken C and Jaschek C (1996) *Light Curves of Variable Stars, A Pictorial Atlas* (Cambridge University Press, Cambridge).

Stibbs D W N (1950) 'A study of the spectrum and magnetic variable star HD 125248', *MNRAS*, 110, 395–404.

Szabó R, Kolláth Z, Molnár L, Kolenberg K and Kurtz D W (2013) 'Period Doubling in Kepler RR Lyrae Stars', in *Stellar Pulsations: Impact of New Instrumentation and New Insights*, edited by Suárez J C, Garrido R, Balona L A and Christensen-Dalsgaard J (Springer-Verlag Berlin Heidelberg), pp. 81–84.

Szymański M, Kubiak M and Udalski A (2001) 'Contact Binaries in OGLE-I Database', *Acta Astron*, 51, 259–277.

Tamuz O, Mazeh T and Zucker S (2005) 'Correcting systematic effects in a large set of photometric light curves', *MNRAS*, 356, 1466–1470.

Tas G, Sipahi E, Dal H A, Goker U D, Tigrak E, Yigen S, Ozdarcan O, Topcu A T, Gungor C, Celik S and Evren S (2004) 'Times of Minima for Some Eclipsing Binaries', *Information Bulletin on Variable Stars*, 5548, 1.

Terrell D (2014) 'APASS colors for 112 short-period W UMa binary candidates', *Information Bulletin on Variable Stars*, 6101, 1.

Terrell D and Gross J (2014) 'Photometry of GSC 3408-0735: a W UMa System Near the Short-period Limit', *Information Bulletin on Variable Stars*, 6104, 1.

Thomas N L, Norton A J, Pollacco D, West R G, Wheatley P J, Enoch B and Clarkson W I (2010) 'SuperWASP observations of long timescale photometric variations in cataclysmic variables', *A&A*, 514, A30.

Tokovinin A (2014a) 'From Binaries to Multiples. I. Data on F and G Dwarfs within 67 pc of the Sun', *AJ*, 147, 86.

Tokovinin A (2014b) 'From Binaries to Multiples. II. Hierarchical Multiplicity of F and G Dwarfs', *AJ*, 147, 87.

Torres G (2013) 'Fundamental properties of lower main-sequence stars', *Astron Nachr*, 334, 4–9.

Torres G, Andersen J and Giménez A (2010) 'Accurate masses and radii of normal stars: modern results and applications', *A&AR*, 18, 67–126.

Tylenda R, Hajduk M, Kamiński T, Udalski A, Soszyński I, Szymański M K, Kubiak M, Pietrzyński G, Poleski R, Wyrzykowski Ł and Ulaczyk K (2011) 'V1309 Scorpii: merger of a contact binary', *A&A*, 528, A114.

Udalski A (2003) 'The Optical Gravitational Lensing Experiment. Real Time Data Analysis Systems in the OGLE-III Survey', *Acta Astron*, 53, 291–305.

Udalski A, Kubiak M and Szymanski M (1997) 'Optical Gravitational Lensing Experiment. OGLE-2 – the Second Phase of the OGLE Project', *Acta Astron*, 47, 319–344.

Udalski A, Szymanski M K, Soszyński I and Poleski R (2008) 'The Optical Gravitational Lensing Experiment. Final Reductions of the OGLE-III Data', *Acta Astron*, 58, 69–87.

Uytterhoeven K, Moya A, Grigahcène A, Guzik J A, Gutiérrez-Soto J, Smalley B, Handler G, Balona L A, Niemczura E, Machado L F, Benatti S, Chapellier E, Tkachenko A, Szabó R, Suárez J C, Ripepi V, Pascual J, Mathias P, Martín-Ruíz S, Lehmann H, Jackiewicz J, Hekker S, Gruberbauer M, García R A, Dumusque X, Díaz-Fraile D, Bradley P, Antoci V, Roth M, Leroy B, Murphy S J, Cat P D, Cuypers J, Kjeldsen H, Christensen-Dalsgaard J, Breger M, Pigulski A, Kiss L L, Still M, Thompson S E and van Cleve J (2011) 'The Kepler characterization of the variability among A- and F-type stars. I. General overview', *A&A*, 534, 125.

Valdes F, Gupta R, Rose J A, Singh H P and Bell D J (2004) 'The Indo-US Library of Coudé Feed Stellar Spectra', *ApJS*, 152, 251–259.

van den Besselaar E J M, Greimel R, Morales-Rueda L, Nelemans G, Thorstensen J R, Marsh T R, Dhillon V S, Robb R M, Balam D D, Guenther E W, Kemp

J, Augusteijn T and Groot P J (2007) 'DE Canum Venaticorum: a bright, eclipsing red dwarf-white dwarf binary', *A&A*, 466, 1031–1041.

Voges W, Aschenbach B, Boller T, Bräuninger H, Briel U, Burkert W, Dennerl K, Englhauser J, Gruber R, Haberl F, Hartner G, Hasinger G, Kürster M, Pfeffermann E, Pietsch W, Predehl P, Rosso C, Schmitt J H M M, Trümper J and Zimmermann H U (1999) 'The ROSAT all-sky survey bright source catalogue', *A&A*, 349, 389–405.

Vogt N (1996) 'Dwarf novae', in *Light Curves of Variable Stars. A Pictorial Atlas*, edited by Sterken C and Jaschek C (Cambridge University Press), pp. 148–161.

Völschow M, Banerjee R and Hessman F V (2014) 'Second generation planet formation in NN Serpentis?', *A&A*, 562, A19.

Walkowicz L M (2012) 'The Future of the Time Domain with LSST', in *New Horizons in Time-Domain Astronomy*, edited by Griffin R E M, Hanisch R J and Seaman R (Cambridge University Press, Cambridge, UK), pp. 158–158.

Welsh W F, Orosz J A, Carter J A, Fabrycky D C, Ford E B, Lissauer J J, Prša A, Quinn S N, Ragozzine D, Short D R, Torres G, Winn J N, Doyle L R, Barclay T, Batalha N, Bloemen S, Brugamyer E, Buchhave L A, Caldwell C, Caldwell D A, Christiansen J L, Ciardi D R, Cochran W D, Endl M, Fortney J J, III T N G, Gilliland R L, Haas M R, Hall J R, Holman M J, Howard A W, Howell S B, Isaacson H, Jenkins J M, Klaus T C, Latham D W, Li J, Marcy G W, Mazeh T, Quintana E V, Robertson P, Shporer A, Steffen J H, Windmiller G, Koch D G and Borucki W J (2012) 'Transiting circumbinary planets Kepler-34 b and Kepler-35 b', *Nat*, 481, 475–479.

Whitelock P A (1996a) 'Mira variables', in *Light Curves of Variable Stars. A*

Pictorial Atlas, edited by Sterken C and Jaschek C (Cambridge University Press), pp. 106–108.

Whitelock P A (1996b) 'Semi-regular and slow irregular variables', in *Light Curves of Variable Stars. A Pictorial Atlas*, edited by Sterken C and Jaschek C (Cambridge University Press), pp. 98–105.

Wils P, di Scala G and Otero S A (2007) 'NSVS 14256825: A New HW Vir Type System', *Information Bulletin on Variable Stars*, 5800, 1.

Wilson R E (1994) 'Understanding Binary Stars Via Light Curves', *International Amateur-Professional Photoelectric Photometry Communications*, 55, 1–20.

Wilson R E and Devinney E J (1971) 'Realization of Accurate Close-Binary Light Curves: Application to MR Cygni', *ApJ*, 166, 605–619.

Wittenmyer R A, Horner J and Marshall J P (2013) 'On the dynamical stability of the proposed planetary system orbiting NSVS 14256825', *MNRAS*, 431, 2150–2154.

Wolszczan A and Frail D A (1992) 'A planetary system around the millisecond pulsar PSR1257 + 12', *Nat*, 355, 145–147.

Wood J H, Zhang E H and Robinson E L (1993) 'HW Virginis - A short period eclipsing binary containing an sdB star', *MNRAS*, 261, 103–112.

Woźniak P R, Vestrand W T, Akerlof C W, Balsano R, Bloch J, Casperson D, Fletcher S, Gisler G, Kehoe R, Kinemuchi K, Lee B C, Marshall S, McGowan K E, McKay T A, Rykoff E S, Smith D A, Szymanski J and Wren J (2004) 'Northern Sky Variability Survey: Public Data Release', *AJ*, 127, 2436–2449.

Wraight K T, Bewsher D, White G J, Nowotny W, Norton A J and Paladini C (2012a) 'STEREO observations of long period variables', *MNRAS*, 426, 816–832.

Wraight K T, Fossati L, Netopil M, Paunzen E, Rode-Paunzen M, Bewsher D, Norton A J and White G J (2012b) 'A photometric study of chemically peculiar stars with the STEREO satellites - I. Magnetic chemically peculiar stars', *MNRAS*, 420, 757–772.

Wraight K T, Fossati L, White G J, Norton A J and Bewsher D (2012c) 'Bright low mass eclipsing binary candidates observed by STEREO', *MNRAS*, 427, 2298–2307.

Wraight K T, White G J, Bewsher D and Norton A J (2011) 'STEREO observations of stars and the search for exoplanets', *MNRAS*, 416, 2477–2493.

Zasche P and Wolf M (2013) 'The first analysis of extragalactic binary-orbit precession', *A&A*, 559, A41.

Zhang X B, Deng L C, Wang K, Yan Z Z, Tian J F, Peng Y J, Pan Y, Luo Z Q, Sun J J, Liu Q L, Xin H Q and Zhou Q (2014) 'NSVS4484038, a Contact Binary System at the Short-period Cutoff', *AJ*, 148, 40.

Zorotovic M and Schreiber M R (2013) 'Origin of apparent period variations in eclipsing post-common-envelope binaries', *A&A*, 549, A95.